Numerical Analysis of the Dynamic Response of Existing Railway Bridges.

Gunnstein Thomas Frøseth

NTNU

Norwegian University of Science and Technology
Faculty of Engineering Science and Technology
Department of Structural Engineering

Masteroppgave for Stud.techn. Gunnstein Thomas Frøseth, våren 2014

Numerisk analyse av den dynamiske responsen til eksisterende jernbanebroer i det norske jernbanenettet

Numerical analysis of the dynamic response of existing railway bridges in the Norwegian railway network

Det norske jernbanenettet består i dag av mer enn 4000 km med spor der ca. 2500 km er elektrifisert og 250 km er dobbeltspor. Videre har den norske nasjonale jernbanenettet mer 2500 broer og er i vekst. I dag blir over 12 millioner tonn gods transportert på jernbanenettet hvert år med et mål om å doble dette innen 2020. Dermed er det av stor betydning å sikre de investeringene som er gjort i norsk jernbaneinfrastruktur. Kravene til jernbanenettet vil øke, spesielt vil en økning i antall avganger og høyere hastigheter øke etterspørselen av detaljert kunnskap om de eksisterende konstruksjonene.

   Oppgaven skal fokusere på eksisterende jernbanebruer. I det norske jernbanenettet eksisterer det mange forskjellige brosystemer med varierende levetid på grunn av varierende degradering. Ved å introdusere nye overvåkningssystemer og etablere numeriske modeller til disse broene kan deres tilstand bli vurdert i dag så vel som deres prestasjoner ved høyere belastning og høyere hastighet. Det er derfor ønskelig å etablere numeriske beregningsmodeller som kan evaluere de statiske og dynamiske egenskapene til ulike jernbanebruer. Fokus vil være på ulike lastmodeller og ulik detaljeringsgrad på de numeriske modellene. Tanken er at sentrale parameterer i den dynamiske responsen skal kunne stilles mot tilsvarende målte verdier. Her er etableringen av dempningsmodeller og komplekse egenfrekvenser viktig å vurdere. Dette skal så implementeres og evalueres i et FE-program. Som del av oppgaven er det tenkt å gjennomføre en kartlegging av ulike laster (statiske og dynamiske) som er spesielle for jernbanebruer, state-of-the-art litteraturstudie. De valgte bruene skal så kontrolleres med ulike laster mot eksisterende regelverk der ulike aktuelle problemstillinger trekkes frem og utforskers. Spesielt er problemstillinger rundt vedlikeholdsbehov og levetidsevaluering noe som bør trekkes frem. Det bør redegjøres for opprinnelige intensjoner og videreføre/utvikle behovene for dagens bruk.

Litteratur studie, analytiske og numerisk modellering, State-of-the-art:
- Aktuelle brotyper, antall og karakteristikk
- Elementmetodemodellering, Abaqus Last modellering (tidsplan og frekvensplan)
- Etablere de dynamiske egenskaper til aktuell bro
- Ulike typer dempingsmodeller, fordeler og ulemper
- Egenverdiproblemet, spesielt utledning og bruk av dempede egenfrekvenser
- Historisk evaluering av utviklingen til laststandarder, hvilke, endringer og nye kontroller
- Kontroll av eksisterende bro, bruk av Abaqus til modellering og eventuell parameterstudie
- Aktuelle problemstillinger til å fokusere på
  - endring i laster, spenningsvekslinger, spesielt utsatte komponenter, vedlikeholdsstøtte
- Muligheter for enkle kontroller, overslag ved hjelp av handberegninger/forenklede metoder

Det vil være opp til kandidaten at selv vektlegge de enkelte delene i oppgaven der oppgaven utføres i henhold til retningslinjer for utførelse av hovedoppgaven ved Institutt for konstruksjonsteknikks gitt på instituttets hjemmesider, **besvarelsen skal leveres innen 10. juni 2014**

Faglærer, Anders Rönnquist, NTNU

Sammendrag

Jernbanen er en viktig del av infrastrukturen i dagens samfunn og for imøtekomme dagens og morgendagens krav til jernbanen er et behov for å styrke og vurdere tilstanden til eksisterenede jernbanebroer. Denne oppgaven fokuserer på numerisk analyse av den dynamiske responsen til jernbanebroer. Oppgaven vurderer forskjellige viskøse dempningsmodeller siden de representer en viktig del av de dynamiske egenskapene til jernbanebroer. Videre studeres problemet med bevegelige laster, og de kvalitative forskjellene til tre last modeller blir etablert gjennom studier på en fritt opplagt bjelke. Resonans fenomener assosiert med bevegelige laster blir også vurdert. Deretter blir et studie på Tallerås jernbanebro presentert, der de dynamiske egenskapene og oppførselen til broa blir studert gjennom en tre dimensjonal element model i Abaqus. Resultatene viser at forskjellen mellom de ulike last modellene skyldes graden av treghetskrefter som er inkludert og mengden energi som dissiperes av modellen. Studien viser at resonans effekter indusert i Tallerås er som følge av den gjentagende belastningen fra togets aksler. Resultatene viser også at det er viktig å inkludere sporet i den dynamiske analysen av fagverksbroer i stål. Oppgaven avsluttes med forslag til videre arbeid.

Abstract

The railway is an important part of the infrastructure in todays society and there is a need to increase the capacity and verify the existing railway network to face the challenges of tomorrow. To meet todays and the future demand set upon the railway network, there is a need to strengthen and assess the condition of existing railway bridges. This thesis focuses on numerical analysis of the dynamic response of railway bridges. First, viscous damping models are considered since they represent an important part of the dynamic properties of the bridge. Then the moving load problem is investigated, and studies on the dynamic response of a simply supported beam under different load models are conducted to determine the qualitative difference between the moving force, moving mass and the sprung mass model. The resonance phenomena induced by the moving loads are also considered. Finally, a case study is presented where the dynamic properties and behavior the Tallerås railway bridge is determined by establishing a three dimensional finite element model of the bridge in the finite element code Abaqus. The results show that the difference between the load models are the level of inertia effects included and the amount of energy dissipated by the load model. The case study indicate that resonance effects induced in the Tallerås railway bridge is due to the repeated loading from railway axles. The results also show that it is important to include the track in dynamic analysis of steel truss bridges. The thesis finishes by suggesting suitable subjects for further work.

Acknowledgements

I would like to thank my supervisor Associate Professor Anders Rönnquist and co-supervisor Associate Professor Ole Øiseth for the opportunity to conduct this thesis under their excellent supervision. Both of them have willingly answered any of my questions and also provided the motivation to finish this thesis. A special thanks to Associate Professor Anders Rönnquist for the long and fruitful discussions on a diverse range of topics.

I would also like to thank the people at the bridge department of the Norwegian Railway Administration, and especially Arne Vik, Pål Buskum and Åsmund Tøsse for their contribution to this work.

Finally, I would like to express my deepest gratitude to Simone Strindberg who has proof read this work and given me the motivation to study all these years.

Contents

Chapter 1

Introduction

The railway is an important part of the infrastructure in todays society. The challenges associated with growing population, climate change and an ever rising need for transport of goods means that the railway will have an ever bigger role in the future. To meet the future demand set upon the railway network, it is necessary not only to construct new railway, but also to strengthen and assess the condition of the existing railway network. An essential part of the railway network are railway bridges. Studies on the railway network in Europe show that more than 60% of the railroad bridges are more than 50 years old [1].

1.1 Problem description

To assess the condition of existing railway bridges and to determine appropriate measures to strengthen these bridges, it is necessary to establish and verify numerical models which are able to reproduce the dynamic behavior of railway bridges under load from moving trains.

1.2 Scope of the thesis

The overall focus of this thesis is on numerical analysis of the dynamic response of railway bridges. The dynamic response of railway bridges is dependent on the dynamic properties of the bridge and the loading imposed by the train.

The dynamic properties of the bridge are determined by the inertial, elastic and dissipative properties of the bridge. The inertial and elastic properties are relatively easily determined once the material and geometry of the bridge is known. The dissipative properties on the other hand is generally a more difficult subject. The first topic of this thesis is therefore to investigate different damping models for dynamic analysis of railway bridges.

In order to verify that the numerical model represents the dynamic properties of the actual bridge, it is necessary to conduct real life measurements on the bridge. The measurements of the bridge are used to calibrate the numerical model through considerations about damping and resonance frequencies. This thesis will not conduct any real life experiments, but rather look at the theoretical background to extract the damping ratios and natural frequencies from the numerical model. The second topic of this thesis is therefore

the quadratic eigenvalue problem and the extraction of natural frequencies and damping ratios.

The train and the loading it imposes on the bridge is then considered. Different ways to represent the train in a numerical analysis is reviewed and dynamic effects associated with moving loads are considered. The third topic is therefore on load models and dynamic effects associated with moving loads.

Finally, a case study of an existing railway bridge will be conducted where the above main topics will be combined to determine the dynamic properties and response of the Tallerås railway bridge.

1.3   Structure of the report

The layout of this thesis is given below.

Chapter 2   briefly considers the single degree of freedom system. Through the derivation of the single degree of freedom system, important concepts and terminology will be introduced which will aid the discussion in the following chapters.

Chapter 3   considers multi degree of freedom systems, viscous damping models and the quadratic eigenvalue problem.

Chapter 4   reviews different methods to model the train and the difference between the load models and their effect on the structure. The section explains how the load models are implemented in Abaqus. The phenomena of resonance from the moving loads is discussed.

Chapter 5   is a study of the Tallerås railway bridge. The work done in the previous chapters will be extended to a full three dimensional model with a real bridge and trains. Different load models, tracks and dynamic phenomena will be discussed.

Chapter 6   contains concluding remarks about the main points found in the thesis and further work.

Chapter 2

Single degree of freedom system

This chapter briefly considers the single degree of freedom (SDOF) dynamic system. Through the derivation of the single degree of freedom system, important concepts and terminology will be introduced which will aid the discussion in the following chapters.

2.1 Viscously damped single degree of freedom systems

In the derivation of the dynamic response of a SDOF system it is assumed that the energy dissipation from the system can be represented by viscous damping. After the SDOF system with viscous damping is derived, non-viscous damping is considered briefly. Figure 2.1a shows a wagon with mass m connected to the surroundings through a spring with stiffness k and a viscous dashpot with damping constant c. The displacement of the wagon is uniquely defined by the horizontal displacement $u(t)$, i.e it is a SDOF system. An external force $P(t)$ is working on the wagon, and it is assumed that there is no friction associated with movement of the wagon. The spring exerts a force f_S on the body equal to the product of the stiffness coefficient k and displacement $u(t)$. Similarly the dashpot exerts a force f_D on the wagon equal to the product of the damping coefficient c and velocity $\dot{u}(t)$. By d'Alemberts principle, the inherent inertia of any body may be defined as a force f_I opposite in direction and equal in magnitude to the product of the mass m and the acceleration $\ddot{u}(t)$. The free body diagram (FBD) in figure 2.1b shows all forces working on the system.
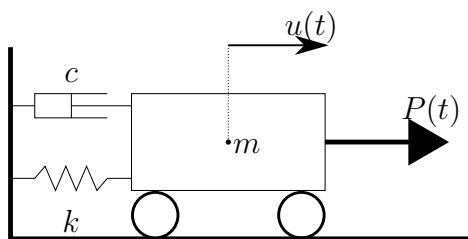
(a) General SDOF system.
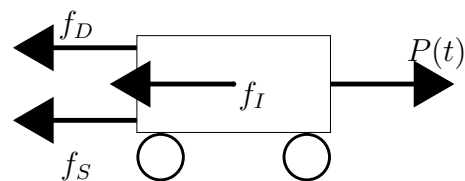
(b) Free body diagram of the SDOF system.

Figure 2.1: The figure shows a single degree of freedom system, and the definition used in the derivation of the response of a single degree of freedom system.

Taking force equilibrium in the horizontal direction yields the equation of motion for a general SDOF, see equation (2.1).

$$m\ddot{u}(t) + c\dot{u}(t) + ku(t) = P(t) \tag{2.1}$$

The solution of equation (2.1) consists of a complementary solution and a particular solution. The complementary solution is obtained by solving the homogeneous version of equation (2.1), i.e $P(t) = 0$, see equation (2.2).

$$m\ddot{u}(t) + c\dot{u}(t) + ku(t) = 0 \tag{2.2}$$

The general solution of equation (2.2) is $u(t) = Ae^{\lambda t}$, the non-trivial solution is then given by the characteristic equation shown below, equation (2.3a).

$$\lambda^2 + \frac{c}{m}\lambda + \frac{k}{m} = 0 \tag{2.3a}$$

$$\lambda = -\frac{c}{2m} \pm \sqrt{\left(\frac{c}{2m}\right)^2 - \frac{k}{m}} \tag{2.3b}$$

It is here appropriate to define the natural frequency[1] ω_n, the critical damping c_{cr} and the damping ratio ξ.

$$\omega_n = \sqrt{\frac{k}{m}} \tag{2.4a}$$

$$c_{cr} = 2m\omega_n \tag{2.4b}$$

$$\xi = \frac{c}{c_{cr}} \tag{2.4c}$$

Introducing equations (2.4) into equation (2.3b) yields equation (2.5).

$$\lambda = -\xi\omega_n \pm \omega_n\sqrt{\xi^2 - 1} \tag{2.5}$$

From equation (2.5), three characteristic solutions to equation (2.1) emerges depending on the value of ξ. If $\xi = 1$, the radical in the characteristic equation (2.5) vanishes and the system is said to be *critically damped*. If the damping is larger than critical damping, i.e $\xi > 1$, the characteristic equation will have two real valued roots and the system is said to be *overdamped*. If the damping is less than the critical damping, i.e $\xi < 1$ the characteristic equation will have two complex roots and the system is said to be *underdamped*. The solution for the damped free vibrating SDOF system is given by equation (2.6), where A and B are constant determined by initial conditions, $u(0)$ and $\dot{u}(0)$.

$$u(t) = \begin{cases} e^{-\xi\omega_n t}\left[A\cos(\omega_d t) + B\sin(\omega_d t)\right] & \text{for } \xi < 1 \\ e^{-\omega_n t}\left[A + B\,t\right] & \text{for } \xi = 1 \\ e^{-\xi\omega_n t}\left[A\cosh(\bar{\omega}t) + B\sinh(\bar{\omega}t)\right] & \text{for } \xi > 1 \end{cases} \tag{2.6}$$

---

[1] ω is strictly speaking known as the circular or angular frequency. The distinction is important when the frequency $f = \frac{\omega}{2\pi}$ is used. In this thesis, the term *frequency* will be used about the angular frequency ω, in cases where f is also used, the context will clearly avoid any ambiguity.

Where $\bar{\omega} = \omega_n\sqrt{\xi^2 - 1}$ and w_d, known as the damped natural frequency, is defined by equation (2.7).

$$w_d = \omega_n\sqrt{1 - \xi^2} \tag{2.7}$$

The damping ratio ξ for a particular system may be determined by measurements or by making an educated guess. Over the years, measurements have been made on a wide range of structures, such that a rational approach to estimating ξ for a structure, would be to utilize data aquired for a similar structure to the one being analyzed. For common engineering structures, where there are no special devices for added damping, the damping ratio ξ is seldom larger than 15%, see [2, p.454].
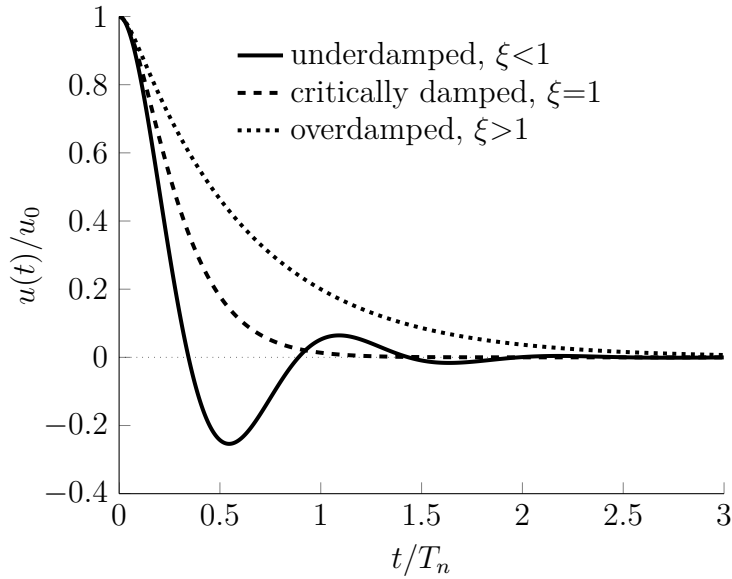
Figure 2.2: The figure illustrates the characteristic response $u(t)$ of an underdamped, critically damped and an overdamped free vibrating SDOF system.

Figure 2.2 shows the characteristic response of an underdamped, a critically damped and an overdamped SDOF system. The critically damped system returns to rest earlier than both the underdamped and the overdamped configuration. The overdamped system has similar characteristics to the critically damped system, but returns to rest at a much lower rate. The underdamped system is different from the two other system in that it oscillates around the final position before it returns to rest.

The particular solution of equation (2.1) depends on the nature of the loading. In the continuation it is assumed that the loading is a simple harmonic, see equation (2.8).

$$P(t) = P_0 \sin(\Omega t) \tag{2.8}$$

The general form of the particular solution is $u(t) = G_1 \cos(\Omega t) + G_2 \sin(\Omega t)$, which means that the particular solution of equation (2.1) is given by equation (2.9).

$$u(t) = \frac{P_0}{k}\frac{1}{(1 - \beta^2)^2 + (2\xi\beta)^2}\left[(1 - \beta^2)\sin(\Omega t) - 2\xi\beta\cos(\Omega t)\right] \tag{2.9}$$

where the frequency ratio β is defined by equation (2.10).

$$\beta = \frac{\Omega}{\omega_n} \tag{2.10}$$

Alternatively, the particular solution given by equation (2.9) may be rewritten through trigonometric identies to be an expression of a single sine with an amplitude and a phase angle, see equation (2.11).

$$u(t) = \frac{P_0}{k} \frac{1}{\sqrt{(1 - \beta^2)^2 + (2\xi\beta)^2}} \sin(\Omega t - \phi) \tag{2.11}$$

where the phase angle ϕ is defined by equation (2.12).

$$\phi = \arctan \frac{2\xi\beta}{1 - \beta^2} \tag{2.12}$$

The amplitude of the alternative form presented by equation (2.11) may be viewed as the product of the static deflection $u^{st} = \frac{P_0}{k}$ to a static load P_0 and an dynamic amplification factor $D(\beta, \xi)$ defined by equation (2.13).

$$D(\beta, \xi) = \frac{1}{\sqrt{(1 - \beta^2)^2 + (2\xi\beta)^2}} \tag{2.13}$$

If there is no damping and the frequency ratio is equal to unity, i.e $\beta = 1$ the dynamic amplification factor goes to infinity, see figure 2.3. The effect that the response of a system radically increases at some load frequencies is known as *resonance*, and the frequency which the response is largest is know as the *resonance frequency* of the system. This means that the resonance frequency for an undamped system is the natural frequency, ω_n. Equation (2.13) also shows that for a viscously damped system, the dynamic amplification is finite and the resonance frequency is lower than the natural frequency of the system. This effect is shown in figure 2.3 for $\xi = 0.2$ which gives resonance frequency at about 96% of the natural frequency.

As mentioned earlier in this chapter, a damping ratio of $\xi = 0.2$ is high for common engineering structures, and it should be noted that even with this high damping ratio the effect on the resonance frequency and the damped natural freqeuency given by equation (2.7) is rather modest for the SDOF system. Although this is illustrated for the SDOF system, this conclusion cannot be easily extended to MDOF systems. In dynamic systems, the resonance frequencies are important quantities in all stages of designing new structures and in the system identification of existing structures. Chapter 3 investigates the effect of damping on the resonance frequencies of a MDOF system by evaluating the quadratic eigenvalue problem.

2.2 Non-viscous damping

Non-viscous damping may roughly be divided into *hysteretic*, *Coulomb* or *radiation* damping. Radiation damping is associated with energy dissipation to the boundaries of the dynamic system, for instance energy loss to the surrounding soil at the supports of a railway bridge. Coulomb damping is associated with dry friction, such as relative movement in the joints of a railway bridge. Hysteretic damping is associated with energy loss due
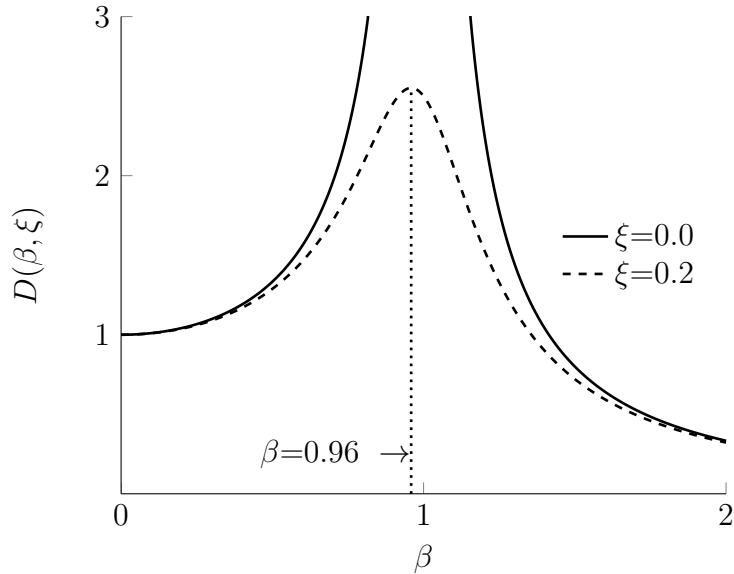
Figure 2.3: The figure shows the dynamic amplification factor plotted versus the frequency ratio for two different values of the damping ratio. No damping yields an infinite dynamic amplification factor at β equal to unity, while any damping yields a finite dynamic amplification and an resonance frequency lower than the natural frequency.

to plastic deformation and internal friction at material level. The non-viscous damping models all have applications which are important in dynamical systems, and there exists vast amount of literature on each of them. It is also important to note that at low levels of damping the difference between the damping models vanishes, such that either model may be utilized to model the energy dissipation from a system [3, p.389].

A number of researchers have studied damping in bridges and even railway bridges in particular. Frýba [4, chap. 5] discusses the difference between the viscous, hysteretic and Coloumb damping models, and concludes that because of the relatively low damping values associated with railway bridges, the practical difference between the models are negligible. In addition, the viscous damping model is more easily represented in the dynamic equations than the other models, and relatively easily implemented in finite element codes.

Although the author recognizes the possible applications of the non-viscous damping models in dynamic simulations of railway bridges, there is also a need to limit the scope and extend of this thesis. Combined with the above discussion, the choice is made to focus further attention on viscous damping models.

Chapter 3

Multi degree of freedom systems

A multi degree of freedom system (MDOF) is defined as a system where there are more than one degree of freedom. This chapter start off by deriving the property matrices $\boldsymbol{M}$ and $\boldsymbol{K}$ in the finite element context, next some of the characteristics of the mass and stiffness matrix are established. After this, the linear eigenvalue problem will be solved because it is important in the following discussion on viscous damping models in MDOF systems. At the end of this section, the quadratic eigenvalue problem will be solved and the use of the quadratic eigenvalue problem and characteristics of the solution with different damping models will be discussed.

3.1 Equation of motion for multi degree of freedom system.

A general continuum may be discretized into a MDOF system by what is known as the finite element method (FEM). The basic idea behind the finite element method is to divide the continuum into a finite set of elements. Within each element the displacement field $\boldsymbol{w}$ is described by a set nodes $\boldsymbol{d}$ and continuous interpolation functions $\boldsymbol{N}$ between those nodes, see equation (3.1).

$$\boldsymbol{w} = \boldsymbol{N}\boldsymbol{d} \tag{3.1}$$

The strain field $\boldsymbol{\epsilon}$ is obtained by appropriate strain-displacement relations, i.e by partial derivates of the displacement field. On matrix form the strain-displacement relation is defined by the operator $\boldsymbol{\partial}$, such that the strain field is defined by equation (3.2).

$$\boldsymbol{\epsilon} = \boldsymbol{\partial}\boldsymbol{w} = \boldsymbol{\partial}\boldsymbol{N}\boldsymbol{d} = \boldsymbol{B}\boldsymbol{d} \tag{3.2}$$

where $\boldsymbol{B} = \boldsymbol{\partial}\boldsymbol{N}$ is known as the strain-displacement matrix. The constitutive matrix $\boldsymbol{E}$ gives the relationship between the stress field $\boldsymbol{\sigma}$ and the strain field $\boldsymbol{\epsilon}$, see equation (3.3).

$$\boldsymbol{\sigma} = \boldsymbol{E}\boldsymbol{\epsilon} \tag{3.3}$$

Imposing the admissible virtual displacement $\delta\boldsymbol{w} = \boldsymbol{N}\delta\boldsymbol{d}$ on an element, yields internal virtual work δW_i, equal to the virtual strain energy, see equation (3.4).

$$\delta W_i = \int_V \delta\boldsymbol{\epsilon}^T \boldsymbol{\sigma} \, \mathrm{d}V = \delta\boldsymbol{d}^T \int_V \boldsymbol{B}^T \boldsymbol{E} \boldsymbol{B} \, \mathrm{d}V \, \boldsymbol{d} \tag{3.4}$$

Similarly, the virtual displacement produces external virtual work δW_e, which may be found by accounting for body forces $\boldsymbol{F}_B$ and surface tractions $\boldsymbol{F}_T$ working on the element and concentrated forces $\boldsymbol{p}^k$ working directly at the nodes. If the inertia forces $(-\ddot{\boldsymbol{w}})\rho\,\mathrm{d}V$, defined by the density $\rho = \frac{\mathrm{d}m}{\mathrm{d}V}$ and the acceleration $\ddot{\boldsymbol{w}} = \boldsymbol{N}\ddot{\boldsymbol{d}}$, are separated from the body forces, the external virtual work is given by equation (3.5)

$$\delta W_e = -\int_V \delta\boldsymbol{w}^T \rho\ddot{\boldsymbol{w}}\,\mathrm{d}V + \int_V \delta\boldsymbol{w}^T \boldsymbol{F}_B\,\mathrm{d}V + \int_S \delta\boldsymbol{w}^T \boldsymbol{F}_T\,\mathrm{d}S + \delta\boldsymbol{d}^T \boldsymbol{p}^k$$

$$= \delta\boldsymbol{d}^T \left(-\int_V \rho\boldsymbol{N}^T\boldsymbol{N}\,\mathrm{d}V\,\ddot{\boldsymbol{d}} + \int_V \boldsymbol{N}^T \boldsymbol{F}_B\,\mathrm{d}V + \int_S \boldsymbol{N}^T \boldsymbol{F}_T\,\mathrm{d}S + \boldsymbol{p}^k \right) \qquad (3.5)$$

Equation (3.4) and equation (3.5) together with the principle of virtual work, $\delta W_i = \delta W_e$, yields the equation of motion for the element, see equation (3.6)

$$\boldsymbol{m}\ddot{\boldsymbol{d}} + \boldsymbol{k}\boldsymbol{d} = \boldsymbol{p} \qquad (3.6)$$

where $\boldsymbol{m}$ is the mass matrix of the element, $\boldsymbol{k}$ is the stiffness matrix of the element and $\boldsymbol{p}$ is the load vector of the element, all defined by equations (3.7).

$$\boldsymbol{m} = \int_V \rho\boldsymbol{N}^T\boldsymbol{N}\,\mathrm{d}V \qquad (3.7a)$$

$$\boldsymbol{k} = \int_V \boldsymbol{B}^T\boldsymbol{E}\boldsymbol{B}\,\mathrm{d}V \qquad (3.7b)$$

$$\boldsymbol{p} = \int_V \boldsymbol{N}^T\boldsymbol{F}_B\,\mathrm{d}V + \int_S \boldsymbol{N}^T\boldsymbol{F}_T\,\mathrm{d}S + \boldsymbol{p}^k \qquad (3.7c)$$

At the system level, there exists another set of degrees of freedom $\boldsymbol{u}$. The system level degrees of freedom can be related to the elemental degrees of freedom $\boldsymbol{d}_j$ of element j, by the connectivity matrix $\boldsymbol{a}_j$, see equation (3.8).

$$\boldsymbol{d}_j = \boldsymbol{a}_j\boldsymbol{u} \qquad (3.8)$$

Introducing equation (3.8) into equation (3.6), premultiplying by $\boldsymbol{a}_j^T$ and summing over all J elements in the system, the equation of motion for the system is obtained, see equation (3.9)

$$\boldsymbol{M}\ddot{\boldsymbol{u}} + \boldsymbol{K}\boldsymbol{u} = \boldsymbol{P} \qquad (3.9)$$

Where $\boldsymbol{M}$ is the *consistent* mass matrix of the system, $\boldsymbol{K}$ is the stiffness matrix of the system and $\boldsymbol{P}$ is the load vector of the system, all defined by equations (3.10)

$$\boldsymbol{M} = \sum_{j=1}^{J} \boldsymbol{a}_j^T \boldsymbol{m}_j \boldsymbol{a}_j = \sum_{j=1}^{J} \boldsymbol{a}_j^T \int_{V_j} \rho\boldsymbol{N}_j^T\boldsymbol{N}_j\,\mathrm{d}V\,\boldsymbol{a}_j \qquad (3.10a)$$

$$\boldsymbol{K} = \sum_{j=1}^{J} \boldsymbol{a}_j^T \boldsymbol{k}_j \boldsymbol{a}_j = \sum_{j=1}^{J} \boldsymbol{a}_j^T \int_{V_j} \boldsymbol{B}_j^T\boldsymbol{E}_j\boldsymbol{B}_j\,\mathrm{d}V\,\boldsymbol{a}_j \qquad (3.10b)$$

$$\boldsymbol{P} = \sum_{j=1}^{J} \boldsymbol{a}_j^T \boldsymbol{p}_j = \sum_{j=1}^{J} \boldsymbol{a}_j^T \left(\int_{V_j} \boldsymbol{N}_j^T\boldsymbol{F}_{B,j}\,\mathrm{d}V + \int_{S_j} \boldsymbol{N}_j^T\boldsymbol{F}_{T,j}\,\mathrm{d}S + \boldsymbol{p}_j^k \right) \qquad (3.10c)$$

3.2 Properties of the mass and the stiffness matrix.

The consistent mass matrix has some important characteristics. It is real, which means that the complex conjugate[1] of the matrix is equal to the matrix itself, i.e $\bar{\boldsymbol{M}} = \boldsymbol{M}$. Furthermore, it is symmetric, i.e $\boldsymbol{M}^T = \boldsymbol{M}$, and it is positive definite, i.e $\boldsymbol{x}^T \boldsymbol{M} \boldsymbol{x} > 0$ for any real non-trivial vector $\boldsymbol{x}$. The consistent mass matrix is not the only possible way to form the mass matrix of a system. Under certain circumstances, e.g hand calculations or formulation for explicit time integration, it is common to construct the mass matrix such that it becomes diagonal. This method is known as particle mass lumping and the corresonding mass matrix is known as the lumped mass matrix. The lumped mass matrix is real and obviously symmetric since it is diagonal. The lumped mass matrix may become singular, i.e $\boldsymbol{M}\boldsymbol{x} = \boldsymbol{0}$ when there are degrees of freedom with no associated inertia[5, p.282]. An example is when inertia related with rotational degrees of freedom are neglected in beam and plate elements. The consequence is that the lumped mass matrix is only positive semidefinite, i.e $\boldsymbol{x}^T \boldsymbol{M} \boldsymbol{x} \geq 0$.

The stiffness matrix is real and symmetric if the constitutive matrix $\boldsymbol{E}_j$ is real and symmetric. $\boldsymbol{E}_j$ is symmetric for any linear *hyperelastic* material [6, p.5-3]. The constitutive matrix may be formulated as complex for dissipative materials, but in the continuation it is assumed that the material is strictly elastic and real such that $\boldsymbol{K}$ is real. Furthermore, the constitutive matrix $\boldsymbol{E}_j$ is also positive definite, the classic justification for this is that work that goes into deforming an elastic body has to be positive [7, p.57] such that $W = 1/2 \int_V \boldsymbol{\epsilon}^T \boldsymbol{E} \boldsymbol{\epsilon} \, dV > 0$. As a consequence, the stiffness matrix $\boldsymbol{K}$ is for most structures positive definite, the exceptions are in systems where the stiffness matrix may become singular, i.e $\boldsymbol{K}\boldsymbol{x} = \boldsymbol{0}$. This occurs in systems where rigid body motion is possible or where reduced numerical integration introduce mechanisms at system level. If $\boldsymbol{x}$ is a rigid body motion or triggers a mechanism, then no internal forces arise in the structure from the displacement, i.e $\boldsymbol{K}\boldsymbol{x} = \boldsymbol{0}$.

The above discussion has revealed that both the mass and the stiffness matrix are in general real, symmetric and only positive semidefinite. The discussion also showed that the mass matrix may be made positive definite if proper precautions are taken in the formulation of the mass matrix. Similarly, the stiffness matrix is positive definite if the structure is properly restrained against rigid body motion and the element formulation is such that mechanisms are not possible at system level. In the continuation of this thesis, it is therefore assumed that proper care has been taken in the formulation of the system equation such that both $\boldsymbol{M}$ and $\boldsymbol{K}$ are positive definite. Equation (3.11) and equation (3.12) postulate the properties of the mass and stiffness matrix.

$$\bar{\boldsymbol{M}} = \boldsymbol{M} \tag{3.11a}$$

$$\boldsymbol{M}^T = \boldsymbol{M} \tag{3.11b}$$

$$\boldsymbol{x}^T \boldsymbol{M} \boldsymbol{x} > 0 \tag{3.11c}$$

---

[1]An overline denotes the complex conjugate, such that the complex conjugate of λ is $\bar{\lambda}$.

$$\bar{K} = K \tag{3.12a}$$

$$K^T = K \tag{3.12b}$$

$$x^T K x > 0 \tag{3.12c}$$

where x is any real and non-trivial vector with proper dimension.

3.3 The linear eigenvalue problem

The solution to the undamped, free vibrating system is the homogeneous solution of equation (3.9), i.e $P = 0$, and it is on the general form given by equation (3.13).

$$u = \phi \, e^{st} \tag{3.13}$$

Introducing equation (3.13) into equation (3.9) yields the linear eigenvalue problem, see equation (3.14).

$$(K - \lambda_n M) \, \phi_n = 0 \tag{3.14}$$

where $\lambda_n = -s_n^2$ is the eigenvalue and ϕ_n is the corresponding eigenvector. Throughout this thesis it is assumed that the eigenvalues are distinct, such that there are no repeated eigenvalues. Equation (3.14) has a solution when the determinant of the matrix in the parenthesis is equal to zero. This produces a Nth order polynomial with N solutions, i.e there are N eigenvectors and eigenvalues, where N is the number of degrees of freedom in the system. Because M and K are real, symmetric and positive definite, the eigenvalues λ_n are real. This can be shown by writing out equation (3.14), taking the complex conjugate of the entire equation and premultiplying with ϕ_n, see equation (3.15a). Similarly, writing out equation (3.14), taking the transpose of the entire equation and postmultiplying with $\bar{\phi}_n$ yields equation (3.15b).

$$\bar{\lambda}_n \phi_n^T M \bar{\phi}_n = \phi_n^T K \bar{\phi}_n \tag{3.15a}$$

$$\lambda_n \phi_n^T M \bar{\phi}_n = \phi_n^T K \bar{\phi}_n \tag{3.15b}$$

Subtracting equation (3.15a) from equation (3.15b) assuming that the eigenvalues are complex, i.e $\lambda_n = \lambda_{Rn} + i \, \lambda_{In}$ yields equation (3.16).

$$\left(\lambda_n - \bar{\lambda}_n \right) \phi_n^T M \bar{\phi}_n = i \, 2\lambda_{In} \phi_n^T M \bar{\phi}_n = 0 \tag{3.16}$$

Since M is real and positive definite, M may be written on the form $M = Q^T Q$, where Q is a real and non-singular matrix[8, p.61]. It follows that that $\phi_n^T M \bar{\phi}_n = \phi_n^T Q^T Q \bar{\phi}_n = y_n^T \bar{y}_n = \sum_{j=1}^{J} y_{n,j} \bar{y}_{n,j} > 0$. Therefore λ_{In} has to be zero for equation (3.15a) to be fullfilled and λ_n is real. Since the eigenvalue λ_n is real, the basis for eigenvector ϕ_n is also real [8, p.57]. To show this consider the case where both the eigenvalues and eigenvectors are complex, i.e $\lambda_n = \lambda_{Rn} + i \, \lambda_{In}$ and $\phi_n = \phi_{Rn} + i \, \phi_{In}$. Inserting the complex eigenvalues and eigenvectors into equation (3.14) and realizing that both the real and the imaginary parts must vanish, yields the following equations.

$$(K - \lambda_{Rn} M) \, \phi_{Rn} = -\lambda_{In} M \phi_{In} \tag{3.17a}$$

$$(K - \lambda_{Rn} M) \, \phi_{In} = \lambda_{In} M \phi_{Rn} \tag{3.17b}$$

Equation (3.17a) show that if the eigenvalues are real, i.e $\lambda_{In} = 0$, then $\boldsymbol{\phi}_{Rn}$ is a valid eigenvector of the eigenvalue $\lambda_n = \lambda_{Rn}$, see equation (3.18)

$$(\boldsymbol{K} - \lambda_n \boldsymbol{M}) \boldsymbol{\phi}_{Rn} = \boldsymbol{0} \tag{3.18}$$

It is here appropriate to point out that the eigenvalue problem only determines the eigenvalues and the direction of the eigenvector, the eigenvalue problem does not define the magnitude or length of the eigenvectors. Since all eigenvalues are distinct, it follows that equation (3.17a) is equal to any multiple of equation (3.17b) and that the complex part of the eigenvector is a multiple $\mathcal{A}$ of the real part of the eigenvector, i.e $\boldsymbol{\phi}_{In} = \mathcal{A}\boldsymbol{\phi}_{Rn}$. Writing out the expression for the complex eigenvector, $\boldsymbol{\phi}_n = (1 + i\,\mathcal{A})\boldsymbol{\phi}_{Rn}$, inserting the result into equation (3.14) again shows that the eigenvector may be *chosen* complex but the basis for the eigenvector is real. Infact, multiplying the basis eigenvector with an arbitrary complex number $\mathcal{C}$, i.e $\boldsymbol{\phi} = \mathcal{C}\boldsymbol{\phi}_{Rn}$ also satisfies equation (3.18). In the continuation of this thesis it is assumed that if there exists a real basis for the eigenvectors, the eigenvectors are chosen real, such that all eigenvectors for the undamped case are hereby referred to as real.

A consequence of real eigenvectors and positive definite property matrices $\boldsymbol{M}$ and $\boldsymbol{K}$ are that the eigenvalues λ_n become positive. Premultiplying equation (3.14) by $\boldsymbol{\phi}_n^T$ and rearranging for the eigenvalue λ_n, and remembering equation (3.11c) and equation (3.12c) yields the following

$$\lambda_n = \frac{\boldsymbol{\phi}_n^T \boldsymbol{K} \boldsymbol{\phi}_n}{\boldsymbol{\phi}_n^T \boldsymbol{M} \boldsymbol{\phi}_n} > 0 \tag{3.19}$$

which clearly states that the eigenvalues become positive. It is here appropriate to relate the eigenvalues of the MDOF system to the natural frequencies of the system given by equation (2.4a). Recall that the eigenvalues where related to the response through $s_n = \pm\sqrt{-\lambda_n}$ in equation (3.13). Equation (3.19) shows that $\lambda_n > 0$ such that it is appropriate to write $s_n = \pm i\sqrt{\lambda_n}$. The response for the undamped free vibrating system is then a non-decaying harmonic function $\boldsymbol{u}_n = \boldsymbol{\phi}_n (A_n \cos \omega_n t + B_n \sin \omega_n t)$, where Euler's formula $e^{i\theta} = \cos\theta + i\sin\theta$ has been employed and natural frequencies are defined by the eigenvalues through equation (3.20).

$$\omega_n = \sqrt{\lambda_n} \tag{3.20}$$

Another important characteristic for real and symmetric matrices are that the eigenvectors are orthogonal with respect to the property matrices $\boldsymbol{M}$ and $\boldsymbol{K}$. To show this consider the two eigenvalue equations for the eigenvalues λ_m and λ_n. Transpose the entire equation for eigenvalue λ_m and postmultiply by the eigenvector $\boldsymbol{\phi}_n$, then premultiply the equation for eigenvalue λ_n by the transposed eigenvector $\boldsymbol{\phi}_m^T$. Finally subtract the equation for λ_n from the equation for λ_m, the following result appears.

$$(\lambda_m - \lambda_n)\boldsymbol{\phi}_m^T \boldsymbol{M} \boldsymbol{\phi}_n = 0 \tag{3.21}$$

Since all eigenvalues are assumed to be distinct, equation (3.21) implies that if $\lambda_m \neq \lambda_n$ or $m \neq n$, then $\boldsymbol{\phi}_m^T \boldsymbol{M} \boldsymbol{\phi}_n$ has to vanish, i.e $\boldsymbol{\phi}_m^T \boldsymbol{M} \boldsymbol{\phi}_n = 0$. If $m = n$ then equation (3.11c) clearly states that $\boldsymbol{\phi}_m^T \boldsymbol{M} \boldsymbol{\phi}_n > 0$, the actual magnitude of $\boldsymbol{\phi}_m^T \boldsymbol{M} \boldsymbol{\phi}_n$ depends on the magnitude of the eigenvectors $\boldsymbol{\phi}_n$. Recall from the earlier discussion that the magnitude of the

eigenvector is unknown, the eigenvalue problem only define its direction. The magnitude of the eigenvectors may therefore be chosen by imposing another constraint or condition. The manner in which the magnitude is chosen is called normalization, and a convenient way of normalizing the eigenvectors is by what in dynamics is known as *mass orthonormalization*[9, p.480] or just mass normalization, i.e demanding that $\boldsymbol{\phi}_n^T \boldsymbol{M} \boldsymbol{\phi}_n = 1$. In a similar fashion it may be shown that $\boldsymbol{\phi}_m^T \boldsymbol{K} \boldsymbol{\phi}_n$ must vanish for $m \neq n$ and with mass normalization $\boldsymbol{\phi}_n^T \boldsymbol{M} \boldsymbol{\phi}_n = 1$, equation (3.19) shows that $\boldsymbol{\phi}_m^T \boldsymbol{K} \boldsymbol{\phi}_n = \lambda_n$ when $m = n$. Equation (3.22) and equation (3.23) summarizes the discussion in this paragraph and shows that the eigenvectors are orthogonal with respect to the property matrices $\boldsymbol{M}$ and $\boldsymbol{K}$.

$$\boldsymbol{\phi}_m^T \boldsymbol{M} \boldsymbol{\phi}_n = \begin{cases} 1 & \text{for } m = n \\ 0 & \text{for } m \neq n \end{cases} \tag{3.22}$$

$$\boldsymbol{\phi}_m^T \boldsymbol{K} \boldsymbol{\phi}_n = \begin{cases} \lambda_n & \text{for } m = n \\ 0 & \text{for } m \neq n \end{cases} \tag{3.23}$$

The orthogonality properties of the eigenvectors can be taken advantage of in obtaining the complete solution of the dynamic equation. The total solution will be a superposition of the homogeneous solution $\boldsymbol{u}_c$ and the particular solution $\boldsymbol{u}_p$ determined by the characteristics of the loading. The homogeneous solution is given by taking the sum of the N different solutions of $\boldsymbol{\phi}_n$ and s_n of equation (3.13), i.e $\boldsymbol{u}_c = \sum_{n=1}^{N} \boldsymbol{\phi}_n A_n \, e^{s_n t} = \sum_{n=1}^{N} \boldsymbol{\phi}_n y_{cn}$. The particular solution can be described by the eigenvectors as well, such that $\boldsymbol{u}_p = \sum_{n=1}^{N} \boldsymbol{\phi}_n y_{pn}$, and the total solution is $\boldsymbol{u} = \boldsymbol{u}_c + \boldsymbol{u}_p = \sum_{n=1}^{N} \boldsymbol{\phi}_n (y_{cn} + y_{pn}) = \sum_{n=1}^{N} \boldsymbol{\phi}_n y_n$. The matrix form of the total solution is given by equation (3.24)

$$\boldsymbol{u} = \boldsymbol{\Phi} \boldsymbol{y} \tag{3.24}$$

where $\boldsymbol{\Phi} = \begin{bmatrix} \boldsymbol{\phi}_1 & \boldsymbol{\phi}_2 & \cdots & \boldsymbol{\phi}_N \end{bmatrix}$ is known as the modal matrix, where modal matrix comes from the fact that the eigenvectors are often referred to as *mode shapes*. $\boldsymbol{y} = \begin{bmatrix} y_1 & y_2 & \cdots & y_N \end{bmatrix}^T$ is a columnvector containing the modal degrees of freedom. Introducing equation (3.24) into equation (3.9) and premultiplying with $\boldsymbol{\Phi}^T$ yields the modal equation of motion.

$$\boldsymbol{\Phi}^T \boldsymbol{M} \boldsymbol{\Phi} \ddot{\boldsymbol{y}} + \boldsymbol{\Phi}^T \boldsymbol{K} \boldsymbol{\Phi} \boldsymbol{y} = \boldsymbol{\Phi}^T \boldsymbol{P} \tag{3.25}$$

The matrix $\boldsymbol{\Phi}^T \boldsymbol{M} \boldsymbol{\Phi}$ is known as the modal mass matrix, and with mass normalized eigenvectors, equation (3.22) implies that the modal mass matrix is equal to the identity matrix, i.e $\boldsymbol{\Phi}^T \boldsymbol{M} \boldsymbol{\Phi} = \boldsymbol{I} = \begin{bmatrix} 1 & 1 & \cdots & 1 \end{bmatrix}$. The matrix $\boldsymbol{\Phi}^T \boldsymbol{K} \boldsymbol{\Phi}$ is known as the modal stiffness matrix, and with mass normalized eigenvectors equation (3.23) implies that the modal stiffness matrix becomes a diagonal matrix containing the eigenvalues, i.e $\boldsymbol{\Phi}^T \boldsymbol{K} \boldsymbol{\Phi} = \boldsymbol{\Lambda} = \begin{bmatrix} \lambda_1 & \lambda_2 & \cdots & \lambda_N \end{bmatrix}$. $\boldsymbol{\Lambda}$ is known as the spectral matrix. Lastly the vector $\boldsymbol{\Phi}^T \boldsymbol{P}$ is the modal load vector $\boldsymbol{P}_\Phi$. With mass normalization the modal equation of motion for the undamped multi degree of freedom system is given by equation (3.26).

$$\ddot{\boldsymbol{y}} + \boldsymbol{\Lambda} \boldsymbol{y} = \boldsymbol{P}_\Phi \tag{3.26}$$

Equation (3.26) is a set of N *uncoupled* equations of motion, basically turning the coupled MDOF system into a set of N SDOF systems which may be easily and effectively

solved for $\boldsymbol{y}$ by the theory and solution outlined in section 2. Once the response in the modal coordiantes are obtained, the response in the physical degrees of freedom $\boldsymbol{u}$ may then be found by employing transformation equation (3.24) once more.

As a side note, it may be mentioned that the displacement $\boldsymbol{u}$ is often dominated by a subset of the eigenvectors, such that very good approximations of the displacement may be found by only taking, say the $M \leq N$ first mode shapes into the solution, i.e $\boldsymbol{u} \approx \sum_{n=1}^{M} \boldsymbol{\phi}_n y_n$. Choosing a subset $M \leq N$ of the eigenvectors to represent the displacement effectively reduces the degrees of freedom in the system from N to M. In cases where the above approximation is appropriate, modal transformation may be very effective in solving the equation of motion and obtaining the dynamic response.

The discussion in this section has shown that the eigenvalues of the undamped equation of motion are positive and real. This section has also shown that the eigenvectors for undamped dynamic systems are real and they exhibit orthogonal properties with respect to the mass and the stiffness matrix, and that the transformation matrix defined by the orthogonal eigenvectors diagonalizes therefore diagonalizes the property matrices. The derivations made about the eigenvalues and eigenvectors in this section will aid the discussion in the following section about viscous damping models and the derivation of the complex eigenvalue problem in section 3.5.

3.4 Viscous damping in multi degree of freedom systems

The equation of motion for a viscously damped system is given by equation (3.27).

$$\boldsymbol{M}\ddot{\boldsymbol{u}} + \boldsymbol{C}\dot{\boldsymbol{u}} + \boldsymbol{K}\boldsymbol{u} = \boldsymbol{P} \tag{3.27}$$

In the derivation of the equation of motion for MDOF system no terms for dissipation of energy or damping was included. If a viscous damping constant c for the continuum could be determined, the derivation of the elemental damping matrix $\boldsymbol{c}$ and the system damping matrix $\boldsymbol{C}$ would follow similar lines to that of the mass matrix, see section 3.1. Separating the viscous damping force $(-\dot{\boldsymbol{w}})c\,\mathrm{d}V$ from the body forces would yield the damping matrix at elemental level $\boldsymbol{c} = \int_V c\boldsymbol{N}^T\boldsymbol{N}\,\mathrm{d}V$ and at system level $\boldsymbol{C} = \sum_{j=1}^{J} \boldsymbol{a}_j^T \boldsymbol{c}_j \boldsymbol{a}_j$. Additional sources of damping, such as friction in joints and radiation loss at the boundaries could also be quantified and terms could be added to the viscous damping matrix to represent these mechanisms.

As it turns out, it is in general difficult and time consuming to directly determine the coefficients of the damping matrix from the specific sources. Instead the damping matrix is often constructed to fit experimental data from the structure being analyzed or experimental data from structures similar to the structure being analyzed. This data is often given in modal form, i.e the modal damping ratio ξ_n is given. If the system is solved with modal analysis this data can then be used directly, but if the system is solved by any other method, e.g numerical integration, the physical damping matrix has to be constructed from the modal damping ratios. Subsection 3.4.1 discusses different ways of constructing the damping matrix from modal damping ratios.

The viscous damping in multi degree of freedom system may be categorized into two different types. If the modal transformation $\boldsymbol{u} = \boldsymbol{\Phi}\boldsymbol{y}$ diagonalizes the damping matrix

C, i.e $\boldsymbol{\Phi}^T\boldsymbol{C}\boldsymbol{\Phi}$ is diagonal, then the *classic* modal analysis outlined at the end of the previous section is applicable and the system is said to possess *classical* damping. If the modal transformation does not diagonalize the damping matrix, the system is said to have *non-classical* damping.

Apart from the fact that the non-classical damping matrix is not diagonalized by the classical modal transformation, its properties are quite general. The non-classical damping matrix mainly appears when the damping matrix is defined directly in the physical coordinates, e.g if the elemental damping constant may be determined such that $c \Rightarrow \boldsymbol{c}_j \Rightarrow \boldsymbol{C}$ or if active viscous dampers are installed on a structure such that the damping properties may be added to the damping matrix in the physical coordinates directly. The non-classical damping matrix affects the resonance and damped frequencies of the system and will be therefore be discussed further in section 3.5.

3.4.1   Classical viscous damping

The classically damped MDOF system yields with modal transformation an uncoupled system, i.e a set of SDOF systems. Writing out the equation of motion for mode n with mass normalized eigenvectors yields the following equation

$$\ddot{y}_n + \tilde{c}_n\dot{y} + \omega_n^2 y_n = P_{\Theta n}$$

where $\tilde{c}_n = \boldsymbol{\phi}_n^T\boldsymbol{C}\boldsymbol{\phi}_n$ is the viscous damping coefficient for mode n. Introducing the modal damping ratio $\xi_n = \frac{\tilde{c}_n}{2\omega_n}$, the equation of motion for mode n may be written in terms of the modal damping ratio ξ_n and the natural frequencies ω_n, see equation (3.28)

$$\ddot{y}_n + 2\xi_n\omega_n\dot{y} + \omega_n^2 y_n = P_{\Theta n} \tag{3.28}$$

Introducing the diagonal modal damping matrix $\boldsymbol{\Xi} = \begin{bmatrix} 2\xi_1\omega_1 & 2\xi_2\omega_2 & \cdots & 2\xi_N\omega_N \end{bmatrix}$ the equation of motion in modal coordinates is given on matrix form in equation (3.29).

$$\ddot{\boldsymbol{y}} + \boldsymbol{\Xi}\dot{\boldsymbol{y}} + \boldsymbol{\Lambda}\boldsymbol{y} = \boldsymbol{P}_\Phi \tag{3.29}$$

As mentioned in section 3.4 if the modal damping ratios ξ_n are known and the system is solved by modal analysis, equation (3.29) may be solved for the modal coordinates and transformed by equation (3.24) to obtain the solution in the physical coordinates. If the damping ratios are known, but modal analysis is not used to obtain the response of the system, the viscous damping matrix $\boldsymbol{C}$ may be determined from the modal damping matrix $\boldsymbol{\Xi}$. The relation between the viscous damping matrix and the modal damping matrix is given by the following equation.

$$\boldsymbol{\Phi}^T\boldsymbol{C}\boldsymbol{\Phi} = \boldsymbol{\Xi}$$

Although the viscous damping matrix may be determined by matrix inversion, i.e $\boldsymbol{C} = \boldsymbol{\Phi}^{-T}\boldsymbol{\Xi}\boldsymbol{\Phi}^{-1}$, it is more efficient and accurate to utilize the properties of the mass normalization. Pre- and postmultiplication of the above equation with $\boldsymbol{\Phi}^T\boldsymbol{M}\boldsymbol{\Phi} = \boldsymbol{I}$ yields the following equation.

$$\boldsymbol{\Phi}^T\boldsymbol{C}\boldsymbol{\Phi} = \boldsymbol{\Phi}^T\boldsymbol{M}\boldsymbol{\Phi}\boldsymbol{\Xi}\boldsymbol{\Phi}^T\boldsymbol{M}\boldsymbol{\Phi}$$

Comparing the right and the left hand side shows that the viscous damping matrix is a product of the modal damping matrix, the modal transformation matrix and the mass matrix, see equation (3.30).

$$\boldsymbol{C} = \boldsymbol{M}\boldsymbol{\Phi}\boldsymbol{\Xi}\boldsymbol{\Phi}^T\boldsymbol{M} \qquad (3.30)$$

The above method of constructing the viscous damping matrix is often called the direct method and a damping matrix constructed by the above method is in the continuation of this thesis called the *direct* damping matrix. The primary advantage of the direct method is that it provides precise control of the actual damping ratios in all modes. The disadvantage of the direct method is that it requires that the damping ratios to be specified in all modes of vibration and that it is necessary to solve the eigenvalue problem to obtain $\boldsymbol{\Phi}$ and the elements of $\boldsymbol{\Xi}$. Furthermore, the direct damping matrix $\boldsymbol{C}$ becomes a full matrix, i.e it is not sparse, which significantly reduces the efficiency of certain numerical integration schemes. More on this at the end of section 3.5.

The direct damping matrix is not the only classical viscous damping matrix, in fact there exists an infinite number of them. If a matrix can be described by what is known as a Caughey series, the matrix becomes diagonal under modal transformation. Thus, if a damping matrix can be described by a Caughey series, the damping matrix is a classical damping matrix. In the following, the Caughey series will be derived and related to the modal damping ratio ξ_n.

To find the Caughey series, it is necessary to rewrite the eigenvalue problem, equation (3.14) to the form shown in equation (3.31).

$$\boldsymbol{M}^{-1}\boldsymbol{K}\boldsymbol{\phi}_n = \lambda_n\boldsymbol{\phi}_n \qquad (3.31)$$

Premultiply both sides of equation (3.31) by $\boldsymbol{\phi}_m^T\boldsymbol{M}$, the right hand side will then be $\boldsymbol{\phi}_m^T\boldsymbol{M}\boldsymbol{\phi}_n$. With mass normalized eigenvectors, equation (3.22) yields the following relation.

$$\boldsymbol{\phi}_m^T\boldsymbol{M}\boldsymbol{M}^{-1}\boldsymbol{K}\boldsymbol{\phi}_n = \begin{cases} \lambda_n & \text{for } m = n \\ 0 & \text{for } m \neq n \end{cases}$$

By premultiplying equation (3.31) by $\boldsymbol{\phi}_m^T\boldsymbol{M}\boldsymbol{M}^{-1}\boldsymbol{K}$ gives through the above equation the following.

$$\boldsymbol{\phi}_m^T\boldsymbol{M}(\boldsymbol{M}^{-1}\boldsymbol{K})^2\boldsymbol{\phi}_n \begin{cases} \lambda_n^2 & \text{for } m = n \\ 0 & \text{for } m \neq n \end{cases}$$

where the notation $\boldsymbol{\phi}_m^T\boldsymbol{M}\boldsymbol{M}^{-1}\boldsymbol{K}\boldsymbol{M}^{-1}\boldsymbol{K}\boldsymbol{\phi}_n = \boldsymbol{\phi}_m^T\boldsymbol{M}(\boldsymbol{M}^{-1}\boldsymbol{K})^2\boldsymbol{\phi}_n$ has been introduced. If the same procedure as the one outlied above is repeated b times, the following equation is found

$$\boldsymbol{\phi}_m^T\boldsymbol{M}(\boldsymbol{M}^{-1}\boldsymbol{K})^b\boldsymbol{\phi}_n = \begin{cases} \lambda_n^b & \text{for } m = n \\ 0 & \text{for } m \neq n \end{cases}$$

If equation (3.31) is premultiplied by $\lambda_n^{-1}(\boldsymbol{M}^{-1}\boldsymbol{K})^{-1}$ and a similar procedure as the one above is applied by premultiplying the equation by $\boldsymbol{\phi}_m^T\boldsymbol{M}\left((\boldsymbol{M}^{-1}\boldsymbol{K})^{-1}\right)^b$ it may be shown that b in the above equation is any integer, i.e $-\infty < b < \infty$.

It can also be seen that the product of an arbitrary constant a_b and the above equation retains the orthogonality properties, in fact the sum of all possible variations of such a product is also orthogonal, see equation (3.32).

$$\sum_b a_b \phi_m^T \boldsymbol{M} (\boldsymbol{M}^{-1} \boldsymbol{K})^b \phi_n = \begin{cases} \sum_b a_b \lambda_n^b & \text{for } m = n \\ 0 & \text{for } m \neq n \end{cases} \tag{3.32}$$

The above equation shows that if the damping matrix $\boldsymbol{C}$ can be described as a linear combination of $\boldsymbol{M}(\boldsymbol{M}^{-1}\boldsymbol{K})^b$, it becomes diagonal under modal transformation, see equation (3.33).

$$\boldsymbol{C} = \sum_b a_b \boldsymbol{M} (\boldsymbol{M}^{-1} \boldsymbol{K})^b \tag{3.33}$$

Equation (3.33) is the Caughey series, after Thomas K. Caughey who first derived the condition and a matrix constructed from a Caughey series is therefore known as a Caughey damping matrix. The Caughey damping matrix may be determined from known modal damping ratios ξ_n. Consider the equation of motion for a MDOF system with viscous damping, equation (3.27), and transfer it to modal coordinates, the following equation appears.

$$\ddot{\boldsymbol{y}} + \boldsymbol{\Phi}^T \boldsymbol{C} \boldsymbol{\Phi} \dot{\boldsymbol{y}} + \boldsymbol{\Lambda} \boldsymbol{y} = \boldsymbol{P}_\Phi \tag{3.34}$$

With Caughey damping, the matrix $\boldsymbol{\Phi}^T \boldsymbol{C} \boldsymbol{\Phi}$ becomes diagonal, i.e $\boldsymbol{\Phi}^T \boldsymbol{C} \boldsymbol{\Phi} = \sum_b a_b \boldsymbol{\Lambda}^b$, and each line in equation (3.34) becomes uncoupled, see equation (3.35). Recall that for the undamped eigenvalue problem, the eigenvalues where related to the natural frequencies by equation (3.20)

$$\ddot{y}_n + \sum_b a_b \omega_n^{2b} \dot{y}_n + \omega_n^2 y_n = P_{\Theta n} \tag{3.35}$$

Comparing equation (3.35) with equation (3.28) it becomes apparent that the relation between the modal damping ratio ξ_n and the Caughey series is given by equation (3.36).

$$\xi_n = \frac{1}{2} \sum_b a_b \omega_n^{2b-1} \tag{3.36}$$

The coefficients a_b may be determined by choosing the damping ratios ξ_n in the modes with natural frequency ω_n, and a equally sized set of b. To illustrate this process consider a case where the damping ratio in modes with natural frequency $\omega_p, \omega_r, \omega_s$ and ω_t are equal to ξ_p, ξ_r, ξ_s and ξ_t. The set $b = [0, 1, 2, 3]$ is chosen, this information yields three different versions of equation (3.36) which is given on matrix form in equation (3.37).

$$\frac{1}{2} \begin{bmatrix} \frac{1}{\omega_p} & \omega_p & \omega_p^3 & \omega_p^5 \\ \frac{1}{\omega_r} & \omega_r & \omega_r^3 & \omega_r^5 \\ \frac{1}{\omega_s} & \omega_s & \omega_s^3 & \omega_s^5 \\ \frac{1}{\omega_t} & \omega_t & \omega_t^3 & \omega_t^5 \end{bmatrix} \begin{bmatrix} a_0 \\ a_1 \\ a_2 \\ a_3 \end{bmatrix} = \begin{bmatrix} \xi_p \\ \xi_r \\ \xi_s \\ \xi_t \end{bmatrix} \tag{3.37}$$

The coefficients a_0, a_1, a_2 and a_3 are then determined by inverting the matrix on the left side, the result for $b = b_1 = [0, 1, 2, 3]$ is shown for all damping ratios equal to ξ_0 in figure 3.1.
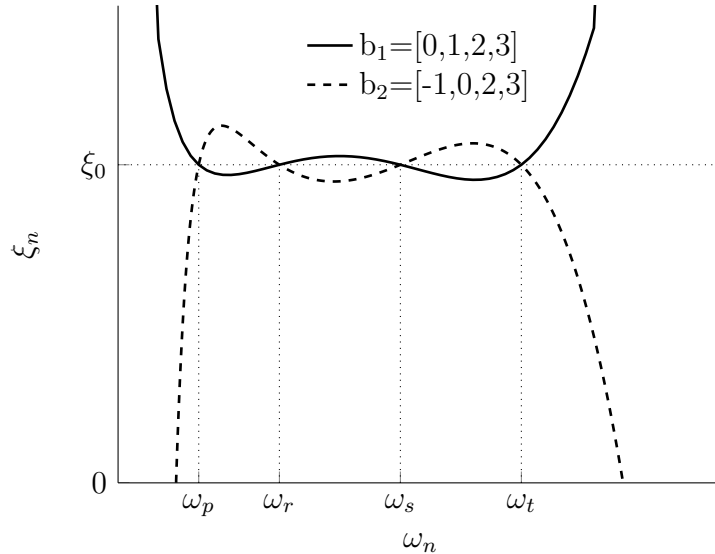
Figure 3.1: The figure depicts the resulting damping ratio ξ_n for Caughey damping with two different sets of b. The figure shows that $b_1 = [0, 1, 2, 3]$ is well behaved for the frequencies specified. The set $b_2 = [-1, 0, 1, 2]$ results negative damping ratio ξ_n for certain modes, which means that the solution diverges.

It is important to note that the set b should be chosen with care, in figure 3.1 the resulting damping ratio for $b_2 = [-1, 0, 2, 3]$ is also shown. The figure shows that the damping ratios within the specified range $\omega_p < \omega_n < \omega_t$ lies close to the specified damping ratio ξ_0, being exact at the specified frequencies for both b_1 and b_2. For frequencies $\omega_n < \omega_p$ and $\omega_n > \omega_t$, i.e below and above the minimum and maximum specified frequncies, the damping ratio is increasing towards infinity for b_1 and decreasing towards negative infinity for b_2. For the case of b_1 this means that the modes outside of the specified frequency range are heavily damped, if the important modes are found in the frequency range, this poses no problem and may be beneficial in damping out numerical noise. For the case of b_2 the damping ratio becomes negative for modes outside of the chosen range. Negative damping ratios means that the exponential $\mathrm{e}^{-\xi_n \omega_n t}$ in the homogeneous solution goes to infinity as time increases, see equation (2.2). In turn, this means that the total response will become unstable and tend towards infinity as time increases.

It should also be noted that even though the set $b_1 = [0, 1, 2, 3]$ behaved well with ξ_0 specified in the frequencies $[\omega_p, \omega_r, \omega_s, \omega_t]$ it is not certain that it does so for another set of frequencies. In figure 3.2 the damping ratio for set $b_1 = [0, 1, 2, 3]$ with ξ_0 specified in the same frequencies $[\omega_p, \omega_r, \omega_s]$, but with the last frequency ω_t changed to $\tilde{\omega}_t$. The figure shows that the damping ratio becomes negative for modes just below $\tilde{\omega}_t$, and the solution will diverge.

The advantage of a general Caughey damping matrix is that the damping matrix may be specified without solving the eigenvalue problem. Another advantage is that the damping ratio may be specified with good precision within a frequency range, e.g $\xi_n \approx \xi_0$ in the range $\omega_p < \omega_n < \omega_t$, with relatively few parameters. The disadvantages of the general Caughey damping matrix is that damping ratios may become negative if the matrix is not determined with care, and that the Caughey damping matrix becomes a full matrix in most combinations of b. As mentioned for the direct damping matrix,

18
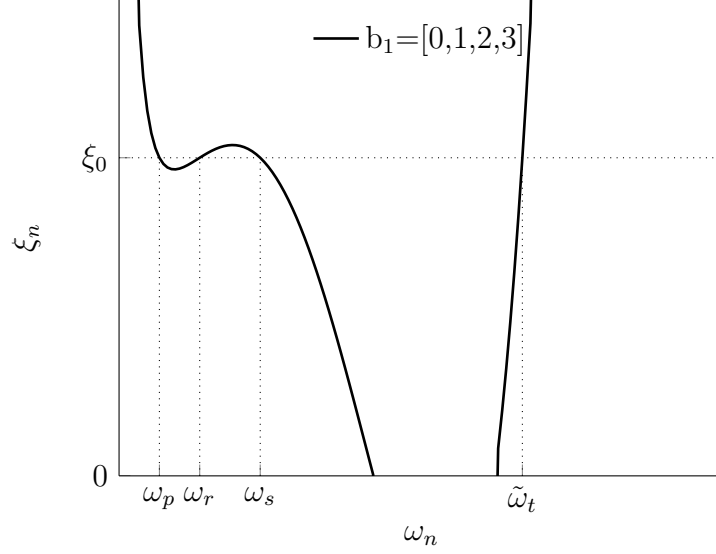
Figure 3.2: The figure shows that the set b_1 yields negative damping ratio ξ_n in certain modes when ξ_0 is specified in frequencies $[\omega_p, \omega_r, \omega_s, \tilde{\omega}_t]$.

a full matrix may significantly reduce the efficiency of numerical integration schemes. I should be noted that the direct damping matrix is a special case of the Caughey damping matrix.

An important special case of Caughey damping is Rayleigh damping, i.e $b = [0, 1]$. Rayleigh damping was named after Lord Rayleigh who first wrote about it in [10, p.130-131] and is because of its simplicity and characteristics often applied in dynamic analysis. It is also widely available in commercial codes and therefore deserves some special attention.

With Rayleigh damping the damping matrix becomes proportional to the mass and the stiffness matrix, see equation (3.38).

$$\boldsymbol{C} = a_0 \boldsymbol{M} + a_1 \boldsymbol{K} \tag{3.38}$$

The damping ratio for Rayleigh damping is given by equation (3.39), and a_0 and a_1 are given by equations (3.40) for damping ratios ξ_p and ξ_r specified in modes with frequency ω_p and ω_r, respectively. See figure 3.3 for the characteristic curve for the damping ratios with Rayleigh damping.

$$\xi_n = \frac{1}{2} \left(\frac{a_0}{\omega_n} + a_1 \omega_n \right) \tag{3.39}$$

$$a_0 = 2\omega_p \omega_r \frac{\omega_p \xi_r - \omega_r \xi_p}{\omega_p^2 - \omega_r^2} \tag{3.40a}$$

$$a_1 = 2 \frac{\omega_p \xi_p - \omega_r \xi_r}{\omega_p^2 - \omega_r^2} \tag{3.40b}$$

Because of the uncertainty related to the modal damping ratios it is in practice common to choose the damping ratios equal to each other, i.e $\xi_p = \xi_r = \xi_0$. Then pick the first frequency equal to the fundamental frequency, i.e the lowest natural frequency $\omega_p = \omega_1$ and chose the second frequency equal to one of the higher frequency components

19
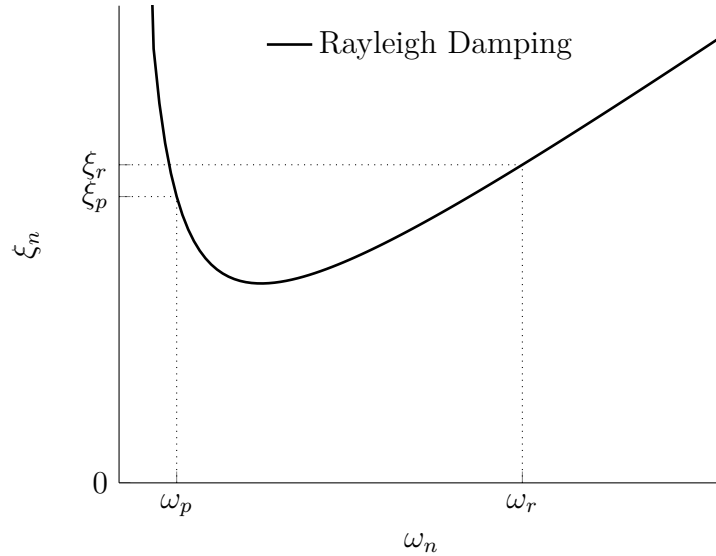
Figure 3.3: The figure depicts the typical shape of the damping raios with Rayleigh damping.

of the loading [11, p.236]. The result is that that the first mode, which often is the most dominant in the total response gets a specified damping ratio while the modes which are within the specified range of frequencies have reasonable damping ratios around the specified damping ratio ξ_0. Modes outside of the specified frequency range, such as high frequency numerical noise, are more heavily damped and thereby contribute less to the overall response.

Although the above procedure is simple and effective in prescribing reasonable damping ratios in the modes of interest, the procedure should not be applied uncritically. If the frequency range becomes large the damping in some modes may become unreasonably small. If the ratio between the lowest and highest specified frequency is defined as $\gamma = \frac{\omega_r}{\omega_p}$ then the minimum damping ratio $\xi_{\min}$ is found in mode with frequency $\omega_{\min}$, see definition in equations (3.41).

$$\gamma = \frac{\omega_r}{\omega_p} \tag{3.41a}$$

$$\omega_{\min} = \sqrt{\gamma}\omega_p \tag{3.41b}$$

$$\xi_{\min} = 2\frac{\sqrt{\gamma}}{1 + \gamma}\xi_0 \tag{3.41c}$$

Figure 3.4 shows the minimum damping ratio as a function of the ratio γ between the lowest and highest specified frequency.

If the system has natural frequencies close to $\omega_{\min}$, these modes will have relatively low damping. The actual effect of this on the response of a system depends on the properties and characteristics of the system. If these low damped modes are excited by either initial conditions or the loading, the effect of low damping in these modes *may* have a significant impact on the overall response. As mentioned earlier, the first is mode is often dominant in the response of a system such that the other modes *may* not affect the total response significantly.

Example 1 and example 2 considers the response of a cantilever beam with a natural
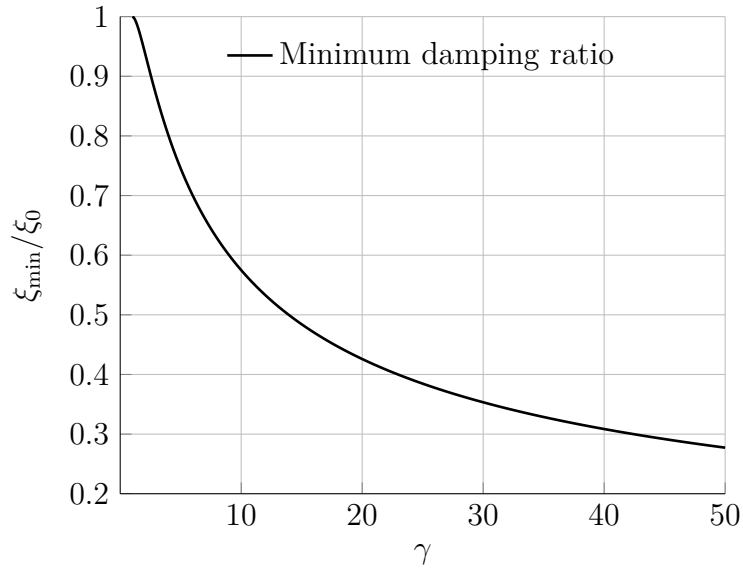
Figure 3.4: The figure shows the minimum damping ratio $\xi_{\min}$ compared to the specified damping ratio ξ_0 with increasing ratio γ between the two specified frequencies.

frequency close to $\omega_{\min}$. In example 1 the loading and the monitored response variable are dominated by the first mode and therefore illustrates a case where the above simplified method is effective in specifying damping ratios. In example 2, the loading and the monitored response are dominated by the second mode which lies close to $\omega_{\min}$ and illustrates the consequence this has on the response.

Example 1. Consider the cantilever beam shown in figure 3.5.

L	$15\,\mathrm{m}$
EI	$1.667 \times 10^6\,\mathrm{N\,m^2}$
m	$100\,\mathrm{kg\,m^{-1}}$
P_0	$1000\,\mathrm{N}$
ξ_0	0.05
Ω	$0 - 100\mathrm{rad\,s^{-1}}$
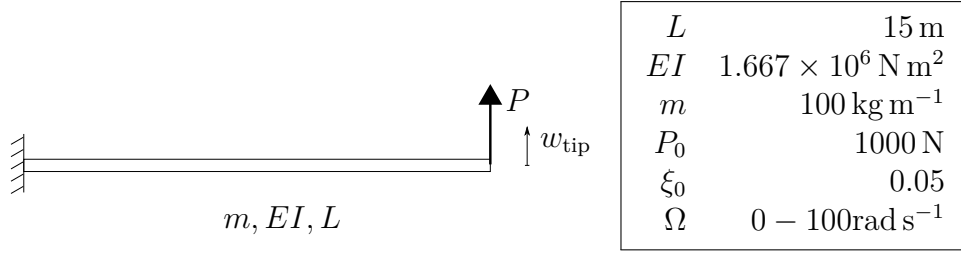
Figure 3.5: The figure shows the beam and the definition of the loading and the observed response variable, the table shows the properties of the beam and the loading.

The beam has a constant cross section with flexural rigidity EI, distributed mass m and length L. The beam is loaded with a harmonic concentrated load $P = P_0 \sin \Omega t$, where the amplitude is P_0 and the load frequency is Ω. Note that the load frequency may range from 0 to 100 rad s^{-1}. Damping in the system is assumed to be around ξ_0 modal damping.

The system is to be analyzed with conventional 4DOF Euler-Bernoulli beam elements. The system is solved with both Rayleigh damping, and the direct damping method. The implications of using Rayleigh damping versus the direct damping matrix is to be determined for the vertical deflection at the tip of the beam.

The element matrices are not stated here but can be found in almost any book on structural dynamics, see for instance [9, chap 18.7]. A preliminary convergence study shows that $N = 4$ elements are sufficient to describe the modes within the specified frequency range of $0 - 100\mathrm{rad\,s^{-1}}$. The resulting mass $\boldsymbol{M}$ and stiffness matrix $\boldsymbol{K}$ for the cantilever beam are given in appendix A. From the mass and the stiffness matrix, the eigenvalues of the system may be obtained through equation (3.14)

The direct damping matrix is determined by employing equation (3.30) with $\xi = \xi_0$ in all modes, see the direct damping matrix $\boldsymbol{C}_{\mathrm{Dir}}$ in appendix A. The Rayleigh damping matrix is constructed with the damping ratios $\xi_p = \xi_r = \xi_0$, and the first frequency is set equal to the first natural frequency, i.e $\omega_p = \omega_1$. The second frequency is chosen equal fourth natural frequency, i.e $\omega_r = \omega_4$. This yields the coefficients $a_0 = 0.1961\,\mathrm{rad\,s^{-1}}$ and $a_1 = 0.0014\,\mathrm{s\,rad^{-1}}$ and the damping matrix $\boldsymbol{C}_{\mathrm{Ray}}$, see appendix A. In the table below, the four first eigenfrequencies of the system are given together with the resulting damping ratios in the corresponding modes with Rayleigh and Direct damping.

Table 3.1: The table shows the four first natural frequencies of the beam and the resulting damping ratios with direct damping and Rayleigh damping.

$\omega_n[\mathrm{rad\,s^{-1}}]$	$\xi_{\mathrm{Rayleigh}}[\%]$	$\xi_{\mathrm{Direct}}[\%]$
2.0	5.0	5.0
12.7	1.6	5.0
35.7	2.7	5.0
70.4	5.0	5.0

With the above Rayleigh damping matrix $\gamma = 35.2$ and $\omega_{\min} = 11.9\,\mathrm{rad\,s^{-1}}$ which

22

is close to the second natural frequency of $12.7\,\mathrm{rad\,s^{-1}}$. The second mode will therefore have little damping, and it is expected that the response in this mode will be significantly different for the two systems with different damping matrices.

Figure 3.6 shows the frequency response plot for the vertical deflection of the tip of the beam w_{tip} normalized against the static deflection of the tip of the beam w_{st}.
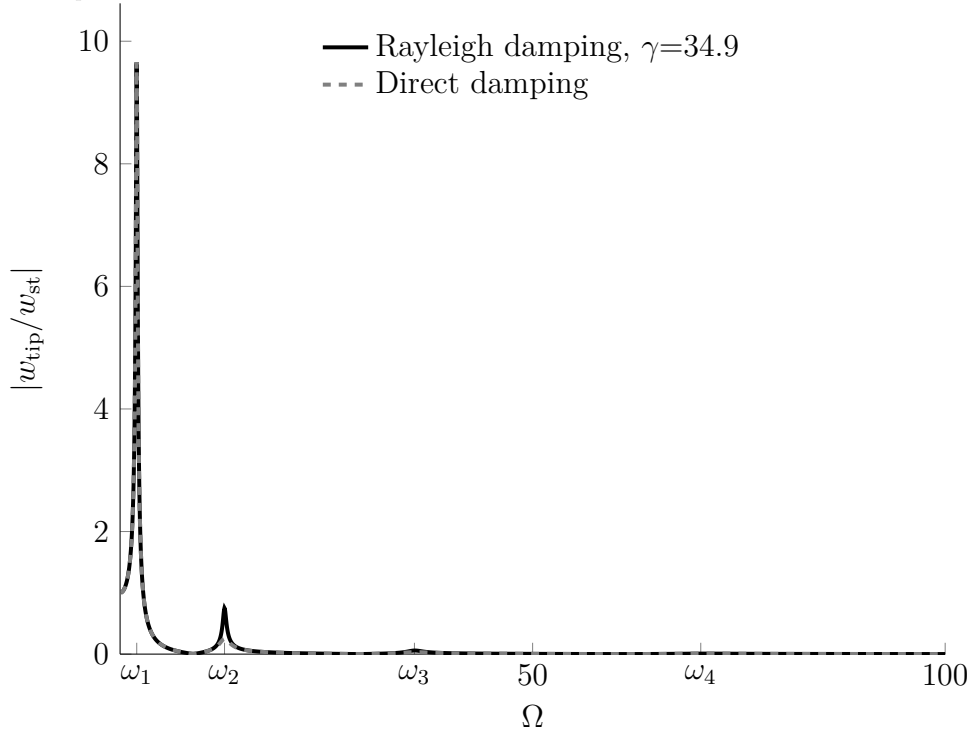
Figure 3.6: The figure shows the frequency response of the beam with direct and Rayleigh damping.

There are several important things which can be seen from the frequency response plot. First of all, the plot shows that the responses in the two systems are different in the second mode, it can also be seen that the responses are different in the third mode. The response in the first and fourth mode are identical. All of this is a consequence of the differing damping ratios, and is as expected.

Secondly, and perhaps the most obvious, it shows that the first mode totally dominates the response of this particular system. This indicates that the loading of the system primarily excites the first mode, and that the first mode has a significant component in the displacement at the tip of the beam.

This means that the difference between the Rayleigh damping and the Direct damping is only prominent when the frequency of the loading is close to the second or third mode. In other words, the difference between using Rayleigh damping and Direct damping is only significant if the loading works in these modes. Furthermore, if the loading has more than one frequency component, and one of them is in the first mode, the relative difference between using Rayleigh damping and Direct damping diminishes.

▲

Example 2. Consider the cantilever beam shown in figure 3.7.

L	$15\,\mathrm{m}$
EI	$1.667 \times 10^6\,\mathrm{N\,m^2}$
m	$100\,\mathrm{kg\,m^{-1}}$
M_0	$1000\,\mathrm{N\,m}$
ξ_0	0.05
Ω	$0 - 100\mathrm{rad\,s^{-1}}$
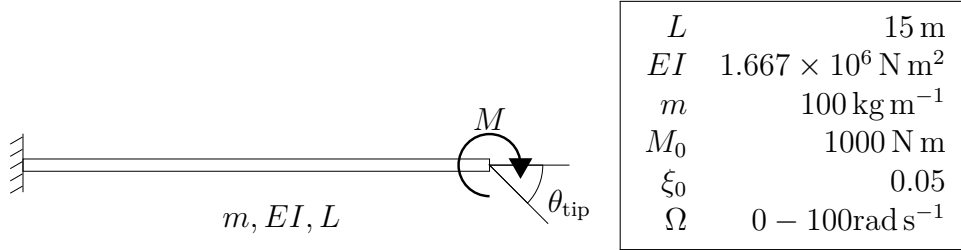
Figure 3.7: The figure shows the beam and the definition of the loading and the observed response variable, the table shows the properties of the beam and the loading.

It is the exact same beam as in example 1, the mass matrix $\boldsymbol{M}$, the stiffness matrix $\boldsymbol{K}$ and the damping matrices $\boldsymbol{C}_{\mathrm{dir}}$ and $\boldsymbol{C}_{\mathrm{Ray}}$ are found in appendix A. The difference in this example is that the beam is loaded with a harmonic concentrated moment $M = M_0 \sin \Omega t$, where the amplitude is M_0 and the load frequency is Ω. The load frequency may still range from 0 to 100 rad s^{-1}.

The natural frequencies and resulting damping ratios are given by the table 3.1, and restated below for convenience.

$\omega_n[\mathrm{rad\,s^{-1}}]$	$\xi_{\mathrm{Rayleigh}}[\%]$	$\xi_{\mathrm{Direct}}[\%]$
2.0	5.0	5.0
12.7	1.6	5.0
35.7	2.7	5.0
70.4	5.0	5.0

In this example, the loading and the monitored response are working to a greater extent in the second mode. Since the second mode has relatively low damping with Rayleigh damping, it is expected that the difference between the response for the direct damping matrix and the Rayleigh damping is significant.

In figure 3.8 the frequency response plot for the rotation of the tip of the beam θ_{tip} normalized against the static rotation of the tip of the beam θ_{st}.
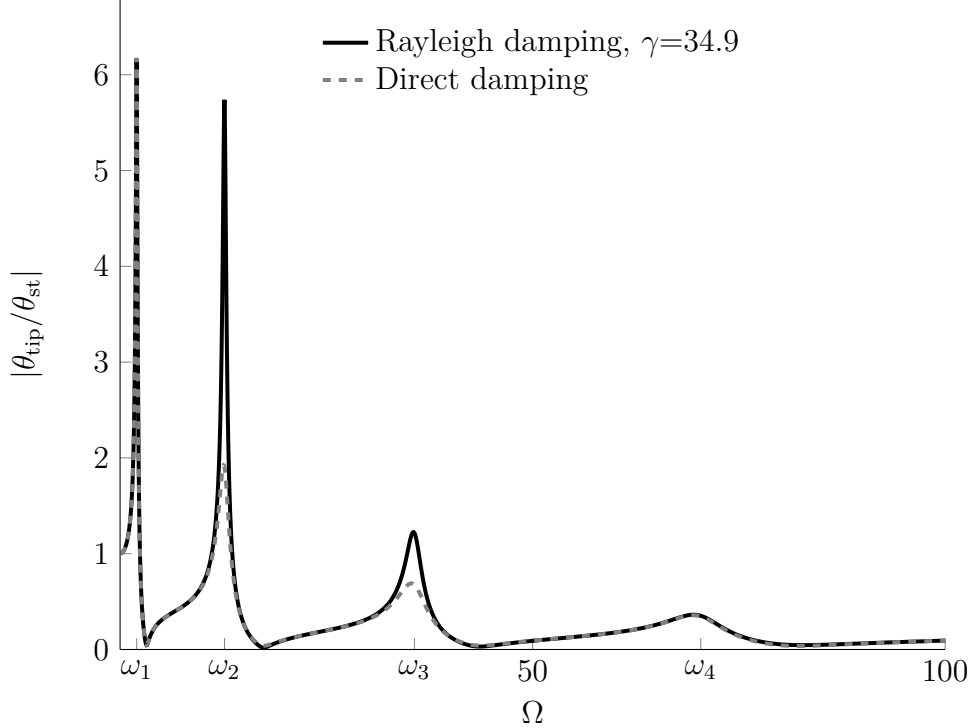
Figure 3.8: The figure shows the frequency response of the beam with direct and Rayleigh damping.

The results show that the response in both the second and third vibration modes are significantly different for the two damping models, the response in the first and forth mode are exactly the same because they have the same damping ratios in with both damping models. This means that if the load has a frequency component in the second or third mode, the difference in the response between the two systems will be significant. If the loading is working in the frequencies in between the frequency of the second and third mode, there will be no difference in the total response of the beam.

▲

Again, it is important to note that the actual modal damping ratios in a system is seldom known such that the above examples provide more of an observation regarding the properties of Rayleigh damping than a categorical shortcoming or error associated with Rayleigh damping. The examples also illustrates another great advantage of Rayleigh damping. Consider the topology of the damping matrices $\boldsymbol{C}_{\mathrm{Dir}}$ and $\boldsymbol{C}_{\mathrm{Ray}}$ provided in appendix A. As stated before, the direct damping matrix $\boldsymbol{C}_{\mathrm{Dir}}$ is a full matrix, while the damping matrix $\boldsymbol{C}_{\mathrm{Ray}}$ keeps the topology of the mass matrix $\boldsymbol{M}$ and the stiffness matrix $\boldsymbol{K}$. This is important both with regards to computer memory use, and in regards to computational efficiency in certain numerical integration schemes. For instance, the commercial finite element code Abaqus uses the Hilber-Hughes-Taylor α-method (HHT α-method) as its default implicit time integration algorithm [12, sec 6.3.2]. The HHT α-method is an extension of the well known Newmark β-method, and involves the inversion of the matrix, $\boldsymbol{K}^{\mathrm{eff}} = h_1 \boldsymbol{M} + h_2 \boldsymbol{C} + h_3 \boldsymbol{K}$, where $h_{1,2,3}$ are coefficients dependent on the numerical coefficients α_H, β, γ and the time step Δt_{n+1}. It is apparent that if $\boldsymbol{C}$ is a full matrix, $\boldsymbol{K}^{\mathrm{eff}}$ is also a full matrix. A full matrix, as opposed to a sparse matrix, is far more memory intensive and computationally expensive to invert, see discussion [13, p.

239-243].

To summarize this discussion on classical viscous damping it is appropriate to point out that while the direct damping matrix and the "higher-order" Caughey damping matrix provide better control over the damping ratios in the specific modes than the Rayleigh damping matrix, the Rayleigh damping matrix provides in many cases better computational efficiency than the two other methods. It has also been pointed out that more often than not, the actual damping ratios of a system is not known, but obtained from experience data from similar structures. These two factors combined, speaks a strong case for Rayleigh damping in comparison to the two other methods of constructing the damping matrix.

3.5 The quadratic eigenvalue problem

In this section it is assumed that the damping matrix C is real and symmetric. The general form of the solution for the damped multi degree of freedom system is the same as for the undamped case, i.e equation (3.13). Introducing equation (3.13) into the homogeneous version of equation (3.27) yields what is known as the quadratic eigenvalue problem, see equation (3.42).

$$\left(s_n^2 M + s_n C + K \right) \phi_n = 0 \tag{3.42}$$

Although the eigenvalues and eigenvectors may be obtained through equation (3.42), it is beneficial to linearize the quadratic eigenvalue problem into a linear eigenvalue problem. This allows to make use of the derivations made for the linear eigenvalue problem in section 3.3. To obtain the linearized form of the eigenvalue problem it is necessary to transfer from the physical coordinates to the state coordinates or the *state space*. By augmenting equation (3.27) and $M\dot{u} - M\dot{u} = 0$, the state space equation of motion is found, see equation (3.43).

$$A\dot{x} + Bx = R \tag{3.43}$$

where x is the state space vector, R is the state space load vector and the matrices A and B are the state matrices, all defined by equations (3.44).

$$A = \begin{bmatrix} 0 & M \\ M & C \end{bmatrix} \tag{3.44a}$$

$$B = \begin{bmatrix} -M & 0 \\ 0 & K \end{bmatrix} \tag{3.44b}$$

$$R = \begin{bmatrix} 0 \\ P \end{bmatrix} \tag{3.44c}$$

$$x = \begin{bmatrix} \dot{u} \\ u \end{bmatrix} \tag{3.44d}$$

The state matrices A and B have dimensions $2N \times 2N$ and are real and symmetric because M, C and K are real and symmetric. The general form of the solution to the homogeneous problem for the state space equation of motion is found to be on the same

form as the general form given by equation (3.13), i.e $\boldsymbol{x} = \boldsymbol{\theta}\,\mathrm{e}^{st}$. Introducing the general solution into the state space equation of motion, the linear eigenvalue problem for the damped multi degree of freedom system is given by equation (3.45)

$$(\boldsymbol{B} - \lambda_n \boldsymbol{A})\boldsymbol{\theta}_n = \boldsymbol{0} \tag{3.45}$$

where $\lambda_n = -s_n$ is the eigenvalue and $\boldsymbol{\theta}_n$ is its corresponding eigenvector. There are $2N$ eigenvalues and eigenvectors, and the eigenvalues are again assumed to be distinct. Since neither $\boldsymbol{A}$, nor $\boldsymbol{B}$ are positive definite, the eigenvalues are in general complex, this can be seen with a similar derivation to the one that produced equation (3.16), but $\boldsymbol{\theta}_n^T \boldsymbol{A} \bar{\boldsymbol{\theta}}_n$ may now be zero and λ_{In} is therefore not necessarily zero. Furthermore the eigenvalues and eigenvectors come in pairs of complex conjugates, this can be verified by taking the complex conjugate of equation (3.45), i.e $(\boldsymbol{B} - \bar{\lambda}_n \boldsymbol{A})\bar{\boldsymbol{\theta}}_n = \boldsymbol{0}$, which shows that also $\bar{\lambda}_n, \bar{\boldsymbol{\theta}}_n$ are also valid eigenvalues and eigenvectors. This means that if $\lambda_n, \boldsymbol{\theta}_n$ is a set of eigenvalues and eigenvectors of equation (3.45), then their complex conjugates $\bar{\lambda}_n, \bar{\boldsymbol{\theta}}_n$ are also a set of eigenvalues and eigenvectors of the same equation.

Since both $\boldsymbol{A}$ and $\boldsymbol{B}$ are symmetric, the eigenvectors $\boldsymbol{\theta}_n$ are orthogonal with respect to $\boldsymbol{A}$ and $\boldsymbol{B}$, the proof is analogous to that of the undamped case, see derivation of equation (3.21). The eigenvectors may also be normalized analogous to mass normalization, such that $\boldsymbol{\theta}_n^T \boldsymbol{A} \boldsymbol{\theta}_n = 1$ and $\boldsymbol{\theta}_n^T \boldsymbol{B} \boldsymbol{\theta}_n = \lambda_n$.

3.5.1 The use of the quadratic eigenvalue problem

The quadratic eigenvalue problem and the complex eigenvalues and eigenvectors may be used to obtain the physical response of a dynamic system by utilizing the complex eigenvectors in a modal transformation. The method for obtaining the response with the eigenvectors and eigenvalues of the quadratic eigenvalue problem is herein called complex modal analysis. Since the quadratic eigenvalue problem includes the damping matrix, the complex modal analysis diagonalizes the system regardless of whether the damping is classical or non-classical. The following section will derive the equation for the complex modal analysis and verify the complex modal analysis in an example by comparing the obtained response from the complex modal analysis against the response obtained by classic modal analysis and implicit numerical integration with the Newmark β-method.

The complex eigenvalues may also be used to determine the resonance frequencies and the effective modal damping ratios of damped multi degree of freedom systems. Once the equations from the complex modal analysis are verified in the following subsection, the same equations will be utilized to show that the complex eigenvalues predict the resonance frequencies of generally damped viscous systems.

Complex modal analysis.

In a similar fashion as for the undamped eigenvalue problem, a damped modal matrix $\boldsymbol{\Theta}$ may be defined from the damped eigenvectors $\boldsymbol{\theta}_n$, i.e $\boldsymbol{\Theta} = \begin{bmatrix} \boldsymbol{\theta}_1 & \boldsymbol{\theta}_2 & \cdots & \boldsymbol{\theta}_{2N} \end{bmatrix}$. The damped modal matrix also defines the linear tranformation from the state space $\boldsymbol{x}$ to the damped modal coordinates $\boldsymbol{z}$, see equation (3.46).

$$\boldsymbol{x} = \boldsymbol{\Theta} \boldsymbol{z} \tag{3.46}$$

Since the eigenvectors of the quadratic eigenvalue problem are orthogonal with respect to the state matrices $\boldsymbol{A}$ and $\boldsymbol{B}$, the modal transformation $\boldsymbol{\Theta}^T \boldsymbol{A} \boldsymbol{\Theta}$ and $\boldsymbol{\Theta}^T \boldsymbol{B} \boldsymbol{\Theta}$ yields two diagonal matrices. If the proper normalization is used, the modal transformation yields the identity matrix $\boldsymbol{I}$ and the spectral matrix $\boldsymbol{S} = \begin{bmatrix} \lambda_1 & \lambda_2 & \cdots & \lambda_{2N} \end{bmatrix}$, see equations below.

$$\boldsymbol{\Theta}^T \boldsymbol{A} \boldsymbol{\Theta} = \boldsymbol{I}$$

$$\boldsymbol{\Theta}^T \boldsymbol{B} \boldsymbol{\Theta} = \boldsymbol{S}$$

Introducing equation (3.46) into equation (3.43) and premultiplying with $\boldsymbol{\Theta}^T$ gives the governing differential equation in the damped modal coordinates.

$$\dot{\boldsymbol{z}} + \boldsymbol{S} \boldsymbol{z} = \boldsymbol{R}_{\boldsymbol{\Theta}} \tag{3.47}$$

where $\boldsymbol{R}_{\boldsymbol{\Theta}} = \boldsymbol{\Theta}^T \boldsymbol{R}$ is the damped modal load vector.

Since the spectral matrix is diagonal, equation (3.47) is $2N$ uncoupled first order differential equations on the form $\dot{z}_n + \lambda_n z_n = R_{\Theta n}$. The complementary solution is $z_{cn} = z_{cn0}\, \mathrm{e}^{-\lambda_n t}$, and is given on matrix form in the equation below.

$$\boldsymbol{z}_c(t) = \mathrm{e}^{-\boldsymbol{S}t} \boldsymbol{z}_{c0}$$

The particular solution $\boldsymbol{z}_p(t)$ is determined by the characteristics of the loading, in the continuation it is assumed that the loading is a single sinusodial, i.e $\boldsymbol{P} = \boldsymbol{P}_0 \sin \Omega t$ and $\boldsymbol{R}_{\boldsymbol{\Theta}} = \boldsymbol{R}_{\boldsymbol{\Theta} 0} \sin \Omega t$, the particular solution is given by the following equation.

$$\boldsymbol{z}_p(t) = (\boldsymbol{S} \sin \Omega t - \Omega \boldsymbol{I} \cos \Omega t) \boldsymbol{D} \boldsymbol{R}_{\boldsymbol{\Theta} 0} \tag{3.48}$$

where $\boldsymbol{D} = (\Omega^2 \boldsymbol{I} + \boldsymbol{S} \boldsymbol{S})^{-1}$. The total solution of the damped modal equations are the sum of the complementary and the particular solution, see below

$$\boldsymbol{z}(t) = \mathrm{e}^{-\boldsymbol{S}t} \boldsymbol{z}_{c0} + (\boldsymbol{S} \sin \Omega t - \Omega \boldsymbol{I} \cos \Omega t) \boldsymbol{D} \boldsymbol{R}_{\boldsymbol{\Theta} 0}$$

The initial conditions of the system in the physical coordinates are $\boldsymbol{u}_0$ and $\dot{\boldsymbol{u}}_0$, which by equation (3.44d) yields the initial conditions in the state space $\boldsymbol{x}_0 = \begin{bmatrix} \dot{\boldsymbol{u}}_0 & \boldsymbol{u}_0 \end{bmatrix}^T$. Through the orthogonality relation for the damped eigenvectors, $\boldsymbol{\Theta}^T \boldsymbol{A} \boldsymbol{\Theta} = \boldsymbol{I}$, and equation (3.46) the initial condition in the modal coordinates can be found to be $\boldsymbol{z}_0 = \boldsymbol{\Theta}^T \boldsymbol{A} \boldsymbol{x}_0$, such that the total solution of in the modal coordinates with the initial conditions is given by the following equation

$$\boldsymbol{z}(t) = \mathrm{e}^{-\boldsymbol{S}t} (\boldsymbol{\Theta}^T \boldsymbol{A} \boldsymbol{x}_0 + \Omega \boldsymbol{D} \boldsymbol{R}_{\boldsymbol{\Theta} 0}) + (\boldsymbol{S} \sin \Omega t - \Omega \boldsymbol{I} \cos \Omega t) \boldsymbol{D} \boldsymbol{R}_{\boldsymbol{\Theta} 0}$$

To obtain the response in the physical coordinates $\boldsymbol{u}$, let the transformation matrix $\boldsymbol{T}$ be defined by $\boldsymbol{T} = \begin{bmatrix} \boldsymbol{0} & \boldsymbol{I} \end{bmatrix}$, such that it gives the relation between the physical coordinates $\boldsymbol{u}$ and the state coordinates $\boldsymbol{x}$, see equation below.

$$\boldsymbol{u} = \boldsymbol{T} \boldsymbol{x} \tag{3.49}$$

By combining this result with equation (3.46), the response in the physical coordinates of a damped multi degree of freedom system with a single harmonic load is finally given by equation (3.50).

$$\boldsymbol{u}(t) = \boldsymbol{T}\boldsymbol{\Theta}\left[\mathrm{e}^{-\boldsymbol{S}t}(\boldsymbol{\Theta}^T\boldsymbol{A}\boldsymbol{x}_0 + \Omega\boldsymbol{D}\boldsymbol{R}_{\Theta0}) + (\boldsymbol{S}\sin\Omega t - \Omega\boldsymbol{I}\cos\Omega t)\boldsymbol{D}\boldsymbol{R}_{\Theta0}\right] \qquad (3.50)$$

In example 3 the above derivation will be verified against the classical modal analysis in a classically-damped system and against the Newmark β-method in a non-classically damped system. Once the above derivation is verified, the resonance frequencies and the effective damped ratios of the system will be determined in the subsequent section. It should be noted that Lallement and Inman [14] provided the inspiration for the following example.

Example 3. Consider the cantilever beam shown in figure 3.9.

|	
L	$15\,\mathrm{m}$
EI	$1.667 \times 10^6\,\mathrm{N\,m^2}$
m	$100\,\mathrm{kg\,m^{-1}}$
P_0	$1000\,\mathrm{N}$
Ω	$10\mathrm{rad\,s^{-1}}$
ξ_0	0.05
ξ_{non}	0 and -7.5
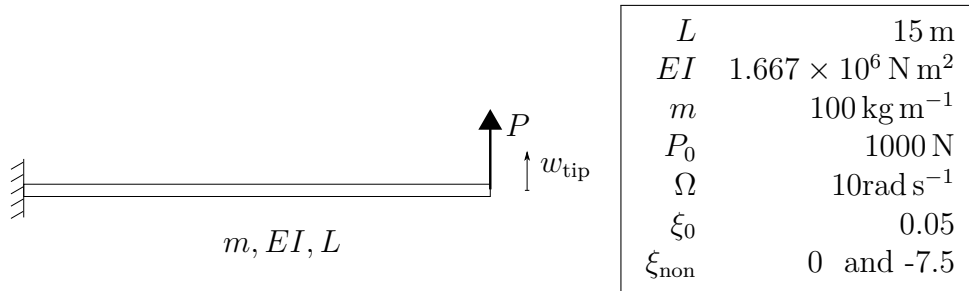
Figure 3.9: The figure shows the beam and the definition of the loading and the observed response variable, the table shows the properties of the beam and the loading.

It is the exact same beam as in example 1 and example 2, and the same discretization of the beam is used such that the mass matrix $\boldsymbol{M}$ and the stiffness matrix $\boldsymbol{K}$ are found in appendix A. The beam is loaded with single harmonic concentrated load $P = P_0\sin\Omega t$ at the tip, where the amplitude is P_0 and the load frequency is Ω.

The damping matrix is a non-classical damping matrix, constructed from a classical direct damping matrix $\boldsymbol{C}_{\mathrm{Dir}}$ with $\xi_n = \xi_0$ in all modes, and a non-classical damping matrix $\boldsymbol{C}_{\mathrm{non}}(\xi_{\mathrm{non}})$, see below.

$$\boldsymbol{C}(\xi_{\mathrm{non}}) = \boldsymbol{C}_{\mathrm{Dir}} + \boldsymbol{C}_{\mathrm{non}}(\xi_{\mathrm{non}})$$

The direct damping matrix $\boldsymbol{C}_{\mathrm{Dir}}$ is the same as the one utilized in example 1 and example 2 and is found in appendix A. The non-classical part is constructed such that modes 1 and 2 are coupled when the classical transformation $\boldsymbol{\Phi}^T\boldsymbol{C}_{\mathrm{non}}(\xi_{\mathrm{non}})\boldsymbol{\Phi}$ is employed, see below.

$$\boldsymbol{\Phi}^T\boldsymbol{C}_{\mathrm{non}}(\xi_{\mathrm{non}})\boldsymbol{\Phi} = \xi_{\mathrm{non}}\begin{bmatrix} 0 & 1 & 0 & 0 & 0 & 0 & 0 & 0 \\ 1 & 0 & 0 & 0 & 0 & 0 & 0 & 0 \\ 0 & 0 & 0 & 0 & 0 & 0 & 0 & 0 \\ 0 & 0 & 0 & 0 & 0 & 0 & 0 & 0 \\ 0 & 0 & 0 & 0 & 0 & 0 & 0 & 0 \\ 0 & 0 & 0 & 0 & 0 & 0 & 0 & 0 \\ 0 & 0 & 0 & 0 & 0 & 0 & 0 & 0 \\ 0 & 0 & 0 & 0 & 0 & 0 & 0 & 0 \end{bmatrix}$$

The non-classical damping matrix $\boldsymbol{C}_{\mathrm{non}}(\xi_{\mathrm{non}})$ is found in the physical coordinates, by utilizing the method for constructing the direct damping matrix, see discussion related

to equation (3.30). Although the physical interpretation for the non-classical damping matrix is that it provides damping between the first and second mode of vibration. An attempt to describe the physical mechanism which leads to such damping is considered secondary, the purpose of this example is to show that the complex modal analysis may be used to obtain the response of a dynamic system and to investigate the implications of coupled modes.

In order to show that the complex modal analysis may be used to obtain the response of a system, the response obtained by the complex modal analysis will be compared to the response obtained by numerical integration with the Newmark β-method and to the response obtained by classical modal analysis.

Specifically, equation (3.50) is employed in the complex modal analysis, the formula and theory for implementation of the Newmark β-method are found in [9] and the constant acceleration version, i.e $\beta = 1/4$ and $\gamma = 1/2$ is adopted.

The scripts used to carry out the analysis are provided in appendix B.7.

First the coupled damping coefficient ξ_{non} is set to zero, such that the system has classical viscous damping with $\xi_n = \xi_0$. With classical viscous damping it is expected that the response obtained by either method will yield exactly the same results.

The results for the deflection of the tip w_{tip} normalized against the static deflection w_{st} are presented in figure 3.10.
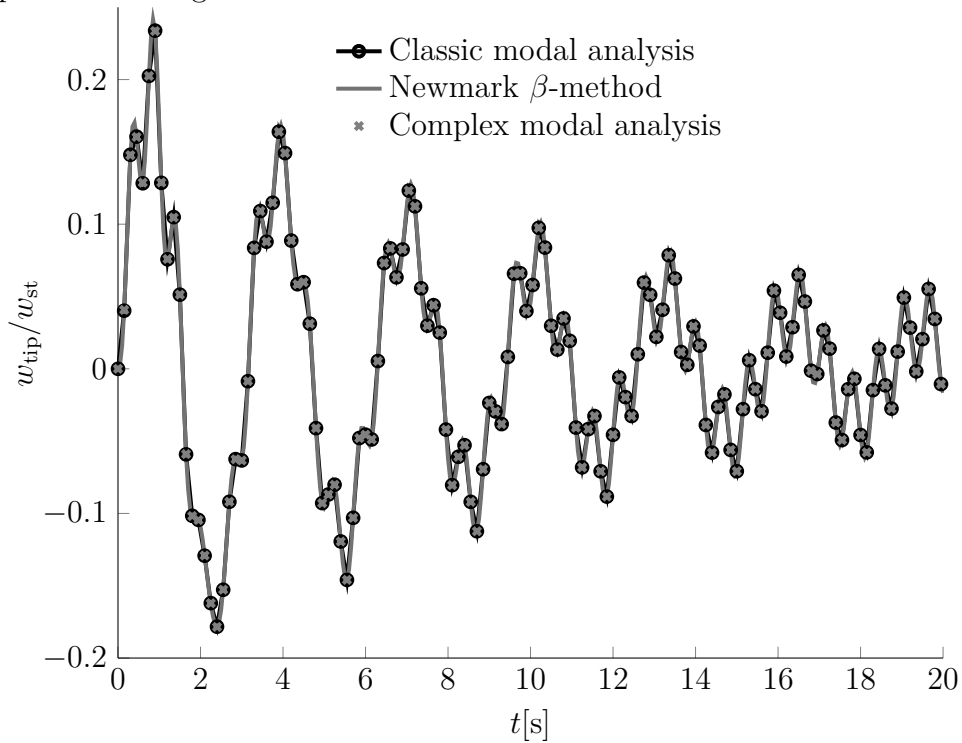
Figure 3.10: The figure shows the response of the tip of the beam with classical viscous damping.

Figure 3.10 shows that all three methods for obtaining the response yields the exact same result. This implies that the methods are implemented correctly in Matlab, and it also implies that the complex modal analysis may be used to obtain the response of a classically damped system.

In the second part of this example, the response of a non-classically damped system

will be obtained. The coupled damping coefficient ξ_{non} is set to -7.5, the number is chosen because it provides significant coupling between the two modes and it yields positive dissipated energy for this *particular* configuration of the system.

The classical modal analysis cannot be utilized to solve a non-classically damped system, the result of the classical modal analysis will be provided with only the classical damping matrix $\boldsymbol{C}_{\mathrm{Dir}}$, such that the new system can be compared to the old one. Regarding the response obtained from the complex modal analysis and the Newmark β-method it is expected that both of them provide the same results.

The results for the deflection of the tip w_{tip} normalized against the static deflection w_{st} are presented in figure 3.11.
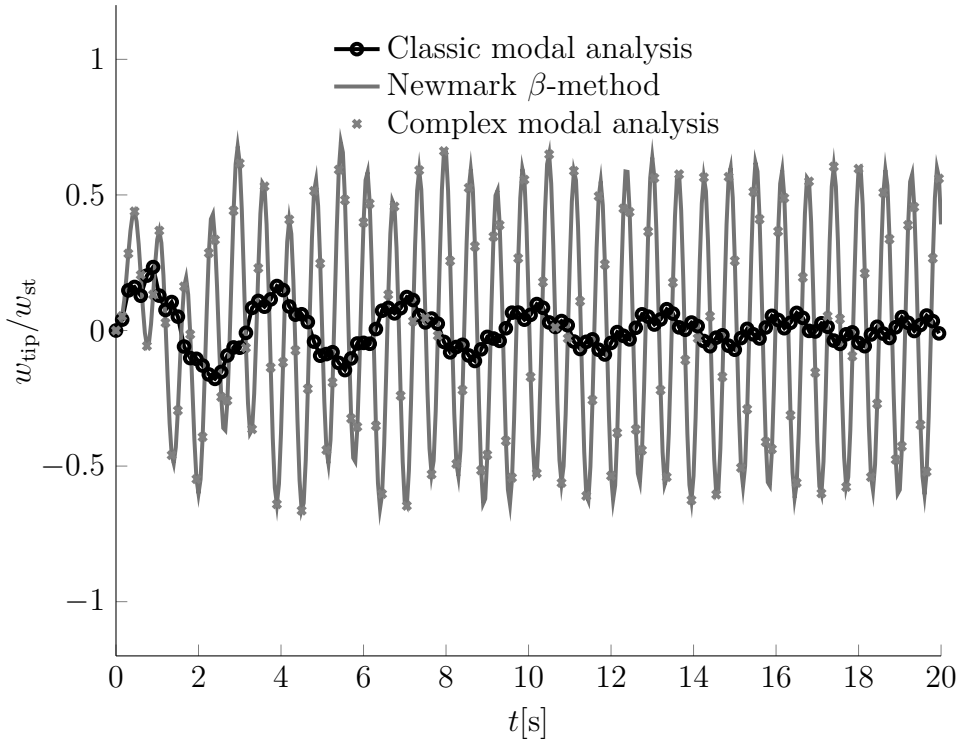

Figure 3.11: The figure shows the response of the tip of the beam with non-classical viscous damping with coupling between the first and the second classical modes.

Figure 3.11 shows that the complex modal analysis and the Newmark β-method both provide the same results, and unless the Newmark β-method is wrongly implemented such that it yields the exact same results as the complex modal analysis, this shows that the complex modal analysis may be used to obtain the response of a non-classically damped system as well.

Regarding the non-classically damped response versus the classically damped response it is seen that introducing the damping between the first and the second mode has actually increased the total response of the system. This is against intuition, because introducing damping to a system usually means that the response of the system is reduced. At second glance, it reveals the actual nature of the geometric *coupling* between the two modes which is introduced with non-classical viscous damping. Consider the equation of motion for the first and second classical mode shown below.

$$\ddot{y}_1 + 2\xi_0\omega_1\dot{y}_1 + 2\xi_{\mathrm{non}}\omega_1\dot{y}_2 + \omega_1^2 y_1 = P_{\Phi,1}$$

31

$$\ddot{y}_2 + 2\xi_{\mathrm{non}}\omega_2\dot{y}_1 + 2\xi_0\omega_2\dot{y}_2 + \omega_2^2 y_2 = P_{\Phi,2}$$

The non-classical damping does not only provide damping between the two first modes, it also provides a *coupling* between the modes. This means that any excitation of either mode, leads to the excitation of the other mode.

In this example the load frequency is $\Omega = 10\,\mathrm{rad\,s^{-1}}$, from example 1 it is known that the second natural frequency of this system is $\omega_2 = 12.7\,\mathrm{rad\,s^{-1}}$, such that the second frequency ratio is $\beta_2 \approx 0.8$. This means that the second mode is strongly excited, and through the coupling provided by the non-classical damping also the first mode is excited. In example 1 the frequency response plot revealed that the first mode dominated the total response at the tip of the beam, such that through the coupling provided by the damping an increase in the response is actually reasonable. In light of this and the fact that the coupling provided by the non-classical damping excites the first modes leads to the question, how does the coupling affect the frequency response of the system? The frequency response plot for the classically and the non-classically damped system are presented below.
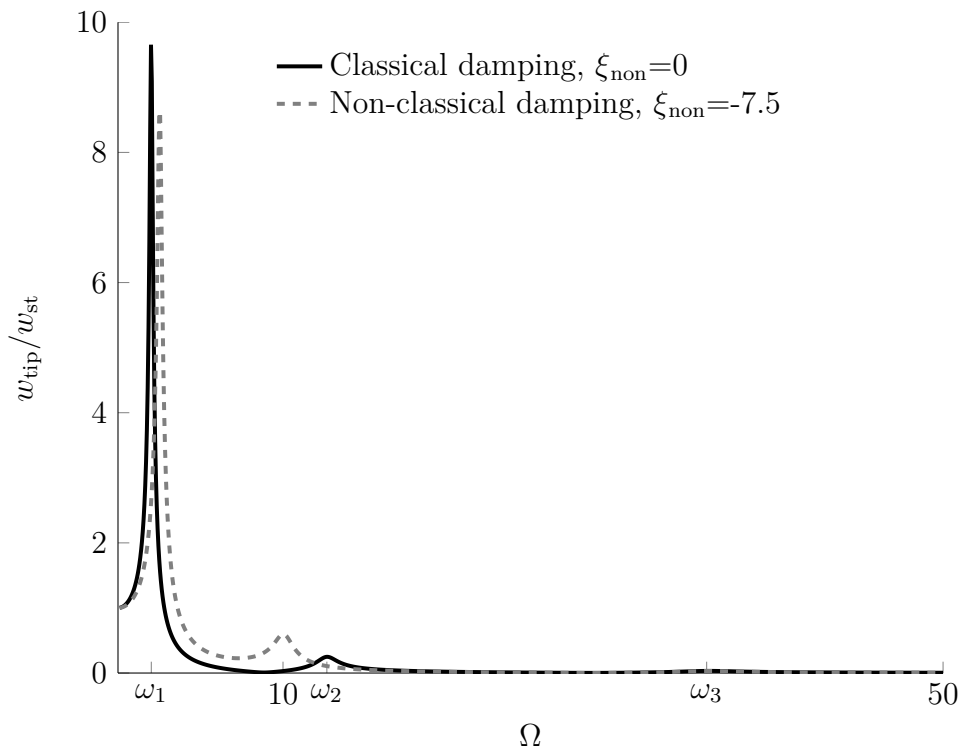
Figure 3.12: The figure shows the frequency response plot of the beam with classical and non-classical damping.

The frequency response plot shows that the resonance frequency for the first and second modes are changed towards each other. This is a result of the geometric coupling provided by non-classical damping. It can be seen that the natural frequencies determined by the linear eigenvalue problem does not coincide with the actual resonance frequencies of the system.

In the subsection following this example, the eigenvalues obtained from the quadratic eigenvalue problem will be used to determine these new natural frequencies of the

system.

▲

Determining the resonance frequencies of the non-classically damped system

In example 3 it was shown that with non-classical damping, the resonance frequencies of the system changes. If the non-classical damping is significant, the undamped natural frequencies determined by the linear eigenvalue problem may not predict the actual resonance frequencies of the system. As discussed before, the resonance frequencies of the system are important in nearly all design states, and being able to predict them is therefore important.

The quadratic eigenvalue may be utilized to determine the resonance frequencies of the non-classically damped system. Recall that the eigenvalues from the quadratic eigenvalue problem are in general complex and come in complex conjugate pairs such that they may be written on the following form,

$$\lambda_n = \lambda_{Rn} \pm i\,\lambda_{In} \tag{3.51}$$

where λ_{Rn} is the real part and λ_{In} is the imaginary part of the eigenvalues. The eigenvalues of the complex eigenvalue problem are usually related to the eigenvalues of the linear eigenvalue problem through the underdamped complementary solution. As discussed before, most structures are infact underdamped, and therefore it is in the continuation assumed that the system is underdamped. Recall that the solution to the characteristic equation for the single degree of freedom system, and the classically underdamped system was found to be

$$\lambda_n = -\xi_n \omega_n \pm i\,\omega_n\sqrt{1 - \xi_n^2}$$

Comparing the real and the imaginary parts of the above equation and equation (3.51) yields the following relations between the eigenvalues obtained by the complex eigenvalue problem and the complex natural frequencies ω_n and the damping ratio ξ_n.

$$\omega_n = \sqrt{\lambda_{Rn}^2 + \lambda_{In}^2} \tag{3.52a}$$

$$\xi_n = -\frac{\lambda_{Rn}}{\sqrt{\lambda_{Rn}^2 + \lambda_{In}^2}} \tag{3.52b}$$

The resonance frequencies of the damped system occurs when the response becomes large. From the proceeding section on the complex modal analysis, the steady state response, i.e the particular solution, for the complex modal coordinates was provided by equation (3.48). Through the transformation matrices from the complex modal coordinates to the physical coordinates, defined by equation (3.46) and equation (3.49), the particular solution in the state space is found to be given by the following equation.

$$\boldsymbol{u}_p(t) = \boldsymbol{T}\boldsymbol{\Theta}(\boldsymbol{S}\sin\Omega t - \Omega\boldsymbol{I}\cos\Omega t)\boldsymbol{D}\boldsymbol{R}_{\Theta 0}$$

Recall that the matrix $\boldsymbol{D}$ was defined by $\boldsymbol{D} = (\Omega^2\boldsymbol{I} + \boldsymbol{S}\boldsymbol{S})^{-1}$, which implies that when the matrix $(\Omega^2\boldsymbol{I} + \boldsymbol{S}\boldsymbol{S})$ is singular, the matrix $\boldsymbol{D}$ tends to infinity, and the system is in resonance. The matrix $(\Omega^2\boldsymbol{I} + \boldsymbol{S}\boldsymbol{S})$ is singular when its determinant is zero, and

the determinant of a diagonal matrix is the product of its diagonal elements. This means that if any of its diagonal elements are zero or close to zero, the dynamic system is in resonance. The condition for resonance is therefore given by the equation below.

$$\Omega^2 + \lambda_n^2 = \Omega^2 + \lambda_{Rn}^2 - \lambda_{In}^2 + i\,2\lambda_{Rn}\lambda_{In} = 0$$

Assuming that the damping ratios ξ_n are small, the real part of the eigenvalue vanishes, i.e $\lambda_{Rn} = -\xi_n\omega_n \approx 0$ and the imaginary part equals the complex natural frequency, i.e $\lambda_{In} \approx \omega_n$, see equations (3.52).

This implies that resonance occurs when the load frequency Ω is equal to the complex natural frequencies ω_n given by equation (3.52a).

To confirm the above discussion and derivation, consider the following brief example where the resonance frequencies for the non-classically damped beam in example 3 are determined with equation 3.52a and compared against the predicted resonance frequencies from the undamped eigenvalue problem.

Example 4. In this example the resonance frequencies found for the non-classically damped system in example 3 are to be determined. The frequency response plot, figure 3.12, given in example 3 is given below for convenience.
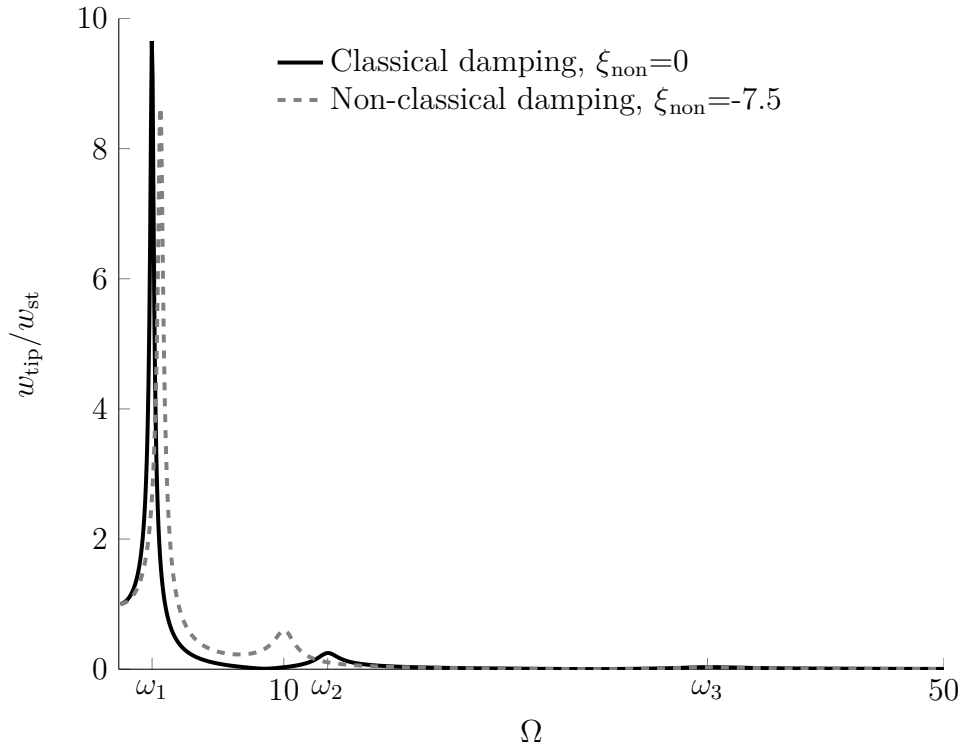
The resonance frequencies where found by employing the inbuilt Matlab function `findpeaks` on the frequency response plot, the result are given in the first column of table 3.2. The natural frequencies calculated by the linear and quadratic eigenvalue problem and are also provided in the second and third column, respectively.

34

Table 3.2: The table shows the resonance frequencies of the cantilever beam of example 3 with non-classical damping and the natural frequencies of the system estimated by the linear and complex eigenvalue problem. The effective damping ratios in the modes are also given.

Resonance frequencies $[\mathrm{rad\,s^{-1}}]$	Linear frequencies $[\mathrm{rad\,s^{-1}}]$	Complex frequencies $[\mathrm{rad\,s^{-1}}]$	Effective modal ratios $[\%]$
2.6	2.0	2.5	5.8
10.0	12.7	10.1	5.8
35.9	35.7	35.7	5.0
71.0	70.4	70.4	5.0
132.1	130.9	130.9	5.0

The table shows that the complex natural frequencies obtained from the quadratic eigenvalue problem estimates the resonance frequencies of the beam for the first and second mode much better than the linear eigenvalue problem. It can also be seen that for the modes which are not coupled, i.e all modes except the first and the second, the natural frequencies obtained the linear and the quadratic eigenvalue problem are the same. The coupling between the first and second mode changes the effective modal damping ratios for these modes, but does not affect damping ratios for the other modes.

▲

The use of the complex natural frequencies are not limited to determining the resonance frequency of a non-classically damped system. With the quadratic eigenvalue problem, the non-classical damping matrix of the system could be determined by inverting the problem in the example above. Imagine that the frequency response of a structure was known from experiments, and the elastic and inertial properties where well defined, i.e the stiffness and the mass matrix was known. Then the damping matrix could be tuned either through a iterative process or an analytical approach, such that the complex natural frequencies coincided with the resonance frequencies of the experimental data.

The main topics in this chapter on multi degree of freedom systems have been the linear eigenvalue problem, viscous damping models and the quadratic eigenvalue problem. The purpose of the section on the linear eigenvalue problem was to provide the basis for development and discussion of the viscous damping models and the derivation of the quadratic eigenvalue problem.

From the discussion on viscous damping models, it is apparent that unless the specific damping ratios of the given structure are known or the non-classical damping matrix is available from experimental data on the specific structure, the Rayleigh damping matrix provides sufficient control over the damping ratios and better computational efficiency than the alternatives. The Rayleigh damping matrix will therefore be adopted in the continuation of this thesis, more specifically in the case study in chapter 5

The discussion on the quadratic eigenvalue problem showed that the complex eigenvalues could be used to determine the resonance frequencies and effective modal damping ratios of a non-classically damped system. These findings will be utilized in chapter 5 to determine the resonance frequencies of the complete structure, and to confirm that the structure has reasonable damping ratios in the significant modes.

Chapter 4

Dynamic load modeling

This section reviews different methods to model the train and the difference between the load models and their effect on the structure. The section explains how the load models are implemented in Abaqus. The phenomena of resonance from the moving loads will be discussed, and it will be shown that there exists two different ways moving loads induce resonance in a structure.

4.1 Moving forces model

In this section the theory for the moving forces load model will be developed. First the problem with a moving load on a simply supported beam will be solved analytically, then the formulation for the moving load on a beam for finite element simulation will be derived. Finally, an example will be used to verify the finite element formulation against the analytical solution.
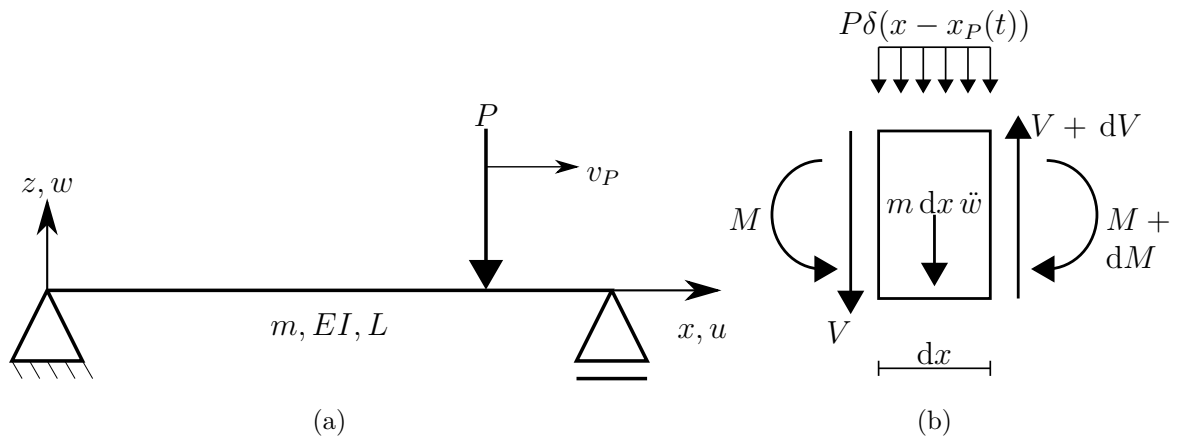
Figure 4.1: The figure shows the properties and definitions used in the derivation of the analytical solution of the moving force problem.

Consider the simply supported beam shown in figure 4.1a. It has constant cross sectional area made up of a linear elastic material. The beam has mass per unit length m, bending stiffness EI and length L. It is assumed that the length of the beam is large compared to its other dimensions such that Naviers hypothesis is valid, i.e plane sections remain plane and perpendicular to the neutral axis. The beam is loaded with a

concentrated force P, moving at constant speed v_P. A coordinate x with origin at the left end of the beam and with direction in the length axis of the beam, may describe the position x_P of the load at time t given the initial position is $x_P(t=0) = x_{P0}$, see equation (4.1).

$$x_P(t) = x_{P0} + v_P t \tag{4.1}$$

The moving load may be represented as a spatially distributed load by introducing the Dirac delta function $\delta(x - x_P(t))$. Figure 4.1b shows the forces working on an infinitesimal element of the beam with internal shear force V, moment M, lateral inertia force $m\,dx\,\ddot{w}$ and the external distributed loading $P\delta(x - x_p(t))$. It should be noted that the inertia associated with angular acceleration is neglected. Taking moment equilibrium about the center of the element and neglecting higher order terms, yields the well known relation between the shear and the moment, $\frac{dM}{dx} = V$. Finally, force equilibrium in the vertical direction and the relation $M = -EIw''$ from Naviers hypothesis yields the governing differential equation (4.2).

$$m\ddot{w} + EIw'''' = -P\delta(x - x_P(t)) \tag{4.2}$$

The solution of the above differential equation is assumed to be on the form of $w(x,t) = \phi(x)y(t)$. Introducing this relation into the homogeneous version of equation (4.2) and rewriting the result slightly yields the following equation.

$$\frac{EI}{m}\frac{\phi''''(x)}{\phi(x)} = -\frac{\ddot{y}(t)}{y(t)}$$

It can be seen that the left hand side of the above equation is only dependent on x and the right hand side of the equation is only dependent on t. The above equation can therefore only be satisfied if both sides equal the same constant λ, which are the eigenvalues of the continuous system. It will be shown that there exists an infinite number of eigenvalues in the continuous system, and the following equations must be satisfied for each of them.

$$\ddot{y}_n(t) + \lambda_n y_n(t) = 0 \tag{4.3a}$$

$$\phi_n''''(x) - \lambda_n \frac{m}{EI}\phi_n(x) = 0 \tag{4.3b}$$

Equation (4.3a) has a general solution on the form $y_n = A_n e^{s_n t}$, which by introduction into equation (4.3a) yields the constant $s_n = \sqrt{-\lambda_n}$. If $\lambda_n < 0$ then $y(t)$ grows exponentially and subsequently the homogeneous solution of $w(x,t)$ diverges. This is clearly unphysical and dictates that $\lambda_n \geq 0$, and it follows that $s_n = i\sqrt{\lambda_n} = i\omega_n$, where $\omega_n = \sqrt{\lambda_n}$ are the natural frequencies of the system.

The general solution of equation (4.3b) is on the form $\phi_n = B_n e^{\alpha_n x}$. Defining $\gamma_n^4 = \lambda_n \frac{m}{EI}$ yields the following relation,

$$\alpha_n^4 - \gamma_n^4 = (\alpha_n^2 + \gamma_n^2)(\alpha_n^2 - \gamma_n^2) = 0$$

which has the solution $\alpha_n = \pm\gamma_n$ and $\alpha_n = \pm i\gamma_n$. Through Euler's formula and hyperbolic identities it is possible to write the general solution of equation (4.3b) as

$$\phi_n(x) = C_{1n}\cos\gamma_n x + C_{2n}\sin\gamma_n x + C_{3n}\cosh\gamma_n x + C_{4n}\sinh\gamma_n x$$

Introducing the boundary conditions of the simply supported beam $w(0,t) = 0$, $w(L,t) = 0$, $w''(0,t) = 0$ and $w''(L,t) = 0$ into the above equation yields $C_{1n} = C_{3n} = 0$, $C_{2n} \sin \gamma_n L = 0$ and $C_{4_n} \sinh \gamma_n L = 0$. Since $\sinh \gamma_n L$ is never zero, C_{4n} has to be zero. A non-trivial solution then demands that $\sin \gamma_n L = 0$, which occurs when $\gamma_n = \frac{n\pi}{L}$.

The nth vibration mode of a simply supported beam is then given by the following equation.

$$\phi_n(x) = C_n \sin \frac{n\pi x}{L}$$

The constant C_n is the magnitude of the mode shape and it can be seen that multiplying $\phi_n(x)$ in equation (4.3b) with the arbitrary constant $\mathcal{C}$ also satisfies equation (4.3b) such that C_n itself is arbitrary. As for the MDOF system, the modes for the continuous system may be mass normalized, to show this recall that the displacement $w_n(x,t)$ due to the nth mode is the product of the mode and the modal coordinate, see equation (4.4).

$$w_n(x,t) = \phi_n(x) y_n(t) \tag{4.4}$$

By introducing equation (4.4) into equation (4.2), multiplying both sides by $\phi_n(x)$ and integrating over the length of the beam, the equation of motion for the nth vibration mode emerges.

$$\int_0^L m[\phi_n(x)]^2 \, \mathrm{d}x \, \ddot{y}_n(t) + \int_0^L EI \phi_n(x) \phi_n''''(x) \, \mathrm{d}x \, y_n(t) = -\int_0^L P \phi_n(x) \delta(x - x_P(t)) \, \mathrm{d}x$$

Choosing the modal mass to be equal to unity, i.e $\int_0^L m[\phi_n(x)]^2 \, \mathrm{d}x = 1$, is known as mass normalization and the nth mass normalized vibration mode is given by equation (4.5).

$$\phi_n(x) = \sqrt{\frac{2}{mL}} \sin \frac{n\pi x}{L} \tag{4.5}$$

Combining equation (4.5) and (4.1) with the equation of motion for the nth vibration mode gives the equation of motion for the nth vibration mode with mass normalized mode shapes [1], see equation (4.6).

$$\ddot{y}_n(t) + \frac{n^4 \pi^4 EI}{mL^4} y_n(t) = -P\sqrt{\frac{2}{mL}} \sin\left(\frac{n\pi v_P t}{L} + \frac{n\pi x_{P0}}{L}\right) \tag{4.6}$$

Comparing equation (4.6) with equation (4.3b) and remembering that $\omega_n = \sqrt{\lambda_n}$ shows that the natural frequency of the system for mode n is given by $\omega_n^2 = \lambda_n = \frac{n^4 \pi^4 EI}{mL^4}$. Note that the derivation does not contain a term which takes damping into account, i.e there is no term which represents energy dissipation from the system. Assuming classical viscous damping, the total energy dissipation from the system is proportional to the modal velocity. Introducing the modal damping ratio ξ_n into the above equation, i.e the left hand side of equation (4.6) is augmented with a term $2\xi_n \omega_n \dot{y}_n(t)$, see equation (4.7).

$$\ddot{y}_n(t) + 2\xi_n \omega_n \dot{y}_n(t) + \omega_n^2 y_n(t) = -P\sqrt{\frac{2}{mL}} \sin\left(\frac{n\pi v_P t}{L} + \frac{n\pi x_{P0}}{L}\right) \tag{4.7}$$

---

[1]Recall the fundamental property of the Dirac delta function, i.e $\int_0^L P \phi_n(x) \delta(x - x_P(t)) \, \mathrm{d}x = P \phi_n(x_P(t))$

From section 2 it is known that there are three distinct solutions to the homogeneous version of equation (4.7), depending on the value of ξ_n. As mentioned in section 2, most engineering structures are underdamped structures. It is therefore assumed that the simply supported beam in figure 4.1a is an underdamped structure. Furthermore, it is assumed that the load starts at the left end, i.e $x_{P0} = 0$, and that the beam is initially at rest, i.e $y_n(0) = 0$ and $\dot{y}_n(0) = 0$. The analytical solution for the modal coordinate y_n is then given by equation (4.8).

$$y_n(t) = \frac{P\sqrt{2mL}L^3/(n^4\pi^4 EI)}{(1-\beta_n^2)^2 + (2\xi_n\beta_n)^2}\left\{2\xi_n\beta_n\cos(\Omega_n t) - (1-\beta_n^2)\sin(\Omega_n t)\right.$$
$$\left. + e^{-\xi_n\omega_n t}\left[\frac{\beta_n(1-\beta_n^2 - 2\xi_n^2)}{\sqrt{1-\xi_n^2}}\sin(\omega_{dn}t) - 2\xi_n\beta_n\cos(\omega_{dn}t)\right]\right\} \tag{4.8}$$

Where Ω_n is the load frequency, ω_n is the natural frequency, β_n is the frequency ratio, ξ_n is the damping ratio and ω_{dn} is the damped natural frequency, see (4.9).

$$\Omega_n = \frac{n\pi v_P}{L} \tag{4.9a}$$

$$\omega_n = \left(\frac{n\pi}{L}\right)^2\sqrt{\frac{EI}{m}} \tag{4.9b}$$

$$\beta_n = \frac{\Omega_n}{\omega_n} \tag{4.9c}$$

$$\omega_{dn} = \omega_n\sqrt{1-\xi_n^2} \tag{4.9d}$$

Inserting equation (4.5) and (4.8) into equation (4.4) and taking the sum of all modes, gives the analytical solution of the displacement field for the simply supported beam, see equation (4.10).

$$w(x,t) = \frac{2PL^3}{\pi^4 EI}\sum_{n=1}^{\infty}\frac{\sin(n\pi x/L)}{n^4[(1-\beta_n^2)^2 + (2\xi_n\beta_n)^2]}\left\{2\xi_n\beta_n\cos(\Omega_n t) - (1-\beta_n^2)\sin(\Omega_n t)\right.$$

$$\left. + e^{-\xi_n\omega_n t}\left[\frac{\beta_n(1-\beta_n^2 - 2\xi^2)}{\sqrt{1-\xi_n^2}}\sin(\omega_{dn}t) - 2\xi_n\beta_n\cos(\omega_{dn}t)\right]\right\}$$
$$\tag{4.10}$$

It should be noted that equation (4.10) is only valid while the loading is on the beam, i.e $0 \leq x_P(t) \leq L$.

In the finite element method, the continous beam is divided into a set of elements, each defined by two nodes. Loads working on the elements, i.e between the nodes, are distributed to the nodes as nodal loads. There are two basic ways of distributing the forces to the nodes in a conventional FEA. First is the consistent load formulation, see equation (3.7c), which utilizes the interpolation functions of the element as weighing functions, in this formulation the distributed loads end up as both nodal point loads and

nodal moments. The second way is by "load lumping", here the forces acting within the elements are distributed to the nodes as nodal forces by linear weighing functions regardless of the polynomial order of the element, see [3, 13]. The consistent formulation is more complex and involved than its counterpart, but yields an exact solution to the mathematical problem. Load lumping involves approximation, but the solution converges as the size of the are elements are reduced. Wu et al. [15] showed that load lumping provides good results for the case of moving concentrated loads. Because of its simplicity and the results obtained by Wu et al., load lumping will be adopted in this thesis.
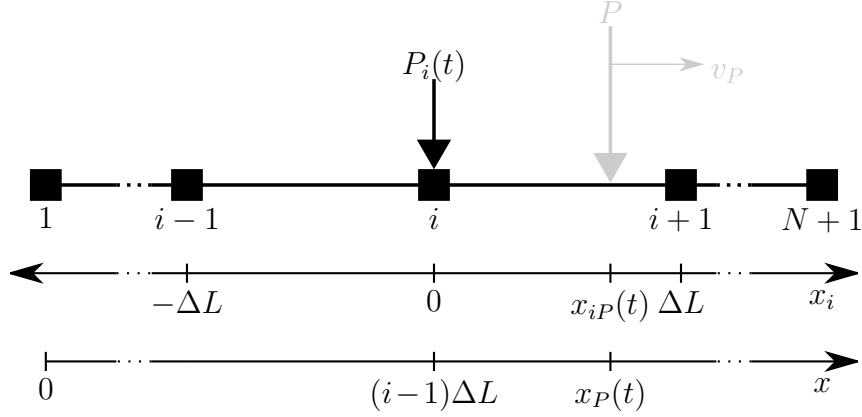

Figure 4.2: The figure shows a continous beam divided into N elements and $N+1$ nodes. The nodal load $P_i(t)$ and the moving load P are also shown. Note that P is shown in gray to signify its indirect effect in the finite element formulation. The figure shows the definition of the local nodal coordinate system x_i and the global coordinate system x, and the position of the moving load in the nodal coordinate system $x_{iP}(t)$ and the global coordinate system $x_P(t)$.

Figure 4.2 shows a continous beam divided into N elements defined by $N+1$ nodes. Assuming that each node is equidistantly spaced, the length of each element is $\Delta L = \frac{L}{N}$. A local coordinate system x_i with origin in node i and direction along the length axis of the beam may define the position x_{iP} of the moving load P. The linear distribution of the moving load P to the nodal load P_i, is then given by equation (4.11).

$$P_i(t) = \begin{cases} \left(1 - \left|\frac{x_{iP}(t)}{\Delta L}\right|\right) P & \text{for } -\Delta L \leq x_{iP}(t) \leq \Delta L \\ 0 & \text{elsewhere} \end{cases} \tag{4.11}$$

The moving load P has the position $x_P(t)$ in the global coordinate system defined with origin in the left end of the continuous beam. With $x_P(0) = x_{P0}$, equation (4.1) is also valid for the position of the moving load depicted in figure 4.2. The relationship between the local and the global position of the moving load is given by equation (4.12).

$$x_{iP}(t) = x_P(t) - (i - 1)\Delta L \tag{4.12}$$

Combining equation (4.1), (4.11) and (4.12) gives the explicit definition of nodal load as a function of time, see equation (4.13).

$$P_i(t) = \begin{cases} \left(1 - \left|\frac{x_{P0} + v_P t - (i-1)\Delta L}{\Delta L}\right|\right) P & \text{for } \frac{(i-2)\Delta L - x_{P0}}{v_P} \leq t \leq \frac{i\Delta L - x_{P0}}{v_P} \\ 0 & \text{elsewhere} \end{cases} \tag{4.13}$$

40

To gain confidence in the proposed finite element formulation for the moving load, example 5 compares the analytical response and the finite element response of a simply supported beam.

Example 5. Consider the simply supported beam shown in figure 4.1. The length of the beam is L and it has a constant cross section with flexural rigidity EI and distributed mass m. The beam is loaded with a moving load with magnitude P and velocity v_p. It is assumed that the beam has Rayleigh damping, with damping ratio ξ_0 specified in the first and second natural frequency, yielding Rayleigh coefficients a_0 and a_1. The example is to be solved with the analytical solution and the proposed moving load formulation for finite elements. The analysis is carried out in Matlab and Abaqus, the scripts carrying out the analysis are provided in appendix B.8.

It is expected that the finite element solution with the moving load formulation, equation (4.13) converges to the analytical solution provided by equation (4.10) as the number of elements increases.

The results of the analysis are presented in figure 4.3 for the deflection of the mid point of the beam.

L	$25\,\mathrm{m}$
EI	$4.375 \times 10^8\,\mathrm{N\,m^2}$
m	$785\,\mathrm{kg\,m^{-1}}$
P	$10^5\,\mathrm{N}$
v_P	$25\,\mathrm{m\,s^{-1}}$
ξ_0	0.05
a_0	$0.9431\,\mathrm{rad\,s^{-1}}$
a_1	$0.0017\,\mathrm{rad^{-1}\,s}$
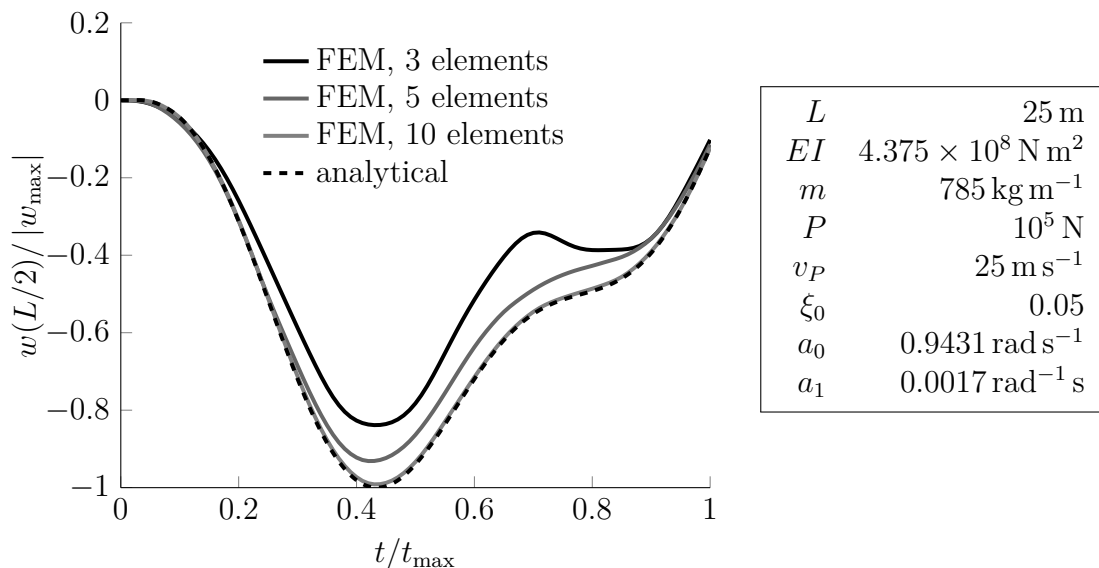
Figure 4.3: The figure shows the deflection of the midpoint of the beam, normalized against the maximum deflection of the beam for different discretization of the beam. The table shows the properties of the beam and the load.

The result shows as expected that the finite element solution converges to the analytical solution as the number of elements are increased.

▲

4.2   Moving mass model

The moving force model does not include the inertia effects from the mass of the train in the analysis. This section considers the basic implications of including the mass of the train in the analysis and under what conditions the inertia effects become significant.
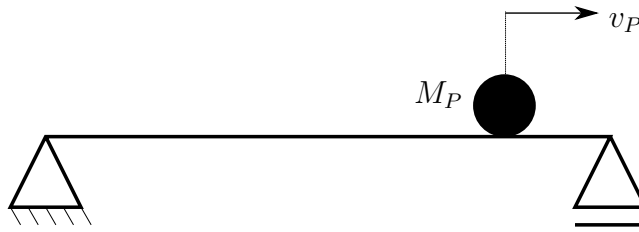
Figure 4.4: The figure shows a simply supported beam with a moving mass.

The differential equation for a moving point mass on a beam can be obtained rather easily, but the analytical solution of the differential equation is difficult to obtain even for a simply supported beam. In any case, the goal is to analyze more complex structures than simply supported beams, such that the problem is solved with contact formulation in the finite element method. The theory behind the contact formulation is considered beyond the scope of this thesis and is therefore not included. It can be noted that Saleeb and Kumar [16] is a good starting point for readers interested in the moving mass problem and contact formulations in commercial finite element codes.

The problems are solved using the contact pair algorithm in Abaqus. The reason for choosing the contact pair algorithm over the other contact formulations is primarily based on the fact that only the contact pair algorithm allows the use of beam elements in 3D contact problems. In addition, specifying contact pairs are considered more efficient and robust than utilizing an all-inclusive general contact formulation [12, sec 35.1.1]. Without going into greater detail, an explanation on how the moving mass is modeled in Abaqus is found in the following paragraph.

The point mass is modeled with a mass element, the rail is modeled with Euler-Bernoulli beam elements. There is a slight difference between the formulation in 2D and 3D. The contact pair algorithm needs to have a master and a slave surface. A single node can be defined as a node based surface, but the node based surface can only be defined a slave surface. A beam element in 2D can be defined a master surface, such that the contact formulation in 2D consists of the node with the moving mass is defined as the slave surface and the beam is defined as the master surface. In contrast, a beam element cannot be defined a master surface in 3D, such that an additional rigid element has to be introduced and attached to the moving mass to constitute the master surface in the contact formulation. The beam may then be defined the slave surface in the contact pair.

In order to gain confidence in the above formulation of the moving mass model consider example 6.

Example 6. The simply supported beam shown in figure 4.4 has length L and a constant cross section with flexural rigidity EI and distributed mass m. It is assumed that the beam has Rayleigh damping, with damping ratio ξ_0 specified in the first and second natural frequency, yielding Rayleigh coefficients a_0 and a_1. The beam is loaded with a moving mass M_P moving with constant velocity v_P.

The example is to be solved with both the moving mass formulation and the moving load formulation with equivalent load $P = M_P g$. The analysis is carried out in Matlab and Abaqus, the scripts are provided in appendix B.9.

The difference between the moving mass formulation and the moving load formulation should vanish if the inertia effects of the train vanish. From equations (4.9a) and (4.9b) the first resonance velocity of this problem is estimated to be $v_{P1} \approx 94\,\mathrm{m\,s^{-1}}$. The velocity of the load is about 1% of the first resonance frequency, and may therefore be considered low. It is therefore expected that the difference in response produced by the two models is negligible.

The results for the deflection of the mid point of the beam are presented in figure 4.5.

| L	$25\,\mathrm{m}$
EI	$4.375 \times 10^8\,\mathrm{N\,m^2}$
m	$785\,\mathrm{kg\,m^{-1}}$
M_P	$10^4\,\mathrm{kg}$
v_P	$1\,\mathrm{m\,s^{-1}}$
ξ_0	0.05
a_0	$0.9431\,\mathrm{rad\,s^{-1}}$
a_1	$0.0017\,\mathrm{rad^{-1}\,s}$
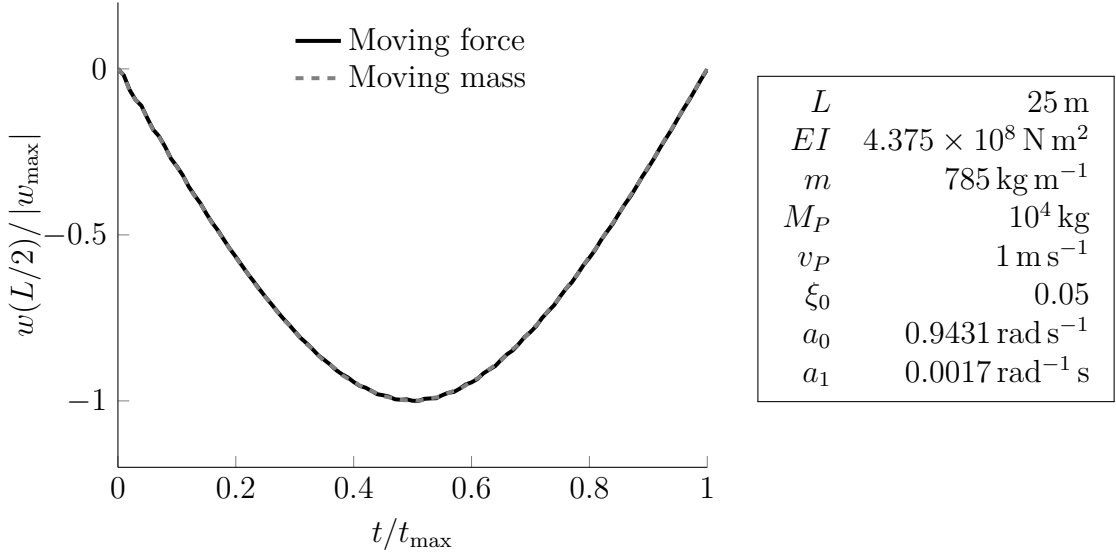
Figure 4.5: The figure shows the deflection of the midpoint of the beam, normalized against the maximum deflection of the beam for different discretization of the beam. The table shows the properties of the beam, the load and the moving mass.

The results shows as expected that the moving mass formulation is equal to the moving force formulation. The prescribed velocity is so low that the accelerations and subsequently the inertia forces of the moving mass vanishes.

▲

To further investigate the difference between the moving force model and the moving mass model, consider the simply supported beam shown in figure 4.4 again. It is exactly the same beam as the one used to develop the moving load model, but now a point mass M_P is moving at constant speed v_P along the beam. A coordinate x with origin at the left end of the beam and with direction in the length axis of the beam, may describe the position x_P of the point mass at time t given the initial position $x_P(t = 0) = x_{P0}$, see equation (4.1).

Assuming that the point mass never looses contact with the beam, the displacement of the point mass $w_P(t)$ is equal to the displacement of the beam $w(x, t)$ at $x = x_P(t)$, i.e $w_P(t) = w(x_P(t), t)$. The total acceleration of the point mass is the sum of the acceleration of the beam at $x = x_P(t)$ and of the gravity g, see the equation below.

$$\ddot{w}_P(t) = g + \ddot{w}(x_P(t), t)$$

By employing d'Alemberts principle, the point mass may be represented as a concentrated force $P_{MM} = M_P \ddot{w}_P(t)$. The connection between the concentrated force P in

the moving load model and the inertia force P_{MM} in the moving mass model is made by realizing that P is equal to the weight of the moving moving mass, i.e $P = M_P g$. The inertia force resulting from the moving mass may then be written as equation (4.14).

$$P_{MM} = P \left(1 + \frac{\ddot{w}(x_P(t), t)}{g} \right) \tag{4.14}$$

Equation (4.14) shows that the difference between moving force model and the moving mass model depends on the magnitude of the acceleration of the beam at $x_P(t)$ relative to the magnitude of the gravity. It also shows that the problem becomes nonlinear as the loading becomes a function of the response of the structure, i.e $P = P(\ddot{w}, t)$. Recall that the velocity of the moving mass is assumed to be constant, see equation (4.1), the acceleration of the beam at point $x_P(t)$ may be written on the following form.

$$\ddot{w}(x_P(t), t) = \left[(v_p)^2 \frac{\partial^2 w(x, t)}{\partial x^2} + 2v_p \frac{\partial^2 w(x, t)}{\partial x \partial t} + \frac{\partial^2 w(x, t)}{\partial t^2} \right]_{x = x_{P0} + v_P t}$$

From the equation above and equation (4.10) an exact expression for the acceleration in the case of the moving force can be determined, see equation (4.15). Note that it is assumed that the moving load starts in the left end of the beam, i.e $x_P(t) = v_P t$ and $P = M_P g$ has been introduced.

$$\ddot{w}(x_P(t), t) = \frac{2M_P g}{mL} \sum_{n=1}^{\infty} \left\{ \sin \Omega_n t \left[2\beta_n^2 D_{1n} \sin(\Omega_n t - \theta_{1n}) + (1 - \beta_n^2) D_{2n} \, \mathrm{e}^{-\xi_n \omega_n t} \sin(\omega_{dn} t - \theta_{2n}) \right] \right.$$
$$- 2\beta_n \cos \Omega_n t \left[\beta_n D_{1n} \cos(\Omega_n t - \theta_{1n}) + D_{2n} \, \mathrm{e}^{-\xi_n \omega_n t} [\xi_n \sin(\omega_{dn} t - \theta_{2n}) \right.$$
$$\left. \left. + \sqrt{1 - \xi_n^2} \cos(\omega_{dn} t - \theta_{2n})] \right] \right\} \tag{4.15}$$

where

$$D_{1n} = \frac{1}{\sqrt{(1 - \beta_n^2)^2 + (2\xi_n \beta_n)^2}}$$

$$D_{2n} = \frac{1}{(1 - \beta_n^2)^2 + (2\xi_n \beta_n)^2} \sqrt{\frac{\beta_n^2 (1 - \beta_n^2 - 2\xi_n^2)^2}{1 - \xi_n^2} + (2\xi_n \beta_n)^2}$$

$$\theta_{1n} = \arctan \frac{2\xi_n \beta_n}{1 - \beta_n^2}$$

$$\theta_{2n} = \arctan \frac{2\xi_n \sqrt{1 - \xi_n^2}}{1 - \beta_n^2 - 2\xi_n^2}$$

To analyze the above equations, recall that the purpose is to investigate the difference between the moving load and moving mass model. All parameters which derive from the properties of the beam may therefore be considered as constants. This means that the two parameters to directly consider in the above equations are M_P and $\beta_n = \frac{n\pi}{\omega_n L} v_P$. First consider the amplification factors D_{1n} and D_{2n}, figure 4.6 shows the behaviour of D_{1n} and D_{2n} as a function of β_n.
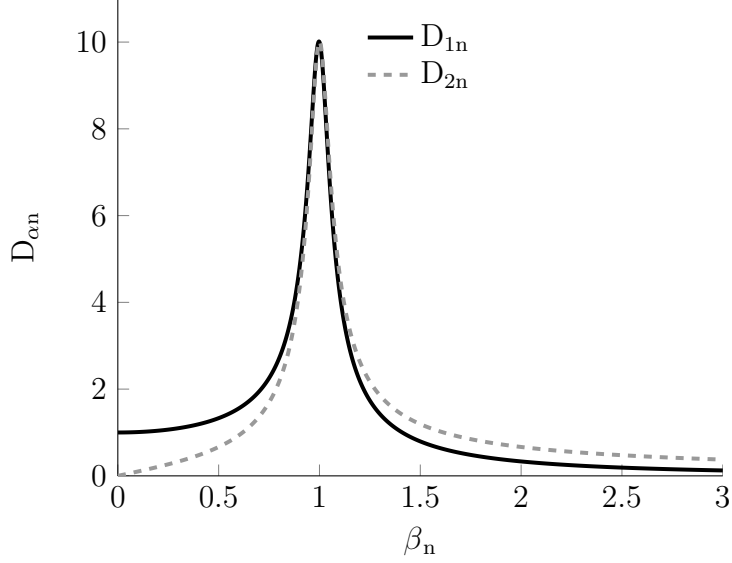
Figure 4.6: The figure shows dynamic amplification factors for the simply supported beam with moving load, the damping factor is set to $\xi_n = 0.05$.

The figure shows that both amplification factors become significant as $\beta_n \approx 1$, i.e close resonance. Since either amplification factor is included in every term in equation (4.15) this implies that the acceleration of the moving load at $x_P(t)$ becomes significant at resonance. Consequently this means that the difference between the moving load and equivalent moving mass load becomes more significant closer to resonance. Example 7 investigates the above observation.

Example 7. The simply supported beam shown in figure 4.4 has length L and a constant cross section with flexural rigidity EI and distributed mass m. It is assumed that the beam has Rayleigh damping, with damping ratio ξ_0 specified in the first and second natural frequency, yielding Rayleigh coefficients a_0 and a_1. The beam is loaded with a moving mass M_P moving with constant velocity v_P.

The example is to be solved with both the moving mass formulation and the moving load formulation with equivalent load $P = M_P g$. The analysis is carried out in Matlab and Abaqus, the scripts for this example are the same as the scripts provided for example 6, but with a different velocity v_P, see appendix B.9.

The velocity of the moving mass $v_P = 90 \, \mathrm{m\,s^{-1}}$ is close to the resonance velocity of the beam at $\approx 94 \, \mathrm{m\,s^{-1}}$. Based on observations made about the acceleration $\ddot{w}(x_P(t), t)$ it is expected that the difference between the moving mass formulation and the moving load formulation is large. The results for the deflection of the mid point of the beam are presented in figure 4.7.

45

| L	$25\,\mathrm{m}$
EI	$4.375 \times 10^8\,\mathrm{N\,m^2}$
m	$785\,\mathrm{kg\,m^{-1}}$
M_P	$10^4\,\mathrm{kg}$
v_P	$90\,\mathrm{m\,s^{-1}}$
ξ_0	0.05
a_0	$0.9431\,\mathrm{rad\,s^{-1}}$
a_1	$0.0017\,\mathrm{rad^{-1}\,s}$
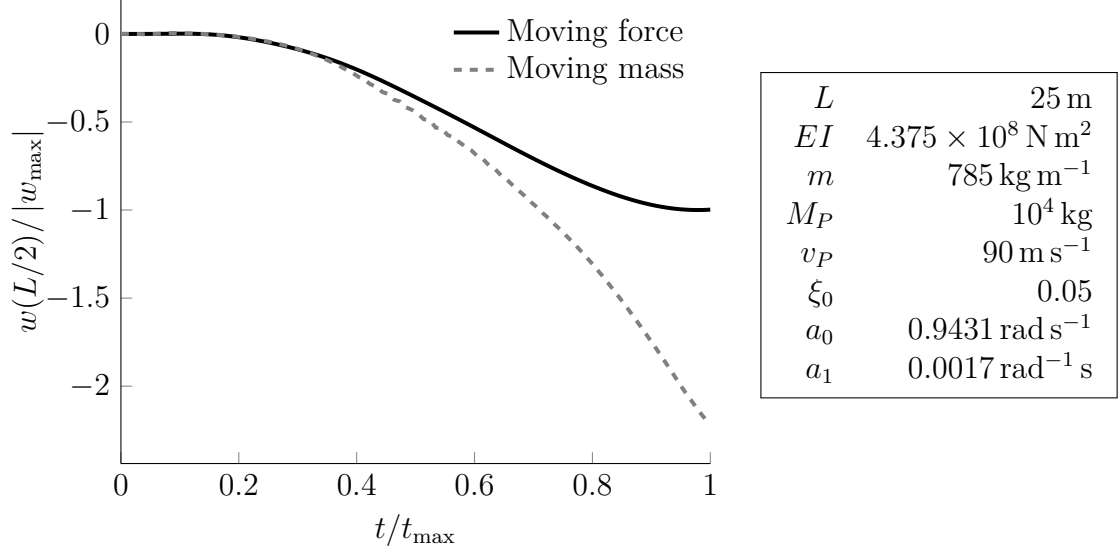
Figure 4.7: The figure shows the response at the midpoint of the beam with the moving force formulation and the moving mass formulation. The table shows the properties of the beam and the loading.

The results show that the two responses are diverging from eachother. When the moving mass is leaving the beam, i.e at $t/t_{\max} = 1$, both the displacement estimated by the two load models and slopes are vastly different. This means that the free vibration phase starting at $t/t_{\max} = 1$ will be different. The example indicate that the difference in the two proposed load models are significant at velocities close to the resonance velocity of the beam.

▲

The second thing that is important to note is that D_{2n} goes to zero as β_n goes to zero. Since every term in equation (4.15) includes either β_n directly or D_{2n}, the acceleration of the moving mass goes to zero as β_n tends to zero. It follows that the difference between the moving load and the equvalent moving mass load vanishes as the velocity tends to zero. This is in accordance with both intuition and what was found in example 6. A final observation regarding β_n is that every term in equation (4.15) is dependent on some power of β_n, either directly or through D_{2n}. This implies that $\ddot{w}(x_P(t), t)$ is sensitive to changes in β_n, and subsequently the velocity of the moving mass v_P. This means that even at moderate velocities, the difference between the two models should become apparent. Example 8 illustrates the sensitivity of $\ddot{w}(x_P(t), t)$ to v_P.

Example 8. The simply supported beam shown in figure 4.4 has length L and a constant cross section with flexural rigidity EI and distributed mass m. It is assumed that the beam has Rayleigh damping, with damping ratio ξ_0 specified in the first and second natural frequency, yielding Rayleigh coefficients a_0 and a_1. The beam is loaded with a moving mass M_P moving with constant velocity v_P.

The example is to be solved with both the moving mass formulation and the moving load formulation with equivalent load $P = M_P g$. The analysis is carried out in Matlab and Abaqus, the scripts for this example are the same as the scripts provided for example 6, but with $v_P = 10\,\mathrm{m\,s^{-1}}$, see appendix B.9.

The first resonance velocity is $v_{P1} \approx 94\,\mathrm{m\,s^{-1}}$, this means that the velocity in this

example is only at 10% of the first resonance velocity. This is by no means a high velocity, but because the acceleration of the moving mass is sensitive to the velocity, it is expected that the response obtained by the moving mass formulation should differ from the response obtained by the moving force model.

The results for the deflection of the mid point of the beam are presented in figure 4.8.
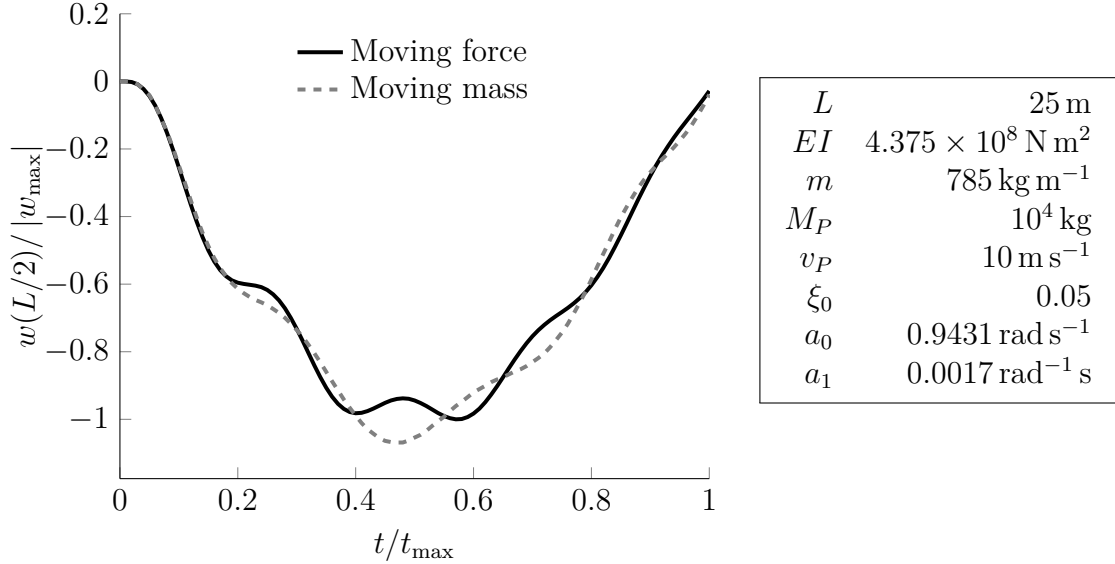
Figure 4.8: The figure shows the response at the midpoint of the beam with the moving force formulation and the moving mass formulation. The table shows the properties of the beam and the loading.

The results shows as expected that even with a modest velocity compared to the resonance velocity, the difference in the response between the two load formulations become apparent.

▲

Although the above example shows that the response is different at relatively low velocities, the magnitude of the deflection of the mid point in the two formulations are largely the same. This means that if the purpose of the analysis is to extract the maximum deflection of the structure and the velocities are moderate, either method may be applied. On the other hand, if for instance the accelerations or stresses are the goal of the analysis, the difference in the results may prove more significant.

The second parameter which differentiate the moving load and the moving mass model is the mass M_P. Equation (4.15) shows that the acceleration at $x_P(t)$ depends on the ratio between the mass of the moving load M_P and the mass of the beam mL. This indicates that if the moving mass becomes small compared to the weight of the bridge, the difference between the two models will be reduced. A final example is presented below to check the above observation and to verify that the moving mass model does capture this behaviour.

Example 9. The simply supported beam shown in figure 4.4 has length L and a constant cross section with flexural rigidity EI and distributed mass m. It is assumed that the beam has Rayleigh damping, with damping ratio ξ_0 specified in the first and

second natural frequency, yielding Rayleigh coefficients a_0 and a_1. The beam is loaded with a moving mass M_P moving with constant velocity v_P.

The example is to be solved with both the moving mass formulation and the moving load formulation with equivalent load $P = M_P g$. The analysis is carried out in Matlab and Abaqus, the scripts for this example are the same as the scripts provided for example 6, but with $v_P = 10\,\mathrm{m\,s^{-1}}$ and $M_P = 1\,\mathrm{kg}$, see appendix B.9.

The mass of the beam is about $20\,000\,\mathrm{kg}$, in example 8 the moving mass was about 50% of the mass of the beam. Under those conditions, the difference between the two load formulations became apparent. In this example, the ratio between the moving mass and the mass of the beam is about 1% of the mass of the beam. According to the discussion proceeding this example, the difference between the two load formulations should vanish as a result of the acceleration of the moving mass vanishes.

The results for the deflection of the mid point of the beam are presented below.

| L	$25\,\mathrm{m}$
EI	$4.375 \times 10^8\,\mathrm{N\,m^2}$
m	$785\,\mathrm{kg\,m^{-1}}$
M_P	$200\,\mathrm{kg}$
v_P	$10\,\mathrm{m\,s^{-1}}$
ξ_0	0.05
a_0	$0.9431\,\mathrm{rad\,s^{-1}}$
a_1	$0.0017\,\mathrm{rad^{-1}\,s}$
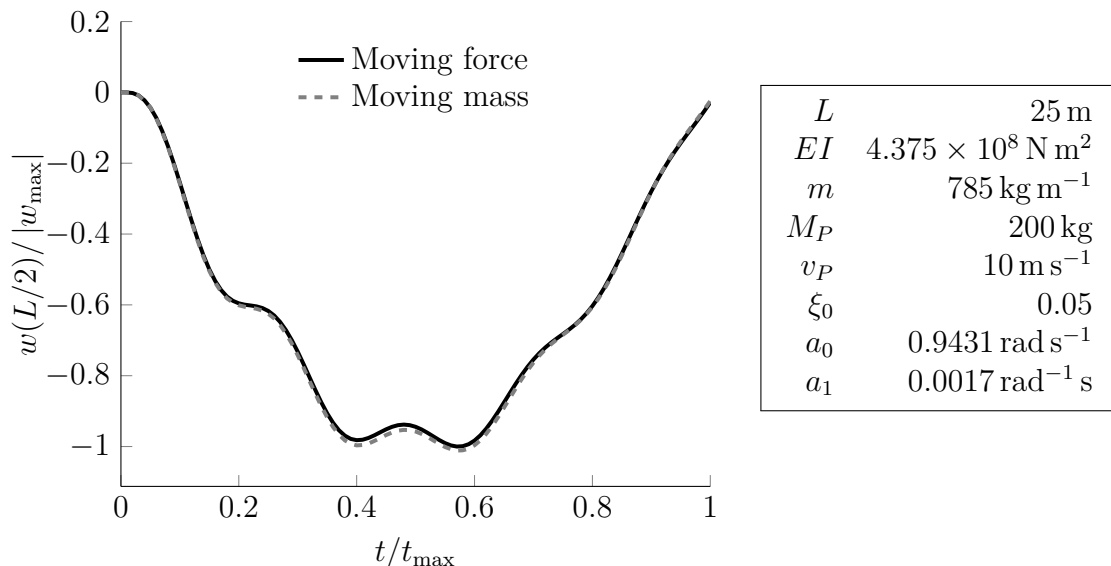
Figure 4.9: The figure shows the response at the midpoint of the beam with the moving force formulation and the moving mass formulation. The table shows the properties of the beam and the loading.

It should be pointed out that the axes of the above plot are scaled, the absolute deflection under the conditions of this example are in them selves negligible. Nevertheless, this example shows that the characteristics of the moving load formulation is similar to the characteristics of the moving force formulation when the moving mass is small compared to the mass of the beam.

▲

This section has outlined the method for implementing the moving mass model in Abaqus. It has been shown that the moving mass formulation produce intuitive and physically sound results compared to the moving force model. The examples indicate that the difference between the two models are negligible at low velocities and when the moving mass is small compared to the mass of the beam. Furthermore, the examples indicate that the difference between the two formulations become apparent at relatively low velocities. This may prove significant if the purpose of the analysis is to extract the

stress history or evaluate the acceleration of the structure. Finally, the results indicate that the difference in the two formulations are vastly different at speeds close to the resonance speed of the structure.

4.3   Sprung mass model

In section 4.1 a method for implementing a moving force across a structure was developed for the finite element method and verified against the analytical solution of a force moving along a simply supported beam. In section 4.2 the moving force model was extended to the moving mass model to include the inertia effect of the physical body represented by the models. More often than not, the physical body is more complicated systems including elastic and dissipative elements, e.g the suspension system of a car or train. This section will extend the moving mass model to a more realistic model and include a spring and viscous dashpot in the formulation, some basic implications of the sprung mass model will also be considered.
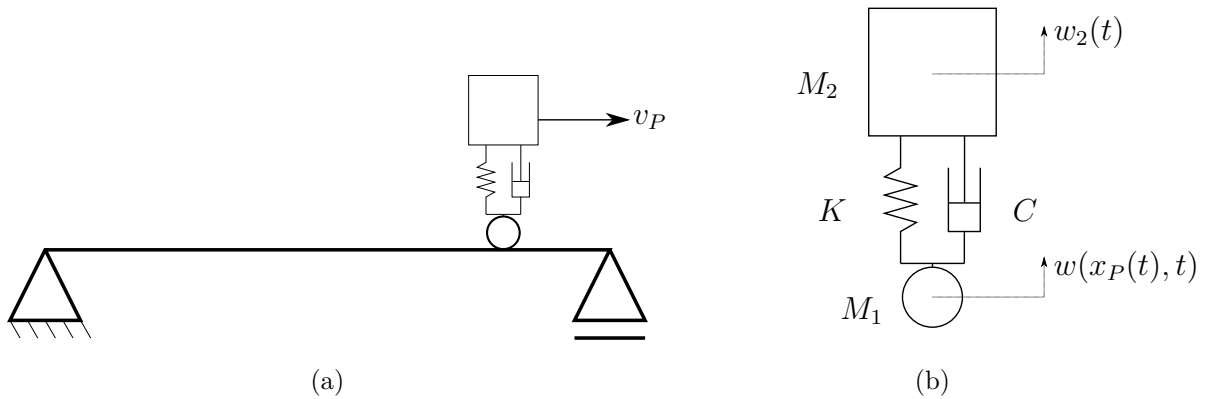

Figure 4.10: The figure shows the sprung mass model moving on a simply supported beam (a), and the quantities used to define the sprung mass model (b).

The analytical solution of the sprung mass moving on a beam involves two coupled and non-linear partial differential equations. As for the moving mass problem, the solution of the above problem is obtained with contact formulation in the finite element method. In the following paragraph, a brief description of the specifics for modeling the sprung mass in the finite element method is presented.

The sprung mass model consists of two nodes, one containing the mass element M_1 and the second containing the mass element M_2. The contact formulation between the mass M_1 and the beam/rail is the same as presented in the beginning of section 4.2. The nodes are connected in the vertical direction with a linear spring element with stiffness K and a viscous dashpot with viscous coefficient C. All degrees of freedom, except the vertical degree of freedom of the node with M_2 are constrained to the corresponding degree of freedom of the node with M_1. Before the presented model is implemented in some practical examples, the following paragraph will analyse the problem from an analytical point of view to gain some insight into the problem.

Consider the simply supported beam shown in figure 4.10a. It is exactly the same beam as the one used to develop the moving load model and the moving mass model,

but now a sprung mass is moving at constant speed v_P along the beam. A coordinate x with origin at the left end of the beam and with direction in the length axis of the beam, may describe the position x_P of the sprung mass at time t given the initial position $x_P(t = 0) = x_{P0}$, see equation (4.1).

As implied by figure 4.10b it is assumed that the point mass M_1 never looses contact with the beam, and the displacement of M_1 is therefore equal to the displacement of the beam $w(x, t)$ at $x = x_P(t)$, i.e the displacement of M_1 is $w(x_P(t), t)$. The acceleration of the first mass is the sum of the acceleration of the beam at $x_P(t)$ and the gravity g. The second point mass M_2 has displacement $w_2(t)$, such that the total acceleration of the second mass is the sum of $\ddot{w}_2(t)$ and the gravity g. By applying d'Alemberts principle and combining the equilibrium equations for the two point masses it is possible to find the equivalent force P_{SM} for the sprung mass. By realizing that the connection between the moving load and the sprung mass model is through the weight of the model, i.e $P = (M_1 + M_2)g$ the following equation appears.

$$P_{SM} = P\left[1 + \frac{M_1}{M_1 + M_2}\frac{\ddot{w}(x_P(t), t)}{g} + \frac{M_2}{M_1 + M_2}\frac{\ddot{w}_2(t)}{g}\right]$$

The above equation shows that the sprung mass model differs from the moving force model by the second and third term in the square brackets. The second term in the square brackets are the inertia effects of the first mass, and the third term in the brackets are the inertia effects related to the second mass M_2.

In practical applications, the first mass M_1 is much smaller than the second mass M_2, for instance M_1 would be the wheel of a train and M_2 would be part of the train and its cargo. This means that in the limit the fraction $M_1/(M_1 + M_2)$ vanishes, while $M_2/(M_1 + M_2)$ becomes equal to unity. Under these conditions the equivalent load for the sprung mass on the beam may be written on the following form.

$$P_{SM} \approx P\left[1 + \frac{\ddot{w}_2(t)}{g}\right] \tag{4.16}$$

The acceleration of the second mass $\ddot{w}_2(t)$ is due to the forces imposed on the second mass by the spring and the dashpot. From equilibrium considerations the acceleration of the second mass can be obtained, see below.

$$\ddot{w}_2(t) = \frac{K}{M_2}[w(x_P(t), t) - w_2(t)] + \frac{C}{M_2}[\dot{w}(x_P(t), t) - \dot{w}_2(t)]$$

The above equation is a second order non-linear differential equation. Instead of trying to solve it to obtain the acceleration of the second mass, it is deemed more productive to determine its value through some physical reasoning.

If the spring stiffness K and the viscous damping coefficient C become small, the forces working on the second mass becomes small. This means that the acceleration $\ddot{w}_2(t)$ becomes small, and in the limit it vanishes. This indicates that with low stiffness and damping of the sprung mass formulation, the equivalent force for the sprung mass becomes equal to the force in the moving load formulation, i.e $P_{SM} = P$.

On the other hand, if the spring stiffness and the damping coefficient are large, the spring and the dashpot acts as rigid links between the first and the second mass. The acceleration of the second mass will then be equal to the acceleration of the first mass such that $P_{SM} = P[1 + \ddot{w}(x_P(t), t)/g] = P_{MM}$.

Although the sprung mass formulation is equal to the two other formulations in the limit of K and C, it is not given that intermediate values of the K and C yield results within the bounds of the two formulations. This is explained by the fact that the acceleration $\ddot{w}_2(t)$ is dependent on the response of the structure itself and thereby the loading P_{SM} is non-linear. In addition, the sprung mass itself is a subsystem with its own dynamic properties which interact with the beam system.

In the following example, the above observations about the sprung mass model compared to the two other models will be investigated.

Example 10. The simply supported beam shown in figure 4.10a has length L and a constant cross section with flexural rigidity EI and distributed mass m. It is assumed that the beam has Rayleigh damping, with damping ratio ξ_0 specified in the first and second natural frequency, yielding Rayleigh coefficients a_0 and a_1.

The example is to be solved with a *flexible*, a *intermediate* and a *stiff* configuration of the sprung mass formulation with M_1, M_2, C, K according to figure 4.10b. The results are to be compared to the moving mass formulation with $M_P = M_1 + M_2$ and the moving load formulation with equivalent load $P = (M_1 + M_2)g$. The analysis is carried out in Matlab and Abaqus, the scripts for this example are provided in appendix B.10.

In the flexible configuration $K = 10^4\,\mathrm{N\,m^{-1}}$ and $C = 100\,\mathrm{N\,s\,m^{-1}}$ and the deflection under gravity alone is close to $10\,\mathrm{m}$, the stiffness of the sprung mass must therefore be considered low. Assuming that C may be considered low as well, it is expected that the response obtained from the flexible sprung mass configuration will be close to the response obtained by the moving force formulation because the acceleration $\ddot{w}_2(t)$ vanishes.

In the intermediate configuration $K = 10^6\,\mathrm{N\,m^{-1}}$ and $C = 10^3\,\mathrm{N\,s\,m^{-1}}$ and the deflection under gravity is about $1\,\mathrm{mm}$, the stiffness of the sprung mass can therefore be considered as intermediate. Assuming that C may be considered intermediate as well, it is difficult to anticipate where the response from the sprung mass will end up compared to the two other formulations because of the nonlinearity of the problem.

In the stiff configuration $K = 10^9\,\mathrm{N\,m^{-1}}$ and $C = 10^5\,\mathrm{N\,s\,m^{-1}}$ and the deflection under gravity negligible, the stiffness of the sprung mass must therefore be considered high. Assuming that C may be considered high as well, it is expected that the response obtained from the stiff sprung mass configuration will be close to the response obtained by the moving mass formulation because the acceleration $\ddot{w}_2(t)$ is close to $\ddot{w}(x_P(t), t)$.

The results for the deflection of the mid point of the beam are presented in figure 4.11.
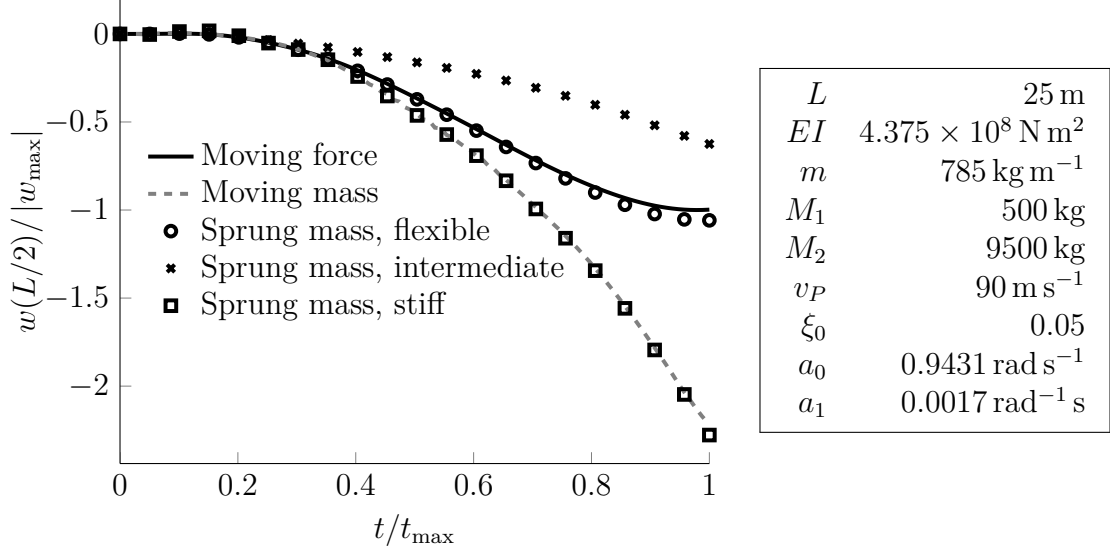
Figure 4.11: The figure shows the response at the midpoint of the beam with different load models. The table shows the properties of the beam and the loading.

The results show as expected that the response obtained by the flexible configuration of the mass sprung formulation is very similar to the moving force formulation, and the response obtained by the stiff configuration of the mass sprung formulation is close to the response of the moving mass formulation. The slight difference shown between the flexible configuration and the moving force formulation may be attributed to the inertia effect of the first mass M_1. The response obtained from the intermediate configuration is less than both the moving force formulation and the moving mass formulations. This characteristic is generally found for intermediate values of the stiffness and damping coefficient. The physical explanation for this is that for intermediate values of stiffness and damping, the damper in the sprung mass model dissipates energy from the system, and thereby reduces the response of the system. This claim is also backed by Majka and Hartnett [17] who makes similar observations about the sprung mass model.

▲

In this section the method for implementing the mass sprung model in the finite element method has been presented. It has also been shown that the moving force model and the moving mass model are limiting cases of the sprung mass model. Regarding actual values of the spring stiffness and the viscous dashpot coefficient this obviously varies with the specific train being modeled. In the literature, Iwnick [18], Yau et al. [19] and Liu et al. [20] among a wealth of others provide values for the vehicle parameters of the sprung mass.

4.4 Vehicle interaction model

In addition to the moving forces, moving mass and the sprung mass model there exists even more complex dynamic systems to model the train, see figure 4.12.

These models are henceforth known as vehicle interaction models, and they are made up of the same basic elements as in the sprung mass model, but in addition the coupling between the axles through the boggies and the coupling between the boggies through the
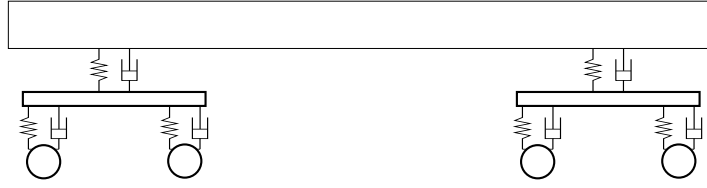
Figure 4.12: The figure depicts an example of a vehicle interaction model

vehicle body are included. The rotational inertia of the boggies and the vehicle bodies are also included. These vehicle interaction models may have up to 35 degrees of freedom, depending on the complexity of the models. The vehicle interaction models have been used by [17], [21],[22], [23] and [24] among others to study the dynamic response of bridges, due to parameters such as velocity, track irregularity, damping and bridge skewness. Although the wide use of complex vehicle interaction models, comparative studies made by [20] and [25] shows that the difference between complex vehicle interaction models and the sprung mass model are small when the dynamics of the bridge, rather than the dynamics of the vehicles are being assessed. In special cases, e.g where the bridge lies in a curve and the lateral deflections of the bridge are to be assessed, a vehicle interaction model may obviously be warranted. Based on the results found in [20] and [25] and the need to limit the scope of this thesis, the choice is made to leave out the more complex vehicle interaction models in this thesis and focus on the moving force and the sprung mass model.

4.5   Resonance from a series of moving loads.

In the previous section on the moving load, moving mass and sprung mass, resonance was considered for the case of a *single* moving load, and it was found that resonance occurs when the moving load travels at the resonance velocity. In reality however, most structures are under a series of moving loads, e.g a wheelset on a train. This section will show that a succession of moving loads will produce resonance at speeds different from those anticipated by the single moving load.

Both Frýba [26] and Yang et al. [27] among others have studied the phenomena of resonance from a series of moving loads. Yang et al. present an detailed derivation of the analytical solution to the problem of a series of moving loads on a simply supported beam which provides great insight into the problem at hand. Instead of reproducing the entire derivation in this thesis, the phenomena of resonance from a series of moving loads will rather be investigated through reasoning and practical examples supported by the analytical solution of Yang et al.. The interested reader is referred to the book [27, chap 2.6-2.7] where the detailed derivation can be found.

Figure 4.13 shows a simply supported beam loaded with a series of moving load with intensity P, velocity v_p and a distance d in between each of them. Consider any section of the beam, say the midsection of the beam. At time $t = t_0$ the first moving load passes over the midsection, at time $t = t_0 + \frac{d}{v_P}$ the second load passes over the midsection and
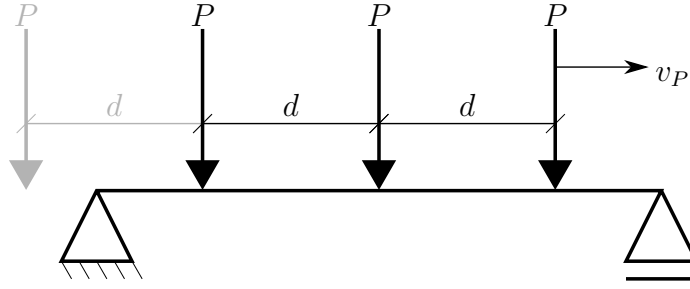
Figure 4.13: The figure shows two forces P, moving at a constant velocity v_P and a constant distance d from eachother.

at time $t = t_0 + n\frac{d}{v_P}$ the nth load passes over the midsection of the beam. In other words, the *period* between each load is $T_P = \frac{d}{v_P}$ and the angular frequency Ω_P of the series of moving loads is given by equation (4.17).

$$\Omega_P = \frac{2\pi}{T_P} = \frac{2\pi v_P}{d} \tag{4.17}$$

Analogous to the case of a single moving load, one might expect that resonance occurs when the frequency of the series of moving loads equals one of the natural frequencies of the beam. The beam in figure 4.13 has flexural rigidity EI, mass per unit length m and length L, which means that the natural frequencies of the beam are given by equation (4.9b), the equation is restated below for convenience

$$\omega_n = (n\pi)^2 \sqrt{\frac{EI}{mL^4}}$$

With the load frequency for the series of moving loads, equation (4.17), and the above equation for the natural frequencies of the beam. The following equation gives the distance between the moving loads which is expected to yield resonance in the first mode with natural frequency ω_1.

$$d = \frac{2\pi v_P}{\omega_1} \tag{4.18}$$

In example 11, the above equation will be evaluated through a practical example.

Example 11. Consider the simply supported beam shown in figure 4.13.
   The length of the beam is L and it has a constant cross section with flexural rigidity EI and distributed mass m. The beam is loaded with N_{lds} moving loads, all with magnitude P, constant velocity v_p and distance d between them. Damping is neglected, i.e $\xi_n = 0$. The example is to be solved with moving load formulation for finite elements with d in the range $[0, L]$, and the displacement of the midpoint of the beam shall be analyzed. The analysis is carried out in Matlab and Abaqus, the scripts carrying out the analysis are provided in appendix B.11.
   First of all, the velocity v_p is about 10% of the resonance velocity at $94\,\mathrm{m\,s^{-1}}$, such that there are no resonance effect from the velocity alone. From equation (4.18) it is suggested that the series of moving loads will be in resonance with the beam at $d = 5.3\,\mathrm{m}$, the response at this configuration is therefore expected to be large compared to distances in the same vicinity.

The results of the analysis are presented in figure 4.14, the distance between the moving loads d are on the abscissa, while the ratio between the maximum displacement at the midpoint of the beam $w_{\max}$ and the maximum displacement $w_{\max,d=0}$ of the midpoint of the beam for $d = 0$ is given on the ordinate.

| L	$25\,\mathrm{m}$
EI	$4.375 \times 10^8\,\mathrm{N\,m^2}$
m	$785\,\mathrm{kg\,m^{-1}}$
N_{lds}	20
P	$5 \times 10^4\,\mathrm{N}$
v_P	$10\,\mathrm{m\,s^{-1}}$
d	$0\text{-}25\mathrm{m}$
ξ_n	0
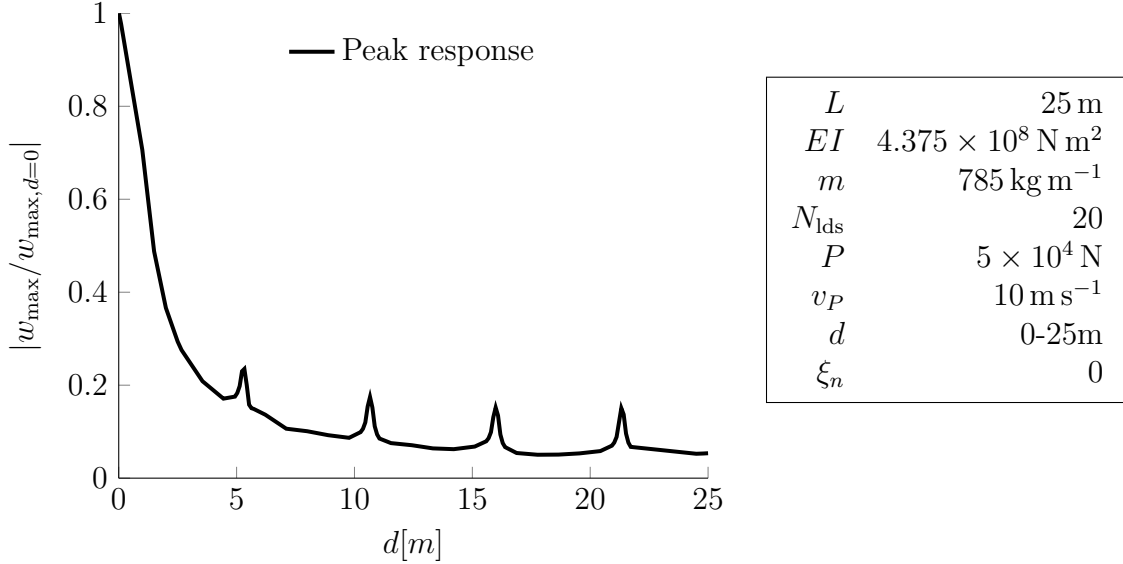
Figure 4.14: The figure shows the maximum amplitude of the response given for the distance d between each moving load. The table gives the properties of the beam and the loading.

The first thing that can be seen is that response is decreasing as the distance between the loads are increasing, this is due to the fact that the load intensity, i.e the loading per distance, decreases with increasing d. The result shows as expected that around $d = 5.3\,\mathrm{m}$ the response at the midspan is exhibiting resonance behavior. The results also shows that resonance occurs at distances around $d = 10.6, 15.9, 21.2\mathrm{m}$, incidentally these are multiples of the resonance distance $d = 5.3\mathrm{m}$. The reason for this is that with loads at the nth multiple of d, the beam is still excited in the same way as for d, but in instead of excite the beam *every* period, it exites the beam every nth period. This will be explained in detail after this example as it is an important point for the case of resonance from a series of multiple loads.

▲

In the above example it was found that resonance occur at distance d and at multiples n of d. This is in accordance with the analytical solution provided both Frýba [26] and Yang et al. [27], where they find that resonance in the first natural mode finds place at distances

$$d_n = n\frac{2\pi v_P}{\omega_1}$$

between the series of loads.

To give an explanation as to why the resonance behavior is found for any multiple of d_1, recall that the system with the moving load formulation is linear, such that the principle of superposition applies. This means that the response from each of the moving loads may be obtained separately, and the total response is found by adding the contribution

55

from each load. Consider figure 4.15, it shows a beam and its first vibration mode ω_1. For now, assume that there is no damping in the system.

(a) d_1, $t = t_0$ (b) d_1, $t = t_0 + T_1$ (c) d_1, $t = t_0 + 2T_1$

(d) $2d_1$, $t = t_0$ (e) $2d_1$, $t = t_0 + T_1$ (f) $2d_1$, $t = t_0 + 2T_1$
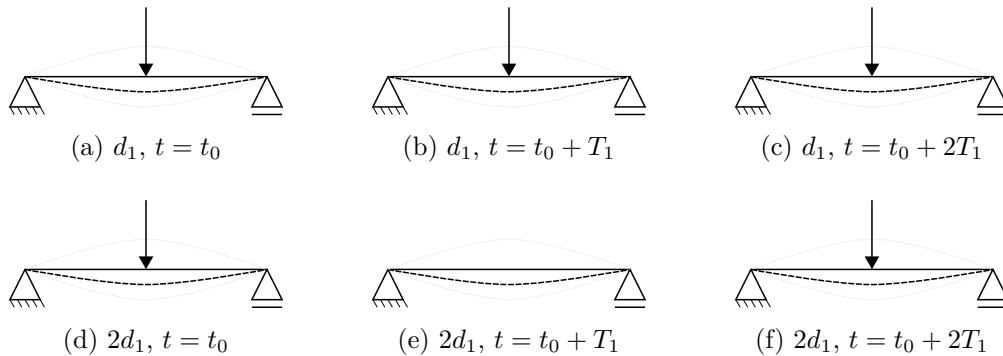
Figure 4.15: Figure (a),(b) and (c) shows snapshots of the beam for $d = d_1$ between moving forces, and figure (d), (e) and (f) shows snapshots of the beam for $d = 2d_1$.

In figure (a), (b) and (c) the distance between the loads are $d_1 = \frac{2\pi v_P}{\omega_1}$, while in figure (d), (e) and (f) the distance is $2d_1$. At time $t = t_0$, a snapshot of the beam is taken, and at this time the first load passes over the midpoint of the beam and in phase with the first vibration mode, see figure (a) and (d). After one period T_1 of the first vibration mode a new snapshot is taken, figure (b) and (e) shows that the vibration mode is in the same state as at time $t = t_0$, but now the second load has not yet reached the midpoint of the beam for case (e), the load for $2d_1$ "skips" the opportunity to excite the beam. After another period T_1 the vibration mode is again in the same state, and now second load acts at the center for the case of $2d_1$ and the third load acts for d_1. The same procedure can be applied to any section of the beam, with the same result. The figure illustrates that the loads for both d_1 and nd_1 works on the beam in the same phase.

Yang et al. [27] also point out that the resonance that occurs from a series of moving loads is different from that of an harmonic load with load frequency equal to the natural frequency of the system. The resonance behavior is created from the fact that the vibration from one load is in phase with the vibration of all the preceeding loads. Any dynamic effect created by the first load, is also added by the subsequent loads. The result is that the response of the system grows at a linear rate until the last load enters the beam, regardless of whether $d = d_1$ or $d = nd_1$.

Regarding the influence of damping on the resonance effect from a series of moving loads it is apparent from the proceeding chapters that damping affects both the transient and free vibration response by limiting the amplitude and changing the vibration frequency. Damping will therefore reduce and create bounds for the resonance effect from the series of moving loads.

In example 12, the undamped response in the time domain of the midpoint of the beam from a series of moving loads will be shown and the effect that damping has on the resonance from a series of moving will be illustrated.

Example 12. Consider the simply supported beam shown in figure 4.13.

The length of the beam is L and it has a constant cross section with flexural rigidity EI and distributed mass m. The beam is loaded with N_{lds} moving loads, all with magnitude P, constant velocity v_p and distance $d = 3d_1$ between them. The response

56

for the midpoint of the beam is to be obtained with both damping neglected, i.e $\xi_n = 0$ and with Rayleigh damping where the damping ratio ξ_0 is specified in the first and second natural frequency. The analysis is carried out in Matlab and Abaqus, the scripts carrying out the analysis is a slightly modified version of the script provided in appendix B.11.

The results of the analysis are presented in figure 4.16.
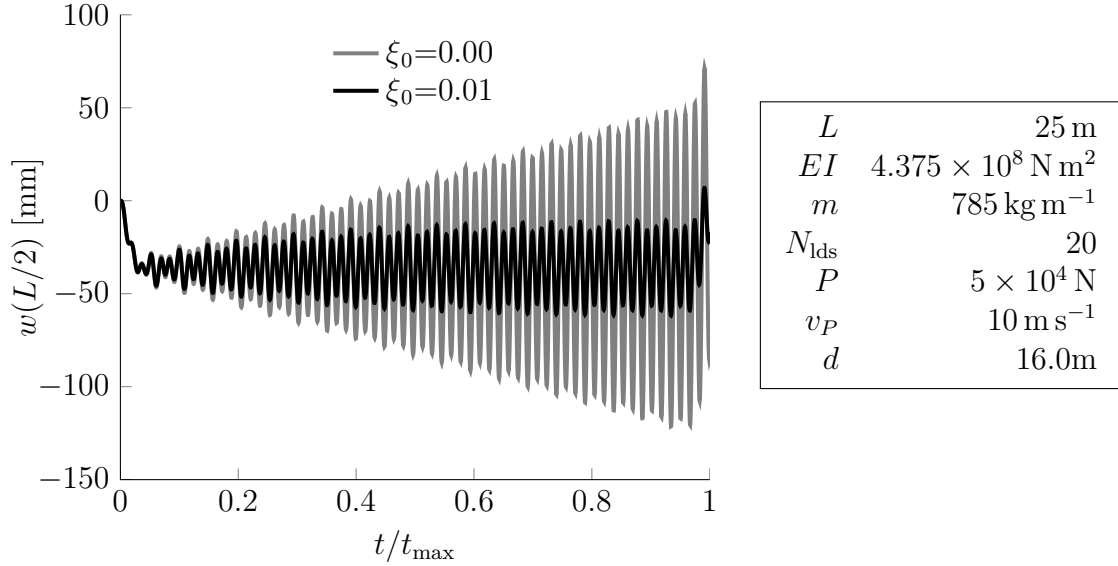
Figure 4.16: The figure shows the response at the midpoint of the beam with and without damping. The table shows the properties of the beam and the loading.

The results show that the response for the undamped system grows linearly until the last load enters the beam, then the total loading on the beam is reduced and the response subsides accordingly, the free vibration after the last load leaves the beam will be substantial. The damped system shows resonance effects, but the response is bound by the dissipation of energy from the system and the fact that each load no longer hits the exact same phase.

▲

Before ending the discussion on it is appropriate to mention the phenomena of *cancellation*. The series of moving loads may induce resonance in the system by repeatedly exciting the system in the same manner as the preceeding loads, in figure 4.15 it was shown that this happened when the successive loads work on the system in the same phase of the observed vibration mode. To illustrate the phenomenon of cancellation consider figure 4.17.

(a) d_1, $t = t_0$ (b) d_1, $t = t_0 + \frac{1}{2}T_1$ (c) d_1, $t = t_0 + T_1$
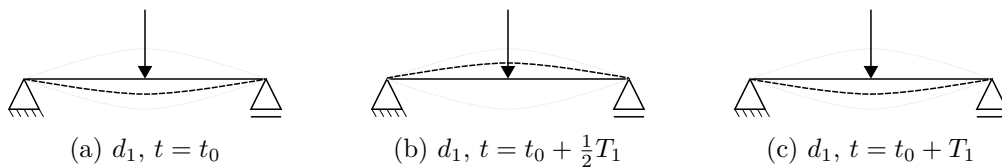
Figure 4.17: The figure illustrates the phenomenon of cancellation.

In figure 4.17, the distance between the loads are $d = 1/2d_n$. The first and the third load shown in figure 4.17a and 4.17c excite the beam in the same opportune state as the other, while the second load in figure 4.17b excite the beam when it is in the opposite state. This means that the the odd numbered loads excite the beam in the same phase and the even numbered loads excite the system in the same phase, but the dynamic effect added by either the odd or the even loads are canceled out by the other set because they work against each other. This can also be seen in figure 4.14 in example 11, at the distance $d = 2.65$m every second load in the series hits the beam in the same phase, but since the other loads work in the opposite phase, no resonance peak can be seen for this distance.

Yang et al. [27] shows that the phenomenon of cancellation does not just happen when the distance between the loads are equal to the half period of the vibration modes. Even if the loads does not work in the absolute opposite phase of the resonance distance, the total sum of the moving loads are bound by each other. This means that not only damping will create bounds the response of a series of moving loads, but also the phenomenon of cancellation.

Extending the discussion about the series of moving loads to the discussion about trains and bridge dynamics it is evident that the configuration of the train will influence the dynamic response the bridge. Such that it is not only necessary to have detailed knowledge about the geometry and properties of the bridge being analyzed, but also the configuration of the trains which will frequent the bridge.

In this chapter the main topics have been load models and resonance from moving loads. The modeling techniques and formulations in the finite element program Abaqus was presented for the moving force, moving mass and sprung mass load model. The analytical solution for the moving load model was derived, and it was used to verify the finite element formulation of the moving force model. The response from the moving mass model and the sprung mass model was then compared against the response for the moving force model, and the comparison yielded reasonable and physically sound results. The implementation of the load models in the finite element code is therefore regarded as successful and providing physical results.

In the discussion of the sprung mass model it was shown that in the limit, the sprung mass model was equal to the moving force and the moving mass model. It was also argued that the sprung mass model could be regarded as the most realistic of the three models since it is able to represent the elastic and dissipative properties often inherent in the physical bodies being modeled. This speaks a strong case for utilizing the sprung mass model in the continuation of the thesis, but from a computational expense point of view, the sprung mass model and the moving mass model was found to be more expensive than the moving force model, especially in three dimensions.

Regarding the use of the load models in the case study in chapter 5, the moving mass model is excluded from further study since it is found more computationally expensive than the moving force model and less realistic than the sprung mass model.

The moving force model may yield less realistic results than the sprung mass model, but only under conditions where the inertia effects of the train become significant. Under circumstances where the inertia effects are small, either due to absent dynamic effects or relatively low mass of the train compared to the bridge, the moving force model and the sprung mass model are expected to yield similar results. This means that the moving force model may be used to locate velocities with significant dynamic effects, but the response obtained by the moving force model at these velocities are not certain to be accurate.

Based on this fact and the argument of computational efficiency, the moving force model will be utilized as the reference load model for the case study and the sprung mass model will be used for comparison.

Chapter 5

Case study: Tallerås railway bridge

In this chapter a case study of the Tallerås railway bridge will be presented. The case study will determine the resonance velocities of two different trains by the moving force model presented in chapter 4 and the reason for the induced resonance will be determined. Once the resonance velocities are determined, the significance of the resonance effects on the stress in the structure will be examined. The response obtained by the moving force model and the sprung mass model will be compared. The case study will also investigate the effects of including two different track models in the dynamic analysis.

5.1 Tallerås railway bridge

Tallerås railway bridge is located on the railway between Otta and Dombås station on the line with name *Dovrebanen*. It was put in service in 1912 and was operational until 1940 when it was disabled by the Norwegian resistance movement during the second world war. It was later repaired and has largely been operational ever since.

Figure 5.1: The picture shows an overview picture of Tallerås railway bridge. Source: Main inspection report Tallerås, autumn 2007. Jernbaneverket/Norconsult.

The bridge is a nailed steel truss bridge with a main span of 52 m, and a width of 5 m. The geometry of the bridge is defined by figure C.1, found in appendix C.

5.1.1 Load carrying system

The load carrying system of the bridge can be divided into a *primary* and a *secondary* system, see figure 5.2. The primary system consists of two identical planar trusses designed

(a) Primary system.
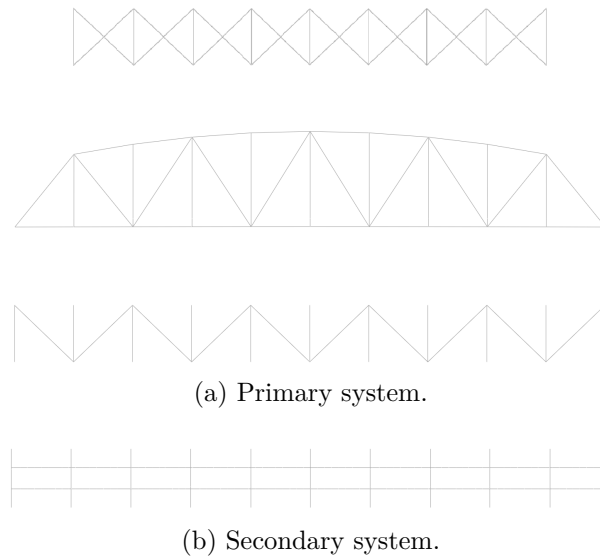
(b) Secondary system.

Figure 5.2: The figure shows a breakdown of the main parts of the bridge.

to carry the vertical loads, connected by an upper truss and a lower truss which are designed to take the horizontal loads. The secondary system consists of 11 continuous cross girders and 20 longitudinal girders, each longitudinal girder is nailed to the web of the adjacent cross girders. The cross girders of the secondary system are connected to the vertical hangers in the planar trusses of the primary system, thereby creating a complete structure, see the picture in figure 5.2.

The bridge has a ballastless track, the track is connected to the bridge by hooks connecting the sleeper and the longitudinal girder. The loading from the train is thereby transfered through the sleepers and onto the longitudinal girders. From the longitudinal girders, the loading is carried to the cross girders and out to the vertical hangers of the primary system. Through the vertical hangers the forces are distributed throughout the truss to the boundary conditions of the bridge.

In the primary system, the truss is carefully designed such that all centerlines at the nodes coincide, this means that the forces are mainly transfered by normal forces. In the secondary system, the loading is carried primarily by bending and shear forces. It should be noted that the cross girders have a length to height ratio of about 5, i.e $L/h \approx 5$ and the longitudinal girders have a length to height ratio of 3. Both the cross and longitudinal girders are I-shaped profiles, and at these length to height ratios, shear deformations are significant. This means that Timoshenko beam theory is necessary, [12, sec 29.3.3] suggests minimum ratio 15 for the Bernoulli beam theory to be applicable. Bell [13, p.283] investigates shear deformations in a I-shaped profile which may be interesting to the unconvinced reader.

5.1.2 Finite element model

The steel in the bridge is assumed throughout the thesis to have $E = 210 \times 10^9 \, \text{N m}^{-2}$, $\nu = 0.33$ and density $\rho = 7850 \, \text{kg m}^{-3}$.

Element types

The primary carrying system in the Tallerås railway bridge primarily carries forces by normal forces. This implies that truss elements can be used to establish the finite element model for the primary system. Although it must be acknowledged that the truss element is more efficient than a beam element, it proved to be alot of effort to establish the primary system with truss elements. It involved a number of linear constraint equations, e.g each of the mid nodes in the upper truss had to be constrained in the plane of the sub truss and the verticals connecting to the secondary system had to be constrained. Any alterations to the model would also involve introducing additional constraints, such that any modification of the model became very tedious. Therefore, the choice was made early on to utilize beam elements in the finite element model for the primary system, fully aware of the implication it has on the efficiency of the model. The beam elements are mainly Euler-Bernoulli beam elements with cubic formulation (B33), any exceptions are given in the following paragraph. The beam sections of the primary system are largely composed of a number of profiles and nails, according to Abaqus beam section library these beam sections are classified as *generalized*.

The secondary carrying system in the Tallerås railway bridge carries forces through bending and shear. As mentioned at the end of the previous subsection, both the cross and longitudinal girders in the secondary system have a low length to height ratio, such that the contribution from shear deformations are considerable in both of these structural elements. The secondary system is therefore modeled with a linear finite Timoshenko beam element (B31). The beam sections in the secondary system are composed by plates, angle bars and nails to make out I-shaped beam section. Since the shear factor k in the Timoshenko beam theory is determined by the beam section type, the beam section type of the secondary system is therefore defined as the I-section in the Abaqus library. The resulting basic finite element model is given in figure 5.3.
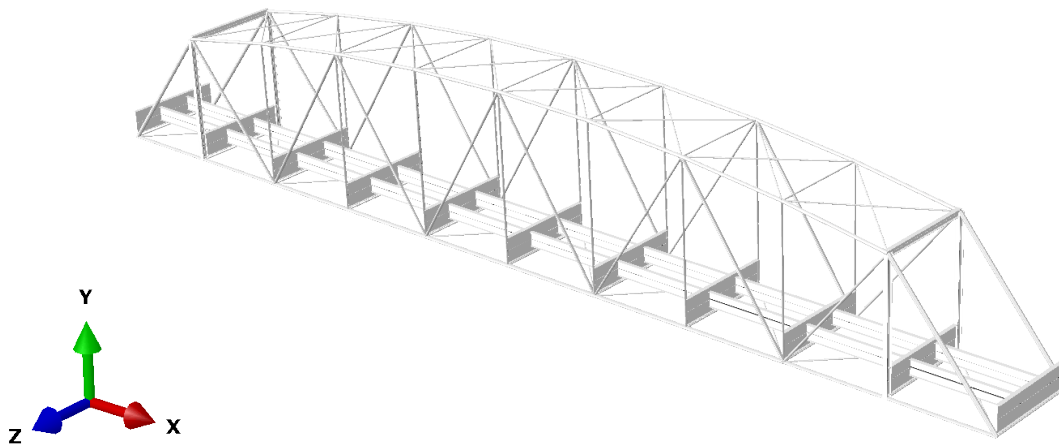

Figure 5.3: The figure shows the basic configuration of the finite element model of the Tallerås bridge.

Boundary conditions

The following discussion about the boundary conditions of the bridge are referred to figure 5.3, the coordinate system in the bottom left corner of the figure has its origin in the furthest away corner of the bridge. The bridge is assumed to be simply supported in the length direction. The bridge is restrained at one end in the x-direction, and it is restrained in all four corners in the y- and z-direction. This is in good agreement with the drawings for the bridge, where one end lies on a series of cylinders free to roll in the x-direction, but restraining the y- and z-direction. The relatively short dimensions in the z-direction means that temperature and membrane effects arising from the above boundary conditions are negligible.

From figure 5.3 it can be seen that the first and the last cross girder of the secondary system are not suspended from any vertical hangers in the primary system. From the picture in figure 5.1 it can be seen that the ends of these cross girders are constrained to the end diagonals of the primary system. These cross girders are therefore constrained at the ends to the respective nodes of the primary system by linear constraint equations in the finite element model.

Other constraints

It is important to realize that imposing constraints increases the stiffness of the system, this in turn means that the natural frequencies of the system increases and the resonance velocity associated with the natural frequency increases. This means that analyzing a overconstrained structure will lead to a non-conservative result by overestimating the resonance velocity of the structure. That being said, it is important to include constraints which are clearly present in the physical system, such that the actual behaviour of the system can be described by the finite element model and over conservative designs can be avoided. This subsection considers details in the actual bridge who impose constraints which are reasonable to include in the finite element model.

With the element model established according to the above description, an eigenvalue analysis was performed. The result showed that the first mode was horizontal displacement in the z-direction of the upper part of the bridge with a frequency $\omega = 16.3\,\mathrm{rad\,s^{-1}}$, see figure 5.4a.

The next significant mode was similar the first mode, but where the lower part of the bridge more dominant in the displacement pattern than the upper part, its frequency was $\omega = 32.7\,\mathrm{rad\,s^{-1}}$. The two lowest significant modes of the basic model indicate that the shear stiffness of the bridge in the z-direction is low compared to the stiffness in the rest of the structure.

Further investigation of the detail drawings of the bridge and the modes of the basic finite element model indicate two main reasons for low shear stiffness in the finite element model.

The first reason is that the portal frame[1] is in reality stiffer than the basic finite element model indicate. Figure 5.4b shows that the corners of the portal frame are stiffened by two 12 mm plates stretching over 0.9 m onto any of the members of the portal frame. The web of the I-beams making out the portal frame are also 12 mm, such that the corners

---

[1]The portal frame are the first verticals and upper horizontal girder in the primary system, in combination with the second cross girder of the secondary system.
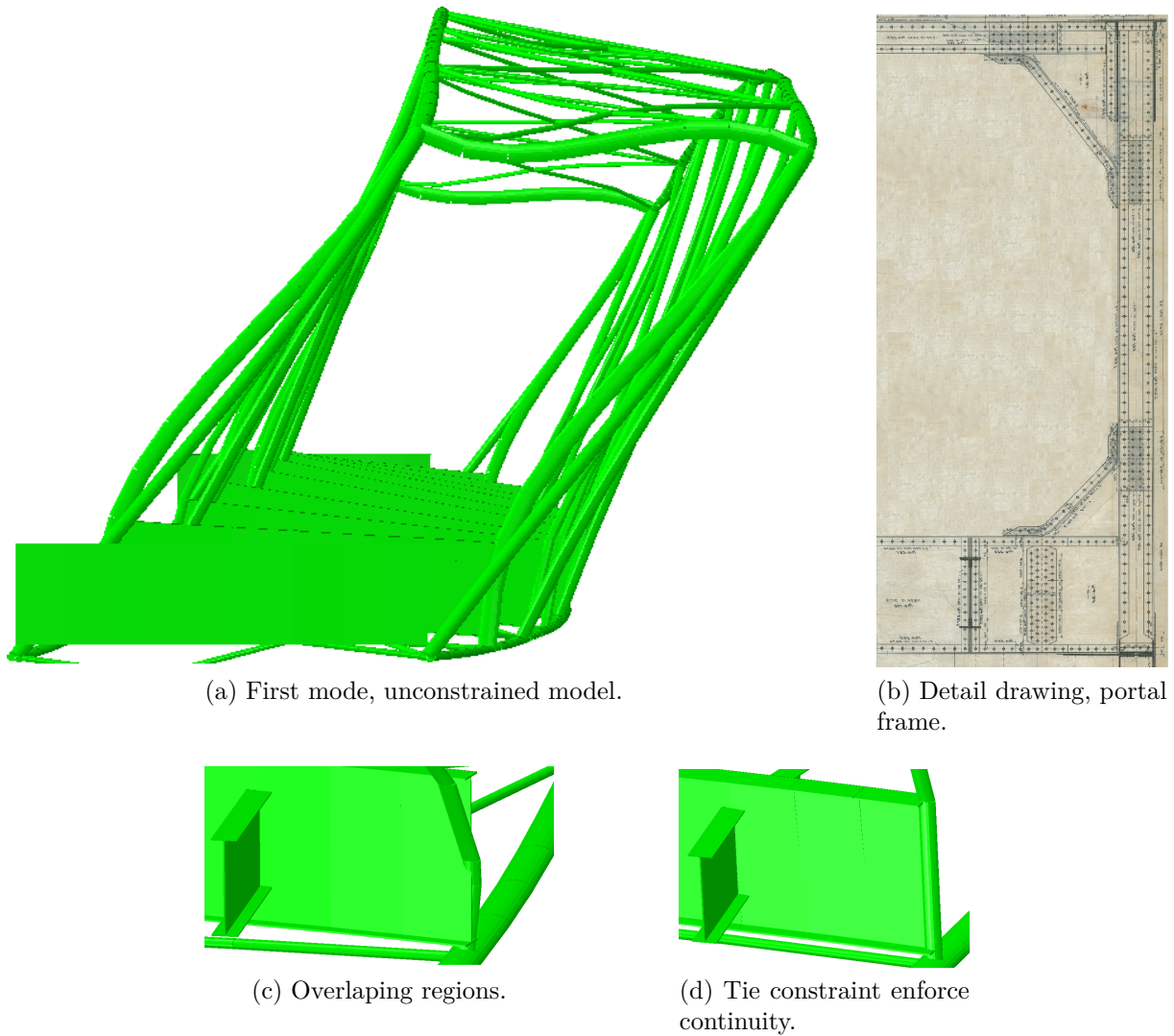
(a) First mode, unconstrained model.

(b) Detail drawing, portal frame.

(c) Overlaping regions.

(d) Tie constraint enforce continuity.

Figure 5.4: Figure (a) shows the first mode of the basic model, which is enlarged because the basic model does not include the constraining detail in the portal frome showed in drawing (b). Figure (c) shows that the vertical hangers are not tied to the cross girders, (d) shows the result after tying the vertical hangers to the end node of the beam.

of the portal frame may be regarded as stiff over the entire span of the stiffener plates. To model this detail in the finite element model, multi point constraints (*MPC,link) are introduced such that the distance between any node within $0.9\,\mathrm{m}$ of the corner node is constant throughout the analysis. A consequence of these constraints, are that the length to height ratio of the top and side beams of the portal frame become around 9, and Timoshenko beams (B31) are introduced in the entire portal frame to ensure that the shear deformations are properly included.

The second thing that reduces the shear stiffness in the z-direction in the finite element model, is that the connection between the vertical hangers of the primary system and the cross girders of the secondary system are not tied together, see figure 5.4c. The vertical hangers will have reduced stiffness from an increased effective length and lower rotational stiffness at the connection point. To remedy this, a node is introduced in the vertical hangers corresponding to the height at the top of the cross girder. This node is then in

a tied multipoint constraint (*MPC,tied) with the end node of the cross girder and the lower node of the vertical hangers, see result in figure 5.4d. The eigenvalue analysis of the basic model also revealed another deficiency in the basic finite element model. In the basic model, the secondary system is only constrained in the length axis of the beam by bending about the weak axis of the cross girders, see figure 5.5a.
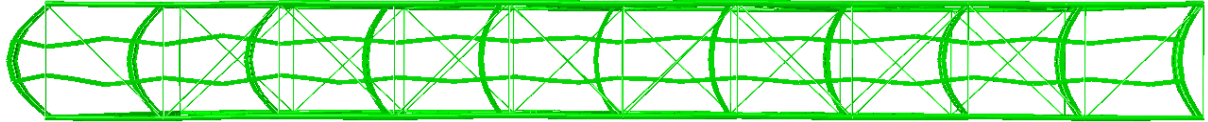
(a) Longnitudal movement of secondary system.
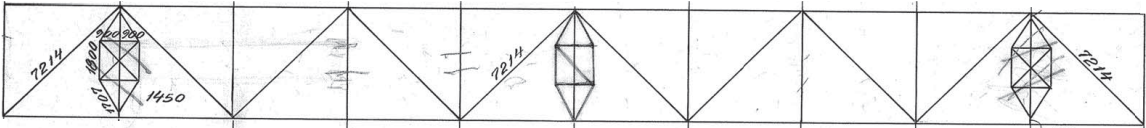
(b) Detail drawing, constraint of secondary system.
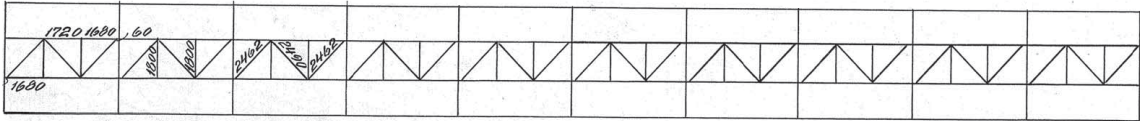
(c) Detail drawing, crossbrace longitudinal girders in secondary system.

Figure 5.5: The figure (a) shows the unrealistic behavior of the basic finite element model, where the secondary system moves in the longitudinal direction relative to the primary system. Figure (b) shows the detail which braces the secondary system to the primary system in the longitudinal direction. Figure (c) shows the crossbrace between the longitudinal girders in the secondary system.

In the detail drawings a brace which constrains this longitudinal behaviour of the secondary system is found, see figure 5.5b. The brace is therefore introduced in the refined finite element model, it should be noted that the two outer braces indicated on the figure was removed according to later drawings and are not included in the refined model either.

Figure 5.5a also shows that the distance between longitudinal girders in the secondary system is not constant along their length. Figure 5.5c shows a cross brace between the longitudinal girders in the secondary system which does not permit this behavior. Although the bracing discussed in the previous paragraph and shown in figure 5.5b removes this problem for the mode shown in figure 5.5a, it does not for certain other modes. The refined model therefore also includes the cross brace shown in figure 5.5c.

Natural frequencies of the bridge

In this subsection, the natural frequencies of the bridge alone are presented. A brief analysis of the modes will be given, but the main purpose of this chapter is to provide a basis for determining the damping of the bridge and to give data for the natural frequencies of the bridge alone and later compare the natural frequencies against those of the complete structure with bridge and track. The natural frequencies are given in table 5.1, and figure C.2 in appendix C shows the corresponding modes.

Table 5.1: The table shows the six first significant modes, their frequencies and a description of the deformation pattern.

Natural Frequency $[\mathrm{rad\,s^{-1}}]$	Description
20.7	1st Horizontal bending mode
39.0	1st Torsional mode
41.4	1st Vertical bending mode
42.2	2nd Horizontal bending mode
72.1	2nd Torsional mode
77.6	2nd Vertical Bending mode

The first thing that is apparent is that the bridge has rather low stiffness in the horizontal plane, the horizontal bending modes is the lowest mode and has a frequency about half the next mode. In [28, p.79] the natural frequencies of a similar steel truss bridge with a span of 50.4 m is presented. The results in [28] also shows a similar characteristic regarding the natural frequencies, the first natural frequency of the presented bridge is even lower with $16.2\,\mathrm{rad\,s^{-1}}$, about half the next natural frequency. This implies that the observed flexibility in the horizontal plane of the Tallerås railway bridge is reasonable, and in the continuation this is assumed to be ok and no further investigations on this characteristic are pursued.

The second thing that can be seen from the natural frequencies is that the third, fourth and fifth significant modes have frequency of about $\omega \approx 40\,\mathrm{rad\,s^{-1}}$. This may mean that the response of the bridge may be significant when the configuration and velocity of the train excites the bridge at this frequency.

As mentioned at the start of this section, the natural frequencies of the bridge will be further discussed in the subsequent chapters on damping and natural frequencies of the complete structure.

Damping in the finite element model

From the discussion on damping in chapters 2 and 3 it is evident that the response of the structure close to resonance speeds is highly dependent on the level of damping in the structure. As mentioned in section 2, a number of researchers have studied damping in bridges and even railway bridges in particular. Frýba [4, chap. 5] discusses the difference between the viscous, hysteretic and Coloumb damping models, and concludes that because of the relatively low damping values associated with railway bridges, the practical difference between the models are negligible. As a result of the above and the fact that the viscous damping model is relatively simply implemented compared to the two other models, he advocates the use of the viscous damping model in dynamic analysis of railway bridges.

Frýba further presents damping data from experiments made on a wide range of different bridges. The results shows a great spread in damping ratios, and finds an dependence between the damping ratio and the amplitude of the displacement of the bridge. This again illustrates that damping in structures is a difficult subject, and that experiments may be necessary on the specific bridge being analyzed. Nevertheless, Frýba recommends a damping ratio of $\xi_n \approx 0.013$ for steel bridges with spans over 20 m.

The governing Eurocode, NS-EN1991-2 [29] also has recommendations for damping in dynamic analysis of railway bridges, and specifies that only lower bound estimates of the damping should be used. For steel bridges with spans above 20 m the Eurocode recommend a damping ratio of $\xi_n = 0.005$.

The case study presented in this thesis will be conducted in Abaqus, using an implicit numerical integration scheme. In light of the discussion about the efficiency of the Rayleigh damping matrix in an implicit integration scheme made in chapter 3, and the relative uncertainty of the damping ratios for railway bridges, the choice is made to use Rayleigh damping in the analysis.

(a)   (b)
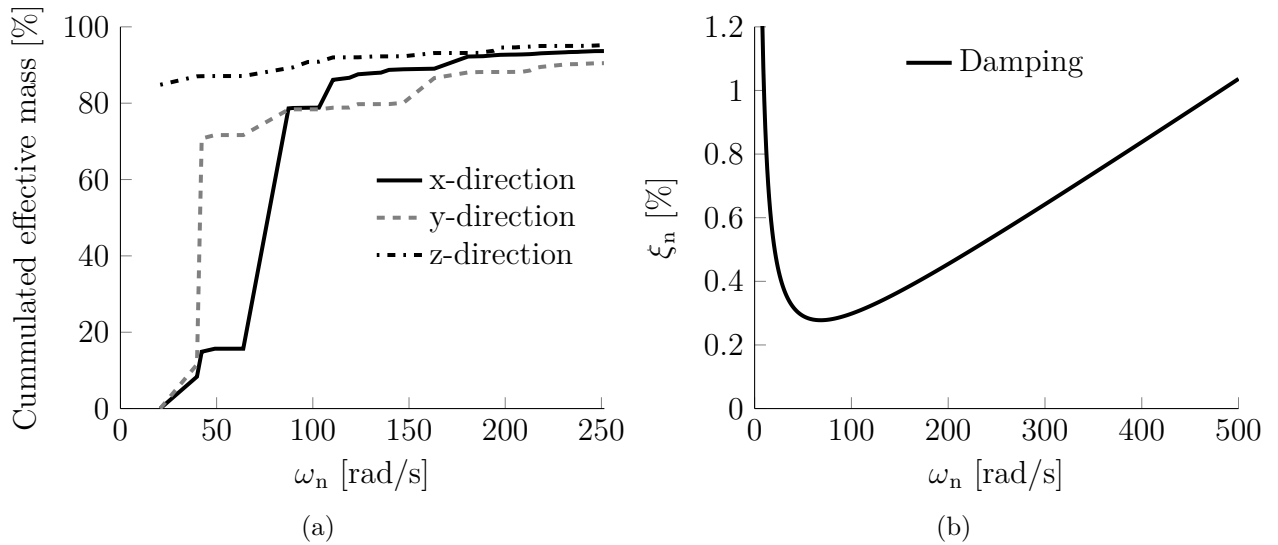
Figure 5.6: Figure (a) shows the percentage of cummulated effective mass against the total mass for the natural frequencies of the system. Figure (b) shows the resulting damping ratios when a damping ratio of 0.5% is chosen in $\omega_1 = 20.7 \, \text{rad s}^{-1}$ and $225 \, \text{rad s}^{-1}$

Recall from chapter 3.4.1 that two frequencies and corresponding damping ratios are specified to define the Rayleigh coefficients a_0 and a_1. The first one is chosen to be the first natural frequency $\omega_p = \omega_1 = 20.7 \, \text{rad s}^{-1}$ with a damping ratio of $\xi = 0.005$. The frequency range of the loading is not known a priori, because it depends on the configuration of the train, see discussion in section 4.4. It is important that a greater portion of the modes in the system have a reasonable damping ratio. Overdamping of significant modes will lead to non-conservative results, and may "hide" resonance frequencies from the response. Figure 5.6a shows the cummulated effective mass against the natural frequencies of the system. The effective mass of a mode says something about how much of the structure is involved in the displacement pattern of that mode. Adding up the effective mass of all possible modes in a system, equals the total mass of the structure. This means that if the cummulated effective mass in one direction of a set of extracted modes are significantly less than the total mass of the structure, the extracted set of modes lack significant modes in that direction [30, sec 2.5.2]. Therefore, choosing the upper frequency for defining the Rayleigh damping at a frequency where, say 90% of the cummulated mass is included in any direction ensures that most of the significant modes does not have damping above the specified damping ratio. From figure 5.6a it can be seen that at $\omega \approx 225 \, \text{rad s}^{-1}$ the cummulated effective mass in any direction is larger than

90%. Choosing a upper frequency equal to $225\,\mathrm{rad\,s^{-1}}$ with a damping ratio of $\xi = 0.005$ yields the damping shown in figure 5.6b.

Figure 5.6b shows that the damping ratios in the range does not exceed the values recommended by Frýba. From equations (3.41) and figure 5.6b the minimum damping ratio is found to be about 0.3%. The discussion earlier in this section has shown that there is great uncertainty related to the damping ratios, such that these damping ratios does not pose a concern. The effective damping ratios of the complete structure with the track will be extracted in a complex frequency analysis in section 5.3 to verify that the complete structure has reasonable damping ratios.

The Rayleigh coefficients with a damping ratio of $\xi = 0.005$ specified in $\omega = 20.7\,\mathrm{rad\,s^{-1}}$ and $\omega = 225\,\mathrm{rad\,s^{-1}}$ are $a_0 = 0.19\,\mathrm{rad\,s^{-1}}$ and $a_1 = 4.1 \times 10^{-5}\,\mathrm{rad^{-1}\,s}$.

5.2 Track used in the case study

In this section the geometry of the track and the physical properties of the track will be discussed, especially some considerations regarding the link between the rails and the bridge. Then two different finite element models for the track of the structure will be presented, one where the elastic, dissipative and inertial properties of the track are included in the formulation and one simplified alternative where only the inertial properties of the track are included.

The bridge has a ballastless track, where the sleepers are connected directly to the long girders of the secondary system. It is assumed that rails are of the standard type "UIC60" with a distributed mass of $60.21\,\mathrm{kg\,m^{-1}}$ and cross-sectional properties are according to the specification by Norwegian National Rail Administration's Technical Regulations, see [31]. The distance between the center of each rail is $1.435\,\mathrm{m}$. The sleepers are assumed to be of type "JBV97" specified in [31] with a total mass of $230\,\mathrm{kg}$ and a center distance of $0.6\,\mathrm{m}$.

In the finite element model, the sleepers are not included in the model as structural elements, but the mass of the sleepers are added to the track by introducing mass elements at the center distance $0.6\,\mathrm{m}$. The reason for including the mass of the sleepers in the model is that the mass of the track is relatively large in comparison to the mass of the bridge, this will be discussed further in section 5.3. The reason for not including the sleepers as structural elements in the finite element model is because there is some uncertainty related to how much the sleepers contribute to the structural integrity of the bridge. The connection between the sleepers and the bridge are made through a hook going through the sleeper and grabbing the flange of the long girders, see figure 5.7.
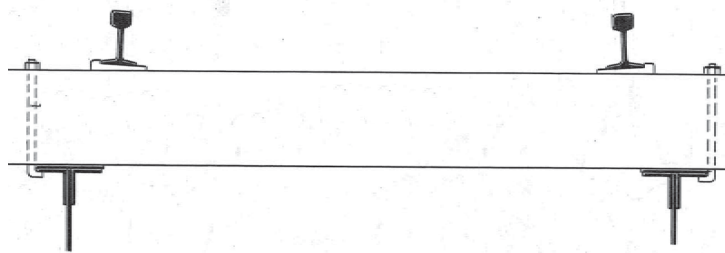

Figure 5.7: The figure shows the hook which connects the sleeper and subsequently the track to the flange of the long girders of the bridge.

Whether this connection transfers moment and force depends on the direction of the forces, the amount of tension in the screw and the friction between the sleeper and the long girders of the bridge. It is also obvious that the latter two of these factors depend on the level of maintenance and time in service of the connection. Because of the uncertainty related to these factors and to avoid the implications of overconstraining the model, i.e increasing natural frequencies of the model, the choice was made to not model the sleepers as structural elements. It should be noted that the cross brace introduced in the refined model in the proceeding section also ensures that the distance between the long girders are constant, such that this behavior is already avoided.

Figure 5.7 shows that the position of the hook is on the "outside" of the flange, this means that as the curvature of the sleeper increases, torsion in the longgirders arise. The distance is $e = 182.5\,\text{mm}$ between the centerline of the rail and longgirder, the height of the sleepers are about $180\,\text{mm}$. Apart from the fact that a certain portion of the forces are transfered as normal stress through the sleeper, it is assumed that the curvature in the sleeper is kept small such that no moment is transfered to the longgirders of the bridge. This means that each of the long girders are loaded mainly with translational forces from the track.

5.2.1 Finite element model of the visco-elastic track

The finite element model of the track presented in this subsection is the same model as "Model III" presented in [32], but without the sub model for the ballast layer. The finite element model of the complete track is built up of a two idealized models of the rail, see figure 5.8.

m_{rail}	$60.21\,\text{kg}\,\text{m}^{-1}$
C_{pad}	$200 \times 10^3\,\text{N}\,\text{s}\,\text{m}^{-1}$
K_{pad}	$500 \times 10^6\,\text{N}\,\text{m}^{-1}$
M_{sleep}	$230\,\text{kg}$
C_{sleep}	$120 \times 10^3\,\text{N}\,\text{s}\,\text{m}^{-1}$
K_{sleep}	$538 \times 10^6\,\text{N}\,\text{m}^{-1}$
D_{sleep}	$0.60\,\text{m}$
h_1	$0.27\,\text{m}$
h_2	$0.50\,\text{m}$
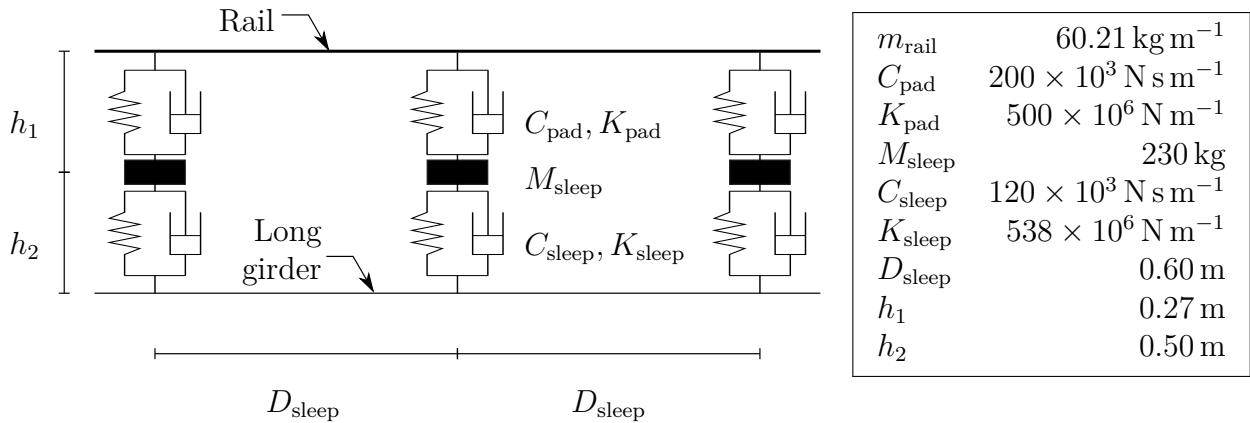
Figure 5.8: The figure shows the finite element model for the track, the values for the track properties are adopted from Rigueiro et al. [32]. Note that the dimensions h_1 and h_2 are adopted from the actual geometry of the bridge.

Each rail consists of the three layers of nodes, the upper node layer defines the rail, the middle node layer contain the mass of the sleepers and the lower node layer contains the surface definition which makes contact with the long girders of the bridge. To model the elastic and dissipative properties of the materials between the node layers, a spring and a dashpot element is introduced between the nodes. The upper set of springs and dashpot represent the elastic and dissipative properties of the shock pad between the rail and the

sleeper, see figure 5.7. The lower set of springs and dashpots represents the elastic and dissipative properties of the sleeper.

Regarding active DOFs in the upper node layer, i.e the nodes defining the rail, the transversal node is constrained to the corresponding node in the long girder by linear constraint equations. The rail is restrained at the nodes against torsion by introducing boundary condition on the corresponding rotational degree of freedom, this ensures that the finite element model captures the physical behavior imposed by the ties connecting the rail and sleeper. All other DOFs are free at the upper node layer and take special note of the fact that the longitudinal nodes of the upper layer are not constrained. This is in accordance with the technical regulations [31, sec 530.3.1.2] where it is specified that bridges with dilatational length between 10 m and 100 m should allow the rail to travel freely in the length direction.

Regarding active DOFs in the middle node layer, i.e the nodes containing the mass of the sleeper, only the vertical DOF is active, all other DOFs are constrained to the corresponding node at the long girder by linear constraint equations.

The track is connected to the bridge through a tie (*TIE) connection of the lower layer of nodes to the long girders of the bridge creating the complete structure.

5.2.2 Finite element model of the simplified track

The above finite element model for the track includes the dissipative and elastic properties of the shock pad and the sleeper. As mentioned before, the values for these properties are adopted from [32]. In comparison to values given by other authors in the literature, for instance [27] and [33] the values are in the same order of magnitude. The static displacement of the track under a 110 kN axle yields a displacement of ≈ 0.5 mm which seems to be an reasonable considering the thing pad and the height of the sleeper. It is difficult to say if these values for the track properties should be considered high or low, but the higher these property values are, the more rigid behavior they will exhibit. At a certain stiffness, the behavior of the track presented above will be the same as a *simplified* track where the elastic and dissipative elements are left out and only the mass and the distribution of the mass are included in the model of the track.

The implementation of the simplified track in Abaqus will be exactly the same as for the fully functional track, but the vertical DOF of the rail node layer and the sleeper node layer will be constrained to the vertical DOF in the long girder through linear constraint equations. Note that the longitudinal DOF in the rail layer is still unconstrained to allow the rail to freely travel in the longitudinal direction.

5.3 Natural frequencies and effective damping ratios of the complete structure

The bridge coupled with the track constitutes a different structure than the bridge alone. It was implied in the previous section that the mass of the track was significant in comparison to the total mass of the structure. A significant increase in mass will obviously affect the natural frequencies of the system and warrants a new analysis of the natural frequencies of the complete structure. What is not completely clear is whether the the natural frequencies of the complete structure are the same with the visco-elastic track as with the

simplified track. The natural frequencies for the complete structure with the visco-elastic track are extracted and compared against the natural frequencies of the bridge alone. The natural frequencies of the complete structure with the simplified track will then be extracted and compared against the natural frequencies of the complete structure with the visco-elastic track. Since the visco-elastic track may introduce non-classical damping, the complex eigenvalue problem is employed to extract the complex natural frequencies for both problems. At the end of this section, the effective modal damping ratios will be extracted from the complex eigenvalues and evaluated to confirm that the structure has reasonable damping ratios.

5.3.1 Natural frequencies with the visco-elastic track

The natural frequencies of the complete structure with a visco-elastic track are presented in table 5.2.

Table 5.2: The table shows the natural frequencies of the bridge alone and the natural frequencies of the complete structure with bridge and track.

Bridge [$\mathrm{rad\,s^{-1}}$]	Bridge + track [$\mathrm{rad\,s^{-1}}$]	Change [%]	Description
20.7	17.7	-14.6	1st Horizontal bending mode
39.0	33.0	-15.4	1st Torsional mode
41.4	35.9	-13.3	1st Vertical bending mode
42.2	42.2	0.0	2nd Horizontal bending mode
72.1	57.0	-21.1	2nd Torsional mode
77.6	81.2	4.7	2nd Vertical bending mode

The table shows that there is a significant decrease in the natural frequencies of the system. The mass of the finite element model of the bridge alone is about $104\,000\,\mathrm{kg}$, with a span of $52\,\mathrm{m}$ this yields a rough estimate of the distributed mass of $m_{\mathrm{Bridge}} = 2000\,\mathrm{kg\,m^{-1}}$. Comparing this to the distributed mass of the ballastless track, $m_{\mathrm{Track}} = (230/0.6 + 2\cdot60)\mathrm{kg\,m^{-1}} \approx 500\,\mathrm{kg\,m^{-1}}$ reveals that the ballastless track adds 25% additional mass to the structure. It should be noted that the estimated mass for the bridge is based off of the effective area for axial load carrying ability. The actual mass of the bridge is slightly higher than the estimate, see figure 5.9.
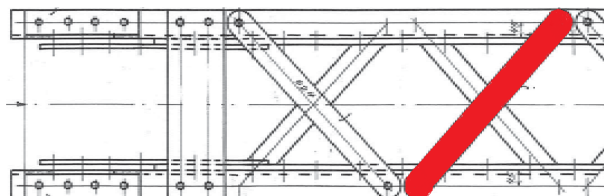

Figure 5.9: The figure shows a cross-brace whos mass is neglected in finite element model, note that all cross-brace components are neglected.

Even if the neglected mass amounts to 30% extra mass, a number which is grossely exagerated, the track still adds about 20% to the total mass of the structure. Without further investigation it is appropriate to conclude that the total mass added to the structure from the track is significant.

From section 3.3 it is known that increasing the mass of a structure generally means that the frequencies of the structure are reduced. This is in accordance with what was found for four out of the six natural frequencies in table 5.2. It is not completely clear why the 2nd horizontal and vertical bending modes does not change significantly.

In any case, the above analysis have shown that the track significantly changes the natural frequencies of the Tallerås railway bridge and it is therefore important to include the track when analyzing the dynamic properties of relatively light bridges. As a side note, it should be mentioned that this has broader implications than the specific bridge. In a time where the cost of materials was high and the cost of labor was low, older bridges in general where built to minimize the use of materials, see discussion Larsen [34, p.74]. As a result, many of the older railway bridges are in fact light bridges, which means that the above results are important in dynamic analysis of existing railway bridges in general.

5.3.2 Natural frequencies with the simplified track

The natural frequencies of the bridge with the simplified track in comparison with the natural frequencies of the bridge with the visco elastic track are presented in table 5.3.

Table 5.3: The table shows the natural frequencies of the complete structure with the visco-elastic track and with the simplified track.

Visco-elastic track [rad s^{-1}]	Simplified track [rad s^{-1}]	Change [%]	Description
17.7	17.7	0.0	1st Horizontal bending mode
33.0	32.9	-0.4	1st Torsional mode
35.9	35.9	0.0	1st Vertical bending mode
42.2	42.2	0.0	2nd Horizontal bending mode
57.0	57.0	0.0	2nd Torsional mode
81.2	81.2	0.0	2nd Vertical bending mode

The table shows that the natural frequencies of the two track types are the same. The small difference of -0.4% seen for the 1st Torsional mode is negligible and will have very little effect on the displacement response of the structure. This means that the visco-elastic track does not introduce significant coupling or damping between the primary modes of deformation. This implies that in order to obtain the displacement response it is not necessary to utilize the visco-elastic model. Regarding other response quantities such as accelerations or the stress history of components in the structure, it is not necessarily so. In the following sections, the simplified track will be used as the reference track, and investigations will be made on the effect of utilizing visco-elastic track on different response parameters.

5.3.3 Effective modal damping ratios of the complete structure

In section 5.1.2, damping of the railway bridge was discussed, and it was pointed out that it is important that the damping ratios are kept at an reasonable level for the significant modes of the structure. Excess damping in the structure may mask resonance frequencies which are important in the design and assessment of any structure. In the previous section it was shown that natural frequencies of the structure changed significantly as the track was added, and the visco-elastic track does change the damping matrix. The complex natural frequency analysis showed that the visco-elastic track and the simplified track had the same natural frequencies, which indicates that the damping ratios are also the same. The expression for the effective modal damping ratios was established in section 3.5 and will be extracted here through Abaqus to control that the bridge still has reasonable damping ratios in the significant modes. Figure 5.10 shows the effective damping ratios in the 150 first modes of the structure.
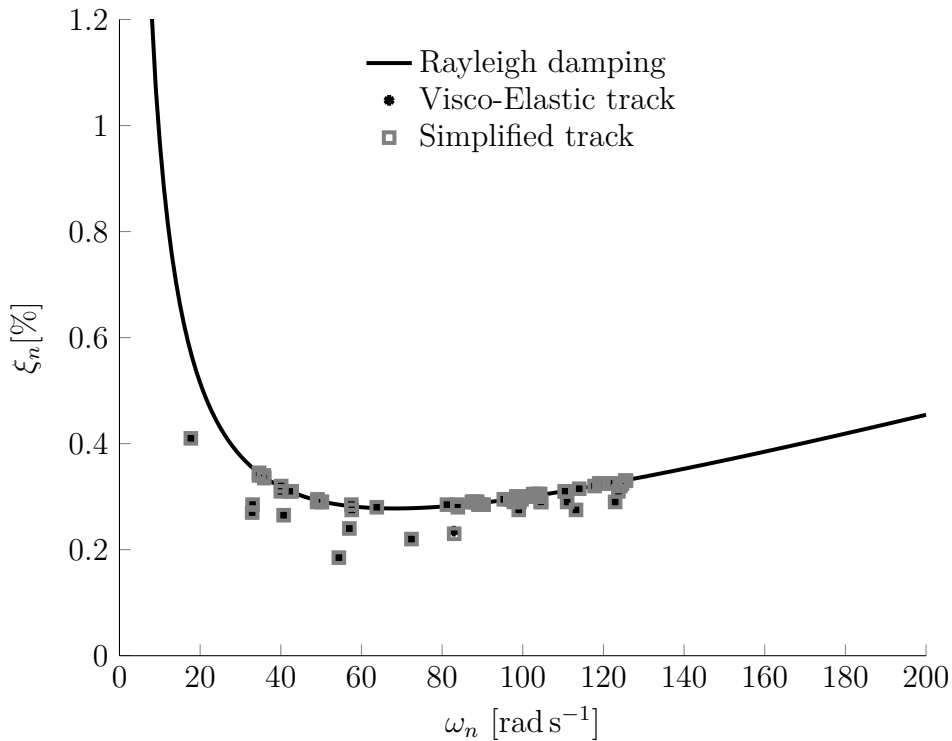
Figure 5.10: The figure shows the effective modal damping ratios of the complete structure with the two different track and the prescribed damping ratios of the bridge.

From the figure it can be seen that the effective damping ratios in all the extracted modes are close to the specified damping ratios. It can also be seen that the damping ratios for the two different tracks are the same, such that it can be concluded that the visco-elastic track does not introduce significant coupling and damping to the primary modes of deformation.

Furthermore, it can be seen that none of the damping ratios are larger than the specified Rayleigh curve, but some of the damping ratios are smaller than the specified damping ratios. The difference between the dynamic system with the specified damping curve and the predicted curves is the track. Such that one might expect that the lower ones might be those affected most by the addition of the track to the structure. An

investigation of the damping ratios does not yield an immediate reason, for instance in the previous section it was shown that the first horizontal bending mode, the first vertical bending mode and the first torsional mode all change their natural frequencies with the addition of the track. Considering the effective modal damping ratios, the horizontal bending mode and the first torsional mode have lower damping ratios than the specified, but the vertical bending mode has damping exactly on the specified curve. In any case, the earlier discussion has pointed out the uncertainty related to the damping, such that the figure shows effective damping ratios well within what can be considered as reasonable damping ratios.

5.4 Trains used in the case study

In this study two different trains will be used to analyze the Tallerås railway bridge. The configuration of the trains are variations of trains described in "Train types for fatigue" in [29, Annex D.3]. The alterations made to the selection of trains in [29] are based on historic and contemporary trains frequenting Dovrebanen. The trains were obtained from an internal report made for Jernbaneverket and was made available through correspondence with Jernbaneverket [35]. Table 5.4 gives a summary of the trains utilized in the study, it can be seen that Train 1 has a lower total load and number of axles than Train 2.

Table 5.4: The table shows a summary of the overall configuration of the trains utilized in the study.

	Total length [m]	Total load [kN]	Distributed load [kN m^{-1}]	Number of axles
Train 1	118.2	2260	22.5	20
Train 2	211.3	7650	36.2	34

In the following subsections, a brief description of the trains and their origin are given.

Train 1
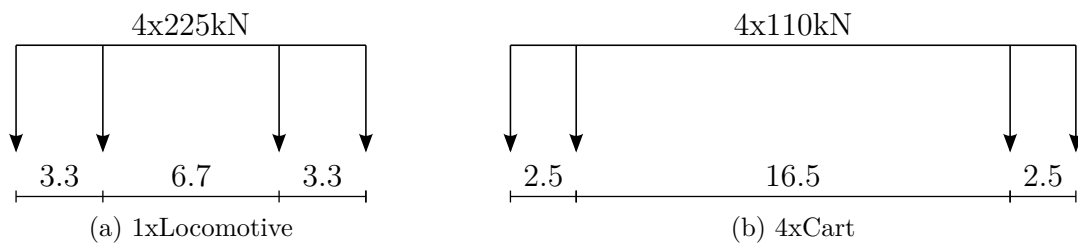
Figure 5.11: The figures show the vehicles making out train 1, the distances are in meters [m].

The first train is modeling a locomotive-hauled passenger train, it is a truncated version of "Type 2 train" [29, Annex D.3]. It consists of a single locomotive, figure 5.11a, and four passenger carts depicted in figure 5.11b. The position of the axles and the loads on each axle are given in detail in appendix C.1.1. The total length of the train is 118.2 m, the total load is 2660 kN and a distributed load is 22.5 kN m^{-1}.

Train 2

6x225kN

2.2 2.2   6.9   2.2 2.2

(a) 1xLocomotive

4x225kN

1.8   11.0   1.8

(b) 7xCart
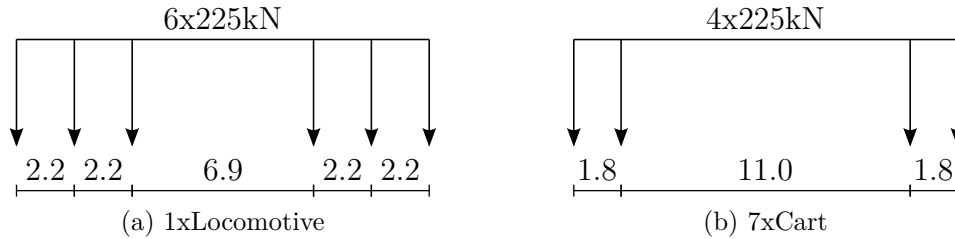
Figure 5.12: The figures show the vehicles making out train 2, the distances are in meters [m].

The second train is modeling a locomotive-hauled freight train, it is a truncated version of "Type 7 train" [29, Annex D.3]. It consists of a single locomotive, figure 5.12a, and seven freight carts depicted in figure 5.12b. The position of the axles and the loads on each axle are given in detail in appendix C.1.2. The total length of the train is 211.3 m, the total load is 7650 kN and a distributed load is 36.2 kN m^{-1}.

5.5 Dynamic behavior of the Tallerås railway bridge.

When assessing the design and performance of a dynamic system, the primary issue is related to avoiding the phenomenon of resonance. When resonance occurs in a dynamic system, the displacement and subsequently the stresses become unduly large and in extreme cases it results in failure of the structure. It is therefore important to establish the velocities which induces resonance in the bridge, and what ranges of velocities which may be considered safe in the operation of the bridge. The resonance velocities of the bridge depend on the natural frequencies of the bridge, and it is therefore necessary to know the natural frequencies of the structure. Since the simplified track is more computationally efficient and the change in the natural frequencies of the structure are insignificant compared to the visco-elastic track, the simplified track and its natural frequencies are chosen as the reference for this section. The implications of choosing the simplified track will be considered in section 5.8.

Regarding the load model, it was argued in chapter 4 that the moving force model is more computationally efficient than the sprung mass model, and the response of the two models are only different at resonance velocities, such that the moving force model will be chosen as the reference load model when obtaining the resonance velocities of the bridge. In section 5.9 an investigation of using the sprung mass model instead of the moving force model will be conducted.

To determine the resonance velocities of the bridge, a simulation of each train at velocities between $20 \, \text{m s}^{-1} (72 \, \text{km h}^{-1})$ and $140 \, \text{m s}^{-1} (504 \, \text{km h}^{-1})$ at increments of $2.5 \, \text{m s}^{-1} (9 \, \text{km h}^{-1})$ was carried out.

The dynamic amplification factor (DAF) is usually defined as the maximum absolute value of the response variable normalized against the maximum absolute value of the the response variable at static or quasi static conditions, see the DAF for the vertical displacement[2] of the midpoint below.

---

[2] Recall from figure 5.3 that x, y, z denotes the coordinate in the longitudinal, vertical and horizontal

$$\text{DAF}_y = \left| \frac{\max(v(L/2, t))}{\max(v^{qst}(L/2, t))} \right|$$

The time domain response of the trains reveals an important characteristic regarding the definition the dynamic amplification factor of the bridge. The time domain response of the midpoint of the bridge is shown for the trains at quasi-static conditions in figure 5.13.


(a) Train 1.

(b) Train 2.
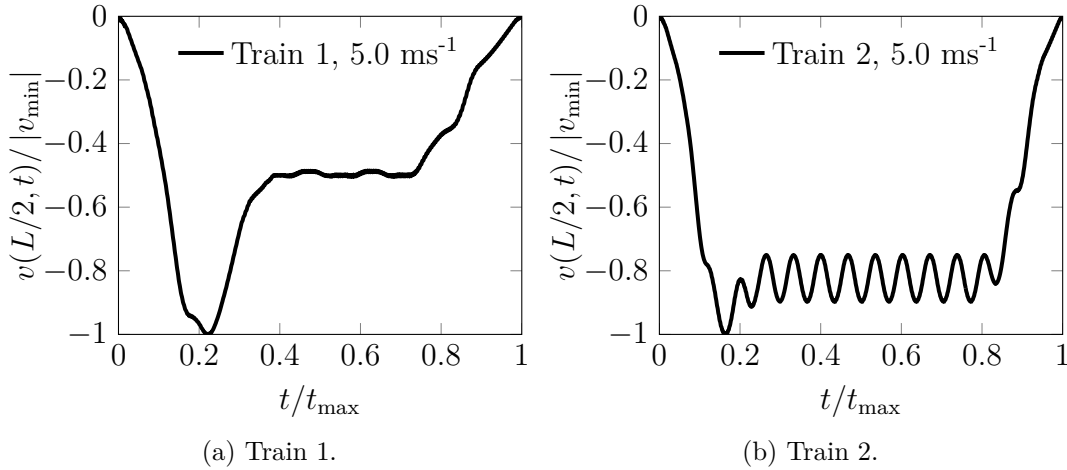
Figure 5.13: The figure shows the dynamic amplification factor of the vertical displacement of the midpoint of the bridge.

Figure 5.13a shows that the maximum displacement of the midpoint for Train 1 occurs very early in the time series and then the response subsides to a plateau at about 50% of the minimum before the bridge returns to its initial position. The reason for this is that the distributed load from the locomotive of the train $q_{loc,1} = 67.7 \, \text{kN m}^{-1}$, is much higher than the distributed load of the carts $q_{cart,1} = 20.5 \, \text{kN m}^{-1}$, such that the maximum displacement of the bridge occurs about the time when the locomotive is in the middle of the bridge. For Train 2, this characteristic is less prominent than for Train 1, figure 5.13b shows that the plateau for Train 2 is at about 85% of the minimum value. The reason for this is that the distributed load from the locomotive of the train $q_{loc,2} = 86.0 \, \text{kN m}^{-1}$, is more comparable to the distributed load of the carts $q_{cart,1} = 61.7 \, \text{kN m}^{-1}$.

The ratio between the distributed loading of the cart and the locomotive is about 0.3 for Train 1 and 0.7 for Train 2. This means, that the above definition of the dynamic amplification factor, may not capture the resonance effect from the repeated loading of the carts, especially in the case of Train 1.

It is therefore appropriate to define a second dynamic amplification factor, DAF2_y and DAF2_z which captures these resonance effects, in this thesis the following definitions are adopted for DAF2_y and DAF2_z .

---

direction of the bridge, and by traditional convention the displacement parameters are u, v, w, respectively.

$$\text{DAF2}_y = \left| \frac{\max(v(L/2,t))}{\max(v^{qst}(L/2,t))} \right|_{t>0.5t_{\max}} \tag{5.1a}$$

$$\text{DAF2}_z = \left| \frac{\max(w(L/2,t))}{\max(w^{qst}(L/2,t))} \right|_{t>0.5t_{\max}} \tag{5.1b}$$

where the quasi static displacement $v^{qst}(L/2,t)$ and $w^{qst}(L/2,t)$ are obtained at a velocity of $v_P = 5\,\mathrm{m\,s^{-1}}$.

Figure 5.14 shows the dynamic amplification factors in both the vertical and horizontal direction, with both the conventional definition and the alternative definition of dynamic amplification factor.

(a) Vertical direction, DAF_y .

(b) Vertical direction, DAF2_y .

(c) Horizontal direction, DAF_z .

(d) Horizontal direction, DAF2_z .
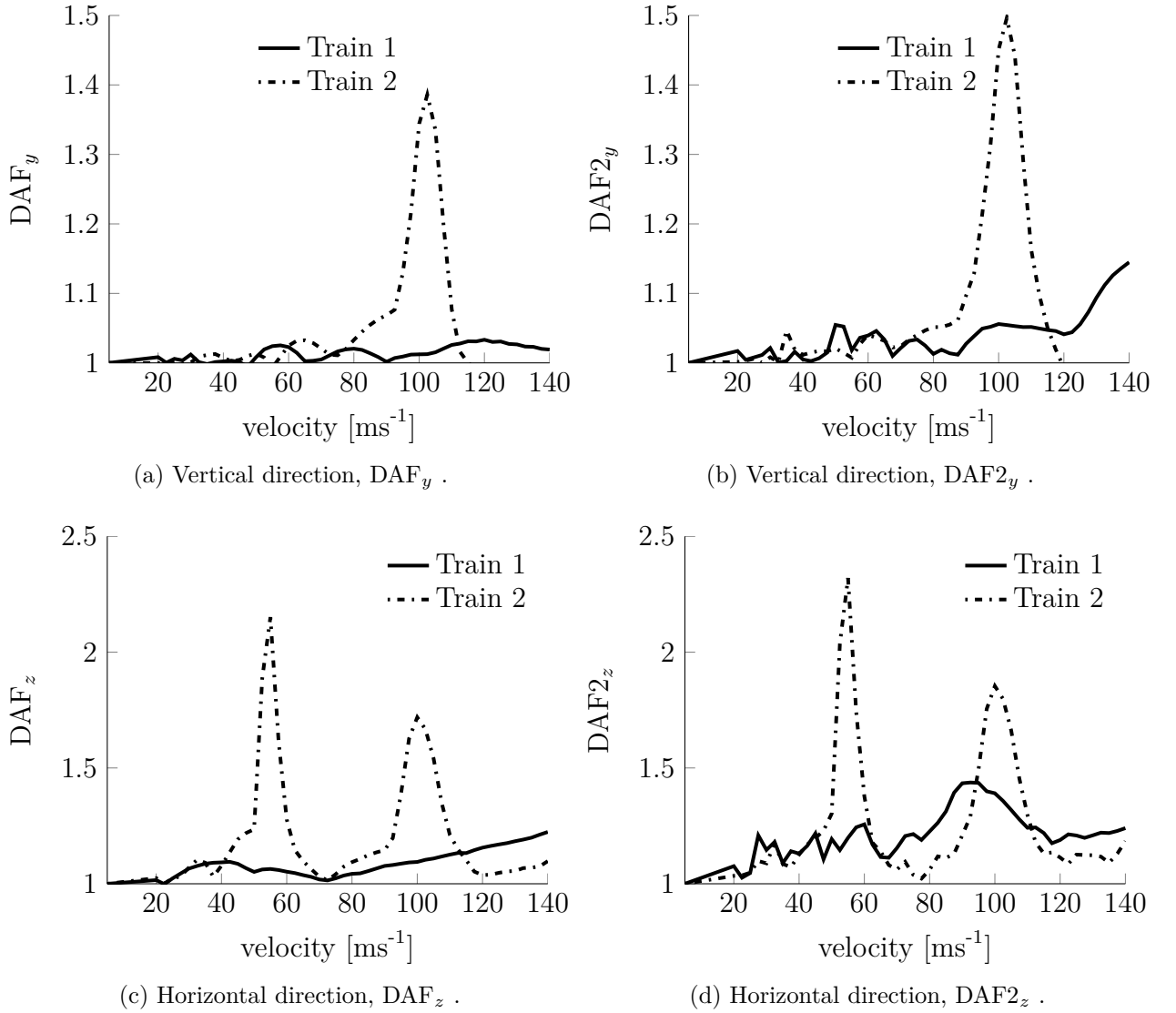
Figure 5.14: The figure shows the dynamic amplification factor of the vertical and horizontal direction in the midpoint of the bridge. Note that the scale on the ordinate axis is different for the vertical and horizontal amplification factor.

Comparing the result in figure 5.14 for the DAF and DAF2 it can be seen that the most prominent results are found with both definitions, but the figures also show that the definition for DAF2 gives a more refined image of the dynamic effects than the DAF definition. This is especially true for Train 1, for instance DAF_z indicates that Train 1 reaches a maximum of 1.2 at a velocity of $140 \, \text{m s}^{-1}$, while DAF2_z indicates the same dynamic amplification at $30 \, \text{m s}^{-1}$. Without further justification, the DAF2 definition will be utilized in the continuation of this thesis.

Figure 5.14b indicate that Train 1 have rather modest dynamic effects in the vertical direction of the bridge, with a dynamic amplification $\text{DAF2}_y \approx 1.05$ for a discrete set of the lower velocities. The dynamic amplification factor increases to a maximum of 1.15 as the velocity increases to $140 \, \text{m s}^{-1}$. Figure 5.14d shows that Train 1 induces a dynamic amplification of $\text{DAF2}_z \approx 1.25$ for the lower velocity range in the horizontal direction of the bridge, but a more prominent dynamic amplification of around $\text{DAF2}_z \approx 1.45$ is found around $90 \, \text{m s}^{-1}$.

Figure 5.14b shows that Train 2 induces significant resonance effects in the vertical direction of the bridge at about $100 \, \text{m s}^{-1}$, and figure 5.14d shows that Train 2 induces significant resonance effects in the horizontal direction of the bridge at velocities velocities of about $50 \, \text{m s}^{-1}$ and $100 \, \text{m s}^{-1}$.

An important question is what should be considered a high value for the dynamic amplification factor, especially with the alternative definition of the dynamic amplification factor since there are little data compare the results with. In section 5.10 this issue will be discussed further.

In chapter 4 it was shown that there are two different types of resonance to consider when trains are moving over a bridge. The first type of resonance is related to the velocity of a single moving load, section 5.6 will discuss the resonance velocities related to this type for the Tallerås railway bridge. The second type of resonance is related to the harmonic excitation given from a series of moving loads, section 5.7 considers this type of resonance for the Tallerås railway bridge and the chosen trains. The focus in the continuation is therefore to find the reason for dynamic effects in the bridge and the significance of the dynamic effects.

5.6 Resonance from velocity alone

In chapter 4, the condition for resonance in a simply supported beam with a single moving load was found to be

$$v_{P,n} = \frac{\omega_n L}{n\pi}$$

The application of the above equation to the Tallerås bridge is not straight forward, since the Tallerås bridge is not a simply supported beam. The equation was derived for a plane problem while the Tallerås bridge is a spatial problem. To give an approximation of the resonance velocity for a single moving load, the bridge can be viewed as an equivalent beam in each respective plane. In table 5.5 the resonance velocity using the natural frequencies for the first and second horizontal and vertical bending mode and the first and second torsional mode, with $L = 52\,\text{m}$ is given.

Table 5.5: The table shows the natural frequencies of the complete structure with the visco-elastic track and with the simplified track.

ω [rad s^{-1}]	$v_{P,n}$ [m s^{-1}]	Description
17.7	293	1st Horizontal bending mode
42.2	350	2nd Horizontal bending mode
35.9	594	1st Vertical bending mode
81.2	672	2nd Vertical bending mode
33.0	546	1st Torsional mode
57.0	471	2nd Torsional mode

From table 5.5 it can be seen that the estimated resonance velocities from a single load are high. The first horizontal bending mode is the lowest estimate and yields $293\,\text{m s}^{-1} \approx 1000\,\text{km h}^{-1}$. This is higher than any commercial train in the market today. The above analysis therefore means that resonance from velocity alone is simply not feasible for the Tallerås railway bridge. Figure 5.14 also confirms that resonance effects from velocity alone does not occur for velocities up to $140\,\text{m s}^{-1}$. If resonance from velocity alone had been introduced in the range, the dynamic amplification factor had increased for all trains at the same velocity. These results are in accordance with Frýba [26] who also considers it unlikely that any actual railway bridge reach resonance from velocity alone. The conclusion is therefore that the resonance from velocity alone will not occur for the Tallerås railway bridge.

5.7 Resonance from a series of moving loads

In section 4.5 it was shown that resonance from a series of moving loads could occur, and it was discussed that the configuration of the train was important for this type of resonance. The following section analyzes the trains by estimating the velocities which may induce resonance effects in the Tallerås railway bridge. The condition for resonance from a series of moving loads is restated below for convenience.

$$v_{Pn} = \frac{\omega_1 d}{2\pi n} \tag{5.2}$$

Regarding the distance d between the moving loads, there are several possible combinations on a train, figure 5.15 shows as set of possible distances for a train with two wheels per boggie, the shown set will be used in the continuation of this thesis.
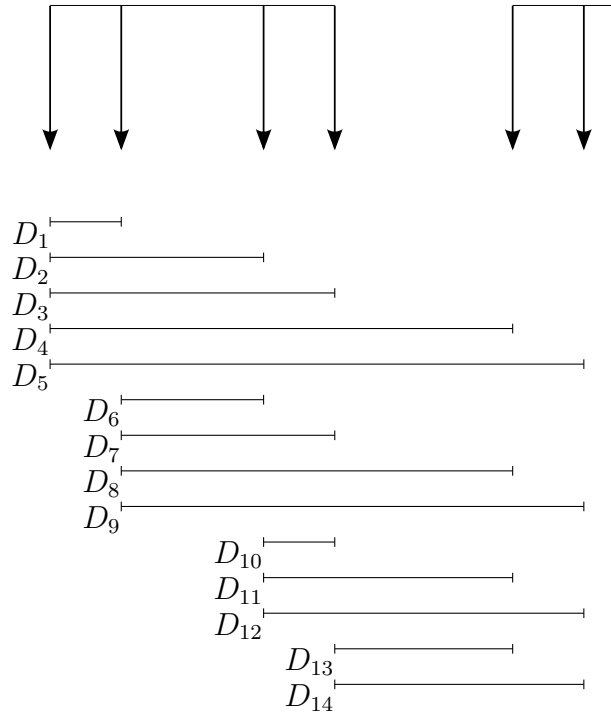
Figure 5.15: The figure shows the distances which may cause resonance in the bridge.

It should be pointed out that there exist a very large number of distances in a train with multiple wagons, and that the above scheme is simply a subset of the possible set.

5.7.1 Train 1

In this section the resonance from a series of moving loads will be considered for the vertical and horizontal direction of Train 1. Figure 5.14 did not indicate a distinct velocity for resonance for Train 1, such that the approach is to consider the configuration train, i.e find the distance which may induce resonance, and then check the time domain response to verify the dynamic amplification.

Vertical direction

The resonance velocities for the first vertical bending mode for Train 1 are given in the table shown in figure 5.16. The velocities are estimated with equation (5.2) for the set of distances D_{1-14} defined by figure 5.15 and multiples in the range $n = 1 - 4$.

The table in figure 5.16 shows that the distances $D_{13} = 5\,\text{m}$, $D_{11} = D_{14} = 7.5\,\text{m}$ and $D_{12} = 10\,\text{m}$ are multiples of $D_1 = D_{10} = 2.5\,\text{m}$. The primary resonance velocity

$d\backslash n$		1	2	3	4
D_1, D_{10}	2.5	14	7	5	4
D_{13}	5	29	14	10	7
D_{11}, D_{14}	7.5	43	21	14	11
D_{12}	10	57	29	19	14
D_6	16.5	94	47	31	24
D_2, D_7	19	109	54	36	27
D_3	21.5	123	61	41	31
D_8	24	137	69	46	34
D_4, D_9	26.5	151	76	50	38
D_5	29	166	83	55	41
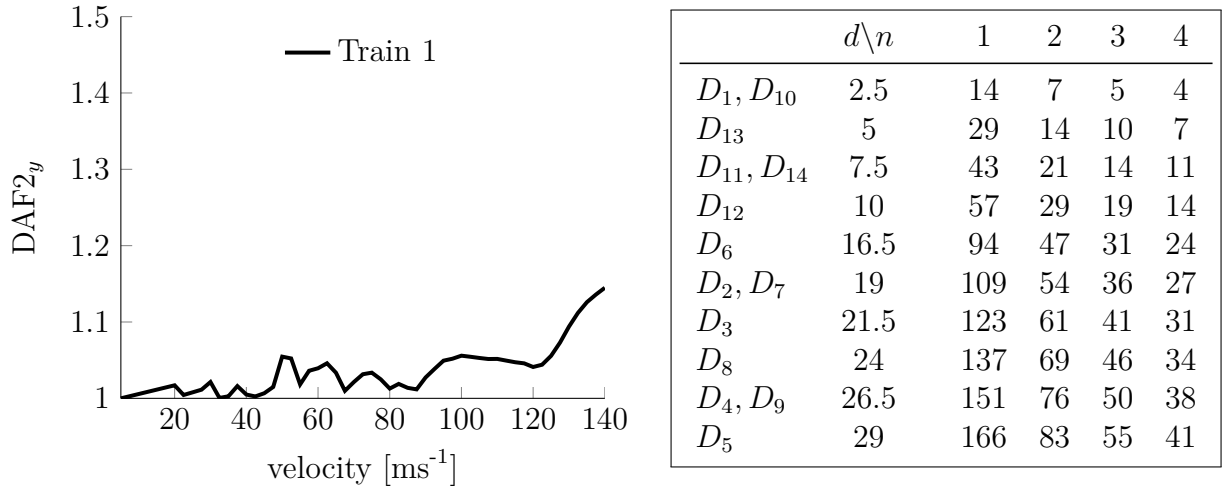
Figure 5.16: The plot shows the dynamic ampliciation factor in the verical direction. The table shows the resonance velocities estimated for Train 1 in the first vertical bending mode with frequency $\omega = 35.9\,\mathrm{rad\,s^{-1}}$ for the distances defined by figure 5.15 and the multiples $n = 1 - 4$.

of distance $2.5\,\mathrm{m}$, which excites the first vertical bending mode with natural frequency $\omega = 35.9\,\mathrm{rad\,s^{-1}}$ is $14\,\mathrm{m\,s^{-1}}$ and this velocity is also found for the multiples of this distance. It would therefore be expected that the response in the vertical direction of the bridge around $14\,\mathrm{m\,s^{-1}}$ would exhibit enhanced dynamic behavior. Figure 5.17 shows the vertical response of the midpoint of the bridge with Train 1 at a velocity of $14\,\mathrm{m\,s^{-1}}$, the response of the same train with velocity of $17\,\mathrm{m\,s^{-1}}$ is also given for comparison.

(a) Time domain

(b) Frequency domain
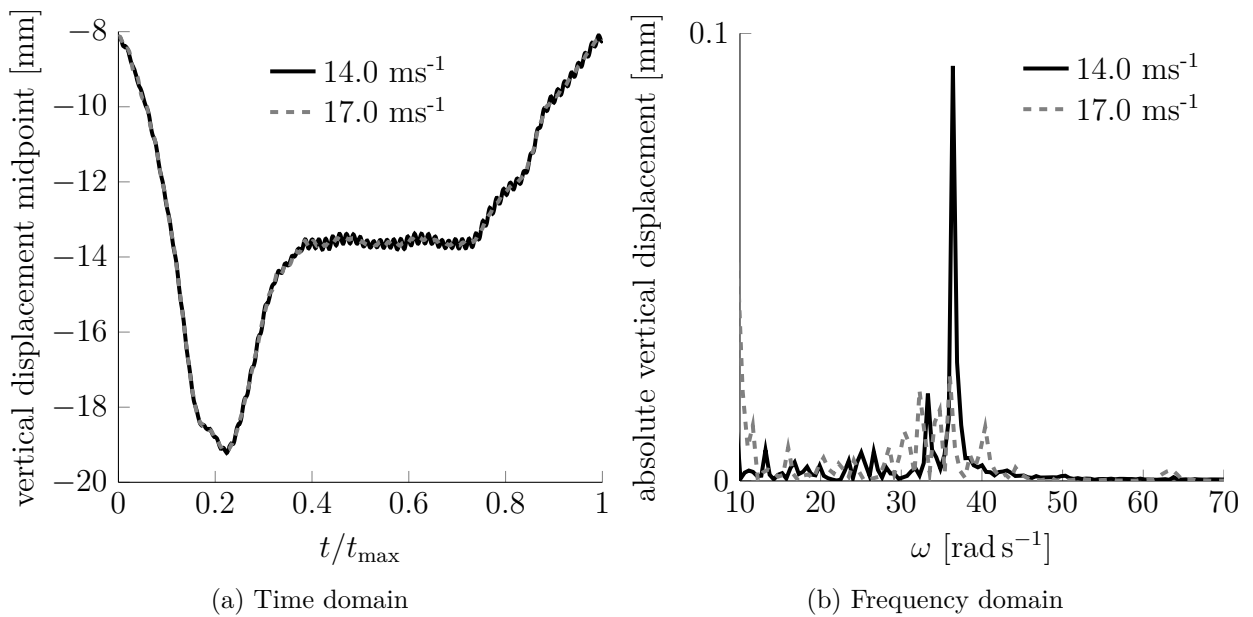
Figure 5.17: The figure shows the vertical displacement of the bridge at the midpoint for the first vertical resonance velocity $14\,\mathrm{m\,s^{-1}}$ of Train 1, compared against a velocity $17\,\mathrm{m\,s^{-1}}$.

Figure 5.17a shows that the overall response is largely the same for the two velocities $14\,\mathrm{m\,s^{-1}}$ and $17\,\mathrm{m\,s^{-1}}$. Even if the overall response is the same, it can be seen that both in the time domain response plot, figure 5.17a and the frequency domain response plot, figure 5.17b Train 1 at $14\,\mathrm{m\,s^{-1}}$ does excite the bridge in its first bending mode $\omega = 35.9\,\mathrm{rad\,s^{-1}}$ to a larger degree than the Train 1 at velocity $17\,\mathrm{m\,s^{-1}}$. The frequency response plot shows that the amplitude of the added frequency component is about $0.1\,\mathrm{mm}$, comparing this to the total span of the bridge at $52\,\mathrm{m}$ the dynamic effect may be negligible.

From the table in figure 5.16 it can be seen that a velocity of about $30\,\mathrm{m\,s^{-1}}$ alot of the distances predict resonance in the bridge, the dynamic amplification plot also indicates a small peak at this velocity. The response in the time and frequency domain at a velocity of $30\,\mathrm{m\,s^{-1}}$ is given in figure 5.18.

(a) Time domain

(b) Frequency domain
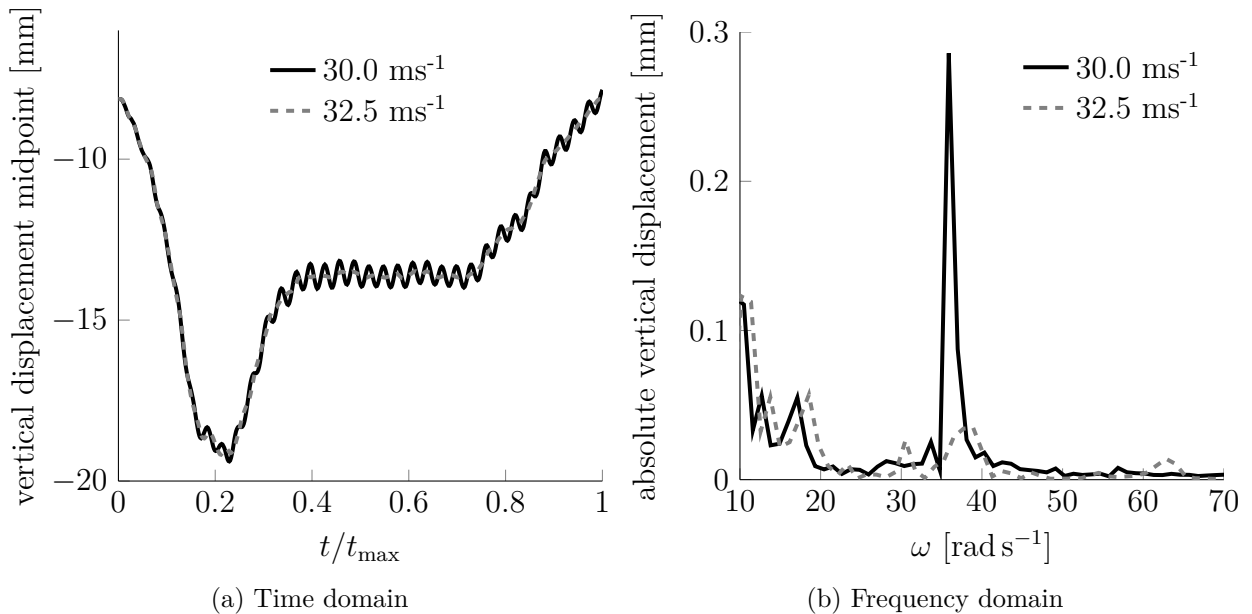
Figure 5.18: The figure shows the vertical displacement of the bridge at the midpoint for the second vertical resonance velocity $30\,\mathrm{m\,s^{-1}}$ of Train 1, compared against a velocity $32.5\,\mathrm{m\,s^{-1}}$.

The results for the train at $30\,\mathrm{m\,s^{-1}}$ show the same characteristic results as for the train at $14\,\mathrm{m\,s^{-1}}$, the overall response is the same but the resonance velocity does induce a slight dynamic effect in the predicted mode.

From the table in figure 5.16, it can be seen that a large number of velocities may induce resonance in the bridge. Most of the primary resonance velocities, i.e velocities in the column with $n = 1$, does indeed induce dynamic effects as the ones shown in figure 5.17 and figure 5.18 for velocities 14 and $30\mathrm{m\,s^{-1}}$. It can be seen from the time domain response in figure 5.18a that the dynamic effect is bound, i.e it does not grow as the train passes the bridge. The reasons for the bound response was discussed in section 4.5. Firstly, damping will provide bounds for the response by dissipating energy from the system, secondly the phenomena of cancellation will create bounds for the response. The third reason is simply that the series of moving loads working in the same phase is not long enough. This is the case for the train at a velocity of $14\,\mathrm{m\,s^{-1}}$, even though there are six distances on each

cart which induce a dynamic effects at this velocity only four loads at a time work in the same phase, see figure 5.19.
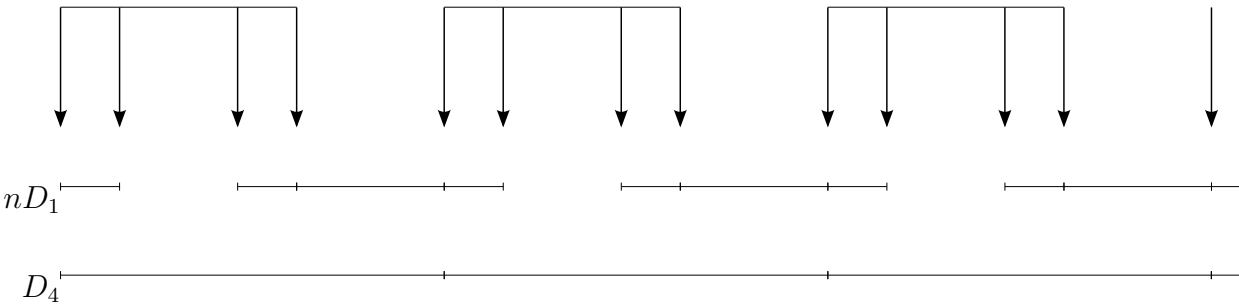

Figure 5.19: The figure shows the distances which may cause resonance in the bridge.

Figure 5.19 illustrates that although there exists several distances which are multiples of $D_1 = 2.5\,\mathrm{m}$, only four at time work in the same phase. This is because the distance D_6, i.e the distance between the two boggies on a cart, is not a multiple of D_1, such that each series of four is "broken" and the build up of dynamic effects stops. The series of distances nD_1 might even work against each other in cancellation.

This is not the case for the distance D_4, as figure 5.19 shows the series of the loads with distance D_4 is continuous throughout the length of the train. From the table in figure 5.16 it can be seen that for the distance $D_4 = 26.5\,\mathrm{m}$ the resonance velocities are $38, 50, 76$ and $151\,\mathrm{m\,s^{-1}}$.

Figure 5.20 shows the time domain response at these velocities, and it can be seen from figure 5.20a, 5.20b and 5.20d that the response for the velocities $38, 50$ and $151\,\mathrm{m\,s^{-1}}$ grows as the train travels across the bridge, all showing clear signs of resonance behavior.

Regarding the response of the train at $76\,\mathrm{m\,s^{-1}}$ figure 5.20c shows that the response of the bridge at this velocity does not share this characteristic, the reason is most likely cancellation, bounds by damping would have created a constantly sized amplitude as the train passed.

Most of the velocities shown in figure 5.20 does induce some dynamic effect similar to the ones shown in figure 5.17, and the dynamic amplification factor reflects the magnitude of these dynamic effects. It can be concluded that the above method may be used to predict velocities where dynamic effects occur and that resonance effects induced by Train 1 are due to the series of moving loads. As mentioned in section 5.5, an interesting question is what should be considered a high dynamic amplification factor? In section 5.10 the effects of the dynamic amplification will be addressed.
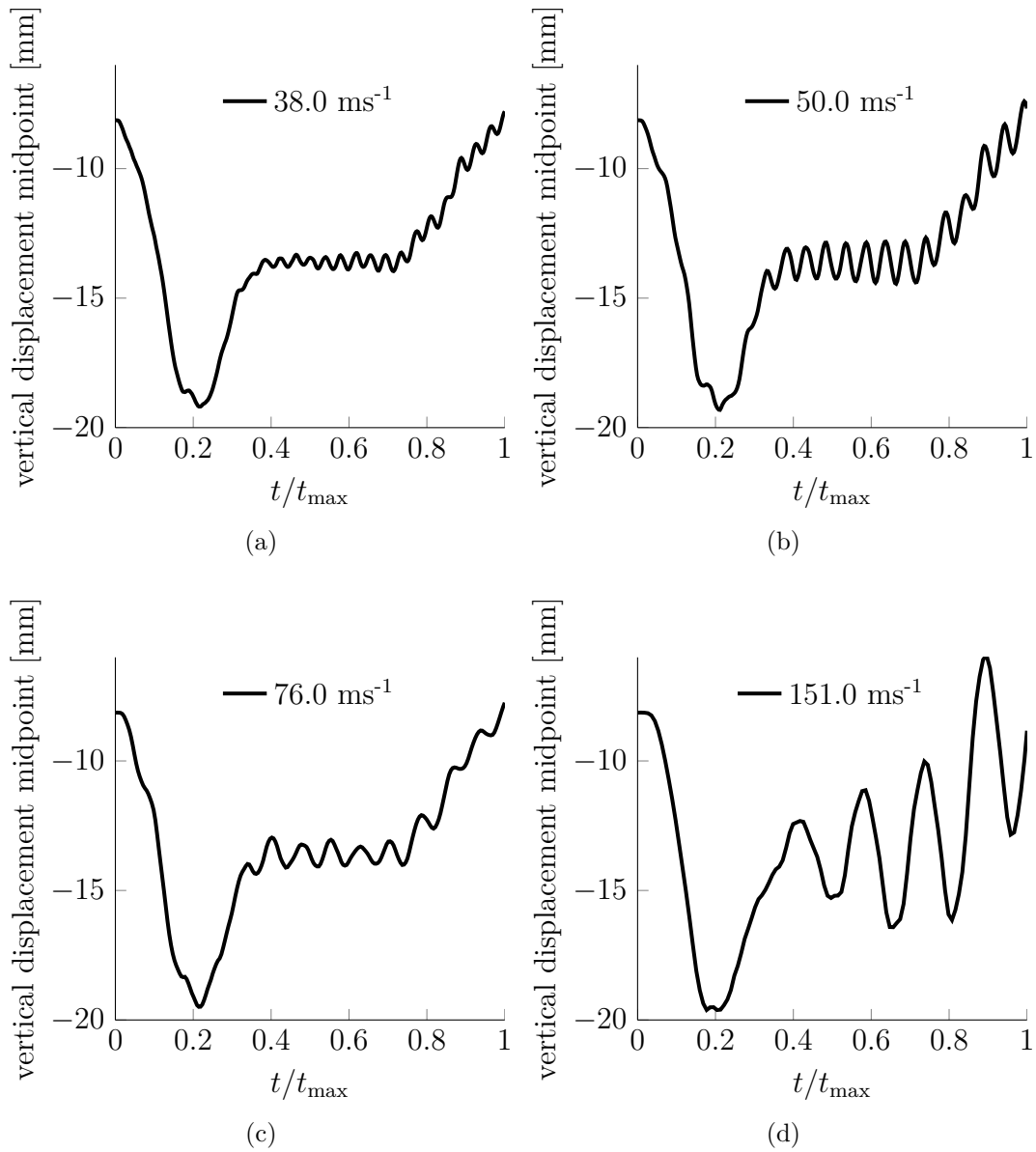
Figure 5.20: The figure shows the time domain simulation for Train 1 at velocities which are expected to induce resonance behavior.

Horizontal direction

The resonance velocities for the first horizontal bending mode for Train 1 are given in the table shown in figure 5.16. The velocities are estimated with equation (5.2) for the set of distances D_{1-14} defined by figure 5.15 and multiples in the range $n = 1 - 4$.

| $d \backslash n$		1	2	3	4
D_1, D_{10}	2.5	7	4	2	2
D_{13}	5	14	7	5	4
D_{11}, D_{14}	7.5	21	11	7	5
D_{12}	10	28	14	9	7
D_6	16.5	46	23	15	12
D_2, D_7	19	54	27	18	13
D_3	21.5	61	30	20	15
D_8	24	68	34	23	17
D_4, D_9	26.5	75	37	25	19
D_5	29	82	41	27	20
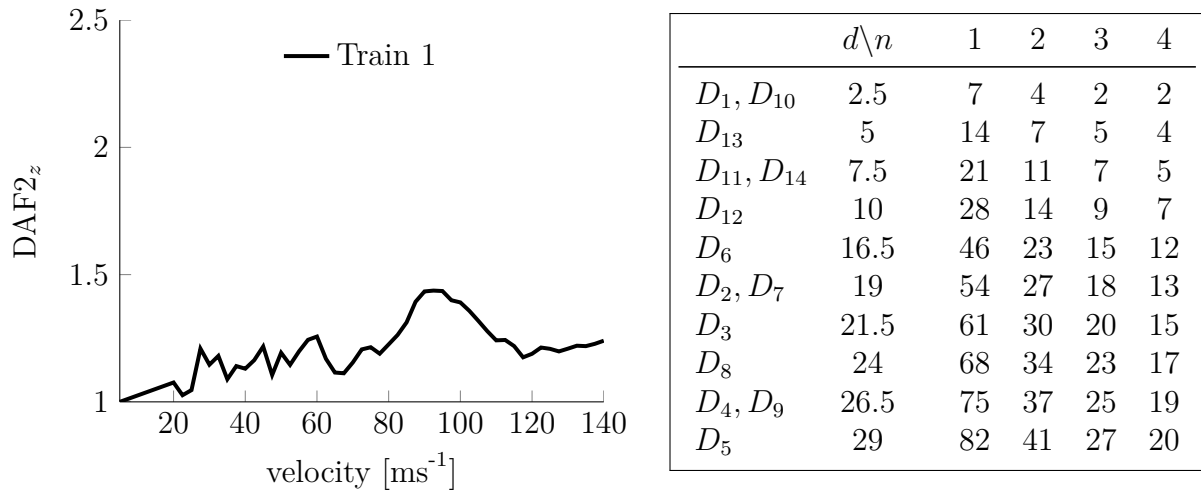
Figure 5.21: The plot shows the dynamic ampliciation factor in the transversal direction. The table shows the resonance velocities estimated for Train 1 in the first transversal bending mode with frequency $\omega = 17.7 \,\mathrm{rad\,s^{-1}}$ for the distances defined by figure 5.15 and the multiples $n = 1 - 4$.

The dynamic amplification factor for Train 1 shown in figure 5.21 is around 1.2 up to $\approx 90 \,\mathrm{m\,s^{-1}}$ where it increases to 1.5, before it subsides to a level of 1.2 again. The plot shows that the horizontal dynamic amplification curve is generally higher than the dynamic amplification curve for the vertical direction shown in the previous subsection. It should also be pointed out that it is continuously high, i.e it does not drop to zero as opposed to the amplification factor for the vertical direction. The reason for this is that the torsional and the vertical modes has a component in the horizontal direction, such that dynamic resonance effects in these modes also translates to resonance effects in the horizontal direction.

In figure 5.22 the time and frequency domain response of the midpoint of the bridge in the horizontal direction is given for Train 1. The figure contains the plot for the train that the quasi static velocity, $5 \,\mathrm{m\,s^{-1}}$ and at the velocity of with the estimated maximum dynamic amplification of $90 \,\mathrm{m\,s^{-1}}$.

The time domain representation, figure 5.22a, shows that there are significant dynamic effects for the train at $90 \,\mathrm{m\,s^{-1}}$, but that the total displacements are still rather modest. Even at the estimated maximum of the dynamic amplification factor, the total displacement in the transversal direction is below $1 \,\mathrm{mm}$, with a total span of the bridge being $52 \,\mathrm{m}$ this seems to be a negligible deformation. In section 5.10 the effects of the dynamic amplification will be addressed further.

The frequency response plot in figure 5.22b shows that the first transversal mode is dominant in the deformation in the horizontal direction ($\omega = 17.7 \,\mathrm{rad\,s^{-1}}$), but also the first torsional mode ($\omega = 32.9 \,\mathrm{rad\,s^{-1}}$) and modes in between the two significant modes contributes to the total dynamic amplification.

(a) Time domain   (b) Frequency domain
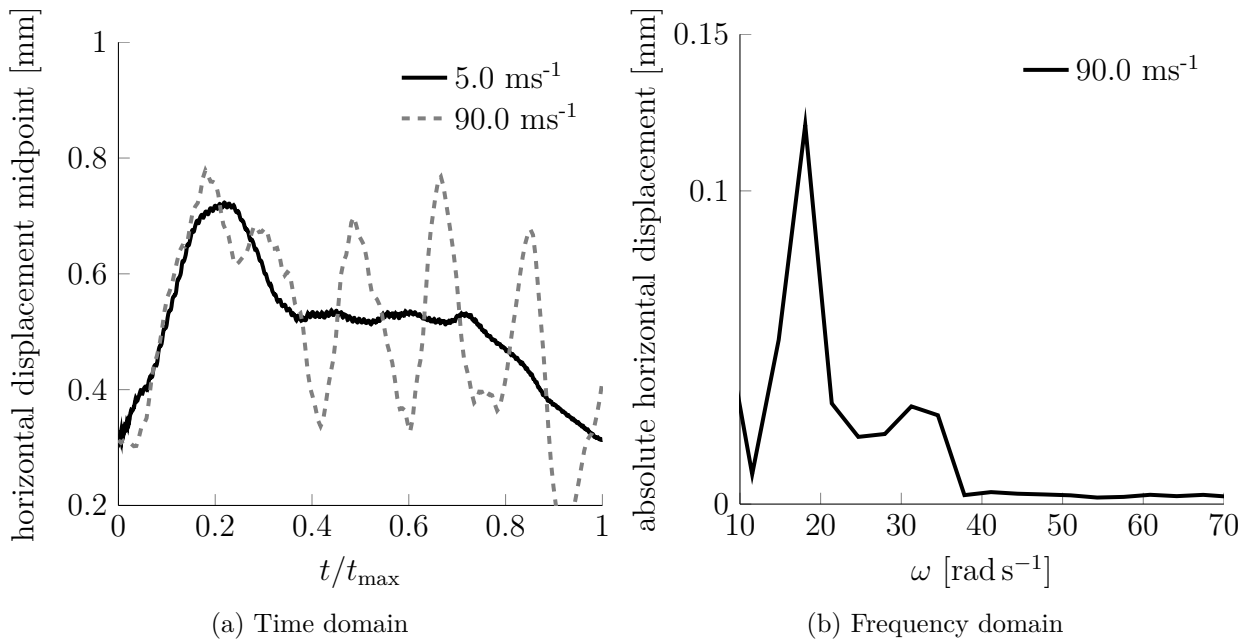
Figure 5.22: The figure shows the horizontal displacement of the bridge at the midpoint for the horizontal resonance velocity $90 \, \mathrm{m \, s^{-1}}$ of Train 1, compared against a velocity $5 \, \mathrm{m \, s^{-1}}$.

It should be noted that the velocity of $90 \, \mathrm{m \, s^{-1}}$ is not predicted in figure 5.21, at this velocity the predicted distance for the first horizontal bending mode is $31.9 \, \mathrm{m}$. It is not possible to find a continuous distance which equals $31.9 \, \mathrm{m}$ on Train 1. Similarly, the predicted distance for the torsional mode is $17.2 \, \mathrm{m}$ and not found as a continuous distance on Train 1 either. The reason that $90 \, \mathrm{m \, s^{-1}}$ yields the largest dynamic amplification is not straight forward, but perhaps the answer lies in the way the vertical displacements translates to displacements in the horizontal direction. Note that the moving force model does not have any component in the horizontal direction, such that the structure is not directly loaded in this plane. Nevertheless, figure 5.22a shows that even for the quasi static velocity, $5 \, \mathrm{m \, s^{-1}}$, the structure has displacement in the horizontal direction. Since there are no forces working in this direction, the reason for these displacement have to be that there are un-symmetries in the bridge structure and placement of the vertical loading. Perhaps this coupling effect between the vertical and horizontal displacement through un-symmetries are the reason for the observed behavior.

Considering the distance D_4, which in the previous section was shown to have a continuous excitation of the bridge, the table in figure 5.21 shows that the corresponding resonance velocities are $19, 25, 37$ and $75 \, \mathrm{m \, s^{-1}}$. The dynamic amplification plot in figure 5.21 confirms that there are dynamic effects at these velocities.

5.7.2 Train 2

For Train 2 the dynamic amplification factor in figure 5.14 indicated resonance at velocities of $102.5\,\mathrm{m\,s^{-1}}$ in the vertical direction and 50 and $100\,\mathrm{m\,s^{-1}}$ in the horizontal direction. In this section, the reasons for the enhanced dynamic effects at these velocities will be examined.

Vertical direction

The distinct dynamic amplification of Train 2 was found at $102.5\,\mathrm{m\,s^{-1}}$, figure 5.23 shows the displacement of the bridge at the midpoint at this velocity, both in the time and frequency domain.


(a) Time domain (b) Frequency domain
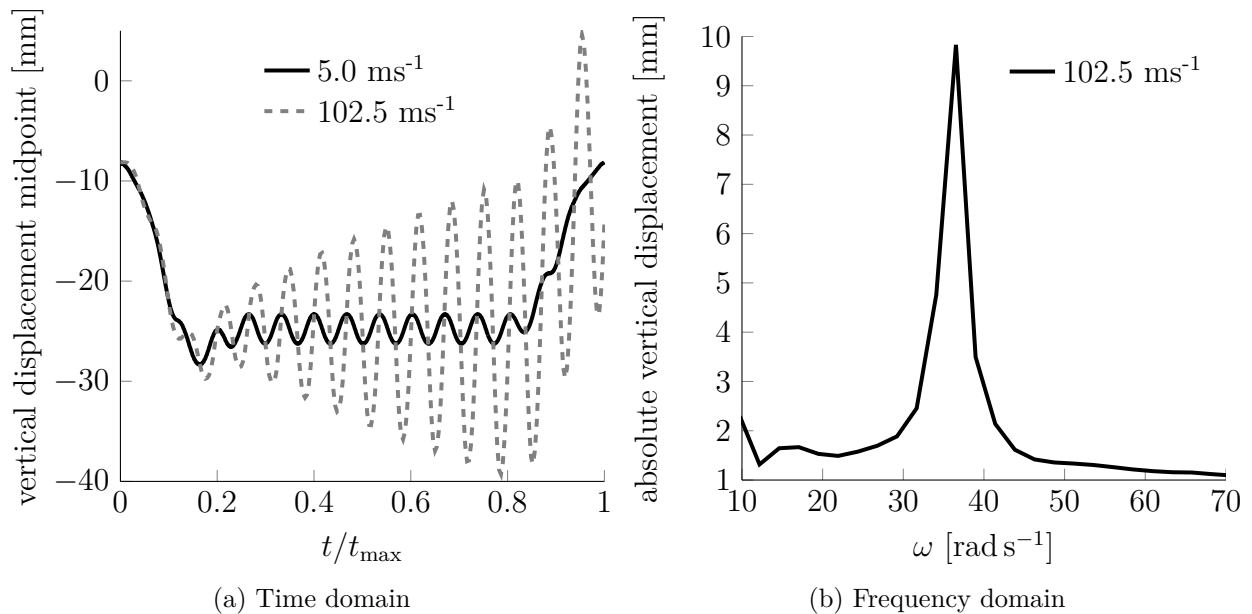
Figure 5.23: The figure shows the vertical displacement of the bridge at the midpoint for the vertical resonance velocity $102.5\,\mathrm{m\,s^{-1}}$ of Train 2, compared against the conditions under quasi static velocity $5\,\mathrm{m\,s^{-1}}$.

Figure 5.23a shows that the system is clearly in resonance when Train 2 is at a speed of $102.5\,\mathrm{m\,s^{-1}}$, the response is growing at a linear rate with a similar characteristic as shown in section 4.5 for resonance from a series of moving loads. The frequency domain representation of the displacement of the midpoint at $102.5\,\mathrm{m\,s^{-1}}$ shows that the train excites the first mode, with frequency $\omega = 35.9\,\mathrm{rad\,s^{-1}}$. It can be seen that the amplitude of the oscillations are in the same magnitude as the static deflections, the maximum deflection is increased by $\approx 40\%$. This will lead to a significant increase in stresses throughout the structure, and stress cycles in the structure which are important in assessing the remaining fatigue life. This will be discussed further in section 5.10.

Regarding the distance on Train 2 which excites the bridge in its vertical bending mode at a velocity of $102.5\,\mathrm{m\,s^{-1}}$, equation (5.2) yields $d = 17.9\,\mathrm{m}$. This is approximately the distance $D_4 = D_9 = 17.8\,\mathrm{m}$ in figure 5.15, i.e the distance between the mth load of cart i to the mth load on cart $i + 1$. This is the same distance which proved to induce resonance behavior in the vertical direction in Train 1, and the reason was shown to be

that the loads at this distance continuously excited the bridge throughout the length of the train.

Horizontal direction

The distinct dynamic amplification in the horizontal direction for Train 2 was found in figure 5.14d at velocities $55\,\mathrm{m\,s^{-1}}$ and $100\,\mathrm{m\,s^{-1}}$. Figure 5.24 shows the displacement of the bridge at the midpoint at these velocities, both in the time and frequency domain. In addition the response for the quasi static velocity $5\,\mathrm{m\,s^{-1}}$ is shown for comparison.


(a) Time domain
(b) Frequency domain
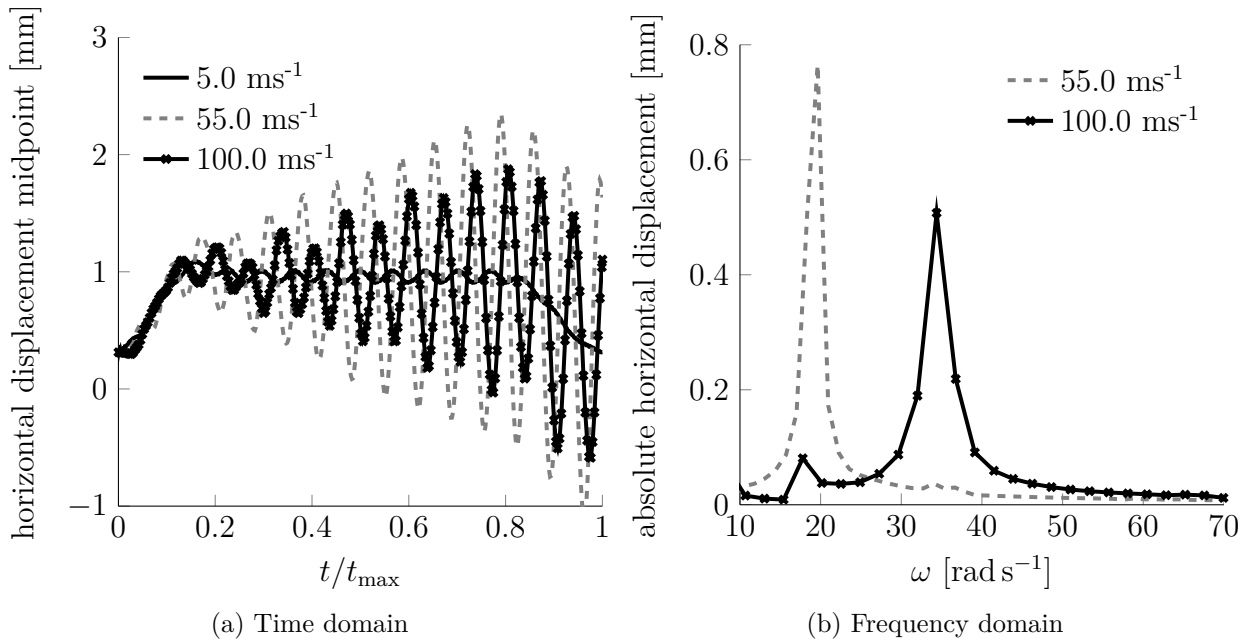
Figure 5.24: The figure shows the vertical displacement of the bridge at the midpoint for the vertical resonance velocity $102.5\,\mathrm{m\,s^{-1}}$ of Train 2, compared against the conditions under quasi static velocity $5\,\mathrm{m\,s^{-1}}$.

Figure 5.24a shows that the system is clearly in resonance when Train 2 is at the two resonance velocities. The frequency domain representation of the displacement shows that Train 2 excites the first transversal bending mode, with frequency $\omega = 17.7\,\mathrm{rad\,s^{-1}}$ at the velocity of $55\,\mathrm{m\,s^{-1}}$ and the first torsional mode with frequency $\omega = 32.9\,\mathrm{rad\,s^{-1}}$ at the velocity $100\,\mathrm{m\,s^{-1}}$. The magnitude of the displacements the maximum transversal displacement is about $2\,\mathrm{mm}$.

With equation (5.2), the distance between a series of loads are found to be $d = 19.5\,\mathrm{m}$ for the velocity of $55\,\mathrm{m\,s^{-1}}$ and first transversal bending mode with frequency $17.7\,\mathrm{rad\,s^{-1}}$. This is approximately the distance $D_5 = 19.6\,\mathrm{m}$ in figure 5.15, i.e the distance between the first axle on cart i to the second axle on cart $i+1$.

The distance calculated for the resonance at velocity of $100\,\mathrm{m\,s^{-1}}$ and first torsional mode with frequency $32.9\,\mathrm{rad\,s^{-1}}$ is $19.1\,\mathrm{m}$, which is approximately the distance $D_5 = 19.6\,\mathrm{m}$.

The distance D_5 is not continuously repeatable along the full length of the train in the same way that the distance $2.5\,\mathrm{m}$ and its multiples was not repeatable for Train 1.

Again it is not completely clear why the maximum horizontal dynamic effects are found to be at a distance on the train which is not a repeatable distance. The coupling between the vertical and the horizontal displacements discussed in the previous section on Train 1 may be the reason system exhibits this behavior.

5.8 The effect of including the Visco-Elastic track

In section 5.3 it was shown that the natural frequencies of the complete structure with the Visco-Elastic track and the simplified track were the same. Since the simplified track is more computationally efficient than the Visco-Elastic track, and the natural frequencies were the same, the simplified track was chosen as the reference track for the study. In this section, the response of the structure with the Visco-Elastic track will be compared to the response of the structure with the simplified track. A series of simulations were run for Train 2 with the Visco-Elastic track to give the data for comparison. Figure 5.25 shows the results of these simulations.

(a) Dynamic amplification vertical direction.

(b) Dynamic amplification horizontal direction.

(c) Peak acceleration, vertical direction.

(d) Peak acceleration, horizontal direction.
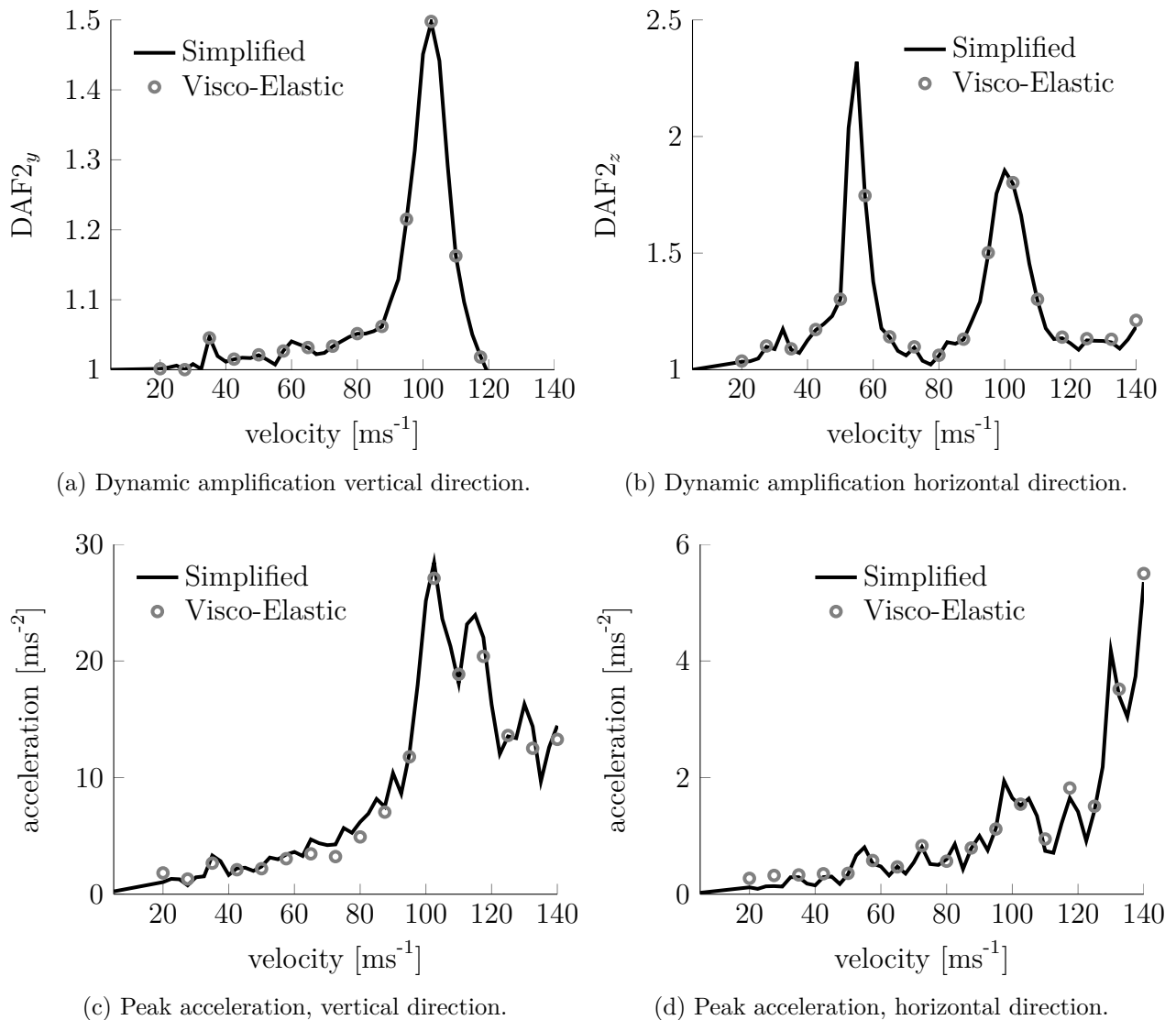
Figure 5.25: The figure shows the results from the simulations of with Train 2 on the bridge with a Visco-Elastic track and a simplified track. Figure (a) and (b) show the dynamic amplification factor for the displacement in the vertical and horizontal direction, while (c) and (d) show the peak acceleration in the vertical and horizontal direction.

Figure 5.25a and figure 5.25b show that the dynamic amplification factors in the verti-

cal and horizontal direction are exactly the same. Time domain simulations and dynamic amplification factors at the 3rd points of the bridge also confirms that the displacements with the two systems are the same, and stresses in the two simulations are also the same. Regarding the peak accelerations shown in figure 5.25c and figure 5.25d the results show that the simplified track and the Visco-Elastic track are largely the same. The negligible difference which can be seen in the figures, might be due to the highly volatile nature of the accelerations, see figure 5.26.
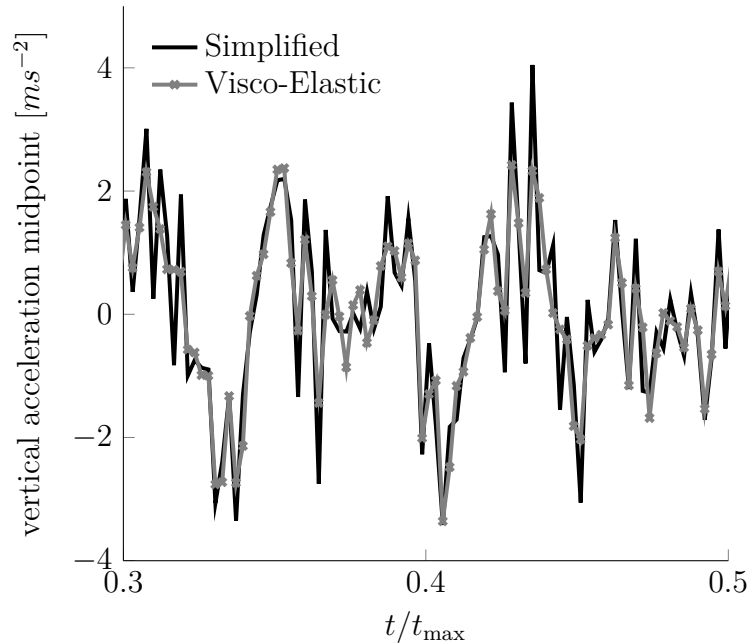
Figure 5.26: The figure shows a time domain accelerations of Train 2 at the midpoint with a velocity of $62.5\,\mathrm{m\,s^{-1}}$ both for the Visco-Elastic and the Simplified track.

Figure 5.26 shows that the overall characteristics and magnitude of the accelerations are the same, but the absolute peaks are not always captured by either plot. One peak is larger for the Simplified track while the other is larger for the Visco-elastic track. If the frequency of which the data is extracted is not very large, and there is a slight shift in the time of extraction of the accelerations between the two simulations the readings may not capture the absolute peak of the acceleration.

Given that the elastic and dissipative properties utilized in this study are realistic, the conclusion is that the difference between the Visco-Elastic and the simplified track are negligible when the moving force model is used. It should be noted that the above results are specific to tracks which have relatively high stiffness. If the stiffness of the track became lower, for instance due to a ballasted track, the results might be different for the displacements and the accelerations. Another interesting question is whether the visco-elastic track changes the response of the system when the sprung-mass model is employed. These subjects are suitable for further work.

5.9 Sprung-Mass vs. Moving-Force load model

In chapter 4 it was shown that the difference between the moving force model and the moving mass/sprung-mass model was a result of the inertia effects associated with the train. It was also shown that the inertia effects became large as the accelerations of the bridge increased. The moving force model was chosen as the reference model for the case study in this thesis because it is more computationally efficient than the sprung-mass model and the response of the two load models where expected to be similar for all cases except resonance. In this section, the response of the structure with the moving-force model will be compared to the response of the structure with the sprung-mass load model. A series of simulations where run for Train 1 with the sprung-mass load model to give the data for comparison. Ideally the same simulations should have been run for Train 2, since this train showed a more dramatic dynamic profile than Train 1, but Train 2 was found to be very computationally expensive compared to Train 1. The reason that Train 2 is more computationally expensive than Train 1, is due to two things. First of all, Train 2 has 70% more axles than Train 1 such that it has more contact points which needs to be iterated to equilibrium. Secondly Train 2 is 80% longer than Train 1, such that the total time of one passing of Train 2 is 55% longer than Train 1. In any case, the conclusions drawn for the simulations of Train 1 are universal and provides the necessary foundation for the discussion in this section.

The properties of the sprung-mass model are chosen with background in the numbers provided in [20].

	110kN	225kN
M_1	$1000\,\mathrm{kg}$	$1000\,\mathrm{kg}$
M_2	$4600\,\mathrm{kg}$	$10\,456\,\mathrm{kg}$
K	$5.5 \times 10^5\,\mathrm{N\,m^{-1}}$	$1.13 \times 10^6\,\mathrm{N\,m^{-1}}$
C	$4 \times 10^4\,\mathrm{N\,s\,m^{-1}}$	$8 \times 10^4\,\mathrm{N\,s\,m^{-1}}$
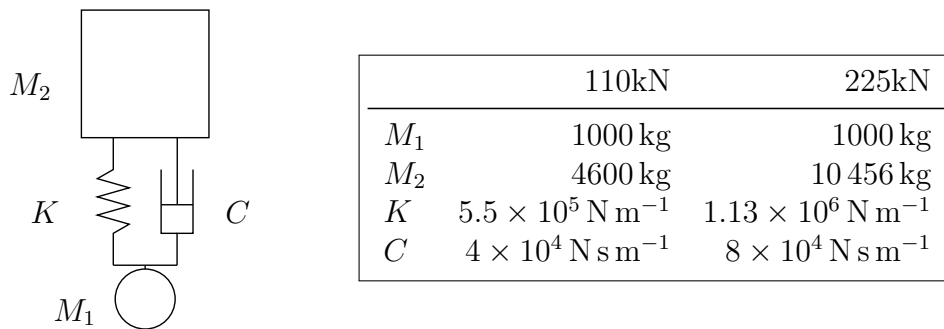
Figure 5.27: The figure shows the sprung mass model, and the properties used in the case study.

Figure 5.28 shows the results of the simulations with Train 1 and the moving load model and the sprung mass model.

Figure 5.28a and figure 5.28b show that the dynamic amplification factors in the vertical and horizontal direction are in the same magnitude for both load models, but there are some differences between the predicted amplifications.

For the vertical amplification factor, values for the sprung-mass load model are largely the same. The amplification factor at $120\,\mathrm{m\,s^{-1}}$ seems to be larger for the sprung mass model, but the time domain response reveals that the difference is negligible, see figure 5.29a.

Going through the time domain simulations, and comparing the results, a more general trend is that the response in the vertical direction estimated from the sprung-mass load
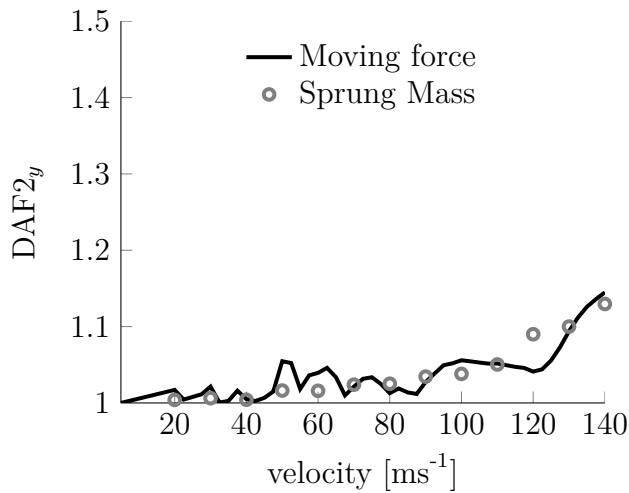
(a) Dynamic amplification vertical direction.
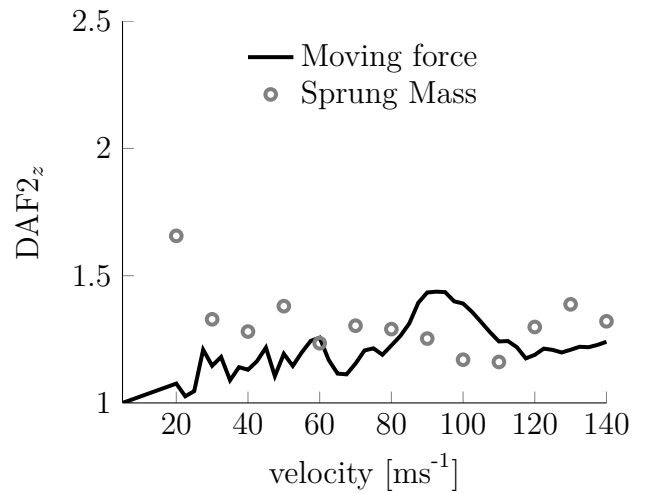
(b) Dynamic amplification horizontal direction.
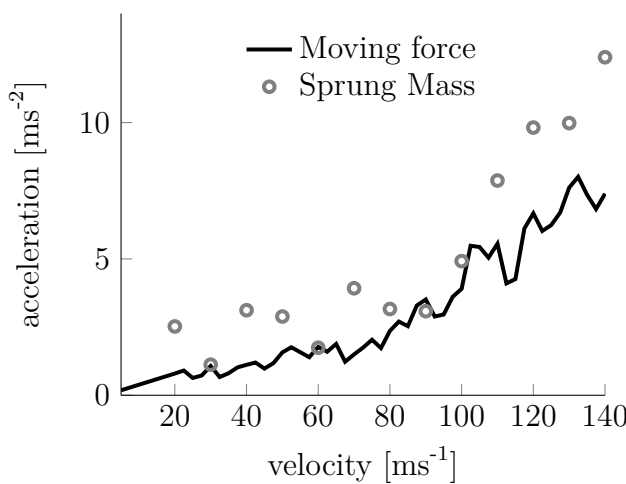
(c) Peak acceleration, vertical direction.
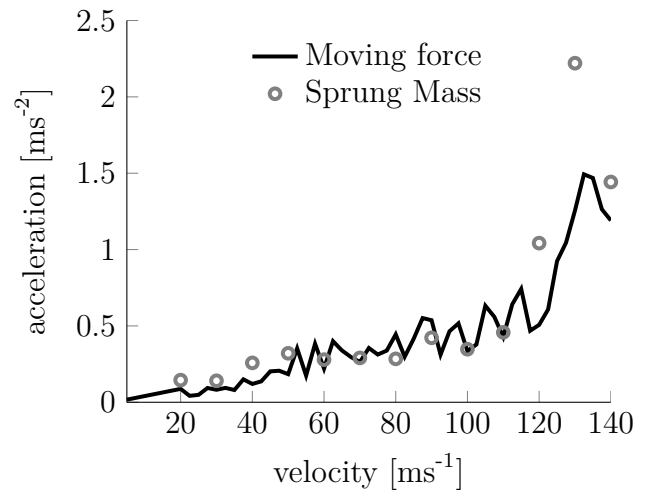
(d) Peak acceleration, horizontal direction.

Figure 5.28: The figure shows the results from the simulations of with Train 1 on the bridge with a moving force load model and a sprung-mass load model. Figure (a) and (b) show the dynamic amplification factor for the displacement in the vertical and horizontal direction, while (c) and (d) show the peak acceleration in the vertical and horizontal direction.

model is lower than the corresponding response obtained from the moving force model. An example of this is given in, figure 5.29b, where the response of the midpoint of the bridge is shown for the moving force model and the sprung mass model at a velocity of $50\,\mathrm{m\,s^{-1}}$. The reason that the response obtained from the sprung-mass model is lower than the response obtained moving-force model was discussed in section 4.3, the sprung mass model dissipates energy from the system through the dashpot in the suspension. This is an important finding for the discussion about the significance of dynamic effects, section 5.10. In figure 5.20d in the discussion about resonance from a series of moving loads for Train 1, it was shown that Train 1 induced resonance in the bridge at a velocity of $151\,\mathrm{m\,s^{-1}}$. In figure 5.29c the response of the two load models are compared at the
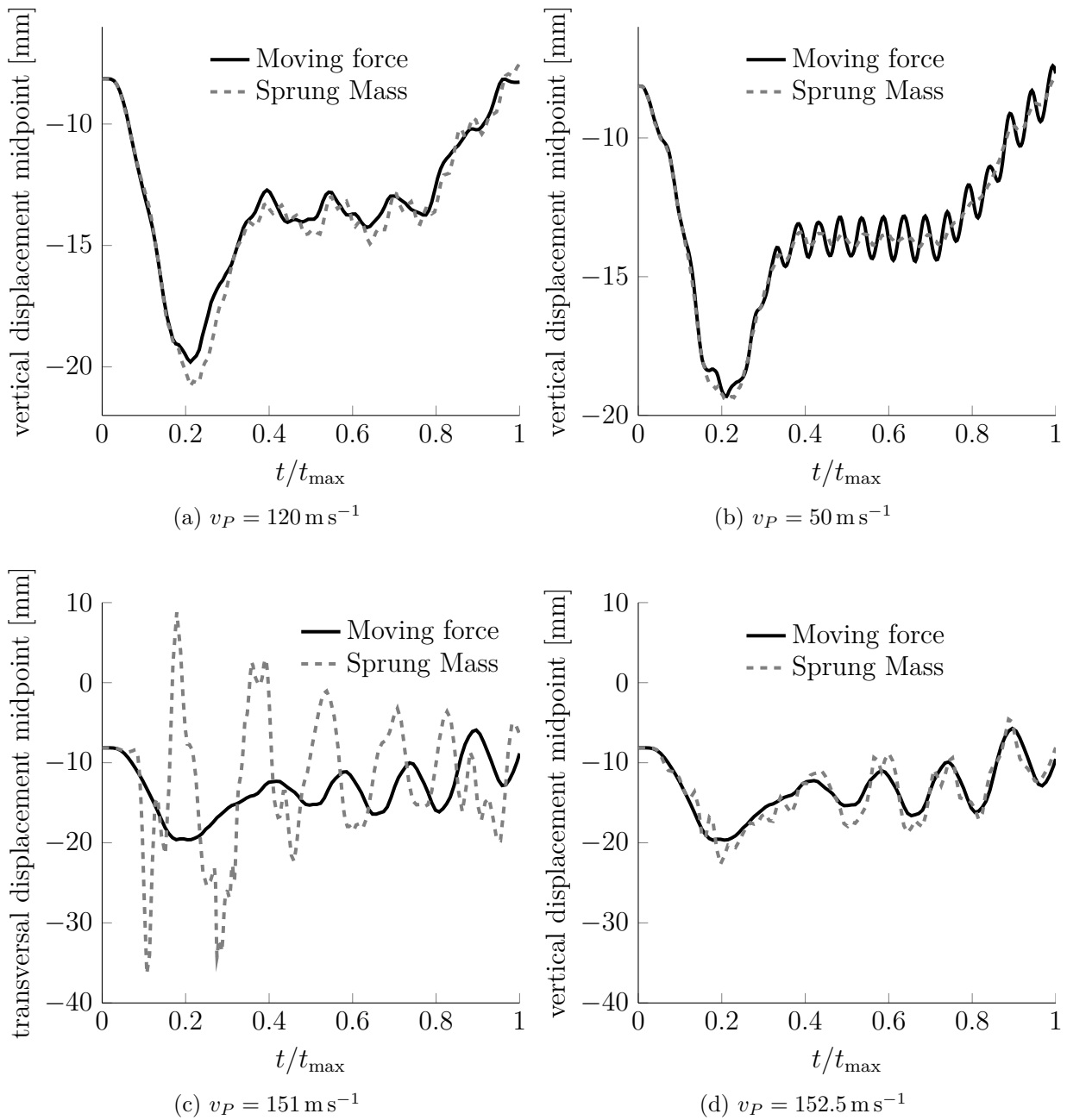
Figure 5.29: The figure shows the vertical displacement of the bridge at the midpoint for the sprung mass and the moving force model. The figure shows that the response in the vertical direction is largely the same for the two load models, but at resonance velocities the reponse is different.

resonance velocity of $151\,\mathrm{m\,s^{-1}}$. The figure shows that the response for the sprung mass model is very different from the response obtained by the moving load model. This was expected because at this velocity the inertia effects are expected to be significant such that the effective loading of the two load models are significantly different. It should be noted that the obtained response for the sprung mass model in figure 5.29c is probably not the actual response of the train at this velocity. It is possible that the contact

algorithm is running into problems due to the violent nature of resonance at this velocity. In figure 5.29d the response of the two different systems are again similar, but here the response of the sprung mass model is slightly higher than the moving force model. A possible explanation is that the added loading from the inertia effects is higher than the dissipated energy from the dashpot.

The horizontal amplification factor is shown in figure 5.28b, the figure shows that predicted amplification are in the same magnitude. The time and frequency domain response shows that the response in the system in the horizontal direction is different for the sprung-mass and the moving force model. In figure 5.30 the time and frequency response for the two load models are compared for the velocity $60 \, \mathrm{m \, s^{-1}}$. Note that at $60 \, \mathrm{m \, s^{-1}}$ the dynamic amplification factor in the horizontal direction shown in figure 5.28b are the same.

(a) Time domain.

(b) Frequency domain.
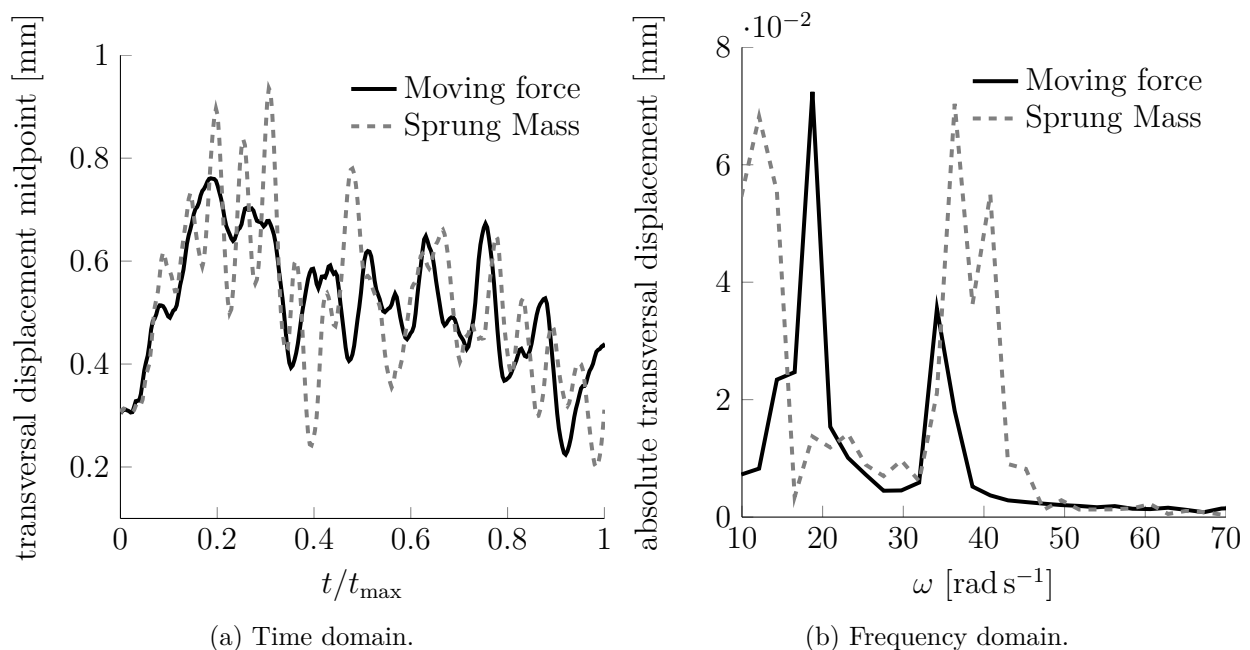
Figure 5.30: The figure shows the horizontal displacement of the bridge at the midpoint with the sprung-mass and the moving force load model for Train 1 at a velocity of $60 \, \mathrm{m \, s^{-1}}$. The figure illustrates that the response in the horizontal direction are different for the two load models.

To explain the reason that the two load models are different in horizontal direction, first recall that the moving load model does not have any load component in the horizontal direction, any horizontal displacement seen for this load model is due un-symmetric components in the structural system, or un-symmetrical loading of the structure in the vertical direction. For the sprung-mass model, there is additional loading in the horizontal direction due to the inertia effects of the mass. The mass in this direction is not sprung, nor damped such that the full mass and inertia effects of the sprung-mass are included in this direction.

It is questionable whether this behavior is actually physical. First of all, the trains in real life are not attached to the rail in the sense that horizontal movement is strictly prohibited. In real trains, the wheel may slide relative to the rail in the horizontal di-

rection. Secondly, real trains may have elastic and dissipative elements in the horizontal direction to allow for better comfort and train-track safety. In the vehicle-interaction models discussed in section 4.4 there are several models which includes elastic and dissipative elements in the horizontal direction of the train. An interesting study would be to compare the response of the bridge obtained with the moving force, sprung mass and such a vehicle interaction model to determine the influence these models have on the horizontal displacement of the bridge. The total displacements in the horizontal direction are still modest, figure 5.30a indicates that the total displacements are below $1\,\text{mm}$, the significance of these displacements will be discussed further in section 5.10.

Regarding the peak accelerations shown in figure 5.28c and figure 5.28d, the magnitude of the peak acceleration in both the vertical and horizontal directions are the same for both load models. It can be seen that the general trend is that the peak accelerations in the vertical direction are larger for the sprung mass model than the moving force model, while in the horizontal direction the accelerations are the same. As mentioned in section 5.8 the peak accelerations are highly volatile and it is difficult to pinpoint the exact reason for this observed behavior. Considerations about the contact algorithm and the sliding direction may provide the answer for this. Without going further into this discussion a deeper analysis of the time and frequency domain response the question is left over to further work.

As a conclusion to this section on the comparison of the sprung-mass model and the moving force model the above discussion have shown that the sprung mass model and the moving force model are largely the same in the vertical direction. In cases where there are resonance effects induced in the bridge, either the sprung mass model underestimates the response in comparison to the moving force model because the energy dissipated exceeds the added loading from inertia effects or the sprung mass model overestimates the response in comparison to the moving force model because the added inertia effects are larger than the dissipated energy. This means that the moving force model may be used to indicate resonance velocities in the vertical direction of the given configuration of the trains, but the response might not be in the correct magnitude. For the horizontal direction, it is found that the displacements are in the same magnitude for the two load models, but that the given response is different for the two load models. The reason for this is most likely due to the fact that the mass is unsprung and undamped in this direction such that the inertia effects in become significant.

5.10 The significance of the dynamic effects on the stresses in the bridge.

This section focuses on the additional stress induced by the dynamic effects in the vertical and the horizontal direction.

5.10.1 Horizontal direction

In section 5.5 and 5.7 it was shown that the maximum dynamic amplification of the bridge in the horizontal direction was found with Train 2 at a velocity of $55\,\mathrm{m\,s^{-1}}$. Figure 5.31a shows that the dynamic amplification in the vertical direction for Train 2 at velocity $55\,\mathrm{m\,s^{-1}}$ is negligible.

(a) Train 2, vertical direction.

(b) Train 2, horizontal direction.
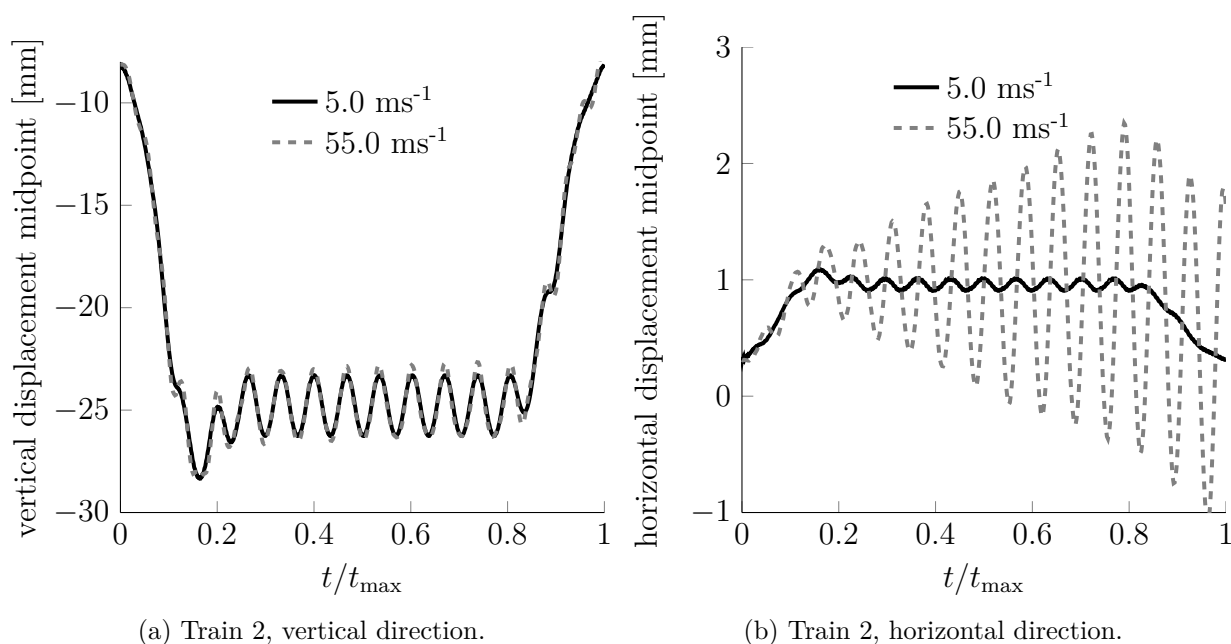
Figure 5.31: The figure shows the vertical and horizontal response of the bridge with Train 2 at a velocity of $55\,\mathrm{m\,s^{-1}}$.

A study of the stresses induced by Train 2 at a velocity of $55\,\mathrm{m\,s^{-1}}$ will therefore isolate the effect of horizontal displacements on the stresses in the bridge. For most of the structure, the stresses remain largely the same for this state. The largest differences in the stresses are found in the structural members furthest away from the neutral plane for bending in the horizontal direction, i.e the vertical plane following the longitudinal direction of the bridge. Figure 5.32a shows the position of the member with the highest difference in stress, and figure 5.32b shows the stresses in the observed structural member for Train 2 at velocity $55\,\mathrm{m\,s^{-1}}$ and at the quasi static velocity $5\,\mathrm{m\,s^{-1}}$ for comparison.

The figure shows that the difference in stress is barely noticeable, even in the member with the highest difference in stress and even in the configuration where the deformation of the bridge is at its maximum in this direction. The reason for this is that the actual deformation in the horizontal direction is only $\approx 2.5\,\mathrm{mm}$, and the amplitude of the fluctuation is merely $1.5\,\mathrm{mm}$. Comparing this to the total span of the bridge, $52\,\mathrm{m}$ it is

(a) Observed structural member.

(b) Stress history of observed member.
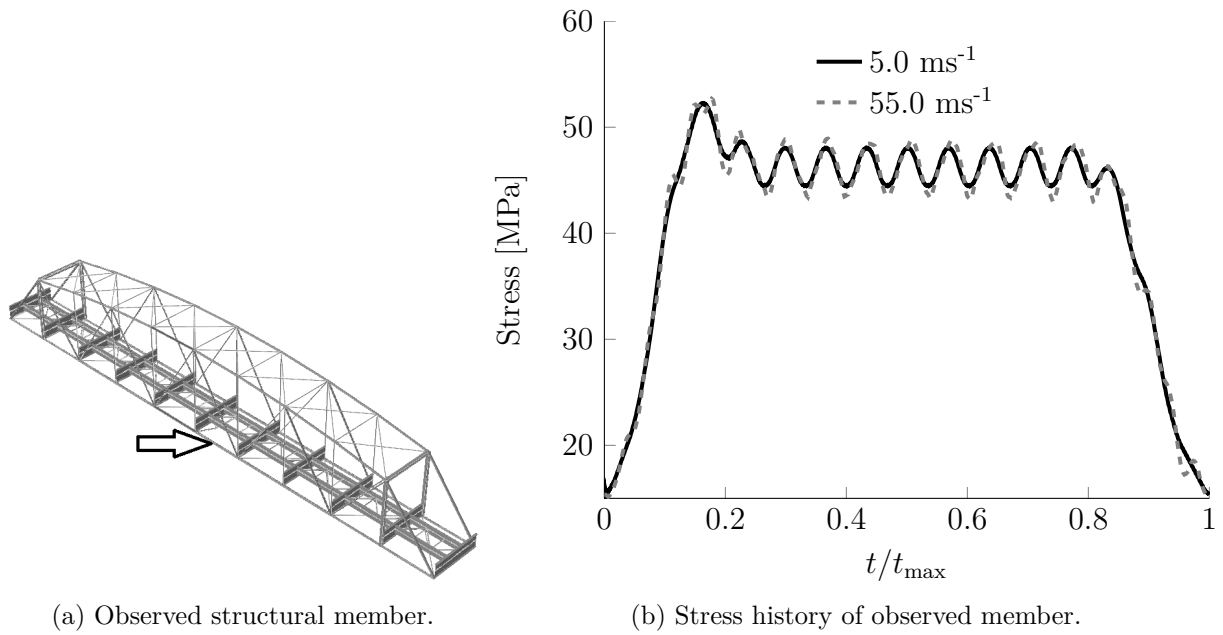
Figure 5.32: The figure shows the stress history in the observed member for Train 2 at velocities 5 and $55\,\mathrm{m\,s^{-1}}$.

actually quite obvious that the added dynamic effect is negligible. Even if Train 2 was considerable longer than it actually is it is difficult to imagine that the displacements in the horizontal direction alone might cause significant increase in stress fluctuations. In light of the discussion regarding the sprung-mass model in section 5.9, it is appropriate to ask the question if the use of the moving force model is the reason that the horizontal displacements are rather small. The discussion on the sprung mass model showed that the response of the structure was not the same in the horizontal direction for the two load models, but the discussion also showed that the magnitude of the displacements where largely the same. Again, it may be appropriate to consider a more sophisticated model to ensure that the displacements in the horizontal direction is properly represented.

5.10.2 Vertical direction

In section 5.5 and 5.7 it was shown that the maximum dynamic amplification of the bridge in the vertical direction was found with Train 2 at a velocity of $102.5\,\mathrm{m\,s^{-1}}$. The same sections also showed that the horizontal dynamic amplification at this velocity was large due to the fact that the torsional mode was excited at this velocity by Train 2. This means that the bridge is in a state of resonance in several of the modes which implies that the stresses and the fluctuation of the stresses in the bridge are large. Stress history plots of the structural members all over the structure confirms this, two examples are given in figure 5.33.

(a) Vertical hanger.

(b) Stress history of vertical hanger.


(c) Cross girder.

(d) Stress history of cross girder.
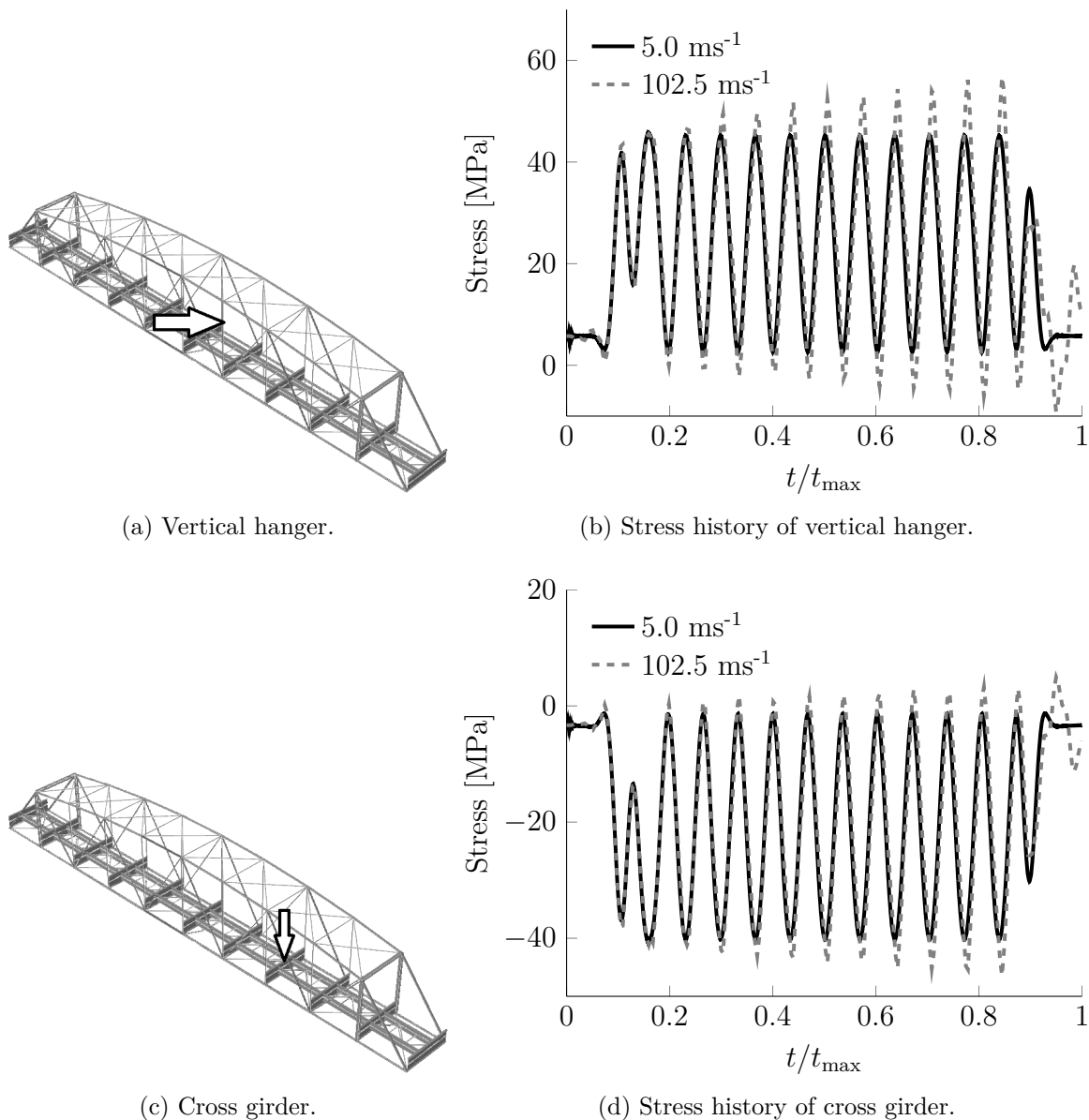
Figure 5.33: The figure shows the stress history in the observed member for Train 2 at velocities 5 and $102.5\,\mathrm{m\,s^{-1}}$. Note that the stresses in the cross girder, figure 5.33d, are taken from the upper flange and contains the bending and normal stresses.

The results in figure 5.33 show that the stresses for both the vertical hanger 5.33a in

the primary carrying system and the cross-girder in the secondary carrying system are increasing throughout the history. It should be pointed out that this is the general trend for nearly all structural members in this state, and is to be expected when the structure is in resonance. Without going into further details it seems obvious that this state should be avoided in design and operation of the structure.

In section 5.5 and 5.7 it was shown that the bridge had more moderate dynamic effects where the response showed dynamic effects, but was bound either by cancellation or that the series of loads was not long enough. Train 1 showed this characteristic at velocities $14 \, \mathrm{m \, s^{-1}}$ and $30 \, \mathrm{m \, s^{-1}}$. Considering the stress history of the structure at $30 \, \mathrm{m \, s^{-1}}$, most of the members in the structure are not affected by the dynamic amplification. In figure 5.34 the stress history of one of the most affected members is shown.

(a) Observed structural member.

(b) Stress history of observed member.
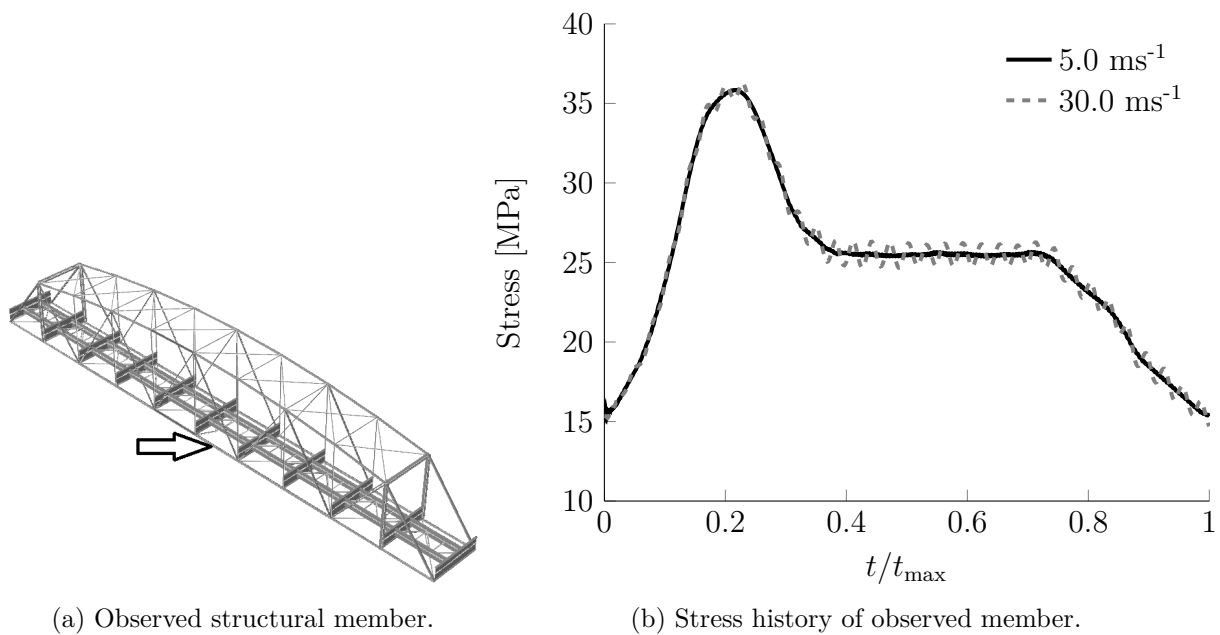
Figure 5.34: The figure shows the stress history in the observed member for Train 1 at velocities 5 and $30 \, \mathrm{m \, s^{-1}}$.

The resulting stress fluctuation in the observed member is about $\Delta \sigma \approx 2 \, \mathrm{MPa}$. The given stress range will obviously increase when the effective area of the member is taken into account, or when a specific detail on the member introduce stress singularities. For the full area of the given member, this stress fluctuation seems to be negligible, and well within margin of error. Taking into account the fact that the sprung mass model damps out these lower dynamic effects in the vertical direction also indicate that these low velocity dynamic effects may be negligible.

Chapter 6

Concluding remarks and further work

The main topics of this thesis have been classical viscous damping models, the quadratic eigenvalue problem, load models and resonance phenomena associated with the moving load problem.

From the study of viscous damping models, it was found that there is great uncertainty related to damping in dynamic systems. Furthermore it was found that the main difference between the different classical viscous damping models was the level of control over the damping ratios and the computational efficiency of the damping model. Rayleigh damping provided lower control, but better computational efficiency than the direct damping model and Caughey damping model. The direct damping model provided the highest level of control, but lower computational efficiency than the two other models due to the topology of the resulting damping matrix.

It was shown that the quadratic eigenvalue problem could be used to determine the response of a classically and non-classically damped dynamic system and to determine the effective modal damping ratios and resonance frequencies of damped multi degree of freedom systems. It was also discussed that the quadratic eigenvalue problem could be used to establish a non-classical damping matrix from experimental data.

From the study on the moving load problem it was found that the difference between the moving force model, the moving mass model and the sprung mass model was the level of inertia effects included by the different load models and the energy dissipated by the load model. The limiting cases of the sprung mass model was found to be the moving force and moving mass model. Furthermore the study on the moving load problem showed that there are two different types of resonance. The first type is associated with the velocity of a single moving load, while the second type is associated with the repeated loading from a series of moving loads.

In the case study of the Tallerås railway bridge, the main points were:

- Resonance in the Tallerås railway bridge was due to the repeated loading from the railway axles. Resonance from velocity alone was found to be unlikely due to very high predicted velocities needed for this type of resonance in the Tallerås railway bridge.

- The displacements in the horizontal direction of the bridge proved to be small for the moving force model, even under resonance conditions. The stresses from these

101

displacements did not seem to be significant.

- The study showed that it is important to include the mass of the track in the simulations, the track contributed significantly to the total mass of the structure. The result was that the natural frequencies of the complete structure was significantly different from the bridge alone.

- The Visco-Elastic track utilized in the case study did not change the response of the structure significantly compared to the simplified track. For ballastless tracks on railway bridges where the stiffness of the track is relatively high, like the track utilized in this case study, the effect of including a visco-elastic track is negligible.

- Simulations with the sprung-mass load model indicated that the response in the vertical direction of the bridge was similar to the response obtained by the moving force model. The response in the horizontal direction for the sprung mass model was different from the response obtained by the moving force model in the horizontal direction because the unsprung mass in this direction added load effects and change the effective structure during the passing.

6.1 Further work

Through the work in this thesis the following topics might be interesting for further work.

- The horizontal displacements of the Tallerås railway bridge was found to be different for the moving force model and the sprung mass model due to the unsprung and undamped mass in this direction and the rigidity of the contact formulation in this direction. A literature study on the contact rigidity and structural elements in the train in this direction is warranted and a numerical study involving a more sophisticated vehicle interaction model may be interesting.

- A deeper analysis of the possible significance of the stress fluctuations at lower velocities in regards to fatigue.

- The peak accelerations of the sprung mass model was found to be generally higher in the vertical direction than the peak accelerations obtained by the moving force model. A study of the time domain and frequency domain characteristics of these accelerations may reveal the reason.

- A study of the visco-elastic track in combination with the sprung-mass model to see the effect of this combination on the response of the bridge.

- The moving force model was far more computationally efficient than the sprung mass model. An investigation of other ways to implement the contact relation, might yield a more efficient solution for the sprung mass model.

Bibliography

[1] Joakim Wallin, John Leander, and Raid Karoumi. Strengthening of a steel railway bridge and its impact on the dynamic response to passing trains. *Engineering Structures*, 33(2):635 – 646, 2011. ISSN 0141-0296. doi: http://dx.doi.org/10.1016/j.engstruct.2010.11.022. URL http://www.sciencedirect.com/science/article/pii/S0141029610004426.

[2] Anil K Chopra. *Dynamics of structures: theory and applications to earthquake engineering*. Pearson Prentice Hall, Upper Saddle River, N.J, 2007.

[3] Robert D. Cook, David S. Malkus, Michael E. Plesha, and Robert J. Witt. *Concepts and applications of finite element analysis*. Wiley, New York, 2002.

[4] Ladislav Frýba. *Dynamics of railway bridges*. Thomas Telford, London, 1996.

[5] Roy R Craig and Andrew J Kurdila. *Fundamentals of structural dynamics*. Wiley, Hoboken, N.J, 2006.

[6] Odd S. Hopperstad and Tore Børvik. Lecture Notes, Material Mechanics Part 1. Norwegian University of Science and Technology, January 2013.

[7] Jacob Lubliner. *Plasticity Theory*. Dover books on engineering. Dover Publications, 2008. ISBN 9780486462905. URL http://www.scribd.com/doc/21551320/Plasticity-Theory-Jacob-Lubliner.

[8] Leonard Meirovitch. *Computational methods in structural dynamics*. Sijthoff & Noordhoff, Alphen aan den Rijn, 1980.

[9] Jagmohan L Humar. *Dynamics of structures*. CRC Press, Boca Raton, 2012.

[10] John William Strutt Rayleigh. *Theory of Sound*, volume 1. Dover, New York, 2nd republication edition, 1945. URL http://app.knovel.com/hotlink/toc/id:kpTSVERE04/theory-sound-volume-1.

[11] Ray W Clough and Joseph Penzien. *Dynamics of structures*. McGraw-Hill, New York, 1993.

[12] Dassault Systèmes. *Abaqus 6.12 User's Manual*. Dassault Systèmes, February 2012.

[13] Kolbein Bell. *Matrisestatikk: statiske beregninger av rammekonstruksjoner*. Tapir akademisk forl., Trondheim, 2011.

[14] Gerard Lallement and Daniel J Inman. A tutorial on complex eigenvalues. In *PROCEEDINGS-SPIE THE INTERNATIONAL SOCIETY FOR OPTICAL ENGINEERING*, pages 490–490. SPIE INTERNATIONAL SOCIETY FOR OPTICAL, 1995.

[15] Jia-Jang Wu, A.R Whittaker, and M.P Cartmell. The use of finite element techniques for calculating the dynamic response of structures to moving loads. *Computers & Structures*, 78(6):789 – 799, 2000. ISSN 0045-7949. doi: http://dx.doi.org/10.1016/S0045-7949(00)00055-9. URL `http://www.sciencedirect.com/science/article/pii/S0045794900000559`.

[16] Atef F. Saleeb and Abhimanyu Kumar. Automated finite element analysis of complex dynamics of primary system traversed by oscillatory subsystem. *International Journal for Computational Methods in Engineering Science and Mechanics*, 12(4):184–202, 2011. ISSN 1550-2287.

[17] Michal Majka and Michael Hartnett. Effects of speed, load and damping on the dynamic response of railway bridges and vehicles. *Computers & Structures*, 86(6):556 – 572, 2008. ISSN 0045-7949. doi: http://dx.doi.org/10.1016/j.compstruc.2007.05.002. URL `http://www.sciencedirect.com/science/article/pii/S0045794907001599`. Civil-Comp Special Issue.

[18] Simon Iwnick. Manchester benchmarks for rail vehicle simulation. *Vehicle System Dynamics*, 30(3-4):295–313, 1998. doi: 10.1080/00423119808969454. URL `http://dx.doi.org/10.1080/00423119808969454`.

[19] Jong-Dar Yau, Yeong-Bin Yang, and Shyh-Rong Kuo. Impact response of high speed rail bridges and riding comfort of rail cars. *Engineering Structures*, 21(9):836 – 844, 1999. ISSN 0141-0296. doi: http://dx.doi.org/10.1016/S0141-0296(98)00037-6. URL `http://www.sciencedirect.com/science/article/pii/S0141029698000376`.

[20] K. Liu, G. De Roeck, and G. Lombaert. The effect of dynamic train-bridge interaction on the bridge response during a train passage. *Journal of Sound and Vibration*, 325 (1-2):240–251, August 2009. ISSN 0022-460X. URL `http://www.sciencedirect.com/science/article/pii/S0022460X09002521`.

[21] M Majka and M Hartnett. Dynamic response of bridges to moving trains: A study on effects of random track irregularities and bridge skewness. *COMPUTERS & STRUCTURES*, 87(19-20):1233–1252, 2009. ISSN 0045-7949.

[22] H. Xia, G. De Roeck, H.R. Zhang, and N. Zhang. Dynamic analysis of train–bridge system and its application in steel girder reinforcement. *Computers & Structures*, 79(20–21):1851 – 1860, 2001. ISSN 0045-7949. doi: http://dx.doi.org/10.1016/S0045-7949(01)00115-8. URL `http://www.sciencedirect.com/science/article/pii/S0045794901001158`.

[23] He Xia and Nan Zhang. Dynamic analysis of railway bridge under high-speed trains. *Computers & Structures*, 83(23–24):1891 – 1901, 2005. ISSN 0045-7949. doi: http://dx.doi.org/10.1016/j.compstruc.2005.02.014. URL `http://www.sciencedirect.com/science/article/pii/S0045794905001173`.

[24] Wanming Zhai, Shaolin Wang, Nan Zhang, Mangmang Gao, He Xia, Chengbiao Cai, and Chunfa Zhao. High-speed train–track–bridge dynamic interactions – part II: experimental validation and engineering application. *International Journal of Rail Transportation*, 1(1-2):25–41, 2013. doi: 10.1080/23248378.2013.791497. URL `http://dx.doi.org/10.1080/23248378.2013.791497`.

[25] B Biondi, G Muscolino, and A Sofi. A substructure approach for the dynamic analysis of train-track-bridge system. *COMPUTERS & STRUCTURES*, 83(28-30):2271–2281, 2005. ISSN 0045-7949.

[26] Ladislav Frýba. A rough assessment of railway bridges for high speed trains. *Engineering Structures*, 23(5):548 – 556, 2001. ISSN 0141-0296. doi: http://dx.doi.org/10.1016/S0141-0296(00)00057-2. URL `http://www.sciencedirect.com/science/article/pii/S0141029600000572`.

[27] Y.B. Yang, J.D. Yau, and Y.S. Wu. *Vehicle-bridge interaction dynamics: with applications to high-speed railways*. United Kingdom: World Scientific Pub Co Pte, 2004.

[28] Raimundo Delgado. *Dynamics of High-Speed Railway Bridges: Selected and revised papers from the Advanced Course on 'Dynamics of High-Speed Railway Bridges', Porto, Portugal, 20-23 September 2005*. United Kingdom: Taylor & Francis Ltd, 2008.

[29] EN 1991-2:2003 Actions on structures, part 2: Traffic loads on bridges, September 2003.

[30] Dassault Systèmes. *Abaqus 6.12 Theory Manual*. Dassault Systèmes, February 2012.

[31] Jernbaneverket. Jernbaneverkets tekniske regelverk, March 2014. URL `https://trv.jbv.no/wiki/Hovedside`.

[32] C Rigueiro, C Rebelo, and LS da Silva. Influence of ballast models in the dynamic response of railway viaducts. *JOURNAL OF SOUND AND VIBRATION*, 329(15):3030–3040, 2010. ISSN 0022-460X.

[33] JCO Nielsen and J Oscarsson. Simulation of dynamic train-track interaction with state-dependent track properties. *JOURNAL OF SOUND AND VIBRATION*, 275(3-5):515–532, 2004. ISSN 0022-460X.

[34] Per Kr. Larsen. *Konstruksjonsteknikk: laster og bæresystemer*. Tapir akademisk forl., Trondheim, 2008.

[35] Jernbaneverket. Personal correspondence, Åsmund Tøsse. E-mail, kl.13:49, 11 February 2014.

Appendix A

Element matrices for examples 1 and 2.

$$
\boldsymbol{M} = \begin{bmatrix}
278.57 & 0 & 48.21 & -43.53 & 0 & 0 & 0 & 0 \\
0 & 100.45 & 43.53 & -37.67 & 0 & 0 & 0 & 0 \\
48.21 & 43.53 & 278.57 & 0 & 48.21 & -43.53 & 0 & 0 \\
-43.53 & -37.67 & 0 & 100.45 & 43.53 & -37.67 & 0 & 0 \\
0 & 0 & 48.21 & 43.53 & 278.57 & 0 & 48.21 & -43.53 \\
0 & 0 & -43.53 & -37.67 & 0 & 100.45 & 43.53 & -37.67 \\
0 & 0 & 0 & 0 & 48.21 & 43.53 & 139.29 & -73.66 \\
0 & 0 & 0 & 0 & -43.53 & -37.67 & -73.66 & 50.22
\end{bmatrix}
$$

$$
\boldsymbol{K} = 10^3 \begin{bmatrix}
758.52 & 0 & -379.26 & 711.11 & 0 & 0 & 0 & 0 \\
0 & 3555.56 & -711.11 & 888.89 & 0 & 0 & 0 & 0 \\
-379.26 & -711.11 & 758.52 & 0 & -379.26 & 711.11 & 0 & 0 \\
711.11 & 888.89 & 0 & 3555.56 & -711.11 & 888.89 & 0 & 0 \\
0 & 0 & -379.26 & -711.11 & 758.52 & 0 & -379.26 & 711.11 \\
0 & 0 & 711.11 & 888.89 & 0 & 3555.56 & -711.11 & 888.89 \\
0 & 0 & 0 & 0 & -379.26 & -711.11 & 379.26 & -711.11 \\
0 & 0 & 0 & 0 & 711.11 & 888.89 & -711.11 & 1777.78
\end{bmatrix}
$$

$$
\boldsymbol{C}_{\mathrm{Dir}} = \begin{bmatrix}
1184.92 & -186.77 & -366.82 & 142.01 & 7.19 & -2.48 & 11.63 & -7.85 \\
-186.77 & 1688.56 & -169.92 & -139.23 & 3.96 & -7.79 & 6.72 & -6.01 \\
-366.82 & -169.92 & 863.54 & -12.20 & -412.74 & 172.70 & 35.59 & -20.33 \\
142.01 & -139.23 & -12.20 & 1484.00 & -177.03 & -148.79 & 18.78 & -16.58 \\
7.19 & 3.96 & -412.74 & -177.03 & 722.18 & -65.71 & -286.15 & 216.62 \\
-2.48 & -7.79 & 172.70 & -148.79 & -65.71 & 1398.17 & -117.29 & -56.63 \\
11.63 & 6.72 & 35.59 & 18.78 & -286.15 & -117.29 & 234.88 & -187.51 \\
-7.85 & -6.01 & -20.33 & -16.58 & 216.62 & -56.63 & -187.51 & 424.65
\end{bmatrix}
$$

$$
\boldsymbol{C}_{\mathrm{Ray}} = \begin{bmatrix}
1102.38 & 0 & -514.42 & 973.72 & 0 & 0 & 0 & 0 \\
0 & 4931.00 & -973.72 & 1220.44 & 0 & 0 & 0 & 0 \\
-514.42 & -973.72 & 1102.38 & 0 & -514.42 & 973.72 & 0 & 0 \\
973.72 & 1220.44 & 0 & 4931.00 & -973.72 & 1220.44 & 0 & 0 \\
0 & 0 & -514.42 & -973.72 & 1102.38 & 0 & -514.42 & 973.72 \\
0 & 0 & 973.72 & 1220.44 & 0 & 4931.00 & -973.72 & 1220.44 \\
0 & 0 & 0 & 0 & -514.42 & -973.72 & 551.19 & -996.71 \\
0 & 0 & 0 & 0 & 973.72 & 1220.44 & -996.71 & 2465.50
\end{bmatrix}
$$

Appendix B

Scripts for examples

B.1 Function ModalSolutionLinEig

```
function u=ModalSolutionLinEig(M,C,K,P0,W,t,u0,dotu0)

%Establishing the matrices and vectors
[Q,S]=eig(K,M);
%Normalizing the eigenvectors Q.'*M*Q=I
for n=1:length(Q(1,:))
    Q(:,n)=Q(:,n)/sqrt(Q(:,n).'*M*Q(:,n));
end

wn=sqrt(diag(S));
Pt0=Q.'*P0;
Xi=Q.'*C*Q; %only diagonal elements are interesting
for n=1:length(Xi(:,1))
    Xi(n,n)=Xi(n,n)/(2*wn(n));
end

y0=Q.'*M*u0;
doty0=Q.'*M*dotu0;

y=zeros(length(y0),length(t));
u=y;
for n=1:length(t)
    for m=1:length(y0)
        b=W/wn(m);
        xi=Xi(m,m);
        wdn=wn(m)*sqrt(1-xi^2);
        rho=Pt0(m)/wn(m)^2*1/sqrt((1-b^2)^2+(2*xi*b)^2);
        phi=atan(2*xi*b/(1-b^2));
        if phi<0
            phi=phi+pi;
        end
        A=y0(m)-rho*sin(-phi);
        B=(doty0(m)+xi*wn(m)*y0(m)-W*rho*cos(-phi))/wdn;
        y(m,n)=exp(-xi*wn(m)*t(n))*(A*cos(wdn*t(n))+B*sin(wdn*t(n)))...
```

```
        +rho*sin(W*t(n)-phi);
    end
    u(:,n)=Q*y(:,n);
end
```

B.2   Function ModalSolutionQuadraticEig

```
function [u,dotu]=ModalSolutionQuadraticEig(M,C,K,P0,W,t,u0,dotu0)

%Establishing the matrices and vectors
N=M*0;
A=[N M;M C];
B=[-M N;N K];
R0=[P0*0;P0];
x0=[dotu0;u0];
[Q,~]=eig(B,-A);


%Normalizing the eigenvectors Q.'*A*Q=I
for n=1:length(Q(1,:))
    Q(:,n)=Q(:,n)/sqrt(Q(:,n).'*A*Q(:,n));
end
S=Q.'*B*Q; %spectral matrix
Rt0=Q.'*R0;
y0=Q.'*A*x0;
D=(W^2*eye(length(S))+S*S)\eye(length(S));

x=zeros(length(y0),length(t));
for n=1:length(t)
    x(:,n)=Q*(expm(-S*t(n))*(Q.'*A*x0+W*D*Rt0)...
        +(S*sin(W*t(n))-W*eye(length(S))*cos(W*t(n)))*D*Rt0);
end

Tu=[N eye(length(M(:,1)))];
Tdotu=[eye(length(M(:,1))) N];
u=Tu*x;
dotu=Tdotu*x;
```

B.3   Function NewmarkMethod

```
function u = NewmarkMethod(M,C,K,P,t,u0,dotu0,b,g)
u=zeros(length(u0),length(t));
dotu=u;
ddotu=u;
u(:,1)=u0;
dotu(:,1)=dotu0;
ddotu(:,1)=M\(P(:,1)-C*dotu(:,1)-K*u(:,1));

for n=1:length(t)-1
    dt=t(n+1)-t(n);
```

```
        Keff=1/(b*dt^2)*M+g/(b*dt)*C+K;
        Peff=P(:,n+1)...
            +M*(1/(b*dt^2)*u(:,n)+1/(b*dt)*dotu(:,n)+(1/(2*b)-1)*ddotu(:,n))...
            +C*(g/(b*dt)*u(:,n)+(g/b-1)*dotu(:,n)+dt*(g/(2*b)-1)*ddotu(:,n));
        u(:,n+1)=Keff\Peff;
        ddotu(:,n+1)=1/(b*dt^2)*(u(:,n+1)-u(:,n)-dt*dotu(:,n))...
            -(1/(2*b)-1)*ddotu(:,n);
        dotu(:,n+1)=g/(b*dt)*(u(:,n+1)-u(:,n))-(g/b-1)*dotu(:,n)...
            -dt*(g/(2*b)-1)*ddotu(:,n);
end
```

B.4   Function SimplySupportedBeam

```
function [t,x]=SimplySupportedBeam(P_train,v_train,k_train,c_train,...
    m_train1,m_train2,L,a_section,b_section,N_elements,jobName,loadModel,...
    a0,a1,ExtractPoint,cpus)
%%%File parameters
if strcmp(loadModel,'MF')||strcmp(loadModel,'MS')||strcmp(loadModel,'MM');
else
    fprintf('%s is not a valid load model.\n',loadModel)
    return
end
fidS=fopen(sprintf('%s%s.inp',jobName,loadModel),'w+');
%%%Numerical parameters
t_max=L/v_train;
t_inc=0.01*t_max;
t_min=0.01*t_inc;
dL_elements=L/N_elements;
rail_elements_type='B23';

%%%Material
density_steel=7850;
E_steel=210e9;
poisson_steel=0.33;

%%%Section
I_section=1/12*a_section*b_section^3;
A_section=a_section*b_section;
fprintf('The ratio of the weight of the train to the weigth
 of the bridge is %.4f\n',...
    (m_train1+m_train2)/(density_steel*A_section*L))
fprintf(fidS,'*Heading\n');
fprintf(fidS,'*Preprint,echo=yes,model=yes,history=yes\n');
fprintf(fidS,'**\n**Model definition\n**\n');
fprintf(fidS,'*Part,Name=Bridge\n');
fprintf(fidS,'*Node,nset=nAll\n');
for n=1:N_elements+1
    fprintf(fidS,'%i, %.4f,0.\n',n,dL_elements*(n-1));
end
```

```
fprintf(fidS,'*Nset,nset=LBC\n1\n');
fprintf(fidS,'*Nset,nset=MidPoint\n%i\n',ceil((N_elements+1)/ExtractPoint));
fprintf(fidS,'*Nset,nset=RBC\n%i\n',N_elements+1);
fprintf(fidS,'*Element,elset=elAll,type=%s\n',rail_elements_type);
for n=1:N_elements
    fprintf(fidS,'%i, %i,%i\n',n,n,n+1);
end
fprintf(fidS,'*Elset,elset=MidPoint\n%i\n',ceil(N_elements/2));
fprintf(fidS,'*Beam Section,elset=elAll,material=Steel,section=Rect\n');
fprintf(fidS,'%.4f,%.4f\n',a_section,b_section);
fprintf(fidS,'*Surface,name=SurfRail\nelAll,SPOS\n');

fprintf(fidS,'*End part\n**\n**\n');


fprintf(fidS,'*Part,name=MassSprung\n');
fprintf(fidS,'*Node,nset=nAll\n');
fprintf(fidS,'1, 0.,0.\n');
fprintf(fidS,'2, 0.,1.\n');
fprintf(fidS,'*Nset,nset=nWheel\n1\n');
fprintf(fidS,'*Nset,nset=nWagon\n2\n');
fprintf(fidS,'*Element,type=MASS,elset=elWheel\n1, 1\n');
fprintf(fidS,'*Element,type=MASS,elset=elWagon\n2, 2\n');
fprintf(fidS,'*Element,type=DashpotA,elset=elDashpot\n4, 1,2\n');
fprintf(fidS,'*Element,type=SpringA,elset=elSpring\n3, 1,2\n');
fprintf(fidS,'*Mass,elset=elWheel\n%.4f\n',m_train1);
fprintf(fidS,'*Mass,elset=elWagon\n%.4f\n',m_train2);
fprintf(fidS,'*Dashpot,elset=elDashpot\n\n%.4f\n',c_train);
fprintf(fidS,'*Spring,elset=elSpring\n\n%.4f\n',k_train);
fprintf(fidS,'*Equation\n2\nnWagon,1,-1., nWheel,1,1.\n');
fprintf(fidS,'*Surface,name=SurfWheel,type=node\nnWheel,1.\n');
if strcmp(loadModel,'MM')
    fprintf(fidS,'*Equation\n2\nnWagon,2,-1., nWheel,2,1.\n');
end
fprintf(fidS,'*End Part\n**\n**\n');

fprintf(fidS,'*Material,name=Steel\n');
fprintf(fidS,'*Elastic\n%.4f,%.4f\n',E_steel,poisson_steel);
fprintf(fidS,'*Density\n%.4f\n',density_steel);
fprintf(fidS,'*Damping,alpha=%f,beta=%f\n',a0,a1);

fprintf(fidS,'*Assembly,name=assemblyBridge\n');
fprintf(fidS,'*Instance,name=instanceBridge,part=Bridge\n0.,0.,0.
\n*End Instance\n');
if strcmp(loadModel,'MS')||strcmp(loadModel,'MM');
    fprintf(fidS,'*Instance,name=instanceTrain,part=MassSprung
    \n0.,0.,0.\n*End Instance\n');
end

fprintf(fidS,'*Nset,nset=nXBC\ninstanceBridge.LBC\n');
```

```
fprintf(fidS,'*Nset,nset=nYBC\ninstanceBridge.LBC\ninstanceBridge.RBC\n');
fprintf(fidS,'*End Assembly\n');

if strcmp(loadModel,'MS')||strcmp(loadModel,'MM');
    fprintf(fidS,'*Surface Interaction,name=surfaceInteraction\n1.,\n');
    fprintf(fidS,'*Friction\n0.,\n');
    fprintf(fidS,'*Surface Behavior,no separation\n');
    fprintf(fidS,'*Contact Pair,interaction=surfaceInteraction
    ,type=node to surface\n');
    fprintf(fidS,'assemblyBridge.instanceTrain.SurfWheel,
    assemblyBridge.instanceBridge.SurfRail\n');
end

fprintf(fidS,'*Step,name=ApplyGravity,inc=10000\n');
fprintf(fidS,'*Static\n1,1,1e-3,1\n');
fprintf(fidS,'*Dload\n,GRAV,9.82,0,-1.\n');
fprintf(fidS,'*Boundary,type=displacement\n');
fprintf(fidS,'assemblyBridge.nXBC,1\nassemblyBridge.nYBC,2\n');
if strcmp(loadModel,'MS')||strcmp(loadModel,'MM');
    fprintf(fidS,'assemblyBridge.instanceTrain.nWheel,1\n');
end
fprintf(fidS,'*End Step\n');
fprintf(fidS,'*Step,name=RunTrain,inc=%i\n',ceil(t_max/t_min+1));
fprintf(fidS,'*Dynamic,application=Transient fidelity
\n%.4f,%.4f,%.4f,%.4f\n',...
    t_inc,t_max,t_min,t_inc);
fprintf(fidS,'*Boundary,op=new,type=displacement\n');
fprintf(fidS,'assemblyBridge.nXBC,1\nassemblyBridge.nYBC,2\n');
if strcmp(loadModel,'MS')||strcmp(loadModel,'MM');
    fprintf(fidS,'*Boundary,op=new,type=velocity\n');
    fprintf(fidS,'assemblyBridge.instanceTrain.nWheel, 1,1,%.4f\n',v_train);
else
    for i=1:N_elements+1
    fprintf(fidS,'*Amplitude, name=AmpCLoadNode%s,
     definition=tabular\n',num2str(i));
    tstart=((i-2)*dL_elements)/v_train;
    tmid=((i-1)*dL_elements)/v_train;
    tend=(i*dL_elements)/v_train;
    fprintf(fidS,'%f,0., %f,1., %f,0.\n',tstart,tmid,tend);
    end
    for i=1:N_elements+1
    fprintf(fidS,'*Cload,amplitude=AmpCLoadNode%s\n',num2str(i));
    fprintf(fidS,'%s, 2,
    %f\n',sprintf('assemblyBridge.instanceBridge.%i',i),P_train);
    end
end
fprintf(fidS,'*OUTPUT,HISTORY,TIME INTERVAL=%.4f\n',t_inc);
fprintf(fidS,'*NODE OUTPUT
,NSET=assemblyBridge.instanceBridge.Midpoint\nU2,A2\n');
fprintf(fidS,'*Element OUTPUT
```

```
,ELSET=assemblyBridge.instanceBridge.MidPoint\nSF\n');
fprintf(fidS,'*End Step\n');
[status,cmdout] = system(sprintf('abaqus job=%s%s interactive cpus=%i',...
    jobName,loadModel,cpus),'-echo')
[t,x]=OdbExtract(sprintf('%s%s',jobName,loadModel),...
    'RunTrain','U2',N_elements,ExtractPoint);
fclose('all');
end
```

B.5   Function analyticalSSB

```
function [t,u]=analyticalSSB(x,P_train,v_train,L,EI,m,a0,a1)
t_max=L/v_train;
t_inc=0.001*t_max;
t=linspace(0,t_max,ceil(t_max/t_inc));
u=t*0;
for n=1:30
    wn=(n*pi/L)^2*sqrt(EI/m);
    Wn=n*pi*v_train/L;
    bn=Wn/wn;
    xin=1/2*(a0/wn+a1*wn);
    if xin<1
    wdn=wn*sqrt(1-xin^2);
    u=u+2*P_train*L^3/(n^4*pi^4*EI)*sin(n*pi*x/L)/((1-bn^2)^2+(2*xin*bn)^2)...
        *(2*xin*bn*cos(Wn*t)-(1-bn^2)*sin(Wn*t)+exp(-xin*wn*t)...
        .*(bn*(1-bn^2-2*xin^2)/sqrt(1-xin^2)*sin(wdn*t)-2*xin*bn*cos(wdn*t)));
    else
        fprintf('The damping ratio is larger or equal to 1, mode %i',n)
    end
end
end
```

B.6   Function MultipleLoadsSimplySupportedBeam

```
function [t,x]=MultipleLoadsSimplySupportedBeam(P_train,N_loads,...
    d_loads,v_train,L,a_section,b_section,N_elements,jobName,a0,a1,...
    ExtractPoint,cpus)
%%%File parameters
fidS=fopen(sprintf('%s.inp',jobName),'w+');
%%%Numerical parameters
t_max=L/v_train+(N_loads-1)*d_loads/v_train;
t_inc=0.01;
t_min=0.01*t_inc;
dL_elements=L/N_elements;
rail_elements_type='B23';

%%%Material
density_steel=7850;%%%% OBS
```

```
E_steel=210e9; %%%% OBS
poisson_steel=0.33;

%%%Section
I_section=1/12*a_section*b_section^3;
A_section=a_section*b_section;
fprintf(fidS,'*Heading\n');
fprintf(fidS,'*Preprint,echo=yes,model=yes,history=yes\n');
fprintf(fidS,'**\n**Model definition\n**\n');
fprintf(fidS,'*Part,Name=Bridge\n');
fprintf(fidS,'*Node,nset=nAll\n');
for n=1:N_elements+1
    fprintf(fidS,'%i, %.4f,0.\n',n,dL_elements*(n-1));
end
fprintf(fidS,'*Nset,nset=LBC\n1\n');
fprintf(fidS,'*Nset,nset=MidPoint\n%i\n',ceil((N_elements+1)/ExtractPoint));
fprintf(fidS,'*Nset,nset=RBC\n%i\n',N_elements+1);
fprintf(fidS,'*Element,elset=elAll,type=%s\n',rail_elements_type);
for n=1:N_elements
    fprintf(fidS,'%i, %i,%i\n',n,n,n+1);
end
fprintf(fidS,'*Elset,elset=MidPoint\n%i\n',ceil(N_elements/2));
fprintf(fidS,'*Beam Section,elset=elAll,material=Steel,section=Rect\n');
fprintf(fidS,'%.4f,%.4f\n',a_section,b_section);
fprintf(fidS,'*End part\n**\n**\n');

fprintf(fidS,'*Material,name=Steel\n');
fprintf(fidS,'*Elastic\n%.4f,%.4f\n',E_steel,poisson_steel);
fprintf(fidS,'*Density\n%.4f\n',density_steel);
fprintf(fidS,'*Damping,alpha=%f,beta=%f\n',a0,a1);

fprintf(fidS,'*Assembly,name=assemblyBridge\n');
fprintf(fidS,'*Instance,name=instanceBridge,part=Bridge\n0.,0.,0.
\n*End Instance\n');
fprintf(fidS,'*Nset,nset=nXBC\ninstanceBridge.LBC\n');
fprintf(fidS,'*Nset,nset=nYBC\ninstanceBridge.LBC\ninstanceBridge.RBC\n');
fprintf(fidS,'*End Assembly\n');

fprintf(fidS,'*Step,name=RunTrain,inc=%i\n',ceil(t_max/t_min+1));
fprintf(fidS,'*Dynamic,application=Transient fidelity
\n%.4f,%.4f,%.4f,%.4f\n',...
    t_inc,t_max,t_min,t_inc);
fprintf(fidS,'*Boundary,type=displacement\n');
fprintf(fidS,'assemblyBridge.nXBC,1\nassemblyBridge.nYBC,2\n');
xP0=0:d_loads:(N_loads-1)*d_loads;
xP0=-xP0;
for j=1:N_loads
    for i=2:N_elements
        fprintf(fidS,'*Amplitude, name=AmpNode%iLoad%i\n',i,j);
        tstart=((i-2)*dL_elements-xP0(j))/v_train;
```

```
            tmid=((i-1)*dL_elements-xP0(j))/v_train;
            tend=(i*dL_elements-xP0(j))/v_train;
            fprintf(fidS,'%f,0., %f,1., %f,0.\n',tstart,tmid,tend);
        end
    end
end
for j=1:N_loads
    for i=2:N_elements
        fprintf(fidS,'*Cload,amplitude=AmpNode%iLoad%i\n',i,j);
        fprintf(fidS,'%s, 2, %f\n',...
            sprintf('assemblyBridge.instanceBridge.%i',i),P_train);
    end
end

fprintf(fidS,'*OUTPUT,HISTORY,TIME INTERVAL=%.4f\n',t_inc);
fprintf(fidS,'*NODE OUTPUT
,NSET=assemblyBridge.instanceBridge.Midpoint\nU2,A2\n');
fprintf(fidS,'*OUTPUT,FIELD,TIME INTERVAL=%.4f\n',t_inc);
fprintf(fidS,'*NODE OUTPUT\nUT\n');
fprintf(fidS,'*Element OUTPUT
,ELSET=assemblyBridge.instanceBridge.MidPoint\nSF\n');
fprintf(fidS,'*End Step\n');
status=system(sprintf('abaqus job=%s interactive cpus=%i',...
    jobName,cpus));
[t,x]=OdbExtract(sprintf('%s',jobName),...
    'RunTrain','U2',N_elements,ExtractPoint);
fclose('all');
end
```

B.7   Main script for example 3

```
clear all
close all
clc

set(0,'DefaultAxesColorOrder',[0 0 0;0.5 0.5 0.5]...
    ,'DefaultAxesLineStyleOrder','-|--|:','DefaultLineLineWidth',1.5)

% Cross sectional properties, box profile
b_sec=0.10; %m
h_sec=0.10; %m
I_sec=1/12*b_sec*h_sec^3; %m^4
A_sec=b_sec*h_sec; %m^2;
E_sec=200e9;
density_sec=10000; %kg/m^3
EI=E_sec*I_sec
m_sec=A_sec*density_sec
% Definition elemental matrices
m_el = @(rho,A,L) rho*A*L/420*[156 22*L 54 -13*L;22*L 4*L^2 13*L -3*L^2;...
                              54 13*L 156 -22*L;-13*L -3*L^2 -22*L 4*L^2];
```

```matlab
k_el = @(E,I,L) E*I/L^3*[12 6*L -12 6*L;6*L 4*L^2 -6*L 2*L^2;...
                          -12 -6*L 12 -6*L;6*L 2*L^2 -6*L 4*L^2];
N1 = @(x,L) 1-3*(x/L)^2+2*(x/L)^3;
N2 = @(x,L) L*(x/L)-2*L*(x/L)^2+L*(x/L)^3;
N3 = @(x,L) 3*(x/L)^2-2*(x/L)^3;
N4 = @(x,L) -L*(x/L)^2+L*(x/L)^3;
N_el = @(x,L)[N1(x,L) N2(x,L) N3(x,L) N4(x,L)];

L=15; %length of beam
N=4; %number of elements

%Establishing mass and stiffness matrix at system level
K=zeros(2*(N+1),2*(N+1));
M=K;
k=k_el(E_sec,I_sec,L/N);
m=m_el(density_sec,A_sec,L/N);
for n=1:N
    a=zeros(4,2*(N+1));
    a(1,2*n-1)=1;
    a(2,2*n)=1;
    a(3,2*n+1)=1;
    a(4,2*(n+1))=1;
    K=K+a'*k*a;
    M=M+a'*m*a;
    a_mat{n}=a;
    clearvars a
end
%Imposing boundary conditions
K=K(3:end,3:end);
M=M(3:end,3:end);

%Solving eigenvalueproblem and mass normalizing eigenvectors
[Q,S]=eig(K,M);
for m=1:length(Q);
    Q(:,m)=Q(:,m)/sqrt(Q(:,m)'*M*Q(:,m));
end
wn=diag(sqrt(S));

%Definition Rayleigh damping matrix
a0Rayleigh = @(w1,w2,xi1,xi2) 2*w1*w2*(w1*xi2-w2*xi1)/(w1^2-w2^2);
a1Rayleigh = @(w1,w2,xi1,xi2) 2*(w1*xi1-w2*xi2)/(w1^2-w2^2);
C_Rayleigh = @(M,K,w1,w2,xi1,xi2) 2*w1*w2*(w1*xi2-w2*xi1)/(w1^2-w2^2)*M...
                          +2*(w1*xi1-w2*xi2)/(w1^2-w2^2)*K;
xi_Rayleigh= @(wn,w1,w2,xi1,xi2)
 1/2*(2*w1*w2*(w1*xi2-w2*xi1)/(w1^2-w2^2)./wn...
                          +2*(w1*xi1-w2*xi2)/(w1^2-w2^2).*wn);
%Definition Direct damping matrix
C_Direct = @(M,Q,S,xi0) 2*xi0*M*Q*sqrt(S)*Q'*M;
%Definition Coupled damping matrix
% C_CoupledM=ones(length(K))-eye(length(K));
```

```matlab
C_CoupledM=zeros(length(K));
C_CoupledM(1,2)=1;
C_CoupledM(2,1)=1;
C_Coupled= @(M,Q,xi_c) xi_c*M*Q*C_CoupledM*Q'*M;

%Definition Load vector
P_Load = @(P0,w,t) P0*sin(w.*t);

%Definition frequency response
U_Freq =@(M,C,K,w,P)
 sqrt(real((K-w^2*M+1i*w*C)\P).^2+imag((K-w^2*M+1i*w*C)\P).^2);

%ExampleDefinition
xi0=0.05;
P0=zeros(length(K),1);
P0(end-1)=1000;
W=10;
xi_c=0*7.5;

C{1}=C_Direct(M,Q,S,xi0)+C_Coupled(M,Q,xi_c)

% The time domain simulations.
t=0:0.01:15;
u0=zeros(length(M),1);
dotu0=u0;

P0=P0*1;
ust=K\P0;
P=zeros(length(P0),length(t));
for n=1:length(t)
    P(:,n)=P0*sin(W*t(n));
end
figure
hold all
% u = NewmarkMethod(M,C,K,P,t,u0,dotu0,b,g)
uModal=ModalSolutionLinEig(M,C{1},K,P0,W,t,u0,dotu0);
uNewmark=NewmarkMethod(M,C{1},K,P,t,u0,dotu0,1/4,1/2);
uComplexModal=ModalSolutionQuadraticEig(M,C{1},K,P0,W,t,u0,dotu0);
plot(t(1:15:end),uModal(end-1,1:15:end)/ust(end-1),'-o')
plot(t(1:5:end),uNewmark(end-1,1:5:end)/ust(end-1),'-','Color',[1 1 1]*0.45)
plot(t(1:15:end),uComplexModal(end-1,1:15:end)/ust(end-1)...
    ,'x','Color',[1 1 1]*0.75)

legendentry={'Classic modal analysis','Newmark \beta-method'
,'Complex modal analysis'}
legend(legendentry,'Location','NorthEast')
xlabel('$t$[\SI{}{\second}]','Interpreter','Latex')
ylabel('$w_{\text{tip}}/w_{\text{st}}$','Interpreter','Latex')
legend boxoff
cleanfigure
```

```
matlab2tikz('.\..\..\..\LaTex\Figures\DampedEigExample1.tikz'
,'width','\ftwowidth')
```

B.8   Main script for example 5

```
clear all
close all
clc
fclose('all')

% %%%%%%%%% Inndata %%%%%%%%%%
%Loading
m_train1=500; %mass of the wheel
m_train2=500; %mass of wagon
P_train=-10000

v_train=25;
k_train=3000000;
c_train=20000;

%Geometry
L=25;
a_section=0.2; %width of beam, out of plane
b_section=0.5; %height of beam
Abeam=a_section*b_section;
Ibeam=1/12*a_section*b_section^3;
EIbeam=210e9*Ibeam;
mbeam=Abeam*7850;
Mbeam=mbeam*L;
xi0=0.05

%File parameters
jobName='Beam';

%Numerical parameters
cpus=8;

wn = @(n) (n*pi/L)^2*sqrt(EIbeam/mbeam);
a0 = @(w1,w2,x1,x2) 2*w1*w2*(w1*x2-w2*x1)/(w1^2-w2^2);
a1 = @(w1,w2,x1,x2) 2*(w1*x1-w2*x2)/(w1^2-w2^2);
vpn= @(n) n*pi/L*sqrt(EI/m);


count=0;
N_elementsM=[3 5 10];
for N_elements=N_elementsM;
    count=count+1;
    [tMF{count},u_FEMMF{count}]=SimplySupportedBeam(P_train,v_train,...
        k_train,c_train,m_train1,m_train2,L,a_section,b_section,...
```

```matlab
        N_elements,jobName,'MF',a0(wn(1),wn(2),xi0,xi0),...
        a1(wn(1),wn(2),xi0,xi0),2,cpus);
end
[tanal,u_anal]=analyticalSSB(L/2,-P_train,v_train,L,EIbeam,mbeam,...
    a0(wn(1),wn(2),xi0,xi0),a1(wn(1),wn(2),xi0,xi0));
set(0,'DefaultAxesColorOrder',[0 0 0;0.5 0.5 0.5;0.75 0.75 0.75],...
    'DefaultAxesLineStyleOrder','-|-.|:','DefaultLineLineWidth',1.5);
figure
hold all
for n=1:count
    plot(tMF{n}/tMF{n}(end),(u_FEMMF{n}-u_FEMMF{n}(1))/abs(min(u_anal)));
    legendEntry{n}=sprintf('FEM, %i elements\n',N_elementsM(n));
end
legendEntry{n+1}='analytical';
plot(tanal/tanal(end),u_anal/abs(min(u_anal)),'--');
xlabel('$\frac{t}{t_{max}}$','Interpreter','Latex');
ylabel('$\frac{w(L/2)}{|w_{max}(L/2)|}$','Interpreter','Latex');
legend(legendEntry,'Location','North');
legend boxoff
xlim([0 1]);
ylim([-1 0.2]);
cleanfigure
matlab2tikz('.\..\..\..\LaTex\Figures\VerificationMF.tikz',...
    'width','\fwidth');
```

B.9   Main script for example 6, 7, 8 and 9

```matlab
clear all
close all
clc
fclose('all')


% %%%%%%%%% Inndata %%%%%%%%%%
%Loading
m_train1=1000; %mass of the wheel
m_train2=9000; %mass of wagon
P_train=-(m_train1+m_train2)*9.82;



v_train=25;
k_train=3000000;
c_train=20000;


%Geometry
L=25;
a_section=0.2; %width of beam, out of plane
b_section=0.5; %height of beam
Abeam=a_section*b_section;
```

```
Ibeam=1/12*a_section*b_section^3;
EIbeam=210e9*Ibeam;
mbeam=Abeam*7850;
Mbeam=mbeam*L;
xi0=0.05

%File parameters
jobName='Beam';

%Numerical parameters
cpus=8;
N_elements=30;

wn = @(n) (n*pi/L)^2*sqrt(EIbeam/mbeam);
a0 = @(w1,w2,x1,x2) 2*w1*w2*(w1*x2-w2*x1)/(w1^2-w2^2);
a1 = @(w1,w2,x1,x2) 2*(w1*x1-w2*x2)/(w1^2-w2^2);
vpn= @(n) n*pi/L*sqrt(EIbeam/mbeam);
beta1= @(v) pi*v/(wn(1)*L);

v_trainM=[1];

count=0;
for v_train=v_trainM;
    count=count+1;
    [tMF{count},u_FEMMF{count}]=SimplySupportedBeam(P_train,v_train,...
        k_train,c_train,m_train1,m_train2,L,a_section,b_section,...
        N_elements,jobName,'MF',a0(wn(1),wn(2),xi0,xi0),...
        a1(wn(1),wn(2),xi0,xi0),2,cpus);
    [tMM{count},u_FEMMM{count}]=SimplySupportedBeam(P_train,v_train,...
        k_train,c_train,m_train1,m_train2,L,a_section,b_section,...
        N_elements,jobName,'MM',a0(wn(1),wn(2),xi0,xi0),...
        a1(wn(1),wn(2),xi0,xi0),2,cpus);
end

[tanal,u_anal]=analyticalSSB(L/2,-P_train,v_train,L,EIbeam,mbeam,...
    a0(wn(1),wn(2),xi0,xi0),a1(wn(1),wn(2),xi0,xi0));
set(0,'DefaultAxesColorOrder',[0 0 0;0.4 0.4 0.4;0.75 0.75 0.75],...
    'DefaultAxesLineStyleOrder','-|:|-.','DefaultLineLineWidth',1.5);


figure
hold all
plotstyle={'-',':','-.','--'};
plotcount=0;
for n=1:count
    plotcount=plotcount+1;
    h{plotcount}=plot(tMF{n}/tMF{n}(end),(u_FEMMF{n}-u_FEMMF{n}(1))/...
        abs(min(u_FEMMF{n}-u_FEMMF{n}(1))),plotstyle{n},'Color',[0,0,0]);
    legendEntry{plotcount}=sprintf('Moving force\n');
end
```

119

```
for n=1:count
    plotcount=plotcount+1;
    h{plotcount}=plot(tMM{n}/tMM{n}(end),(u_FEMMM{n}-u_FEMMM{n}(1))/...
        abs(min(u_FEMMF{n}-u_FEMMF{n}(1))),'--','Color',[0.75,0.75,0.75]);
    legendEntry{plotcount}=sprintf('Moving mass\n');
end

xlabel('$t/t_{\max}$','Interpreter','Latex');
ylabel('$w(L/2)/\abs{w_{\max}}$','Interpreter','Latex');
legend(legendEntry,'Location','North');
legend boxoff
xlim([0 1]);
ylim([-1.2 0.2]);
cleanfigure
matlab2tikz('.\..\..\..\LaTex\Figures\ExampleMM.tikz',...
    'width','\fwidth');
```

B.10   Main script for example 10

```
clear all
close all
clc
fclose('all')

% %%%%%%%%% Inndata %%%%%%%%%%
%Loading
m_train1=500; %mass of the wheel
m_train2=9500; %mass of wagon
P_train=-(m_train1+m_train2)*9.82;



v_train=90;
k_train=1e4;
c_train=100;

%Geometry
L=25;
a_section=0.2; %widt of beam, out of plane
b_section=0.5; %height of beam
Abeam=a_section*b_section;
Ibeam=1/12*a_section*b_section^3;
EIbeam=210e9*Ibeam;
mbeam=Abeam*7850;
Mbeam=mbeam*L;
xi0=0.05

%File parameters
jobName='Beam';
```

```
%Numerical parameters
cpus=8;
N_elements=100;

wn = @(n) (n*pi/L)^2*sqrt(EIbeam/mbeam);
a0 = @(w1,w2,x1,x2) 2*w1*w2*(w1*x2-w2*x1)/(w1^2-w2^2);
a1 = @(w1,w2,x1,x2) 2*(w1*x1-w2*x2)/(w1^2-w2^2);
vpn= @(n,m) n*pi/L*sqrt(EIbeam/m);
beta1= @(v) pi*v/(wn(1)*L);


v_trainM=v_train*[1];


count=0;
for v_train=v_trainM;
    count=count+1;
    [tMF{count},u_FEMMF{count},SM1_FEMMF{count}]=SimplySupportedBeam(
    P_train,v_train,k_train,c_train,m_train1,m_train2,L,a_section
    ,b_section,N_elements,jobName,'MF',a0(wn(1),wn(2),xi0,xi0)
    ,a1(wn(1),wn(2),xi0,xi0),2,cpus);
    [tMM{count},u_FEMMM{count},SM1_FEMMM{count}]=SimplySupportedBeam(
    P_train,v_train,k_train,c_train,m_train1,m_train2,L,a_section
    ,b_section,N_elements,jobName,'MM',a0(wn(1),wn(2),xi0,xi0)
    ,a1(wn(1),wn(2),xi0,xi0),2,cpus);
    [tSM{count},u_FEMSM{count},SM1_FEMSM{count}]=SimplySupportedBeam(
    P_train,v_train,k_train,c_train,m_train1,m_train2,L,a_section
    ,b_section,N_elements,jobName,'MS',a0(wn(1),wn(2),xi0,xi0)
    ,a1(wn(1),wn(2),xi0,xi0),2,cpus);
    [tSM2{count},u_FEMSM2{count},SM1_FEMSM2{count}]=SimplySupportedBeam(
    P_train,v_train,1e9,1e5,m_train1,m_train2,L,a_section
    ,b_section,N_elements,jobName,'MS',a0(wn(1),wn(2),xi0,xi0)
    ,a1(wn(1),wn(2),xi0,xi0),2,cpus);
end

[tanal,u_anal]=analyticalSSB(L/2,-P_train,v_train,L,EIbeam,mbeam,...
    a0(wn(1),wn(2),xi0,xi0),a1(wn(1),wn(2),xi0,xi0));
set(0,'DefaultAxesColorOrder',[0 0 0;0.4 0.4 0.4;0.75 0.75 0.75],...
    'DefaultAxesLineStyleOrder','-|:|-.','DefaultLineLineWidth',1.5);



figure
hold all
plotstyle={'-',':','-.','--','-','-.'};
plotcount=0;
for n=1:count
plotcount=plotcount+1;
h{plotcount}=plot(tMF{n}/tMF{n}(end),(u_FEMMF{n}-u_FEMMF{n}(1))/...
    abs(min(u_FEMMF{n}-u_FEMMF{n}(1))),plotstyle{n},'Color',[0,0,0]);
legendEntry{plotcount}=sprintf('Moving force\n');
end
```

```
for n=1:count
plotcount=plotcount+1;
h{plotcount}=plot(tMM{n}/tMM{n}(end),(u_FEMMM{n}-u_FEMMM{n}(1))/...
    abs(min(u_FEMMF{n}-u_FEMMF{n}(1))),'--','Color',[0.75,0.75,0.75]);
legendEntry{plotcount}=sprintf('Moving mass\n');
end
for n=1:count
plotcount=plotcount+1;
h{plotcount}=plot(tSM{n}(1:5:end)/tSM{n}(end),
(u_FEMSM{n}(1:5:end)-u_FEMSM{n}(1))/abs(min(u_FEMMF{n}-u_FEMMF{n}(1)))
,'o','Color',[0.75,0.75,0.75]);
legendEntry{plotcount}=sprintf('Sprung mass, flexible\n');
end
for n=1:count
    plotcount=plotcount+1;
    h{plotcount}=plot(tSM2{n}(1:5:end)/tSM2{n}(end)
    ,(u_FEMSM2{n}(1:5:end)-u_FEMSM2{n}(1))/...
        abs(min(u_FEMMF{n}-u_FEMMF{n}(1))),'s','Color',[0.,0.,0.]);
    legendEntry{plotcount}=sprintf('Sprung mass, stiff\n');
end
xlabel('$t/t_{\max}$','Interpreter','Latex');
ylabel('$w(L/2)/\abs{w_{\max}}$','Interpreter','Latex');
legend(legendEntry,'Location','West');
% legend(legendEntry,'Position','South');

legend boxoff
xlim([0 1]);
ylim([min((u_FEMMM{1}-u_FEMMM{1}(1)))/abs(min(u_FEMMF{1}-u_FEMMF{1}(1)))
*1.1 0.2]);
cleanfigure
matlab2tikz('.\..\..\..\LaTex\Figures\ExampleSM1.tikz',...
    'width','\fwidth');
```

B.11   Main script for example 11 and 12

```
clear all
close all
clc
fclose('all')

% %%%%%%%%% Inndata %%%%%%%%%
% Loading
P_train=-50000

v_train=10;
N_loads=20;
d_loads=1;
% Geometry
L=25;
```

```
a_section=0.2; %width of beam, out of plane
b_section=0.5; %height of beam
Abeam=a_section*b_section;
Ibeam=1/12*a_section*b_section^3;
EIbeam=210e9*Ibeam;
mbeam=Abeam*7850;
Mbeam=mbeam*L;
xi0=0.00

% File parameters
jobName='Beam';
d_resonance=2*v_train/pi*sqrt(mbeam*L^4/EIbeam)
% Numerical parameters
cpus=8;
N_elements=33;

wn = @(n) (n*pi/L)^2*sqrt(EIbeam/mbeam);
a0 = @(w1,w2,x1,x2) 2*w1*w2*(w1*x2-w2*x1)/(w1^2-w2^2);
a1 = @(w1,w2,x1,x2) 2*(w1*x1-w2*x2)/(w1^2-w2^2);
vpn= @(n) n*pi/L*sqrt(EIbeam/mbeam);
d_resonance2=2*pi*v_train/wn(1);

d_loadsM=[0.1 1:0.5:2.5];
u_FEMMF_MAX=d_loadsM*0;
count=0;
for d_loads=d_loadsM;
    count=count+1;
    fprintf('Run %i of %i\n',count,length(d_loadsM));
    [tMF{count},u_FEMMF{count}]=MultipleLoadsSimplySupportedBeam(...
        P_train,N_loads,d_loads,v_train,L,a_section,b_section,...
        N_elements,jobName,a0(wn(1),wn(2),xi0,xi0),a1(wn(1),wn(2),...
        xi0,xi0),2,cpus);
    u_FEMMF_MAX(count)=max(abs(u_FEMMF{count}));
end
[tanal,u_anal]=analyticalSSB(L/2,-P_train,v_train,L,EIbeam,mbeam,...
    a0(wn(1),wn(2),xi0,xi0),a1(wn(1),wn(2),xi0,xi0));
set(0,'DefaultAxesColorOrder',[0 0 0;0.4 0.4 0.4;0.75 0.75 0.75],...
    'DefaultAxesLineStyleOrder','-|:|-.','DefaultLineLineWidth',1.5);
figure
hold all
for n=1:count
    plot(tMF{n}/tMF{n}(end),(u_FEMMF{n}-u_FEMMF{n}(1))/abs(min(u_anal)));
    legendEntry{n}=sprintf('FEM, d=%.2f\n',d_loadsM(n));
end
legendEntry{n+1}='analytical';
plot(tanal/tanal(end),u_anal/abs(min(u_anal)),'--');
xlabel('$t/t_{\max}$','Interpreter','Latex');
ylabel('$w(L/2)/\abs{w_{\max}}$','Interpreter','Latex');
legend(legendEntry,'Location','North');
legend boxoff
```

```
xlim([0 1]);
% ylim([-1 0.2]);

figure
hold all
plot(d_loadsM,u_FEMMF_MAX)

D=[d_loadsM' u_FEMMF_MAX'];
save('Run5.mat','D');
load Run3.mat
load Run4.mat

C=[A;B;D];
[C(:,1),ind]=sort(C(:,1));
C(:,2)=C(ind,2);

figure
hold all
plot(C(:,1),C(:,2)/C(1,2))
xlabel('$d [m]$','Interpreter','Latex');
ylabel('$\abs{w_{\max}/w_{\max,d=0}}$','Interpreter','Latex');
legend('Response series of moving loads','Location','North');
legend boxoff

cleanfigure
matlab2tikz('.\..\..\..\LaTex\Figures\MultipleLoads.tikz',...
    'width','\fwidth');
```

Appendix C

Tallerås bridge

Figure C.1: The figure shows a picture of the original hand drawings of the bridge.
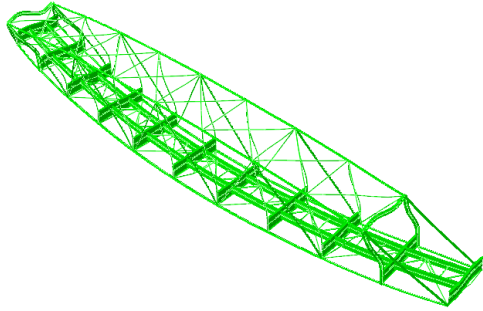
(a) Mode 1, $20.7\,\mathrm{rad\,s^{-1}}$
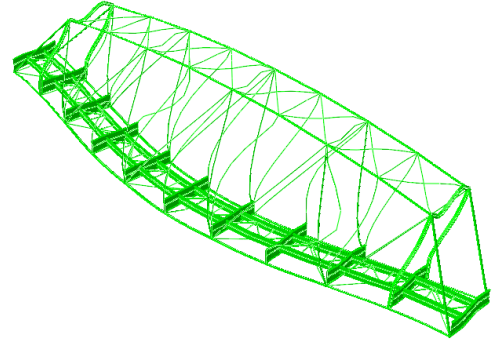
(b) Mode 8, $39.0\,\mathrm{rad\,s^{-1}}$
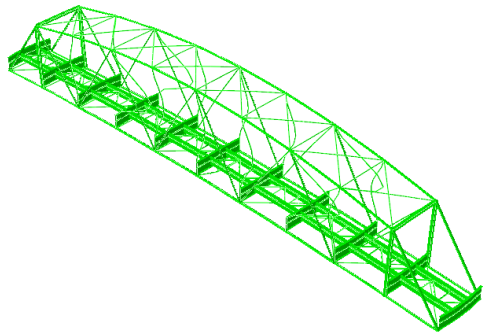
(c) Mode 13, $41.4\,\mathrm{rad\,s^{-1}}$
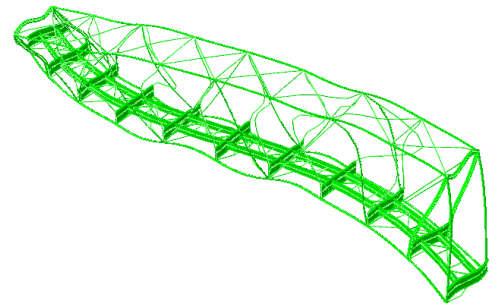
(d) Mode 14, $42.2\,\mathrm{rad\,s^{-1}}$
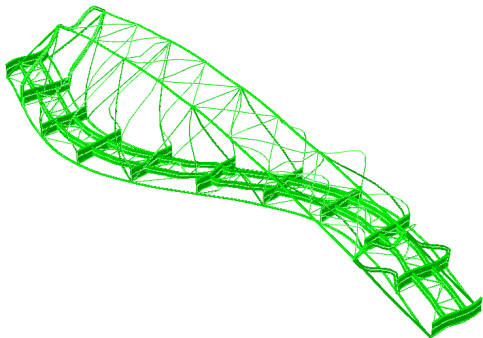
(e) Mode 39, $72.1\,\mathrm{rad\,s^{-1}}$


(f) Mode 40, $77.6\,\mathrm{rad\,s^{-1}}$

Figure C.2: The figure shows the six first significant modes of the bridge.

C.1 Train configuration

C.1.1 Train 1

Axle position [m]	Axle load [kN]
0	225
3.3	225
10	225
13.3	225
17.2	110
19.7	110
36.2	110
38.7	110
43.7	110
46.2	110
62.7	110
65.2	110
70.2	110
72.7	110
89.2	110
91.7	110
96.7	110
99.2	110
115.7	110
118.2	110

C.1.2 Train 2

Axle position [m]	Axle Load [kN]	Axle position [m]	Axle load [kN]
0	225	107.7	225
2.2	225	109.5	225
4.4	225	120.5	225
11.3	225	122.3	225
13.5	225	125.5	225
15.7	225	127.3	225
18.7	225	138.3	225
20.5	225	140.1	225
31.5	225	143.3	225
33.3	225	145.1	225
36.5	225	156.1	225
38.3	225	157.9	225
49.3	225	161.1	225
51.1	225	162.9	225
54.3	225	173.9	225
56.1	225	175.7	225
67.1	225	178.9	225
68.9	225	180.7	225
72.1	225	191.7	225
73.9	225	193.5	225
84.9	225	196.7	225
86.7	225	198.5	225
89.9	225	209.5	225
91.7	225	211.3	225
102.7	225		
104.5	225		

C.2   Main script for moving force model

```
clear all
close all
clc

%Inndata
kpad=500e6;
cpad=200e3;
msleep=230/2;
ksleep=538e6;
csleep=120e3;
mbal=412;
kbal=1000e6;
cbal=50e3;

UIC60_A=60.21/7850; %m^2
UIC60_I11=3038.30e-8; %m^4
UIC60_I12=0; %m^4
UIC60_I22=512.30e-8; %m^4
UIC60_J=UIC60_I11+UIC60_I22;

LB=52;

CC_sleepers=0.6;
CC_rail=1.435;

v_TrainM=[5 20:2.5:140]
for TrainN=1:2
    for SpeedN=1:length(v_TrainM)
jobName=sprintf('Train%iSpeed%.0f',TrainN,v_TrainM(SpeedN)*10);
partFilename='BridgeTalleraasRefined.mypart';
fidPart=fopen(partFilename,'r+');
fid=fopen(sprintf('%s.inp',jobName),'w+');
TrainM=load(sprintf('Train%i.txt',TrainN));
LT=TrainM(end,1);
v_Train=v_TrainM(SpeedN);
% %%%%%%%%%%%%%%%%%%%%%%%%%%%%%%%%% Parts %%%%%%%%%%%%%%%%%%%%%%%%%%%%%%%%%%
% Generating the rails
generatePartTrack(fid,'LeftRail','Left',LB,LT,CC_sleepers,CC_rail,kpad,ksleep,...
    kbal,cpad,csleep,cbal,msleep,mbal,1)
generatePartTrack(fid,'RightRail','Right',LB,LT,CC_sleepers,CC_rail,kpad,ksleep,...
    kbal,cpad,csleep,cbal,msleep,mbal,1)

% Importing the bridge.
tline=fgets(fidPart);
while ischar(tline)
    fprintf(fid,tline);
    tline=fgets(fidPart);
end
```

```
%Assembly
fprintf(fid,'*Assembly,name=AssemblyBridge\n');

fprintf(fid,'*Instance,name=leftRail,part=LeftRail\n');
fprintf(fid,'0, 0., %f\n',-CC_rail/2);
fprintf(fid,'*End instance\n');

fprintf(fid,'*Instance,name=rightRail,part=RightRail\n');
fprintf(fid,'0, 0., %f\n',CC_rail/2);
fprintf(fid,'*End instance\n');

fprintf(fid,'*Instance,name=Bridge,part=Bridge\n');
fprintf(fid,'0,%f,%f,\n',-(0.77+0.721),-2.5);
fprintf(fid,'*End instance\n');

fprintf(fid,'*Nset,nset=BC1\nBridge.BC1,leftRail.BC1,rightRail.BC1\n');
fprintf(fid,'*Nset,nset=BC2\nBridge.BC2\n');
fprintf(fid,'*Nset,nset=BC3\nBridge.BC3\n');
fprintf(fid,'*Nset,nset=BC4\nleftRail.BC4,rightRail.BC4\n');
fprintf(fid,'*Nset,nset=BCFixed\nleftRail.BCFixed,rightRail.BCFixed\n');

fprintf(fid,'*Tie,position tolerance=%f,adjust=no
,name=RailToBridgeTie,type=node to surface,no thickness\n',0.01);
fprintf(fid,'leftRail.TrackBridgeInterface,Bridge.LongGirders\n');
fprintf(fid,'rightRail.TrackBridgeInterface,Bridge.LongGirders\n');
fprintf(fid,'*End assembly\n');

fprintf(fid,'*Step,name=ApplyGravity,inc=10000\n');
fprintf(fid,'*Static\n');
fprintf(fid,'%f, %f, %f, %f\n',1,30,1e-5,30);
fprintf(fid,'*Dload\n');
fprintf(fid,',GRAV,9.82,0,-1,0\n');
fprintf(fid,'*Boundary,type=displacement\n');
fprintf(fid,'AssemblyBridge.BCFixed,Encastre\n');
fprintf(fid,'AssemblyBridge.BC1,1\n');
fprintf(fid,'AssemblyBridge.BC2,2\n');
fprintf(fid,'AssemblyBridge.BC3,3\n');
fprintf(fid,'AssemblyBridge.BC4,4\n');
fprintf(fid,'*End step\n');

fprintf(fid,'*Step,name=MoveTrain,inc=10000\n');
fprintf(fid,'*Dynamic\n');
fprintf(fid,'%f, %f, %f, %f\n',1e-2,(LT+LB)/v_Train,1e-3,1e-2);
fprintf(fid,'*Output,history,frequency=1\n');
fprintf(fid,'*Node output,nset=AssemblyBridge.Bridge.OutputMidnode\nUT,AT\n')
fprintf(fid,'*Node output
,nset=AssemblyBridge.Bridge.Output3rdPoint\nUT,AT\n')
```

```
fprintf(fid,'*Element output
, elset=AssemblyBridge.Bridge.OutputSpotS\n\nS\n');
fprintf(fid,'*Boundary,op=new,type=displacement\n');
fprintf(fid,'AssemblyBridge.BCFixed,Encastre\n');
fprintf(fid,'AssemblyBridge.BC1,1\n');
fprintf(fid,'AssemblyBridge.BC2,2\n');
fprintf(fid,'AssemblyBridge.BC3,3\n');
fprintf(fid,'AssemblyBridge.BC4,4\n');
x0P=-TrainM(:,1)-0.2;
dL=CC_sleepers;
for n=1:87
    for m=1:length(x0P)
        t1=((n-2)*dL-x0P(m))/v_Train;
        t2=((n-1)*dL-x0P(m))/v_Train;
        t3=(n*dL-x0P(m))/v_Train;
        fprintf(fid,'*Amplitude,name=AmpNode%iAxle%i\n',n,m);
        fprintf(fid,'%.4f,0\n %.4f,1\n %.4f,0\n',t1,t2,t3);
    end
end
for n=1:87
    node=1000+n;
    for m=1:length(x0P)
        fprintf(fid,'*Cload,amplitude=AmpNode%iAxle%i\n',n,m);
        fprintf(fid,'AssemblyBridge.leftRail.%i,2,%.2f\n'
        ,node,-TrainM(m,2)/2*1000);
        fprintf(fid,'AssemblyBridge.rightRail.%i,2,%.2f\n'
        ,node,-TrainM(m,2)/2*1000);
    end
end
fprintf(fid,'*End step\n');

system(sprintf('abaqus job=%s interactive cpus=8',jobName),'-echo');
fclose('all')

    end
end
```

131

C.3 Main script for sprung mass model

```
clear all
close all
clc

% Inndata
kpad=500e6;
cpad=200e3;
msleep=230/2;
ksleep=538e6;
csleep=120e3;
mbal=412;
kbal=1000e6;
cbal=50e3;

UIC60_A=60.21/7850; %m^2
UIC60_I11=3038.30e-8; %m^4
UIC60_I12=0; %m^4
UIC60_I22=512.30e-8; %m^4
UIC60_J=UIC60_I11+UIC60_I22;

LB=52;

CC_sleepers=0.6;
CC_rail=1.435;

v_TrainM=[20:10:140];

for TrainN=1:2
    for SpeedN=1:length(v_TrainM)
        jobName=sprintf('Train%iSpeed%.0f',TrainN,v_TrainM(SpeedN)*10);
        partFilename='BridgeTalleraasRefined.mypart';
        fidPart=fopen(partFilename,'r+');
        fid=fopen(sprintf('%s.inp',jobName),'w+');
        TrainM=load(sprintf('Train%i.txt',TrainN));
        LT=TrainM(end,1);
        v_Train=v_TrainM(SpeedN);

% %%%%%%%%%%%%%%%%%%%%%%%%%%%%%%%%% Parts %%%%%%%%%%%%%%%%%%%%%%%%%%%%%%%%%%
% Generating the rails
generatePartTrack(fid,'LeftRail','Left',LB,LT,CC_sleepers,CC_rail,kpad,ksleep,...
    kbal,cpad,csleep,cbal,msleep,mbal,1)
generatePartTrack(fid,'RightRail','Right',LB,LT,CC_sleepers,CC_rail,kpad,ksleep,...
    kbal,cpad,csleep,cbal,msleep,mbal,1)

% Importing the bridge.
tline=fgets(fidPart);
while ischar(tline)
    fprintf(fid,tline);
```

```
        tline=fgets(fidPart);
end

% Generating the Sprung masses
mWheel=1000;
KSM110=5.55e5;
CSM110=4e4;
KSM225=1.125e6;
CSM225=8e4;
generatePartMS(fid,'SM110',110/2*1000/9.82-mWheel,mWheel,KSM110,CSM110);
generatePartMS(fid,'SM225',225/2*1000/9.82-mWheel,mWheel,KSM225,CSM225);
generatePartSurfMS(fid,'SurfMS');


%Assembly
fprintf(fid,'*Assembly,name=AssemblyBridge\n');
fprintf(fid,'*Instance,name=leftRail,part=LeftRail\n');
fprintf(fid,'0, 0., %f\n',-CC_rail/2);
fprintf(fid,'*End instance\n');

fprintf(fid,'*Instance,name=rightRail,part=RightRail\n');
fprintf(fid,'0, 0., %f\n',CC_rail/2);
fprintf(fid,'*End instance\n');

fprintf(fid,'*Instance,name=Bridge,part=Bridge\n');
fprintf(fid,'0,%f,%f,\n',-(0.77+0.721),-2.5);
fprintf(fid,'*End instance\n');
xposAxle=-(TrainM(:,1)+0.01);
for m=1:length(xposAxle)
    fprintf(fid,'*Instance,name=leftMS%i,part=SM%i\n',m,TrainM(m,2));
    fprintf(fid,'%f, 0., %f\n',xposAxle(m),-CC_rail/2);
    fprintf(fid,'*End instance\n');
    fprintf(fid,'*Instance,name=rightMS%i,part=SM%i\n',m,TrainM(m,2));
    fprintf(fid,'%f, 0., %f\n',xposAxle(m),CC_rail/2);
    fprintf(fid,'*End instance\n');
    fprintf(fid,'*Instance,name=leftSurf%i,part=SurfMS\n',m);
    fprintf(fid,'%f, 0., %f\n',xposAxle(m),-CC_rail/2);
    fprintf(fid,'*End instance\n');
    fprintf(fid,'*Instance,name=rightSurf%i,part=SurfMS\n',m);
    fprintf(fid,'%f, 0., %f\n',xposAxle(m),CC_rail/2);
    fprintf(fid,'*End instance\n');
    fprintf(fid,'*Equation\n');
    for n=1:6
        fprintf(fid,'2\n leftMS%i.connectNode,%i,-1
        , leftSurf%i.connectNode,%i,1\n',m,n,m,n)
        fprintf(fid,'2\n rightMS%i.connectNode,%i,-1
        , rightSurf%i.connectNode,%i,1\n',m,n,m,n)
    end
end
```

```
fprintf(fid,'*Nset,nset=BC1\nBridge.BC1,leftRail.BC1,rightRail.BC1\n');
fprintf(fid,'*Nset,nset=BC2\nBridge.BC2\n');
fprintf(fid,'*Nset,nset=BC3\nBridge.BC3\n');
fprintf(fid,'*Nset,nset=BC4\nleftRail.BC4,rightRail.BC4\n');
fprintf(fid,'*Nset,nset=BCFixed\nleftRail.BCFixed,rightRail.BCFixed\n');
fprintf(fid,'*Nset,nset=BCROT\n');
for n=1:length(TrainM(:,1))
    fprintf(fid,'leftSurf%i.BCROT\n',n);
    fprintf(fid,'rightSurf%i.BCROT\n',n);
end

fprintf(fid,'*Tie,position tolerance=%f,adjust=no,
name=RailToBridgeTie,type=node to surface,no thickness\n',0.01);
fprintf(fid,'leftRail.TrackBridgeInterface,Bridge.LongGirders\n');
fprintf(fid,'rightRail.TrackBridgeInterface,Bridge.LongGirders\n');
fprintf(fid,'*End assembly\n');

%%%Contact pair
fprintf(fid,'*Surface interaction,name=TrainTrackSurfaceInteraction\n1\n');
% fprintf(fid,'*Friction,anisotropic\n0.,1e4\n');
fprintf(fid,'*Friction\n0.,\n');
fprintf(fid,'*Surface behavior,no separation\n');
fprintf(fid,'*Contact pair,type=node to surface
,interaction=TrainTrackSurfaceInteraction\n');
for n=1:length(TrainM(:,1))
    fprintf(fid,'AssemblyBridge.leftRail.RailSurf
    ,assemblyBridge.leftSurf%i.Wheel\n',n);
    fprintf(fid,'AssemblyBridge.rightRail.RailSurf
    ,assemblyBridge.rightSurf%i.Wheel\n',n);
end
%%%End contact pair

fprintf(fid,'*Step,name=ApplyGravity,inc=10000\n');
fprintf(fid,'*Static\n');
fprintf(fid,'%f, %f, %f, %f\n',1,30,1e-5,30);
fprintf(fid,'*Dload\n');
fprintf(fid,',GRAV,9.82,0,-1,0\n');
fprintf(fid,'*Boundary,type=displacement\n');
fprintf(fid,'AssemblyBridge.BCFixed,Encastre\n');
fprintf(fid,'AssemblyBridge.BC1,1\n');
fprintf(fid,'AssemblyBridge.BC2,2\n');
fprintf(fid,'AssemblyBridge.BC3,3\n');
fprintf(fid,'AssemblyBridge.BC4,4\n');
fprintf(fid,'AssemblyBridge.BCROT,1\n');
fprintf(fid,'AssemblyBridge.BCROT,3\n');
fprintf(fid,'AssemblyBridge.BCROT,4\n');
fprintf(fid,'AssemblyBridge.BCROT,5\n');
fprintf(fid,'AssemblyBridge.BCROT,6\n');
fprintf(fid,'*End step\n');
```

```
fprintf(fid,'*Step,name=MoveTrain,inc=10000\n');
fprintf(fid,'*Dynamic\n');
fprintf(fid,'%f, %f, %f, %f\n',1e-2,(LT+LB)/v_Train,1e-5,1e-2);
fprintf(fid,'*Output,history,frequency=1\n');
fprintf(fid,'*Node output
,nset=AssemblyBridge.Bridge.OutputMidnode\nUT,AT\n');
fprintf(fid,'*Node output
,nset=AssemblyBridge.Bridge.Output3rdPoint\nUT,AT\n');
fprintf(fid,'*Element output
, elset=AssemblyBridge.Bridge.OutputSpotS\n\nS\n');
fprintf(fid,'*Boundary,op=new,type=displacement\n');
fprintf(fid,'AssemblyBridge.BCFixed,Encastre\n');
fprintf(fid,'AssemblyBridge.BC1,1\n');
fprintf(fid,'AssemblyBridge.BC2,2\n');
fprintf(fid,'AssemblyBridge.BC3,3\n');
fprintf(fid,'AssemblyBridge.BC4,4\n');
fprintf(fid,'AssemblyBridge.BCROT,4\n');
fprintf(fid,'AssemblyBridge.BCROT,5\n');
fprintf(fid,'AssemblyBridge.BCROT,6\n');
fprintf(fid,'*Boundary,op=new,type=velocity\n');
fprintf(fid,'AssemblyBridge.BCROT,1,1,%f\n',v_Train);
fprintf(fid,'*End step\n');

system(sprintf('abaqus job=%s interactive cpus=8',jobName),'-echo');
fclose('all');
    end
end
```

C.4 Function generatePartTrack

```
function generatePartTrack(fid,partName,LeftRight,LB,LT...
,CC_sleepers,CC_rail,kpad,ksleep,...
    kbal,cpad,csleep,cbal,msleep,mbal,Nrail)
% This script generates a part with "partName" in file with fileID "fid"
% "fid" has to be open before script is run.
% LeftRight ~ 'Left'/'Right' whether the rail is the left or right one.
% LB ~ length of bridge
% LT ~ length of train
% CC_sleepers ~ CC sleepers
% kpad ~ stiffness of pad between sleepers and rail
% ksleep ~ stiffness of sleeper
% kbal ~ stiffness of ballast
% cpad ~ damping for pad
% csleep ~ damping for sleeper
% cbal ~ damping for ballast
% msleep ~ mass of sleeper
% mbal ~ mass of ballast
% NR ~ number of elements on rail between sleepers.
```

```
UIC60_A=60.21/7850; %m^2
UIC60_I11=3038.30e-8; %m^4
UIC60_I12=0; %m^4
UIC60_I22=512.30e-8; %m^4
UIC60_J=UIC60_I11+UIC60_I22;

if strcmp(LeftRight,'Left')
    bridgeZ=-abs(CC_rail/2-0.9);
elseif strcmp(LeftRight,'Right')
    bridgeZ=abs(CC_rail/2-0.9);
else
    disp('The option LeftRight has to be either "Left" or "Right"\n')
end


x0Bridge=(LB-floor(LB/CC_sleepers)*CC_sleepers)/2;
LPrePostRail=ceil((LT)/CC_sleepers)*CC_sleepers+CC_sleepers-x0Bridge;
x_nodesRail=-LPrePostRail:CC_sleepers:(LPrePostRail+LB);
x_nodesRailExtra=-LPrePostRail:CC_sleepers/2:(LPrePostRail+LB);
[~,ia]=setdiff(int16(x_nodesRailExtra*10),int16(x_nodesRail*10));
x_nodesRailExtra=x_nodesRailExtra(ia);
y_nodesRailBridge=[0 -0.221 -(0.221+0.500)];
nodeBridgeStart=find(x_nodesRail>0.01,1);
nodeBridgeEnd=find(x_nodesRail>(LB-CC_sleepers),1);
nsetPreBridge=1:1:nodeBridgeStart-1;
nsetBridge=nodeBridgeStart:1:nodeBridgeEnd;
nsetPostBridge=nodeBridgeEnd+1:1:length(x_nodesRail);
fprintf(fid,'*Part,name=%s\n',partName);
fprintf(fid,'*Node,nset=nodesBridge\n');
for m=1:3
    for n=1:length(nsetBridge)
        if m<3
            fprintf(fid,'%i, %f, %f, %f\n',m*1000+n...
                ,x_nodesRail(nsetBridge(n)),y_nodesRailBridge(m),0);
        else
            fprintf(fid,'%i, %f, %f, %f\n',m*1000+n...
                ,x_nodesRail(nsetBridge(n)),y_nodesRailBridge(m),bridgeZ);
        end
    end
end
nsetExtra=1000001:1:(1000000+length(x_nodesRailExtra));
fprintf(fid,'*Node,nset=nodesRailExtra\n');
for n=1:length(nsetExtra)
    fprintf(fid,'%i, %f, %f, %f\n',nsetExtra(n),x_nodesRailExtra(n),0,0);
end


fprintf(fid,'*Nset,nset=BridgeContactNodes,generate\n%i,%i,1\n'...
    ,3001,3000+length(nsetBridge));

fprintf(fid,'*Node,nset=nodesPreBridge\n');
```

```
for m=1:4
    for n=1:length(nsetPreBridge)
            fprintf(fid,'%i, %f, %f, %f\n',m*10000+n...
                ,x_nodesRail(nsetPreBridge(n)),-(m-1)*0.1,0);
    end
end

fprintf(fid,'*Node,nset=nodesPostBridge\n');
for m=1:4
    for n=1:length(nsetPostBridge)
            fprintf(fid,'%i, %f, %f, %f\n',m*100000+n...
                ,x_nodesRail(nsetPostBridge(n)),-(m-1)*0.1,0);
    end
end
fprintf(fid,'*Nset,nset=Rail,generate\n%i,%i,1\n%i,%i,1\n%i,%i,1\n'...
    ,1001,1000+length(nsetBridge),10001,10000+length(nsetPreBridge)...
    ,100001,100000+length(nsetPreBridge));
%
fprintf(fid,'*Nset,nset=BCFixed,generate\n%i,%i,1\n%i,%i,1\n'...
    ,40001,40000+length(nsetPreBridge)...
    ,400001,400000+length(nsetPostBridge));
fprintf(fid,'*Nset,nset=BC1\n1001\n');
fprintf(fid,'*Nset,nset=BC4\nRail\n');
n_els=0;
nodesetRail=[10001:1:10000+length(nsetPreBridge) ...
    1001:1:1000+length(nsetBridge) 100001:1:100000+length(nsetPostBridge)];
A=[nodesetRail nsetExtra];
B=[x_nodesRail x_nodesRailExtra];
[B,ic]=sort(B);
A=A(ic);
% Rail elements
fprintf(fid,'*Element,type=B33,elset=Rail\n');
for n=1:length(A)-1
    n_els=n_els+1;
    fprintf(fid,'%i, %i, %i\n',n_els,A(n),A(n+1));
end
% Spring elements
fprintf(fid,'*Element,type=Spring2,elset=Kpad\n');
for n=1:length(nsetPreBridge)
    n_els=n_els+1;
    fprintf(fid,'%i, %i, %i\n',n_els,10000+n,20000+n);
end
for n=1:length(nsetBridge)
    n_els=n_els+1;
    fprintf(fid,'%i, %i, %i\n',n_els,1000+n,2000+n);
end
for n=1:length(nsetPostBridge)
    n_els=n_els+1;
    fprintf(fid,'%i, %i, %i\n',n_els,100000+n,200000+n);
end
```

```
fprintf(fid,'*Element,type=Spring2,elset=Ksleep\n');
for n=1:length(nsetPreBridge)
    n_els=n_els+1;
    fprintf(fid,'%i, %i, %i\n',n_els,20000+n,30000+n);
end
for n=1:length(nsetBridge)
    n_els=n_els+1;
    fprintf(fid,'%i, %i, %i\n',n_els,2000+n,3000+n);
end
for n=1:length(nsetPostBridge)
    n_els=n_els+1;
    fprintf(fid,'%i, %i, %i\n',n_els,200000+n,300000+n);
end
fprintf(fid,'*Element,type=Spring2,elset=Kbal\n');
for n=1:length(nsetPreBridge)
    n_els=n_els+1;
    fprintf(fid,'%i, %i, %i\n',n_els,30000+n,40000+n);
end
for n=1:length(nsetPostBridge)
    n_els=n_els+1;
    fprintf(fid,'%i, %i, %i\n',n_els,300000+n,400000+n);
end
% Damper elements.
fprintf(fid,'*Element,type=Dashpot2,elset=Cpad\n');
for n=1:length(nsetPreBridge)
    n_els=n_els+1;
    fprintf(fid,'%i, %i, %i\n',n_els,10000+n,20000+n);
end
for n=1:length(nsetBridge)
    n_els=n_els+1;
    fprintf(fid,'%i, %i, %i\n',n_els,1000+n,2000+n);
end
for n=1:length(nsetPostBridge)
    n_els=n_els+1;
    fprintf(fid,'%i, %i, %i\n',n_els,100000+n,200000+n);
end
fprintf(fid,'*Element,type=Dashpot2,elset=Csleep\n');
for n=1:length(nsetPreBridge)
    n_els=n_els+1;
    fprintf(fid,'%i, %i, %i\n',n_els,20000+n,30000+n);
end
for n=1:length(nsetBridge)
    n_els=n_els+1;
    fprintf(fid,'%i, %i, %i\n',n_els,2000+n,3000+n);
end
for n=1:length(nsetPostBridge)
    n_els=n_els+1;
    fprintf(fid,'%i, %i, %i\n',n_els,200000+n,300000+n);
end
fprintf(fid,'*Element,type=Dashpot2,elset=Cbal\n');
```

```
for n=1:length(nsetPreBridge)
    n_els=n_els+1;
    fprintf(fid,'%i, %i, %i\n',n_els,30000+n,40000+n);
end
for n=1:length(nsetPostBridge)
    n_els=n_els+1;
    fprintf(fid,'%i, %i, %i\n',n_els,300000+n,400000+n);
end
fprintf(fid,'*Element,type=mass,elset=Msleep\n');
for n=1:length(nsetPreBridge)
    n_els=n_els+1;
    fprintf(fid,'%i,%i\n',n_els,20000+n);
end
for n=1:length(nsetBridge)
    n_els=n_els+1;
    fprintf(fid,'%i,%i\n',n_els,2000+n);
end
for n=1:length(nsetPostBridge)
    n_els=n_els+1;
    fprintf(fid,'%i,%i\n',n_els,200000+n);
end
fprintf(fid,'*Element,type=mass,elset=Mbal\n');
for n=1:length(nsetPreBridge)
    n_els=n_els+1;
    fprintf(fid,'%i,%i\n',n_els,30000+n);
end
for n=1:length(nsetPostBridge)
    n_els=n_els+1;
    fprintf(fid,'%i,%i\n',n_els,300000+n);
end

fprintf(fid,'*Beam General Section, elset=Rail
,poisson=0.33,density=7850.,section=GENERAL\n');
fprintf(fid,'%f, %f, %f, %f, %f\n',UIC60_A,UIC60_I11,UIC60_I12,UIC60_I22,UIC60_J);
fprintf(fid,'0.,0.,-1\n');
fprintf(fid,'%f, %f\n',2.1e+11,8.1e+10);
fprintf(fid,'*Spring,elset=Kpad\n2,2\n%f\n',kpad);
fprintf(fid,'*Spring,elset=Ksleep\n2,2\n%f\n',ksleep);
fprintf(fid,'*Spring,elset=Kbal\n2,2\n%f\n',kbal);
fprintf(fid,'*Dashpot,elset=Cpad\n2,2\n%f\n',cpad);
fprintf(fid,'*Dashpot,elset=Csleep\n2,2\n%f\n',csleep);
fprintf(fid,'*Dashpot,elset=Cbal\n2,2\n%f\n',cbal);
fprintf(fid,'*Mass,elset=Msleep\n%f\n',msleep);
fprintf(fid,'*Mass,elset=Mbal\n%f\n',mbal);
fprintf(fid,'*Equation\n');
% SET pM to pM=[1 3 4 5 6] to get fully functional rails!!
pM=[1 2 3 4 5 6];
% pM=[1 3 4 5 6];
for n=1:length(nsetPreBridge)
    for m=2:3
```

```
            for p=pM
            fprintf(fid,'2\n%i,%i,-1,%i,%i,1\n',m*10000+n,p...
                ,40000+n,p);
            end
    end
end
for n=1:length(nsetPostBridge)
    for m=2:3
        for p=pM
        fprintf(fid,'2\n%i,%i,-1,%i,%i,1\n',m*100000+n,p...
            ,400000+n,p);
        end
    end
end
for n=1:length(nsetBridge)
    for m=2:2
        for p=pM
        fprintf(fid,'2\n%i,%i,-1,%i,%i,1\n',m*1000+n,p...
            ,3000+n,p);
        end
    end
end
% %%% Constrain railnodes
pM=[1 2 3];
% pM=[1 3];

for n=1:length(nsetPreBridge)
    for m=1
        for p=pM
        fprintf(fid,'2\n%i,%i,-1,%i,%i,1\n',m*10000+n,p...
            ,40000+n,p);
        end
    end
end
for n=1:length(nsetPostBridge)
    for m=1
        for p=pM
        fprintf(fid,'2\n%i,%i,-1,%i,%i,1\n',m*100000+n,p...
            ,400000+n,p);
        end
    end
end

pM=[2 3];
% pM=[3];
for n=1:length(nsetBridge)
    for m=1
        for p=pM
        fprintf(fid,'2\n%i,%i,-1,%i,%i,1\n',m*1000+n,p...
            ,3000+n,p);
```

```
        end
    end
end
fprintf(fid,'*Surface,name=RailSurf,type=element\nRail\n');
fprintf(fid,'*Surface,name=TrackBridgeInterface,type=node\nBridgeContactNodes,1\n');
fprintf(fid,'*End part\n');
```

C.5   Function generatePartSurfMS

```
function generatePartSurfMS(fid,partName)
% This script generates a part with "partName" in file with fileID "fid"
% "fid" has to be open before script is run.
% Mwa ~ mass of the wagon.
% Mwh ~ mass of one wheel.
% K ~ stiffness of spring in MS model.
% C ~ viscous damping coeff in MS model.

h1=0.2;
h2=0.1;
h3=0.2;

fprintf(fid,'*Part,name=%s\n',partName);
fprintf(fid,'*Node,nset=allNodes\n');
fprintf(fid,'1, %f,%f,%f\n',-h1/2,-h2,h3/2);
fprintf(fid,'2, %f,%f,%f\n',h1/2,-h2,h3/2);
fprintf(fid,'3, %f,%f,%f\n',h1/2,-h2,-h3/2);
fprintf(fid,'4, %f,%f,%f\n',-h1/2,-h2,-h3/2);
fprintf(fid,'5, %f,0,%f\n',h1/2,0);
fprintf(fid,'6, %f,0,%f\n',-h1/2,0);
fprintf(fid,'*Nset,nset=BCROT\n1\n');
fprintf(fid,'*Nset,nset=connectNode\n1\n');
fprintf(fid,'*Element,type=R3D4,elset=Wheel\n1, 1,2,5,6\n2, 6,5,3,4\n');
fprintf(fid,'*Rigid body,elset=Wheel,ref node=1\n');
fprintf(fid,'*Surface,name=Wheel,type=element\nWheel,SNEG\n');
fprintf(fid,'*End part\n');
```

C.6   Function generatePartMS

```
function generatePartMS(fid,partName,Mwa,Mwh,K,C)
% This script generates a part with "partName" in file with fileID "fid"
% "fid" has to be open before script is run.
% Mwa ~ mass of the wagon.
% Mwh ~ mass of one wheel.
% K ~ stiffness of spring in MS model.
% C ~ viscous damping coeff in MS model.

fprintf(fid,'*Part,name=%s\n',partName);
fprintf(fid,'*Node,nset=allNodes\n');
fprintf(fid,'1, 0,0,0\n');
```

```
fprintf(fid,'2, 0,1,0\n');
fprintf(fid,'*Nset,nset=connectNode\n1\n');
fprintf(fid,'*Element,type=mass,elset=massWheel\n1, 1\n');
fprintf(fid,'*Element,type=mass,elset=massWagon\n2, 2\n');
fprintf(fid,'*Mass,elset=massWheel\n%f\n',Mwh);
fprintf(fid,'*Mass,elset=massWagon\n%f\n',Mwa);
fprintf(fid,'*Element,type=springA,elset=spring\n3, 1,2\n');
fprintf(fid,'*Spring,elset=spring\n\n%f\n',K);
fprintf(fid,'*Element,type=dashpotA,elset=dashpot\n4, 1,2\n');
fprintf(fid,'*Dashpot,elset=dashpot\n\n%f\n',C);
fprintf(fid,'*Equation\n');
for n=[1 3 4 5 6]
    fprintf(fid,'2\n 2,%i,-1, 1,%i,1\n',n,n);
end
fprintf(fid,'*End part\n');
```